Preparation and Characterization of MnSi, MnGe and $Mn_{1-x}Fe_xSi$ Thin Films: Magnetic Properties under the Influence of Strain and Finite Size Effects

Von der Fakultät für Elektrotechnik, Informationstechnik, Physik
der Technischen Universität Carolo-Wilhelmina zu Braunschweig
zur Erlangung des Grades einer Doktorin
der Naturwissenschaften (Dr. rer. nat.)
genehmigte

Dissertation

von

Josefin Engelke
aus Hildesheim

Eingereicht am 14.11.2014
Disputation am 13.02.2015

1. Referent: Priv.-Doz. Dr. Dirk Menzel
2. Referent: Prof. Dr. Paul Fumagalli

Druckjahr: 2015

Vorabveröffentlichungen von Ergebnissen der Dissertation

Teilergebnisse aus dieser Arbeit wurden mit Genehmigung der Fakultät für Elektrotechnik, Informationstechnik, Physik, vertreten durch den Mentor der Arbeit, in folgenden Beiträgen vorab veröffentlicht.

Publikationen:

J. Engelke, T. Reimann, L. Hoffmann, S. Gass, D. Menzel, and S. Süllow: *Spin-Spin Correlation Length in MnSi Thin Films*, J. Phys. Soc. Jpn. **81**,124709 (2012).

D. Menzel, J. Engelke, T. Reimann, and S. Süllow: *Enhanced critical fields in MnSi thin films*, J. Kor. Phys. Soc. **62**, 1580-1583 (2013).

J. Engelke, D. Menzel, and V. A. Dyadkin: *Thin films MnGe grown on Si(111)*, J. Phys.: Condens. Matter **25**, 472201 (2013).

J. Engelke, D. Menzel, H. Hidaka, T. Seguchi, and H. Amitsuka: *Suppressed magnetic order and non-Fermi-liquid behavior in MnSi thin films under hydrostatic pressure*, Phys. Rev. B **89**, 144413 (2014).

Tagungsbeiträge:

J. Engelke, T. Reimann, D. Menzel, and S. Süllow: *Morphology and magnetism of MnSi thin films* (Vortrag), Frühjahrstagung der DPG 2012, Berlin.

J. Engelke, N. van Elten, T. Reimann, D. Menzel, and S. Süllow: *Magnetic and transport properties of MnSi thin films* (Poster), Frühjahrstagung der DPG 2013, Regensburg.

J. Engelke, T. Reimann, N. Van Elten, and D. Menzel: *Magnetic and transport properties of MnSi thin films* (Vortrag), International Workshop: Dzyaloshinskii-Moriya Interaction and Exotic Spin Structures, DMI 2013, Veliky Novgorod, Russland.

J. Engelke, T. Reimann, N. Van Elten, and D. Menzel: *Hall effect of MnSi thin films* (Poster), International Workshop: Dzyaloshinskii-Moriya Interaction and Exotic Spin Structures, DMI 2013, Veliky Novgorod, Russland.

J. Engelke, D. Menzel, V. A. Dyadkin: *MnGe grown as a thin film - a new aspirant in skyrmion research* (Vortrag), Frühjahrstagung der DPG 2014, Dresden.

J. Engelke, D. Menzel, H. Hidaka, T. Seguchi, H. Amitsuka: *Behavior of MnSi thin films under hydrostatic pressure* (Poster), Frühjahrstagung der DPG 2014, Dresden.

J. Engelke, D. Menzel, V. A. Dyadkin: *MnGe grown on Si(111) - a new aspirant in skyrmion research* (Poster), SKYMAG 2014, Paris, Frankreich.

Contents

Chapter 1

Introduction

In recent years the field of spintronics has aroused the interest not only of solid state physicists but also of companies developing data processing technology, which has led to fast progress in this field of research. The term 'spintronics' is a made-up word for a branch of science combining the magnetic and the electric properties of the electron, i. e. its spin and its charge [1].

The connection between magnetism and electric transport has been known since the middle of the 19th century, when the anisotropic magnetoresistance (AMR) effect was discovered by W. Thomson [2]. Nevertheless the spin of an electron did not play a role in the development of electronics for a long time. This was mainly owing to the fact that the AMR effect is rather small: The resistivity of a metal changes by only a few percent, when a magnetic field is switched from parallel to perpendicular to the current direction. Spintronics started to make progress, when thin film technology had developed to a point, where the production of layered structures with nanometer thicknesses was possible. The preparation and investigation of multilayers of ferromagnetic Fe and antiferromagnetic Cr led to the discovery of the giant magnetoresistance (GMR) effect in 1988 [3, 4]. The size of the GMR effect considerably exceeds the AMR effect and brings the phenomenon closer to applications.

The crucial property of the layered structures of Fe and Cr is the antiferromagnetic coupling of two Fe layers through a Cr layer. This coupling makes sure that the magnetization vectors of next-neighbored Fe layers point into opposite directions in zero magnetic field, while an applied field forces the magnetization of all layers into the same direction. The large difference in resistivity between the parallel and the antiparallel alignment of the magnetization in two layers defines the GMR effect. Its occurrence can be explained by spin dependent scattering of conduction electrons in the different layers [4].

Shortly after the GMR effect was discovered, even larger tunneling mag-

netoresistance (TMR) effects were found to exist in multilayers of magnetic materials separated by an insulating layer [5, 6]. This offered new opportunities for data storage devices based on magnetism. One promising example is the magnetoresistive random-access memory (MRAM) [7]. Here, the storage elements arranged in an array consist of two ferromagnetic layers and an insulating layer in between. While the magnetization of one layer is pinned to a certain direction, the second layer can be magnetized parallel or antiparallel with regard to the first one, which corresponds to '0' and '1', respectively. The advantage of storing information in the form of magnetization directions is the non-volatility. In contrast to storage media that work with electric charges MRAMs do not need any refreshing cycles to retain the information.

Another concept for a magnetic memory device was introduced by Parkin *et al.* in 2003 [8, 9]. The proposed device is called Racetrack Memory and consists of magnetic nanowires, which are attached perpendicularly to a Si wafer. In these ferromagnetic wires domains with opposite magnetization direction are separated by domain walls arranged at periodic distances. Data can be stored in the orientation of the magnetization of single domains and these domains can be moved through the wire, so that they pass reading and writing devices positioned in the middle of this 'racetrack'. The propagation of domain walls can be achieved by a pulsed current taking advantage of spin momentum transfer. With each pulse a spin polarized current moves through a domain wall, where the local magnetization rotates from one direction to the opposite continuously. Because of the s-d interaction the spins of the conduction electrons follow the magnetic moments in the wall [1]. Consequently the magnetic moments rotate in a reverse sense, which leads to a motion of the domain wall.

A great advantage of the Racetrack Memory is the combination of non-volatility with the three-dimensional structure, where nanowires are arranged perpendicular on an underlying wafer. This allows much higher storage density than in flat two-dimensional devices and, furthermore, only one reading and one writing unit are needed for each nanowire containing many bits, whereas MRAMs need a reading and writing unit for every bit [10].

However, when it comes to the implementation of Racetrack Memory devices, the technology depends sensitively on the current density necessary to move a domain wall and on the velocity of its movement. Thereby the domain wall velocity must be in the order of $100\,\mathrm{m/s}$ in order to reach the speed of data processing achieved by competing storage media [9]. The required current density is governed by defects such as pinning sites, which are needed to stabilize domain walls in certain positions. If only a small amount of such defects is present in a thin film, the current density for domain wall motion is in the order of $10^7\,\mathrm{A/cm^2}$ [11], which is quite large regarding the Joule heating that is caused by the current. Since the compact design of Racetrack Memories is very sensitive to heat, and since thermal

fluctuations can eventually move domain walls or even switch magnetization directions, the high currents are a big problem for this technology.

One possibility to overcome the problem is to find a magnetic 'object', which can be moved smoothly at low current densities. A promising aspirant for this purpose is the skyrmion. A skyrmion is a whirl-like magnetic structure, which has recently been discovered in the so-called A-phase of the cubic helimagnet MnSi [12]. Although skyrmions occur in just a very small phase pocket close to the magnetic ordering temperature, a great deal of attention has been concentrated on this new magnetic structure because of its potential application in the field of spintronics. A skyrmion offers new prospects in data processing, since the topologically stable magnetic whirl can be moved with current densities in the order of $100\,\mathrm{A/m^2}$ [13], which is around 100,000 times less than needed for the motion of a domain wall. Moreover, skyrmions have a diameter of just a few nanometers, which offers good perspectives for the miniaturization of storage devices.

Soon after the discovery of skyrmion textures in MnSi by small-angle neutron scattering [12] the same magnetic structure has been identified in a number of different materials. On the one hand the skyrmion phase is inherent to the metallic B20 compounds, which possess a helimagnetic ground state, such as MnGe [14], FeGe [15], $Fe_{1-x}Co_xSi$ [16–18] and $Mn_{1-x}Fe_xSi$ [19]. Here the skyrmions can be observed by small-angle neutron scattering in the case of bulk material or, when thin layers of the B20 compounds are prepared, Lorentz TEM offers an excellent tool to get a real-space image of the skyrmion lattice. On the other hand also insulators can possess a magnetic phase diagram with a skyrmion phase appearing close to the ordering temperature, as observed for example in Cu_2OSeO_3 [20]. All listed materials exhibit a crystal structure, which lacks inversion symmetry and thereby promotes the Dzyaloshinskii-Moriya (DM) interaction. This magnetic interaction favors a canting of magnetic moments and by the interplay with ferromagnetic exchange a helical magnetic ground state is formed. Although skyrmions only appear as a metastable state, they can be stabilized by thermal fluctuation closely below the ordering temperature [12].

For the future use of skyrmions in spintronic applications it is especially interesting to investigate skyrmionic phases occurring in thin films, since thin films can easily be implemented in many devices. It is a nice coincidence that skyrmions in thin layers are more stable than in bulk and that they cover a larger part of the magnetic phase diagram [18, 21, 22].

An example, where good progress has been made in recent time, is an iron monolayer on an Ir(111) surface [22, 23]. In these films the DM interaction is not caused by the properties of the crystal structure, but is induced by the surfaces and interfaces. At 8 K it can be observed by spin polarized STM that a helix propagating in the film plane is the magnetic ground state of the system. In magnetic fields around 1 T, however, a hexagonal skyrmion lattice appears, which is transformed into a saturated state with ferromagnetic spin

alignment at 1.8 T. Very interesting and promising physics arise, when the temperature of the sample is lowered to 4.2 K. At this temperature a field sweep does not generate the expected magnetic phases, but the Fe monolayer stays in its current state although the field strength is reached, where a different state is energetically preferable. Romming *et al.* [24] argue that an energy barrier separates the magnetic states, which can be overcome at 8 K, because the thermal energy is sufficient. At lower temperatures, however, the energy to pass the barrier cannot be provided by thermal fluctuations and the sample persists in the energetically unfavorable state. This scenario offers the possibility to write and to delete single skyrmions. When the sample is in the saturated state and the field is lowered until the the skyrmion phase possesses the lowest energy, the spins stay ferromagnetically aligned, but adding locally a small amount of energy will stimulate the formation of a skyrmion. It has been shown that performing a voltage sweep on a STM tip positioned close to the surface can provide the needed energy to create or to destroy skyrmions by this mechanism [24]. It is self-explanatory that the deliberate manipulation of skyrmions offers great perspectives for the development of spintronic devices.

Also cubic B20 compounds like MnSi offer a good chance to prepare thin films with a large skyrmion phase. In thin films uniaxial anisotropy is induced by the finite size effects and by eventually occurring strain due to lattice mismatches between the substrate and the film. It was shown by energy minimization calculations that skyrmions can be stabilized by uniaxial anisotropy in cubic magnets without inversion symmetry and that they tend to occur in larger regions of the magnetic phase diagram than in bulk crystals [21].

This theoretical result has been confirmed for MnSi by measurements on a thin layer with 50 nm thickness, which has been prepared from a bulk crystal by mechanical polishing and argon ion thinning [25]. In such a layer uniaxial anisotropy is induced by the surfaces and promotes skyrmions in certain field ranges. While helices propagating in the film plane are observed by Lorentz TEM in small magnetic fields, skyrmions occur in a field range from approximately 0.15 T to 0.4 T. In this case the field is applied perpendicular to the surface of the layer and the skyrmions are aligned in the same direction [25] (compare figure 1.1). The fact that skyrmions have already been observed in these thin layers of MnSi and also in $Fe_{1-x}Co_xSi$ [18] emphasizes how promising the B20 compounds are.

As a substrate for growing thin films of B20 compounds silicon is very suitable. Comparing the (111) planes of Si and MnSi the lattice mismatch amounts only -3 %, which means that epitaxial growth with small tensile strain is possible [26]. Also MnGe fits the Si(111) plane with a mismatch of 2 %. Moreover, growing thin films on Si substrates is very convenient for applications in data processing technology, where silicon-based integrated circuits are well established.

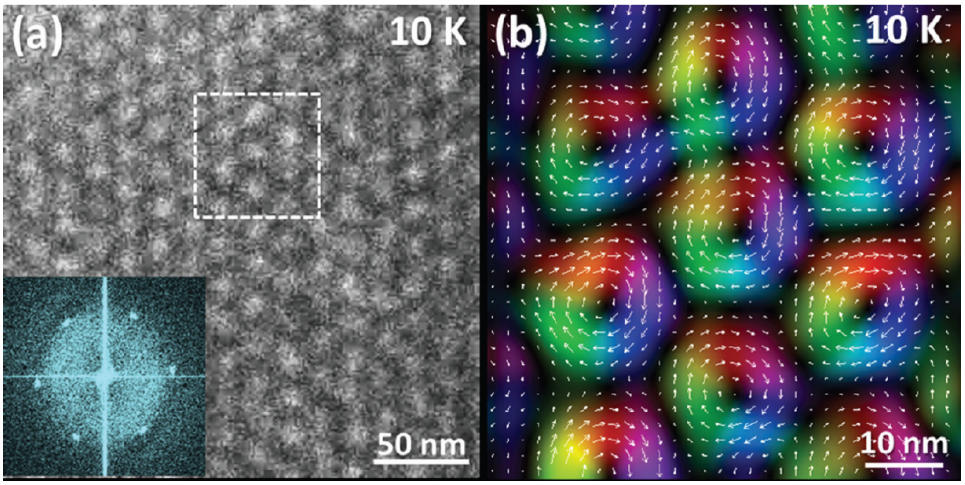

Figure 1.1: (a) Lorentz TEM image of a MnSi thin layer in a perpendicular magnetic field of 0.18 T, inset: Fourier transformation of the real space image, taken from [25], (b) magnetization distribution in the film plane, taken from [25]

This work aims to investigate the potentials of thin films of different B20 compounds. Therefore films of MnSi, MnGe, and $Mn_{1-x}Fe_xSi$ are grown by molecular beam epitaxy (MBE). The first ambition with all three different materials is to prepare samples of excellent morphological and structural quality. Afterwards the work proceeds with the characterization of the thin films, especially with regard to their magnetic and transport properties.

Next to the skyrmion phase MnSi provides another very interesting field of research, which is its quantum criticality. A lot of work has been spent on this phenomenon and its nature is still under lively discussion [27–29]. When hydrostatic pressure is applied on a MnSi single crystal, the magnetic ordering temperature can be decreased. At a pressure of 1.46 GPa magnetic order is suppressed and in the close surrounding of the quantum phase transition non-Fermi-liquid behavior is observed manifesting itself by a deviation from the T^2 behavior of the resistivity. A similar suppression of magnetism is effected by substituting approximately 15 % of the Mn atoms by Fe [30, 31].

Even though, at a first glance, this phenomenon is not related to the search for skyrmions, one part of this work will be concerned with analyzing the occurrence of quantum criticality in MnSi thin films under pressure and in samples with Fe doping. This fundamental research is crucial in order to expand the knowledge about the mechanisms, which govern the behavior of the compound, and it will be helpful for a complete understanding of the investigated system. Since recent findings indicate the existence of fluctuating skyrmionic textures beyond the critical pressure [32], there might even be a close connection between the non-Fermi-liquid behavior near to the quantum

phase transition and the appearance of skyrmions.

In the following a short overview of the organization of this thesis will be given.

In the beginning chapter 2 provides the theoretical framework needed for the understanding of the presented work. This includes the physical basics and theories of magnetism and electric transport. Here mainly three issues are addressed. The first section deals with the magnetism of cubic systems without inversion symmetry and in this context also the properties of skyrmions are discussed. Then a section on the different Hall effect contributions is followed by an overview of the theories on non-Fermi-liquid behavior. The second part of chapter 2 contains details on the preparation of thin films. The mechanisms of film growth are addressed and afterwards the MBE system with its equipment is described. Since RHEED is the most important technique to characterize a deposited layer in situ, a section is dedicated to the theory of this method.

Chapter 3 contains all results that have been obtained for MnSi thin films. As an introduction the properties of bulk MnSi are summarized. In the following two methods to grow MnSi thin films are presented and discussed. For the morphological and structural characterization of the samples RHEED, AFM and TEM images are analyzed. Susceptibility measurements reveal a thickness dependence of the magnetic ordering temperature T_{ord}, which is explained by reduced spin-spin interactions in very thin films. Field dependent magnetization and magnetoresistance data reveal that the critical field values are considerably enhanced compared to bulk samples, especially when magnetic fields are applied perpendicular to the film plane. In the same field configuration Hall effect measurements give evidence for a topological Hall contribution in a large field and temperature range. The transport measurements with in-plane fields show additional transitions, which are not known from bulk MnSi. Combining all these data magnetic phase diagrams are established for MnSi thin films, where the cases of magnetic fields applied perpendicular and parallel to the film plane are considered. The last part of chapter 3 will describe resistivity measurement on MnSi thin films under hydrostatic pressure. A decrease of T_{ord} under pressure indicates that the observed enhancement of T_{ord} in the thin films is connected to strain. Furthermore non-Fermi-liquid behavior occurring close to the point, where magnetic order is suppressed, is discussed to be a consequence of fluctuating skyrmion textures.

In chapter 4 the preparation and characterization of MnGe thin films on Si(111) will be described. For these films the structural analysis of the samples by RHEED and AFM reveals island growth. Comparing MnGe to MnSi thin films, the susceptibility suggests that the magnetic structure of MnGe is close to antiferromagnetism, while MnSi is a weak ferromagnet. Magnetization and magnetoresistance measurements hint to very large saturation fields, which leads to the conclusion that the helical spin structure is much

more rigid in MnGe than in MnSi.

Finally, in chapter 5 the suppression of magnetic order is investigated for $Mn_{1-x}Fe_xSi$ thin films. A first series of samples was prepared by codeposition and a second series was codeposited and additionally annealed afterwards. The properties of these two different types of films are compared and discussed. For all films with Fe doping a reduced ordering temperature is observed and a complete suppression of magnetic order occurs for $x = 0.15 \pm 0.05$ in codeposited films. However, the investigation of non-Fermi liquid behavior is hardly accessible by resistivity measurements, since a Kondo minimum masks the possibly occurring deviation from the T^2-law.

Chapter 2

Theoretical Framework

2.1 Magnetic Phases in Chiral Systems

Since the scope of this work is the preparation of thin films of chiral magnets, in this section an overview of the different magnetic phases occurring in these systems will be given. In MnSi as well as in the isostructural compounds MnGe and $Mn_{1-x}Fe_xSi$ a large variety of exotic spin modulations can be realized, which is mainly owing to their B20 crystal structure. As it lacks inversion symmetry, the asymmetric Dzyaloshinskii-Moriya (DM) interaction does not cancel out, but leads to a tilting between neighboring spins. This results in helical, conical and skyrmionic phases occurring for instance in MnSi as it can be viewed in figure 2.1 [12]. In the following the theory for calculating the stable magnetic states of a cubic magnet without inversion symmetry will briefly be presented. Afterwards some properties of the skyrmionic phase will be discussed and in the end of this section the case of thin films will be addressed, where additional anisotropies can stabilize skyrmions in larger regions of the magnetic phase diagram.

For a system close to a phase transition the Ginzburg-Landau theory is an adequate tool to find its equilibrium magnetic state. The theory describes continuous phase transitions phenomenologically by introducing an order parameter, which is finite in the ordered phase and zero above the ordering temperature. For a ferromagnet the magnetization $\vec{M}$ serves as the order parameter and the free energy functional $\mathcal{F}$ is written as a function of $\vec{M}$. Under the assumption of smoothly varying and sufficiently small $\vec{M}$ close to the phase transition $\mathcal{F}$ can be expanded in powers of $\vec{M}$, which leads to [33]

$$\begin{aligned}\mathcal{F}\left[\vec{M}\left(\vec{r}\right)\right] &= \int d^3r \left[a\vec{M}^2 + \frac{1}{2}b\left(\vec{M}^2\right)^2 + c\left(\nabla\vec{M}\right)^2 - \vec{H}\vec{M}\right] \\ &= \int d^3r\, w(\vec{M}).\end{aligned} \tag{2.1}$$

Here a, b and c are phenomenological parameters, which need to be determined for the system under investigation, and $\vec{H}$ is an external magnetic

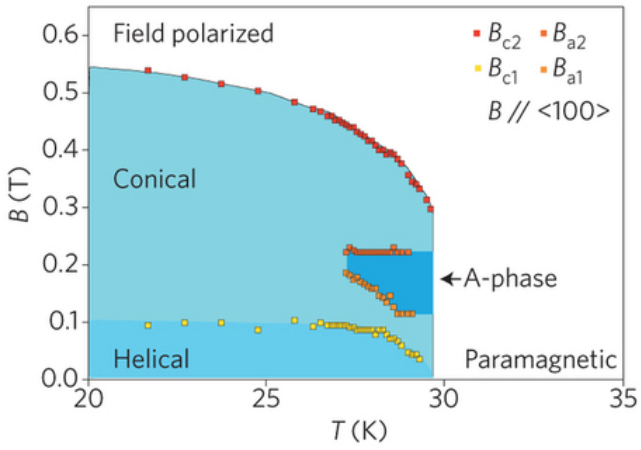

Figure 2.1: Phase diagram of MnSi as a function of the temperature and the magnetic field. The graphic is taken from [12].

field. The expression in square brackets is the free energy density that is denoted by w in the second line. Minimizing the energy functional with respect to the magnetization $\vec{M}(\vec{r})$ gives the equilibrium magnetic state, which is a magnetization along the direction of the magnetic field for the ferromagnet. For $\vec{H} = 0$ the system is isotropic, i. e. there is no preferential direction for $\vec{M}$.

For non-centrosymmetric systems as for example the helimagnet MnSi Dzyaloshinskii [34] and Bak and Jensen [35] have developed a theoretical approach based on the Ginzburg-Landau formalism, which includes antisymmetric terms of the spin density. Following their theory the energy density w_0 for a cubic helimagnet in its simplest form can be written as [21, 36, 37]

$$w_0 = A\left(\mathrm{grad}\vec{M}\right)^2 - D\vec{M}\cdot\mathrm{rot}\vec{M} - \vec{M}\cdot\vec{H}. \tag{2.2}$$

Here the first term denotes the ferromagnetic exchange energy with the exchange stiffness A, which favors a parallel alignment of the magnetic moments. The second contribution describes the asymmetric DM interaction with the Dzyaloshinskii constant D, which is proportional to the strength of the spin-orbit coupling [38]. The DM interaction, existing only in systems without inversion symmetry, prefers a perpendicular orientation of the magnetic moments. The last term accounts for the Zeeman energy in the applied magnetic field $\vec{H}$.

The energy contributions listed in equation 2.2 are essential to stabilize helical spin order and also skyrmions in certain field and temperature ranges. As it can be seen in figure 2.1 in MnSi helical and conical phases are stable in the largest part of the ordered phase below the saturation field. These are one-dimensional modulations of the magnetization, where every spin is tilted

with respect to its neighbor by a certain angle. The rotation sense is thereby determined by the sign of the Dzyaloshinskii constant. The modulation length λ of the helix considerably exceeds the lattice parameter and the helix wave vector is defined as a vector with the length $k = 2\pi/\lambda$ pointing along the propagation direction. The value of k is given by the ratio of the DM interaction and the ferromagnetic exchange [34, 35]:

$$k = \frac{D}{A}\,. \tag{2.3}$$

In a helical structure all spins are arranged in a plane that is perpendicular to the propagation direction. Thus, the net magnetization over a full period is zero. In an applied magnetic field the helix axis aligns with the field and all spins are tilted slightly into field direction and form a cone. The net magnetization, which depends on the cone angle θ, amounts $M_{cone} = M\cos\theta$ [37], where M is the local magnetization.

Until now the helimagnetic system described by equation 2.2 is still isotropic with no fixed direction of helix propagation. In real systems, however, anisotropies pin the helix to particular directions, for instance in MnSi the helical modulation tends to propagate along the $< 111 >$ crystal directions. To include the essential interactions for this pinning, the following terms of anisotropic energy density have to be included [21, 36, 37]:

$$w_a = \sum_{i=1}^{3}\left[B_{ea}\left(\frac{\partial M_i}{\partial r_i}\right)^2 + K_c M_i^4\right], \tag{2.4}$$

where the first term describes the exchange anisotropy and the second considers the cubic anisotropy of the crystal structure. The energy scales of the anisotropy are considerably smaller than the ferromagnetic exchange and give just a small correction to the magnetic state.

Besides the helical and the cone phases a skyrmion phase may occur in the magnetic phase diagram of cubic magnets without inversion symmetry. In 2009 the first evidence for skyrmions was found in the A-phase of MnSi [12], where the state was described as a superposition of three helices lying in a plane perpendicular to the magnetic field and its stability was explained by considering corrections to the free energy due to Gaussian thermal fluctuations. However, although the approach of superimposed helices is a good approximation of the magnetic state, it does not correctly reproduce the topology of skyrmions.

The name 'skyrmion' originates from the British physicist Tony Skyrme, who postulated the existence of these particle-like objects in the beginning of the 1960s. However, in his theory skyrmions were solutions from modeling the low energy dynamics of mesons and baryons [39] and were not related to magnetism. Later the idea of skyrmions was adapted for localized and topologically stable field configurations, excluding singularities. Such configurations are for example magnetic vortices, which can be stabilized in

certain crystals with magnetic order as Bogdanov showed theoretically in 1989 [40]. In contrast to the definition of a skyrmion as a three-dimensional object, in magnetic materials skyrmions are mostly two-dimensional modulations of the spin density. While no modulations occur in the z-direction, which is defined parallel to the applied magnetic field, the spin structure in the x-y-plane can be imagined as spins wrapping a sphere and being projected onto the plane. Thus, an isolated skyrmion forms a tube, whose core magnetization is antiparallel with respect to the surrounding magnetization direction.

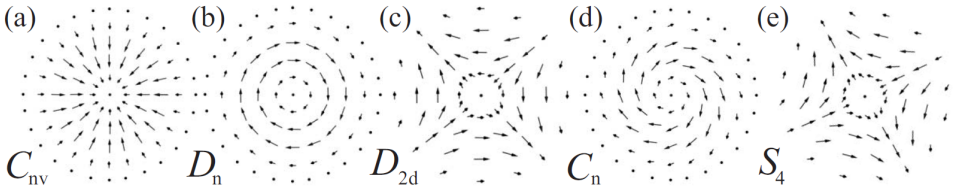

Figure 2.2: Stucture of skyrmions in crystals from different symmetry groups. The spins are projected to the plane perpendicular to the skyrmion axis, taken from [37]

The inner structure of a skyrmion depends on the crystal structure and its symmetry [37]. The spin arrangements expected in crystals of common symmetry classes are shown in figure 2.2. The common feature of all these structures is that the direction of the local magnetization in the core is opposite to the surrounding magnetization. In fact, it was shown that the skyrmion can only be stable, if the rotation angle between the core spin and those surrounding the vortex is equal to π or any multiple of π [41].

A skyrmion is an object with non-trivial topology, i. e. it cannot be unwound and smoothly be transformed into a collinear spin alignment with trivial topology. This property can be measured by the winding number W:

$$W = \frac{1}{4\pi} \int dx\, dy\, \vec{n} \cdot \left(\frac{\partial \vec{n}}{\partial x} \times \frac{\partial \vec{n}}{\partial y} \right), \tag{2.5}$$

where $\vec{n} = \vec{M}/|\vec{M}|$ is a unit vector pointing in the direction of the magnetization. W counts how many times the magnetization turns by 2π on a trajectory through the skyrmion. For MnSi the winding number is $W = -1$, where the negative sign implies that the magnetization in the core of the skyrmions is antiparallel to the applied magnetic field [42]. So, actually, the A-phase contains antiskyrmions.

In a magnetically ordered phase skyrmions tend to condensate into a lattice. As evidenced by neutron scattering experiments [12] as well as by Lorentz microscopy [25] they form a hexagonal lattice as shown in figure 2.3 in the case of MnSi. This phase is often compared with the vortex state in

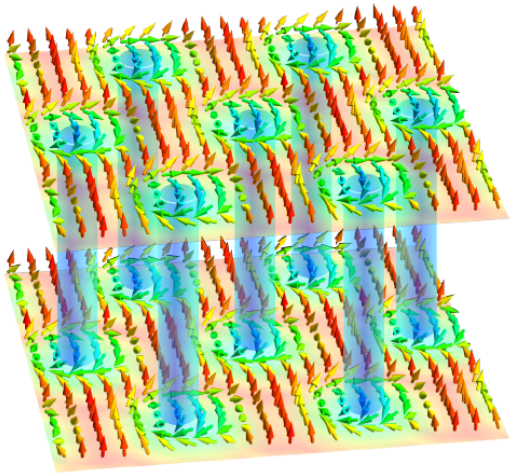

Figure 2.3: Image of a hexagonal skyrmion lattice, taken from [38]

type II superconductors, which is also composed of topologically protected tubes running along the field direction [38].

In mean field theory of cubic helimagnets skyrmions are always a metastable state, which is energetically disadvantageous against the conical phase [40]. However, for the A-phase of MnSi it has been shown that including thermal fluctuations around the mean field solution can explain the existence of the skyrmion lattice [12].

Nevertheless, the question arises, whether skyrmions may be stabilized by different mechanisms. Since the A-phase in MnSi is rather small, it would be desirable to extend it to a larger region of the magnetic phase diagram. In this context uniaxial anisotropy has been proposed to be an important parameter, which can easily be introduced into the system by distortions [21]. For example in thin films strain and surface effects give an additional contribution to the free energy and thereby affect the stability of the magnetic states. For symmetry reasons the uniaxial anisotropy axis will be normal to the film plane.

For the calculation of the stable magnetic states in a cubic helimagnet with induced uniaxial anisotropy it must be considered, which energy terms need to be included in the free energy density. The essential contributions are those given in equation 2.2 and an additional term with the uniaxial anisotropy constant K. The cubic anisotropies included in w_a as written in equation 2.4 are much smaller than the uniaxial contribution and can be neglected for a rough estimation of the stable magnetic phases. The free energy density is then described by [21]

$$w = w_0 + KM_z^2, \tag{2.6}$$

which defines the z-direction as the axis of the uniaxial distortion. Including

these energy contributions it can be calculated that a skyrmionic phase is stabilized in a wide range of parameters [21] as shown in the phase diagram depicted in figure 2.4. Here the globally stable states were calculated as a function of the magnetic field H/H_D, which is applied along the z-direction, and the uniaxial anisotropy K/K_0 by minimizing the energy given in equation 2.6. H_D is the field, where the cone phase is suppressed in a system with zero anisotropy, and K_0 is the value of uniaxial anisotropy that suppresses the cone in zero field. While in the absence of uniaxial distortions the conical phase is the stable state for all magnetic fields below H_D, already small positive values of K can suppress the cones and stabilize skyrmions and helicoids, where the term helicoid describes a helix that is distorted perpendicular to its propagation direction [36].

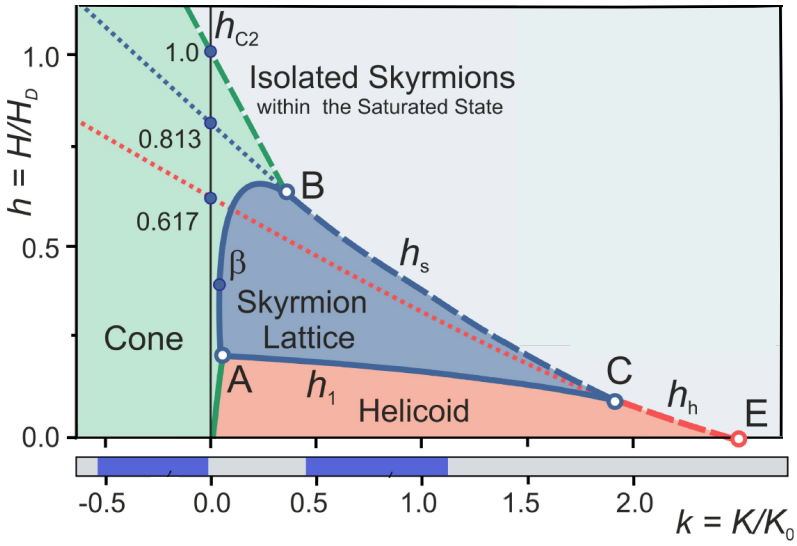

Figure 2.4: Equilibrium states in a noncentrosymmetric cubic helimagnet with magnetic field applied parallel to the axis of induced uniaxial distortions, i. e. out-of-plane, taken from [43]

The left side of the phase diagram, however, summarizes the outcome for $K < 0$. Here the calculations predict the cone phase to be the stable spin configuration for all fields below the saturation field and in the whole range of anisotropy values [43]. Thus, according to this model no skyrmions can be expected in out-of-plane magnetic fields, when the uniaxial anisotropy constant is negative.

A different situation is encountered, when a magnetic field is applied perpendicular to the axis of uniaxial anisotropy. This case has been considered in a paper by Karhu *et al.* [44], in which energy minimization calculations were published for $H \perp z$. The theoretical phase diagram contains a

skyrmionic phase, which occurs for anisotropies larger than a threshold value of $0.1\,K_0$. However, these skyrmions are aligned in the film plane along the field direction, i. e. perpendicular to the anisotropy axis. For this reason the centrosymmetric shape of the skyrmions is distorted [45].

2.2 The Hall Effect

In the previous section the main properties of skyrmions occurring in chiral magnets have been introduced and it was shown that uniaxial anisotropy is able to stabilize extended skyrmion phases in thin films. Searching for these phases Hall effect measurements provide an excellent tool, since the non-trivial topology of the skyrmions causes the occurrence of a special Hall contribution, the so-called topological Hall effect (THE). When such a Hall signal can be identified, it serves as an indication for the existence of topologically non-trivial spin structures, and its sudden onset reveals the boundaries of the implied phase in the magnetic phase diagram. However, not only the THE but also the 'usual' Hall contributions, i. e. the normal and the anomalous Hall effect, can give precious information about the properties of magnetic materials. Therefore, in this section, the principles of the Hall effect in general will be introduced, before the THE is brought into focus.

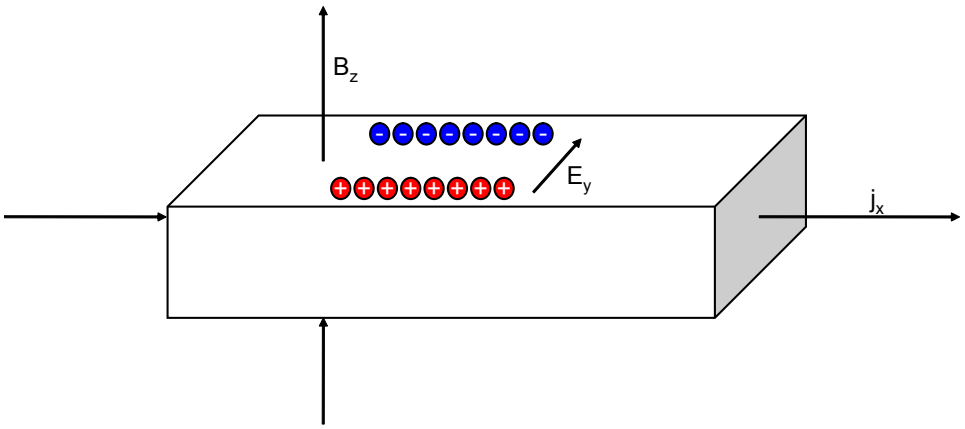

Figure 2.5: Geometry of a Hall effect measurement.

Generally, for a Hall effect measurement the sample is cut into the shape of a bar with rectangular cross section as it is shown in figure 2.5, where the geometry of a Hall experiment is depicted. A current propagates along the bar, which defines the x-direction, while a magnetic field is applied in z-direction. This leads to the emergence of an electric field E_y in y-direction, i. e. perpendicular to both the current and the magnetic field [46]. The Hall resistivity ρ_{xy} is defined as

$$\rho_{xy} = \frac{E_y}{j_x}, \tag{2.7}$$

where j_x is the current density in x-direction.

If the sample is non-magnetic, only the normal Hall effect will be observed, which is caused by the deflection of the moving electrons due to the Lorentz force. This contribution is proportional to the applied magnetic field

B:

$$\rho_{xy}^{normal} = R_0 B \tag{2.8}$$

A derivation of the normal Hall effect constant R_0 can be found in most textbooks on solid state physics as for example in references [47] and [48]. In a one-band model, where only one type of charge carriers is considered, R_0 provides a measure for the carrier concentration n:

$$R_0 = \frac{1}{nq}, \tag{2.9}$$

where q is the charge of the particles conducting the current, i. e. its value is $-e$ in the case of electrons and $+e$ in the case of positively charged holes. Thus, the sign of the Hall constant reveals which type of carriers is predominant.

In addition to the normal Hall resistivity an anomalous Hall effect (AHE) can be measured in materials that exhibit magnetic order. This anomalous contribution scales with the magnetization and therefore the total Hall effect can be written as

$$\rho_{xy} = R_0 B + \mu_0 R_s M. \tag{2.10}$$

Here μ_0 is the magnetic permeability constant. R_s, however, is not a constant, but contains the field and temperature dependence of the AHE, which is mainly determined by the resistivity of the investigated material. The understanding of this anomalous part is very sophisticated, since different mechanisms contribute to the observed signal [49].

In general, extrinsic effects, which are caused by impurities, must be distinguished from the intrinsic effect that is determined only by the band structure of the material. An early theory for the intrinsic AHE was published by Karplus and Luttinger in 1954 [50]. They showed that in the presence of spin-orbit interactions electrons acquire an anomalous velocity, when an electric field is applied. In a non-magnetic material the sum over all anomalous velocity contributions for the occupied electronic states is zero, but for a ferromagnet a net velocity remains, which is perpendicular to the electric field and to the magnetization. The transverse anomalous velocity gives a contribution to the Hall effect, which is proportional to the square of the longitudinal resistivity ρ_{xx}. Although the Karplus Luttinger theory was controversial for almost half a century, today it is accepted that the anomalous velocity can be associated with a Berry phase, which is acquired by the electrons traveling in k-space [51]. A similar concept of a Berry phase, though collected in real space, explains the emergence of the THE and will be discussed in more detail in the last part of this section.

A rival theory to the anomalous velocity is the so-called skew scattering mechanism [52, 53]. This theory assumes that the AHE cannot occur in perfect crystals, but impurities are needed as scattering centers. When conduction electrons are scattered from an impurity, they will be deflected into a

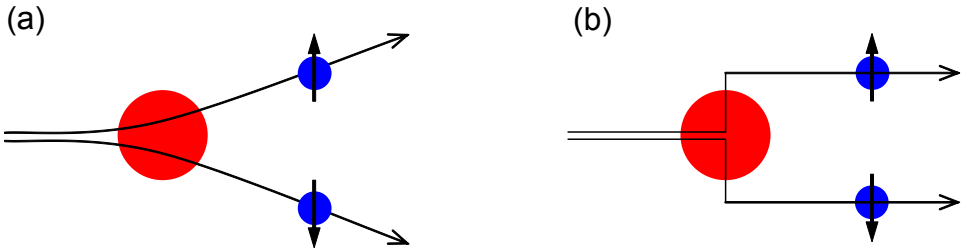

Figure 2.6: Illustrations of scattering events of conduction electrons on impurity atoms: (a) the skew scattering and (b) the side-jump effect.

preferred direction depending on their spin, which is a result of the spin-orbit coupling. This scenario illustrated in figure 2.6a leads to an imbalance of the scattering direction for the polarized electrons in a ferromagnet. The original skew-scattering theory predicts an anomalous Hall contribution which is linear in ρ_{xx}, however, recently it has been shown that it is sufficient to take the residual resistivity ρ_{xx0} for the scaling [54]. This is reasonable, since the temperature dependence of ρ_{xx} mainly reflects phonon contributions, which are negligible for the skew scattering. In contrast, ρ_{xx0} is only governed by impurities.

Another extrinsic mechanism is the side-jump effect [55], which is depicted in figure 2.6b. When an electron is scattered by an impurity atom with spin orbit interaction, it is displaced transverse to its direction of motion. This side jump is in the order of 10^{-11} m and its direction depends on the spin of the electron. In a ferromagnet it can be measured as a Hall signal that is proportional to ρ_{xx0}^2 [54].

In many magnetic materials exhibiting an AHE, all three mechanisms contribute to the observed signal and the anomalous Hall resistivity ρ_{xy}^{anom} can be written as

$$\rho_{xy}^{anom} = \alpha M \rho_{xx0} + \beta M \rho_{xx0}^2 + b M \rho_{xx}^2, \tag{2.11}$$

where the first, the second and the third term describe the skew scattering, the side jump effect and the intrinsic anomalous velocity, respectively. In this case the different contributions must be separated by their temperature and field dependencies. While the skew scattering can be identified by its linear dependence on ρ_{xx0}, the part of the AHE, which behaves as ρ^2, still contains the intrinsic and the side-jump contributions. These two can only be separated with the help of ac-Hall-conductivity measurements, which quantify the intrinsic AHE.

In addition to the normal and the anomalous Hall effect a topological contribution to the Hall resistivity may occur, when the sample is brought into a magnetic state that contains non-trivial spin structures as for example skyrmions [57]. In this case the spin of a conduction electron traveling

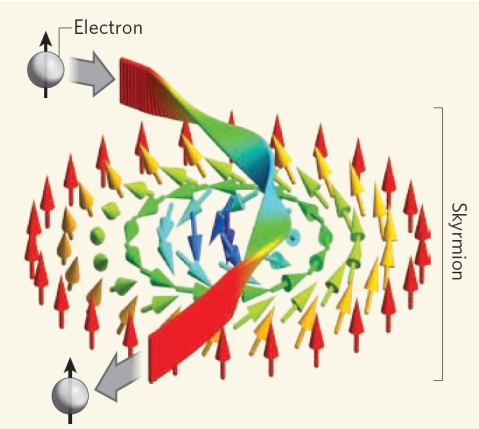

Figure 2.7: Trajectory of an electron through the spin structure of a skyrmion, taken from [56]

through the spin textures follows the direction of the local magnetization, for example it turns by 2π on a trajectory through the center of the skyrmion as shown in figure 2.7. Thereby the electron collects a geometric phase known as the Berry phase introduced by Michael Berry in 1984 [58]. In general, this geometric phase γ_n is acquired, whenever a vector moves through a non-uniform smoothly varying vector field and, in the adiabatic limit, continuously adapts to the field direction. Regarding a closed loop C of the parameter $\vec{R}$ the Berry phase can be written as

$$\gamma_n(C) = i \oint_C d\vec{R} \, \langle \psi_n | \nabla_R | \psi_n \rangle, \tag{2.12}$$

where ψ_n is a non-degenerate eigenstate of the system. After a full cycle along C the system will be in the same eigenstate as before, but it has picked up a quantum mechanical phase factor.

The Berry phase can alternatively be understood as an emergent magnetic field B_e experienced by the moving particle [59, 60]. In this field the electron is deflected perpendicular to both, B_e and its direction of motion, in the same way as by the Lorentz force in a real magnetic field, which leads to the topological Hall contribution

$$\rho_{xy}^{top} = P R_0 B_e. \tag{2.13}$$

Here R_0 is the normal Hall constant and P is the spin polarization, which is important, since majority and minority spins are deflected into opposite directions. The emergent field is given by [61, 62]

$$B_e = \phi_0 \vec{\phi} \tag{2.14}$$

with the flux quantum for an electron ϕ_0 and the skyrmion density $\vec{\phi}$, which measures the winding number W, when integrated over a magnetic unit cell.

The direction of the emergent field due to the Berry phase is antiparallel to the applied magnetic field and therefore the THE is expected to have opposite sign as the normal Hall effect [63]. Since the non-trivial spin configuration is essential for the emergent fields, the THE provides a powerful tool to find the phase boundaries of skyrmionic phases.

2.3 Non-Fermi Liquid Behavior

Non-Fermi liquid (NFL) behavior is a phenomenon, which has aroused great interest since the beginning of the 1990s. The term describes the appearance of unusual low temperature properties occurring under certain conditions in a number of metals. Regarding the temperature dependence of the specific heat, the susceptibility and the resistivity of these materials they show a behavior that is in disagreement with the predictions of Fermi liquid theory. Depending on the particular compound different scenarios are made responsible for the deviating low temperature behavior. To get an idea of the mechanisms, which promote NFL behavior, it is advisable to first recollect the principles of Fermi liquid theory as introduced by Landau in 1957 [64], which is normally applicable for the description of the behavior of metals at low temperatures.

The starting point for Landau's theory is the Fermi gas, where electrons are regarded as non-interacting particles that obey the Pauli exclusion principle. In their ground state the electrons fill all energy states up to the Fermi energy E_F, where they have the momentum $p = \hbar k_F$. Excitations of the system are electron-hole excitations made by electrons from just below the Fermi surface, which jump into a higher energy level above E_F and leave behind holes in the filled Fermi sea. The Fermi gas theory predicts a linear temperature dependence of the specific heat at low temperatures and a constant magnetic susceptibility. Although these relations can be proven in experiments on many common metals, the theory is strictly speaking insufficient, since it neglects the interactions between electrons.

In his theory of a Fermi liquid Landau introduces these interactions by adiabatically switching on a potential V, which adds to the kinetic energy of the electrons in the Hamiltonian [64]. It is important that the interaction does not evoke any symmetry breaking or phase transitions. Because of the adiabatic continuity the system can adapt to the perturbation, so that the eigenstates of the initial and the final Hamiltonian correspond to each other and can be labeled by the same quantum numbers. An excitation of the interacting system still involves an electron, which is lifted into an empty state above the Fermi surface, but since this influences the states of all other electrons, one speaks of an excited 'quasiparticle' instead of an electron. In contrast to the non-interacting case the energy of a Fermi liquid is not just the sum of all excitations. To account for the interaction of the quasiparticle with the Fermi sea, Landau replaces the mass m of the electron by its effective mass $m^\star$ in the quantitative description. Furthermore the 'f-function' is needed to include the interaction between quasiparticles. The theory predicts the following thermodynamic properties for an isotropic system [65]:

$$C = \frac{m^\star k_F}{3} k_B^2 T \tag{2.15}$$

for the specific heat and

$$\chi = \frac{1}{1+F_0^a}\frac{\mu_B^2 k_F m^\star}{\pi^2} \tag{2.16}$$

for the magnetic susceptibility. For the effective mass holds

$$\frac{m^\star}{m} = 1 + \frac{F_1^s}{3}. \tag{2.17}$$

Here F_0^a and F_1^s are Landau parameters. Comparing these expressions to the Fermi gas it turns out that only the prefactors have been modified, while the linear temperature dependence of the specific heat as well as the temperature independence of the susceptibility are identical to the predictions of Fermi gas theory, which have been proven in experiments.

The validity of the Fermi liquid model is restricted by the lifetime τ of the quasiparticles, which needs to be long enough for the quasiparticles being stable eigenstates of the system. Since τ becomes very small for high energy excitations, only energy states near the Fermi surface can participate in these processes. Furthermore the temperature must be sufficiently low. The decay rate $1/\tau$ is also an important parameter for the description of transport properties and determines the low temperature resistivity ρ, which is proportional to T^2.

In metals showing NFL behavior some assumptions of Landau's theory are violated and, thus, the predicted behavior does not occur. This can happen on the basis of different mechanisms depending on the particular class of materials. There are different kinds of models, which are used to explain the emergence of NFL behavior in different types of three-dimensional systems [65, 66]. After shortly describing the basic ideas of these models, the main part of this section focuses on the theory, which applies to MnSi.

One category of models are the multichannel Kondo models for materials, where local magnetic moments can be viewed as impurities carrying spin $\frac{1}{2}$. In a Kondo scenario the conduction electrons interact antiferromagnetically with this impurity spin and thereby compensate its magnetic moment. The ground state is a singlet state with zero spin. In the multichannel models one assumes to have different seas of conduction electrons, which can interact with the impurity ion but not with each other. Now the impurity spin cannot simply choose one of the electron 'channels' for making a singlet, since none of them should be preferred. Complex mathematics are required to solve this problem and the outcome is a particle carrying half of a spin $\frac{1}{2}$. Calculating the low temperature properties of the system yields to $C \propto T \ln T$, $\chi \propto \ln T$ and $\rho \propto \sqrt{T}$ for the heat capacity, the susceptibility and the resistivity, respectively. The Kondo model can, for example, be applied to some heavy-fermion superconductors such as UBe_{13} [67].

Another possibility to explain NFL behavior in a Kondo scenario is given by the so-called disordered Kondo models. In this case only one sea of con-

duction electrons is present, which should usually lead to Fermi liquid behavior below the characteristic Kondo temperature T_K, but disorder among the impurity ions leads to a distribution of T_K. Therefore NFL behavior is observed below the averaged T_K. An example for a disordered Kondo system is $UCu_{5-x}Pd_x$, where the Pd atoms randomly occupy the Cu sites [68].

The third type of materials, where NFL behavior can arise, are systems which can be brought near to a quantum critical point (QCP). Such a phase transition occurring at $T = 0\,\mathrm{K}$ affects the properties of the system even at finite but low temperatures. Regarding MnSi there are two possibilities to tune the magnetic ordering temperature to zero. On the one hand doping with a few percent of Fe ($x_{c,Fe} = 0.192$) or Co ($x_{c,Co} = 0.084$) suppresses the magnetically ordered state [31] and on the other hand an applied pressure of 1.46 GPa is sufficient to achieve the same [27]. However, as discussed in the following, no QCP occurs in the case of high pressure.

In general a QCP exists, when a second order phase transition is forced to zero by a control parameter, that is not the temperature, but for example a magnetic field, doping or applied pressure. Regarding a second order phase transition from a paramagnetic to an ordered state at finite temperature, fluctuations of the order parameter play an important role. When the transition is approached the fluctuations will slow down and increase in wavelength, which enhances the scattering cross-section of quasiparticles [65]. This process is limited by the crossing of the transition temperature, which restores Fermi liquid behavior at low temperatures. However, if a phase transition is forced to $T = 0\,\mathrm{K}$, this limit does not exist. In this case the fluctuation wavelength and the scattering cross-section diverge and this leads to a breakdown of Fermi liquid theory.

In contrast to a phase transition at finite temperature a quantum phase transition occurring at $T = 0\,\mathrm{K}$ is driven by quantum fluctuations, since thermal fluctuations do not exist at absolute zero. These fluctuations can be characterized by an energy scale Δ. In the vicinity of the QCP Δ decreases as a function of the tuning parameter δ and vanishes at δ_c, where the quantum critical point is reached. Simultaneously the characteristic length scale ξ of the fluctuations diverges. The relation between those two scales is described with the help of the dynamic critical exponent z [69]:

$$\Delta \sim \xi^{-z} \tag{2.18}$$

Although the quantum phase transition takes place only at 0 K and is therefore out of reach for measurements, quantum critical behavior can be observed at finite temperatures close to the QCP. At $T > 0\,\mathrm{K}$ $k_B T$ defines the energy scale for thermal fluctuations. As long as $\Delta > k_B T$ the system behaves classical, but when $k_B T$ exceeds Δ the system will become quantum critical, i. e. the quantum and the thermal fluctuations are both important for the behavior of the system and the classical description is no longer applicable.

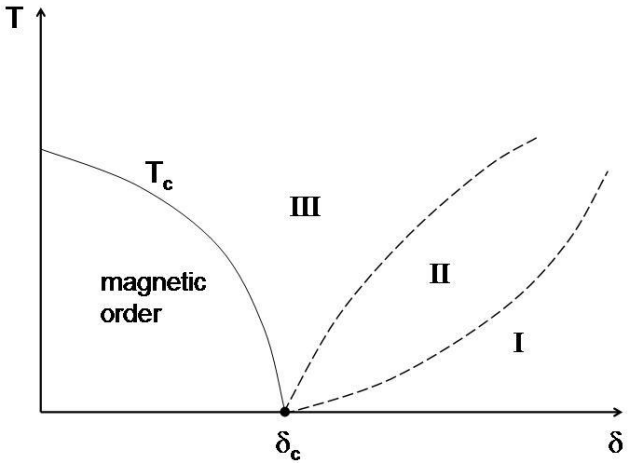

Figure 2.8: Phase diagram of an itinerant electron system as derived by Millis [70].

MnSi is a weak itinerant ferromagnet [71] and the properties of itinerant systems near a quantum phase transition have been calculated by Hertz and Millis [70, 72] using renormalization-group theory. They consider systems that develop from a Fermi-liquid state and are above their upper critical dimension d_c^+, which is fulfilled for $d + z > 4$ with the physical dimension d and the dynamic critical exponent $z = 2$ and $z = 3$ for the antiferromagnetic and the ferromagnetic case, respectively. Their approach leads to a phase diagram as shown in figure 2.8, where the occurring phases are depicted as a function of the temperature and the tuning parameter δ. For $\delta < \delta_c$ and below the transition line defined by the ordering temperature T_c the system is magnetically ordered. The regimes named as I, II and III are characterized by different energy scales, that determine their properties. In region I the fluctuations have energies much larger than $k_B T$ and the system is described by quantum mechanics. The thermodynamic properties are those of a Fermi liquid. Region II is a crossover regime between quantum and classical behavior and in region III the system behaves classical, as it is controlled by thermal rather than by quantum fluctuations. In experiments, however, the region II and III cannot be distinguished, since the system shows the same NFL behavior. For the resistivity, for example, a $T^{3/2}$ law is predicted for a three-dimensional antiferromagnet and ρ will be linear in T in the ferromagnetic case.

A different theory based on spin fluctuations has been developed by Moriya and Takimoto [73] for a heavy electron system around its antiferromagnetic instability. They make use of a self-consistent renormalization model and include couplings between different spin fluctuation modes.

This theory predicts a NFL behavior with a resistivity proportional to $T^{3/2}$. Adopting the theory for the case of a ferromagnet leads to a $T^{5/3}$ resistivity [74].

All theories described in the previous paragraphs assume the existence of a QCP, which implies that a second order phase transition is forced to zero. This scenario may possibly occur, when the magnetic order in MnSi is suppressed by doping [31], but until now only little effort has been made in studying the quantum phase transitions in $Mn_{1-x}Fe_xSi$ and $Mn_{1-x}Co_xSi$. Regarding MnSi under applied pressure, however, the situation is somewhat different, since the transition is first order,[1] probably due to a coupling of the magnetization to non-critical soft modes [83]. Furthermore MnSi exhibits an unusual temperature dependence of the resistivity not only around the critical pressure, but in an extended region above p_c.

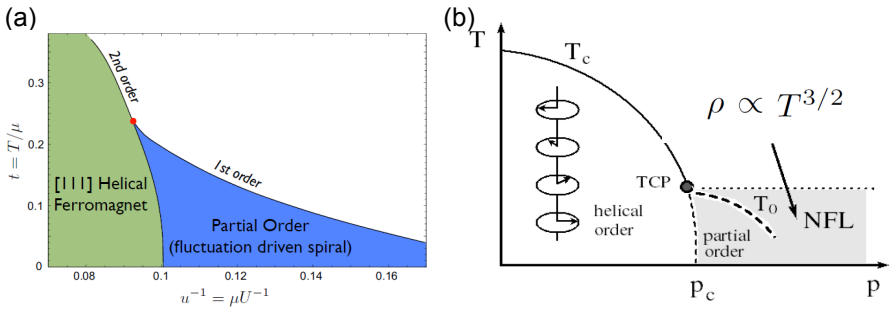

Figure 2.9: (a) Phase diagram as calculated by the quantum order-by-disorder approach. The axes are labeled by the inverse interaction $u^{-1} = \mu/U$ and the temperature $t = T/\mu$ with the chemical potential μ and the contact interaction between electrons U, taken from [84], (b) Schematic phase diagram of MnSi as experimentally evidenced, taken from [85].

A relatively new approach to understand this critical behavior is a so-called quantum order-by-disorder model that can be applied to MnSi [84]. The idea is that close to the quantum phase transition deformations of the Fermi surface occur, which enlarge the phase space for quantum fluctuations with low energy. In order to benefit from this newly available phase space the propagation vectors of the spin spirals, which form the magnetic ground state of MnSi, start to vary their length and to fluctuate around new directions. This leads to a partially ordered state as shown in the phase diagram in figure 2.9a. This model can explain critical behavior on the basis of spin

[1] The first order nature of the phase transition in MnSi was for a long time believed to arise beyond a tricritical point located at a pressure of 1.2 GPa [27, 75]. There was a lively discussion about the existence of this tricritical point and the order of the transition at ambient pressure [76–79]. Today it is the general belief that no crossover from second to first order exists on the phase transition line, since the transition from the helimagnetic to the paramagnetic state is first order even at ambient pressure [32, 80–82].

spirals, but the $T^{3/2}$ temperature dependence of the resistivity cannot be derived.

Another approach to explain the NFL resistivity above p_c is the idea of a partially ordered regime consisting of two-dimensional modulated spin structures. It was calculated perturbatively that fluctuations of columnar spin textures, which can be, but do not need to be skyrmions, can establish a $T^{3/2}$ resistivity in systems in a weak-disorder regime [85]. The calculations are in excellent agreement with the experimental situation in MnSi (compare figure 2.9b). Furthermore the observation of a large topological Hall signal above p_c confirms the existence of skyrmionic textures in this regime [32]. If fluctuating skyrmions are responsible for the unusual behavior of the resistivity, the mechanism must be identified, which stabilizes them. Probably anisotropies will play a role, since they were shown to suppress conical phases and thereby favor skyrmions [21].

In conclusion the long lasting question concerning the origin of the NFL behavior in MnSi under high pressure seems to find an answer in the partial order, which occurs beyond p_c. Nevertheless the theories of quantum critical behavior in MnSi, which have kept researchers busy for a few decades, must not be for nothing. Possibly they find their application, when the quantum phase transition induced by doping is investigated.

2.4 Growth of Thin Films by MBE

During this work thin films of MnSi, $Mn_{1-x}Fe_xSi$ and MnGe were prepared by molecular beam epitaxy (MBE). Thereby the first step always was to grow the desired compound with the right crystal structure and the second step was to improve the film morphology. A qualitatively good film is characterized by its flatness and a crystal structure with only a little amount of defects and impurities. In order to obtain such a film many conditions concerning the experimental environment have to be fulfilled and a large number of parameters has to be chosen in a suitable way. The film growth is for example affected by the choice of materials, the quality of the substrate, the deposition rates and the temperature during the growth process. In the following some basic aspects of film growth are described, which are needed to understand, how the properties of a film can be controlled.

The growth of thin films can be carried out by a number of different techniques and it depends on the film and substrate materials as well as on the application requirements, which method is best suited. There are several methods, including MBE, where particles, i. e. atoms or molecules, from a vapor phase condense on a substrate to form a thin film. Regarding a single particle, which is deposited on a surface, it has different possibilities to contribute to the film growth. If it does not re-evaporate immediately, it can move on the surface by a diffusion process and thereby reach a site that is favorable for adsorption. Such sites are defects, steps and edges in the crystal structure of the substrate or of the already grown film. When many particles get together, they may form a cluster that serves as a new nucleus for film or island growth, if it is larger than the critical nucleus size. This critical size depends on geometrical aspects and on the surface tensions of the film and substrate materials [86]. Considering the particles that have already condensed on the substrate they can exchange their sites with neighboring atoms of the film or the substrate by a process called interdiffusion.

All these processes proceed simultaneously, and each of them is characterized by an activation energy that determines its probability. For example the re-evaporation rate is proportional to $exp(-E_{des}/kT)$, where E_{des} is the energy needed for the desorption of a particle [87]. Depending on the substrate and film materials some processes are more favorable than others and therefore the resulting films will have different morphology for different materials. The temperature of the evaporated particles and of the substrate also plays an important role as higher temperatures promote the surface mobility of the particles, which is advantageous for smooth films.

On the basis of the different processes and their distribution, three types of growth can be distinguished, which are illustrated in figure 2.10. It depends on the surface tensions γ_s and γ_f of the substrate and the film and on the interfacial tension γ_i between film and the substrate, which of the modes

is dominant [87]. If the relation

$$\gamma_s \geq \gamma_f + \gamma_i \tag{2.19}$$

is fulfilled, it is energetically favorable to cover the surface of the substrate with film material and therefore Frank - van-der-Merwe growth will be observed, where every layer of the film is completed, before the next layer starts to grow. Thereby atomically flat surfaces with almost perfect crystal structure are obtained. Volmer - Weber island growth, however, is the predominant growth mode, when

$$\gamma_s < \gamma_f + \gamma_i. \tag{2.20}$$

A mixture of these two is the Stranski - Krastanov growth mode, which may occur in the presence of a lattice mismatch. In this case the crystal structure of the first few layers of the film can be strained to match the lattice of the substrate, but at some point the potential energy of the elastic strain exceeds the adhesion forces inside the film material. Then island growth is preferable.

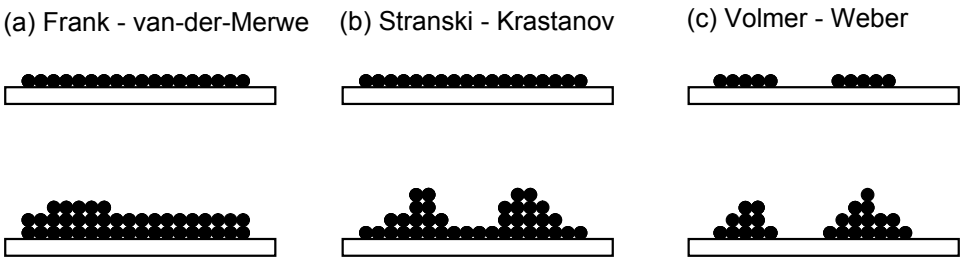

Figure 2.10: Three different modes of film growth that determine the morphology of the film.

Molecular beam epitaxy is a very sophisticated technique to grow films of high quality. The film material is evaporated from effusion cells in ultra-high vacuum. Single atoms or molecules leave the cell in a well defined direction and allow for a uniform deposition on the substrate. Very low growth rates of a few tenth of an angstrom per second can be realized and the molecular beam can be achieved to consist of very pure material. This enables the preparation of thin films of excellent crystalline quality and pureness.

The term epitaxy is used for crystalline film growth, where the orientation of the film reflects the crystal structure of the substrate. This kind of growth can only be achieved, if the substrate and the film material are chosen with crystal structures that fit to each other. The easiest case, where this is realized, is homoepitaxy, where the substrate and the film material are identical. Another possibility is to choose a substrate, which possesses the same crystal structure and a similar lattice constant as the film. In a

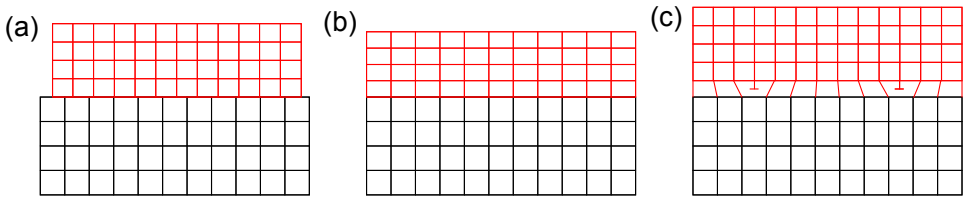

Figure 2.11: Three possibilities to orient a film on a substrate (a) incoherent growth, (b) coherent or pseudomorphous growth and (c) semi-coherent growth.

more general case the surface mesh of the substrate has to match the two-dimensional lattice periodicity in the plane of the film or the lattice of the film can be brought into agreement with superlattices or surface reconstructions of the substrate. Epitaxial growth can occur, if the deviation between the crystal lattices does not exceed a few percent of misfit. The misfit is defined as the relative difference between the lattice spacings of the film and the substrate [88]

$$f = \frac{a_f - a_s}{a_s}, \tag{2.21}$$

where a_s and a_f are the lattice constants of the substrate and the film, respectively. If the two crystal structures are not identical, the two-dimensional mesh in the plane of contact has to be regarded.

If there is a misfit, three different ways of film growth can be distinguished, which are characterized by the relation between the crystal lattice of the film and the substrate (compare figure 2.11). Whenever there is no plane in the crystal structure of the film that matches the surface mesh of the substrate or the misfit between the two is large, the film will grow incoherently. This means that both crystal structures conserve their lattice constants and there is no correlation between the atomic positions in the film and the substrate. In most of these cases the film will not grow as a single crystal but it will be polycrystalline. Coherent growth, however, can be observed, when the lattice planes of the film and the substrate match perfectly or with a very small misfit of a few percent. In this case the deposited atoms arrange at well defined positions and the periodicity of the substrate is reflected by the film. A misfit leads to tensile or compressive strain in the layer. This kind of growth is also called pseudomorphous, since the film possesses a crystal structure that would not occur under equilibrium conditions. If the misfit is larger, semi-coherent growth may be observed, where dislocations in the film contribute to a relaxation of the strain.

Also in the case of pseudomorphous growth dislocations will start to occur at some point in the growth process. The larger the thickness of the film the larger will also be the strain energy per unit area. At a certain thickness it exceeds the energy needed to form a dislocation. By setting equal the strain

energy and the energy of an edge dislocation the following expression for the critical thickness d_c can be obtained [89]:

$$d_c = \frac{b}{8\pi(1+\nu)f}\left(\ln\frac{d_c}{b}+1\right). \tag{2.22}$$

Here b denotes the value of the Burgers vector of the dislocation and ν is the Poisson's ratio of the film material. When the film thickness exceeds d_c dislocations will occur, which release part of the strain.

2.5 The MBE System

During this work thin films of the B20 compounds MnSi, MnGe and $Mn_{1-x}Fe_xSi$ were grown on Si(111) substrates. The thin film growth was carried out in an ultra high vacuum (UHV) chamber using molecular beam epitaxy (MBE). In this section the MBE system will be described in order to point out its abilities and the principle of operation.

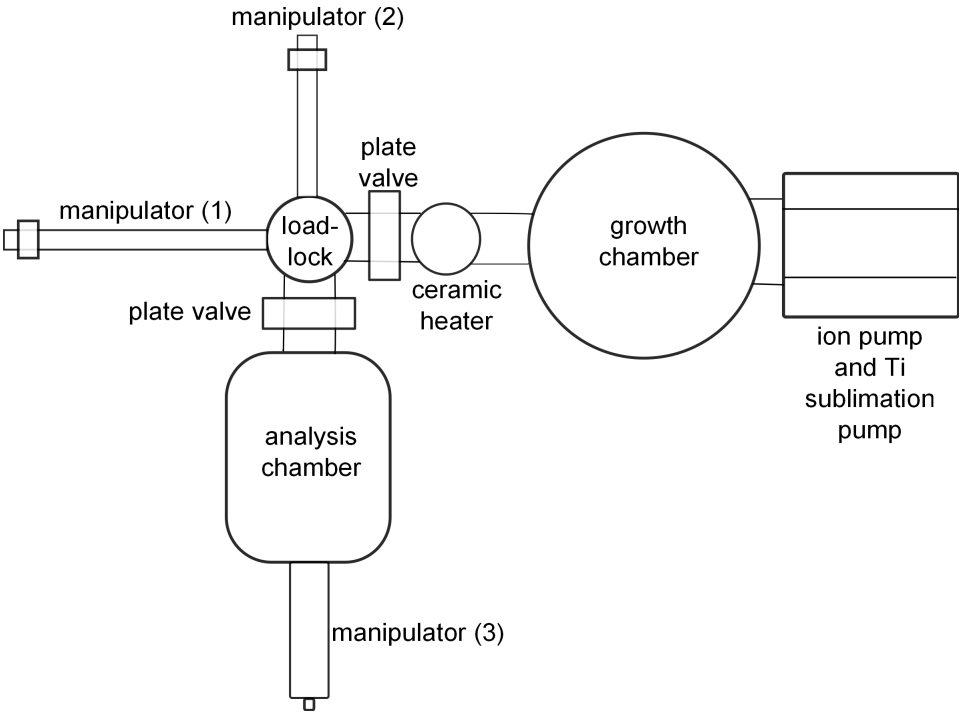

Figure 2.12: Top view of the UHV facility

The UHV facility is located in a clean room. A rough top view of the MBE system is depicted in figure 2.12. It consists of three chambers, namely the load lock chamber, the growth chamber and the analysis chamber, each of which can be separated by plate valves [90]. This way, the load lock chamber can be vented and new samples can be put into the system, where at the same time the growth and analysis chambers stay under UHV. The base pressure, which is of the order 10^{-10} mbar, is achieved by three different kinds of pumps. The main one is a turbomolecular pump with a magnetic bearing installed directly at the load lock chamber. It is capable of establishing UHV in this chamber within approximately 20 minutes, which means that the inserting of a new sample takes only a short time. Furthermore the growth and the analysis chamber are equipped with one ion pump and one Ti sublimation pump each to ascertain the high quality vacuum needed for film growth.

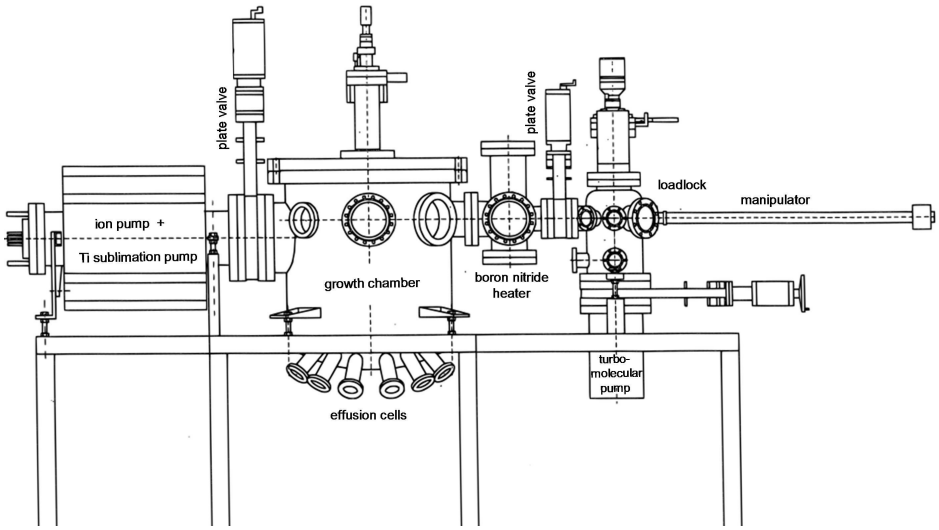

Figure 2.13: Side view of the growth chamber, the load lock and the ceramic heater in between.

Inside the UHV system the samples are handled on plate-like specimen holders, where two screws are used to fix the substrates at the bottom side of the plates. The specimen holders and the screws are made of molybdenum, which can endure temperatures exceeding $1000\,°C$. Four of these plates can be stored on a horizontal rotating table in the load lock chamber, from where they can be transferred into one of the other chambers by the manipulators (1) and (2) (compare figure 2.12). With manipulator (1) the sample can be brought into the growth chamber or to the ceramic heater placed halfway between the load lock and the growth chamber. The manipulator (2) can transfer the specimens into the analysis chamber, where manipulator (3) can take over.

The analysis chamber offers the possibility to investigate the films directly after growth. The samples stay under UHV conditions all the time, so that the surfaces will not suffer any contamination. The system offers the equipment for performing Auger and ultraviolet photoelectron spectroscopy. Furthermore a sputtering system is installed in the analysis chamber.

As the name implies the growth chamber is the place, where the film growth is performed. However, before a film can be grown on a substrate, its surface needs to be clean. For this purpose a heater is installed between the load lock and the growth chamber, which is used to remove the oxide layer from the Si substrates. A description of this heater and its calibration can be found in the appendix A.1.

In figure 2.13 it can be seen that the growth chamber possesses six junctions for effusion cells at the lower part of the chamber, however, only two different cells, an effusion cell and a mini-electron beam evaporator, were

used during this work to evaporate Mn and Fe, respectively. On the opposite side of the chamber an electron beam evaporator is installed, which was used for the evaporation of Si and Ge. The growth rate can be monitored and controlled by a deposition rate controller. In the middle of the chamber there is a holder for the specimens, which is equipped with a resistive heater made of tantalum wire (compare appendix A.2). This is used to hold the sample at temperatures between room temperature and $700°C$ during film growth and to anneal the deposited layers after growth. Furthermore a RHEED system is implemented inside the growth chamber, which makes it possible to get diffraction patterns of the substrates and film surfaces at any step of the growth process.

2.5.1 The Effusion Cell

The term effusion describes a process, where gas escapes from a reservoir trough a hole, which is smaller in diameter than the mean free path of the particles in the gas. The gas will pass through the hole atom by atom (or molecule by molecule) and, in contrast to a diffusion process, the particle flux will only proceed in one direction. The velocity of effusion depends essentially on two parameters, which are the temperature T and the molecular mass M of the material. The effusion rate γ can be written as [91]

$$\gamma = \frac{pA_0N_A}{\sqrt{2\pi MRT}}. \tag{2.23}$$

Here p denotes the partial pressure of the material inside the reservoir and A_0 is the area of the hole. N_A and R are the Avogadro constant and the gas constant, respectively. In the case of an effusion cell p depends on the temperature and is normally smaller than 10^{-4} mbar, thus the mean free path of the particles can be estimated to be in the order of 1 m or larger. Since the diameter of the crucible is approximately 1 cm, the condition for effusion is fulfilled.

As mentioned before the growth chamber offers the opportunity to mount six effusion cells. However, during this work only one cell was used for the evaporation of manganese. This cell was a so-called High Temperature Cell, which can be operated in a temperature range from 300 °C to 1700 °C. The structure of such an effusion cell is depicted in figure 2.14. The manganese is in a crucible made of molybdenum. It is important to chose a crucible material, which will not react with the evaporating substance even at high temperature. The crucible is surrounded by a resistive heating made of tungsten wires. The temperature is measured by a W/Re thermocouple placed directly below the crucible and can be controlled by a PID (proportional integral derivative) controller. In order to obtain a constant growth rate it is necessary to stabilize the temperature within a range of ± 1 °C. The effusion

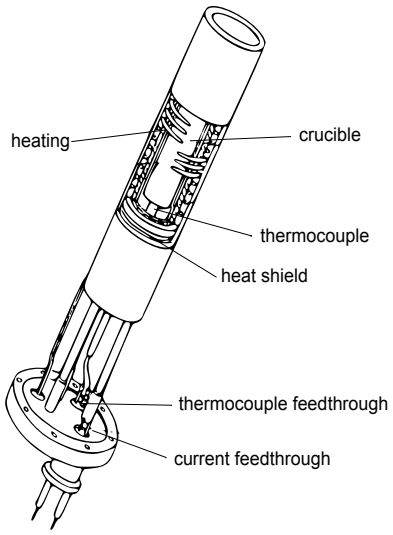

Figure 2.14: Set-up of an effusion cell [92]

cell can be closed by a pneumatic shutter, which is especially important to prevent any dirt from falling into the crucible.

When new material is filled into an effusion cell, the growth rate has to be calibrated. Therefore the rate at different cell temperatures is measured by the deposition rate controller (compare section 2.5.4).

2.5.2 The Electron Beam Evaporator

The electron beam evaporator is positioned in the growth chamber directly below the substrate. By the use of magnetic fields an electron beam is directed on the material, which is provided in a graphite crucible. By the energy of the incoming electrons the material is heated up locally. To achieve a uniform warming of the material the beam can be swept across the crucible, which has a diameter of around 2 cm. While the electron energy is at a constant value, the growth rate can be controlled by the current. Similar to the case of the effusion cells the growth rate must be calibrated using the deposition rate controller. However in the case of the electron beam evaporator the rate is less stable and normally decreases with proceeding evaporation time. This causes difficulties in the preparation of thick films, where the evaporation time exceeds 15 minutes. Eventually the electron current must be readjusted or films must be grown in two steps, where the electron beam evaporator is cooled down between growing the first and the second part of the film.

The electron beam evaporator offers the possibility to place four crucibles with different materials in a revolver. The crucible holder is cooled by water to ensure moderate temperatures in the area around the heated crucible.

During this work the electron beam evaporator was used to evaporate silicon and germanium.

2.5.3 The Mini Electron Beam Evaporator

For the evaporation of iron a mini e-beam evaporator was used. In contrast to the evaporator described in the previous paragraph, in this device no electron beam is formed, which is directed onto a crucible, but the electrons are directly accelerated towards the target. The filament is a spiral with only one and a half loops and a relatively large diameter of 10 mm. When the source is used to evaporate a metal, the material is provided in the form of a rod with a diameter of 2 mm to 6 mm. The tip of this rod is positioned approximately in the middle of the filament, but does not touch it. During evaporation a current of approximately 7 A is heating the filament and a voltage of around 1.5 kV is applied between the filament and the metal rod. Thus, the target material acts as the anode and is heated by the impinging electrons until the tip of the rod is emitting atoms. The advantage of the mini electron beam evaporator is its ability to evaporate materials with a high melting point with a very low heat transfer to the surroundings of the source, which leaves the background pressure in the range of $1 \cdot 10^{-9}$ mbar.

2.5.4 The Deposition Rate Controller

The deposition rate controller is an instrument, which measures the thickness of a deposited layer in-situ. The main element of the rate controller is an oscillating crystal, which is placed in the growth chamber very close to the substrate holder. During film growth this quartz crystal must be at the same height as the substrate, so that the same amount of material will be deposited on the crystal and on the substrate. Since the resonance frequency of the quartz changes, when it is covered by a layer of material, the mass and thereby thickness of the grown layer can be calculated from this change.

To get the correct rate for different materials, the deposition rate controller has to be calibrated for each of them. Therefore three parameters need to be determined [93]. The first is the mass density of the deposited material, which is needed to calculate the layer thickness from its mass. The second is the so-called z-factor defined by

$$z = \sqrt{\frac{D_q \cdot U_q}{\frac{D_f}{U_f}}}, \tag{2.24}$$

where D_q and D_f are the densities of the quartz and the film, respectively. U_q and U_f are the corresponding shear moduli. The third parameter to be determined is the tooling-factor, which accounts for geometry corrections in the case, that not the same amount of material is deposited on the crystal

and on the substrate. In order to find the tooling-factor a relatively thick film (approximately 200 nm) must be deposited on a substrate and its thickness must be measured by the rate controller with the tooling-factor set to 100 %. Then the real thickness of the film must be determined, for example by a Dektak surface profiler. The tooling percentage is given by

$$tooling = 100 \cdot \frac{film\ thickness}{displayed\ thickness} \tag{2.25}$$

When these three parameters – the density, the z-factor and the tooling-factor – are memorized in the controller, the correct film thickness and deposition rate will be displayed during growth. However, when no pure element is deposited but an alloy, it is more difficult to determine the film thickness, since the rates of the different materials do not simply add up. In this case the film thickness must be calculated from the rates, that were determined for the elements prior to growth. In practice the number of Mn atoms deposited on a cm^2 was calculated from the deposition time and the growth rate. Taking the B20 crystal structure of MnSi or MnGe as a basis, four Mn atoms will arrange in a unit cell, which has a volume of a^3 with a denoting the lattice constant. With these information the film thickness can be calculated easily. However, the thickness value is burdened with an uncertainty of up to 20 %, since the deposition rate may fluctuate and possibly not every Mn atom is incorporated into the film.

2.6 Reflection High Energy Electron Diffraction

Reflection High Energy Electron Diffraction (RHEED) is a special technique of electron scattering from crystalline samples. The method is characterized by the extremely small angle of incidence in the range of 0.5 ° to 5 ° [94] between the electron beam and the sample surface. This grazing incidence effects that the electrons despite of their high kinetic energy can only penetrate a few atomic layers into the surface of the sample, since their momentum perpendicular to the surface is small. Therefore, RHEED is well suited for the investigation of thin films and surfaces, where it is possible to obtain information about the lattice structure as well as the morphology. Especially during the preparation of thin films RHEED is of major importance, as this method can be deployed in-situ during film growth. The setup, which is shown in figure 2.15, is organized in a way that the electron gun as well as the detection unit are installed outside the area, where material flow takes place. Because of this, changes of the sample surface can be observed directly during growth and in the case of layer by layer growth even the speed of growth can be determined from the oscillating brightness of the RHEED pattern.

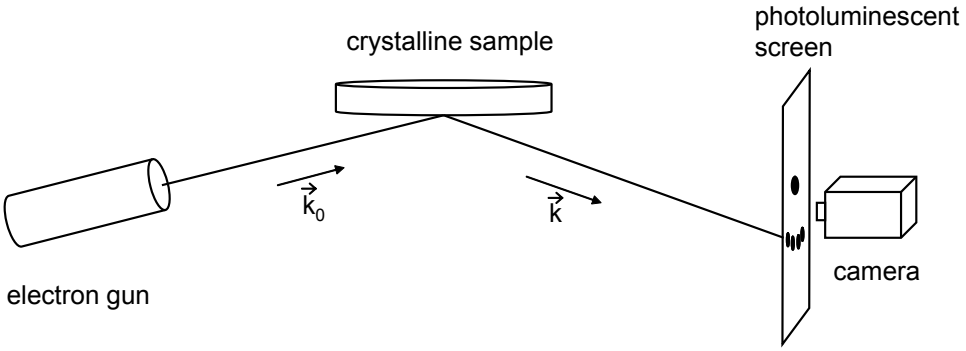

Figure 2.15: Schematic view of the RHEED setup

The RHEED setup used during this work is integrated into the vacuum chamber, where film growth by MBE is performed. The high voltage unit offers the possibility to accelerate the electrons by a voltage of up to 25 kV, but usually an electron energy of 20 keV was adjusted for the investigation of the thin films.

2.6.1 Diffraction Theory

An incident electron can be described by its wave vector $\vec{k_0}$, which specifies its direction and energy. The absolute value of $\vec{k_0}$ correlates with the kinetic

energy E via the following equation [95]:

$$k_0 = \frac{1}{\hbar}\sqrt{2m_0E + \frac{E^2}{c^2}} \tag{2.26}$$

Here m_0 is the rest mass of the electron. It is important to notice that the relativistic correction for electrons with an energy of 20 keV amounts already 1 % and, therefore, the relativistic term cannot be neglected.

The incoming beam can be described as a plane wave, which is scattered by the atoms of the crystal surface and, considering large distances from the scattering center, also the scattered electrons possess the properties of plane waves. The wave function of an electron scattered from the atom indexed with zero can be written as [96]

$$\Psi_0 = f_0(\vec{k_0}, \vec{k}, \vec{r}) \exp{(i\vec{k}\vec{r})}, \tag{2.27}$$

where f_0 is the atomic form factor. Regarding the waves scattered from all the rest of the atoms in the crystal, these have the same form and only differ by a phase factor.

$$\Psi_i = \Psi_0 \exp{(i\vec{K}\vec{R}_i)} \tag{2.28}$$

$\vec{K} = \vec{k} - \vec{k_0}$ describes the scattering vector, whereas $\vec{R}_i$ specifies the position of the atom under consideration. The total intensity observed on the screen is [96]

$$I = |\Psi|^2 = |\sum_i \Psi_i|^2 = \left|\sum_{\substack{j=1\\basis}}^{J} \Psi_{0j}\right|^2 \cdot \left|\sum_{\substack{j=1\\lattice}}^{N} \exp{(i\vec{K}\vec{R}_i)}\right|^2 = |F|^2 \cdot |G|^2 \tag{2.29}$$

The structure factor F is determined by the sum over all atoms inside one unit cell. Properties such as the atomic positions, the scattering behavior of single atoms and multiple scattering processes are contained in F. G is called the lattice factor. Its value only depends on the alignment of unit cells in the lattice and, therefore, G can be calculated much easier. Considering a diffraction pattern, the position of any reflex and its sharpness is given by the lattice factor, whereas its intensity is determined by the structure factor. In the case, where F is zero, the corresponding reflex will not appear at all.

In order to explain the appearance of a particular diffraction pattern, at first only elastic scattering is taken into account, while multiple scattering processes are neglected. The elastic scattering of electrons from the planes of the crystalline lattice and their subsequent interference can be described by the kinematic scattering theory. For the occurrence of an intensity maximum on the screen, i. e. for constructive interference, the Laue condition has to be fulfilled, which requires that the difference in wave vector between incoming in reflected electron must match a reciprocal lattice vector $\vec{G}$.

$$\vec{k_0} - \vec{k} = \vec{G} \tag{2.30}$$

Because of the small angle of incidence in the case of RHEED the electrons only reach the topmost layers, which means that a two-dimensional lattice plane can be considered as being accountable for the diffraction pattern. In the case of a two-dimensional lattice the reciprocal lattice vectors are defined by [97]

$$\vec{a_1^*} = 2\pi \vec{a_2} \times \vec{n}/A, \tag{2.31}$$

$$\vec{a_2^*} = 2\pi \vec{n} \times \vec{a_1}/A. \tag{2.32}$$

$A = \vec{a_1} \cdot \vec{a_2} \times \vec{n}$ is the area of the unit mesh in real space and $\vec{n}$ is the normal unit vector. As the vector component perpendicular to the surface is not specified in this two-dimensional case, the reciprocal lattice points degenerate into lattice rods perpendicular to the surface mesh.

The positions of reflection spots on the RHEED screen can now be de-

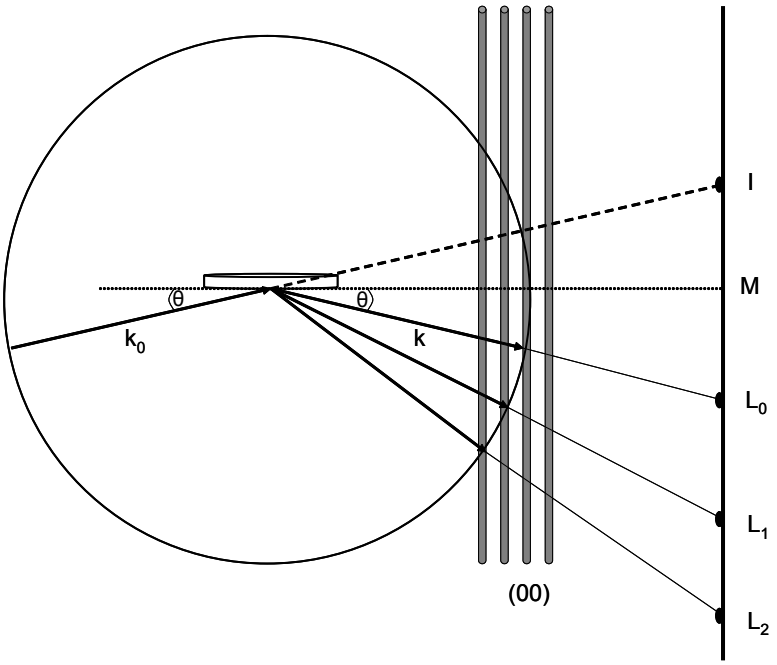

Figure 2.16: Construct of the Ewald's sphere

termined using the so-called Ewald's sphere depicted in figure 2.16. The Ewald's sphere is a geometric construct to find the points, where the Laue condition is fulfilled. The origin of the sphere is located at the position, where the electron beam hits the surface of the sample, and its radius agrees with the length of the wave vector of the incoming electrons. The absolute value of the wave vector of any elastically scattered electron equals k_0 and, thus, starting in the origin of the Ewald's sphere it ends on its surface. In addition the scattered wave vector has to encounter a point of the reciprocal

lattice in order to satisfy the Laue condition. Therefore, the points of intersect between the constructed sphere and the reciprocal lattice rods define the occurring reflections and the projection of these points onto the screen leads to the observed diffraction pattern.

Due to the geometric shape of the Ewald's sphere the reflexes are aligned on concentric circles named Laue circles and abbreviated with L_0, L_1, etc. The origin M of all circles is positioned on a horizontal line, which is on a level with the sample and is called the shadow edge, as it separates the diffraction pattern from the upper dark area of the screen. Another special point is the mirror reflection, which is normally the brightest spot of the diffraction pattern, as it stems from the direct reflection of the beam from the sample surface. This point as well as the point of direct incidence I are located on the zero order Laue circle.

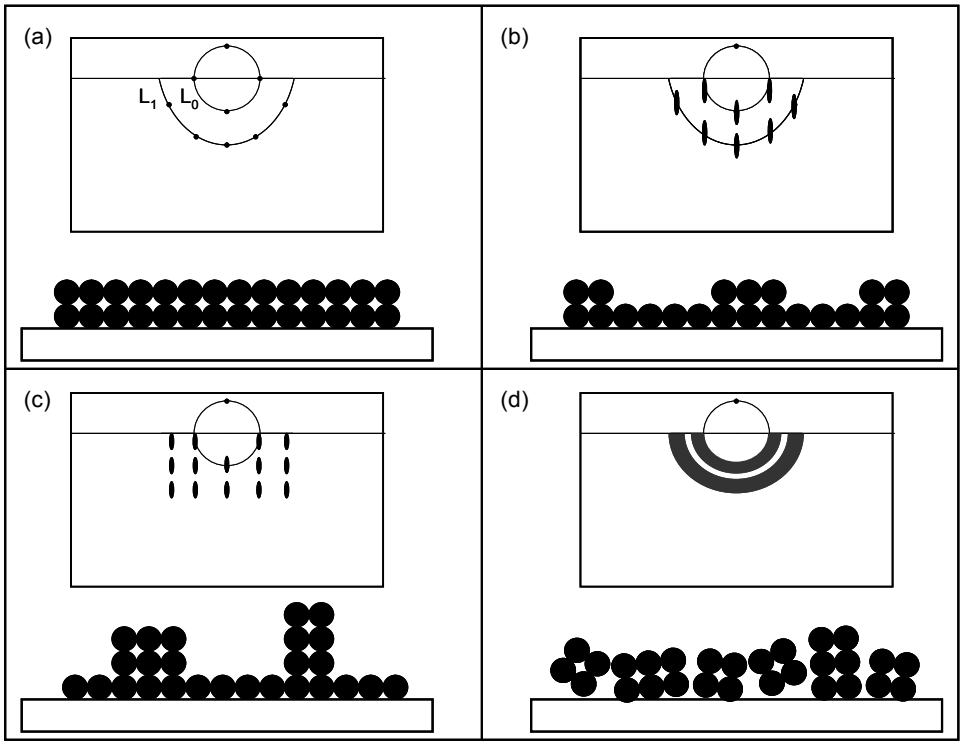

Figure 2.17: Diffraction patterns originating from surfaces with different morphologies: (a) perfectly flat, (b) flat with atomical steps, (c) islands and (d) polycrystalline surface.

Until now only diffraction patterns originating from electrons scattered on a perfectly flat surface were considered. In practice, however, the surfaces investigated with RHEED can possess a variety of defects. Regarding the case of different surface quality RHEED is a suitable tool to obtain information not only about the crystal structure but also about the morphology

[96].

In the case of a surface, that is perfectly even, well defined reflections positioned on Laue circles occur as it was explained in the preceding paragraphs and as it is depicted in figure 2.17a.

If the surface contains steps, which have the dimensions of single atomic layers, the spots of the diffraction pattern will be distorted into streaks as shown in figure 2.17b. These streaks are oriented perpendicular to the shadow edge, but they still remain in their positions on the Laue circles. The occurrence of the streaks can be explained by a broadening of the reciprocal lattice rods due to the defects on the surface. Therefore, the points of intersect between the rods and the Ewald's sphere become elliptically elongated.

A different diffraction pattern is observed, when there are islands on the surface under investigation. In this case the electrons can penetrate through the islands as long as their dimensions are smaller than the mean free path of the electrons. Naturally, the islands cannot be regarded as a two-dimensional lattice plane, but they have three-dimensional character, which leads to different conditions for the reflection spots on the screen. Therefore, a pattern, which consists of spots aligned on lines parallel to the shadow edge, can be observed for a surface occupied with islands (compare figure 2.17c).

If the surface of the sample is even less well-ordered and possesses polycrystalline character, the RHEED pattern will be composed of rings as depicted in figure 2.17d. Just as in the case of electron scattering from a powdered sample, there does not exist a well defined orientation of the crystal lattice, but the different diffraction patterns of differently oriented crystallites are superimposed and Debye-Scherrer rings are formed.

A completely amorphous surface can be identified by an RHEED image without any distinguishable features. Only a diffuse background is observed.

2.6.2 Kikuchi Lines

In addition to the diffraction spots RHEED patterns often contain some bright and dark lines on a diffuse background. These are called the Kikuchi lines and were observed and theoretically described for the first time in 1928 by Seishi Kikuchi [98]. The appearance of these lines is caused by multiple scattering events, where an electron is inelastically scattered by a phonon or plasmon [99], before it suffers elastic scattering in a second step. The direction of the electron's wave vector $\vec{k_0}$ is randomized by the inelastic scattering, while its energy is changed only by a few meV in the case of phonons [100]. The scattering events including plasmons need higher excitation energies in the range of eV [101]. However, these are still small changes of the absolute value of k_0, since the electrons possess energies of some keV.

An inelastically scattered electron can only be scattered elastically afterwards, if the Laue condition is fulfilled. Because of this, for the construction

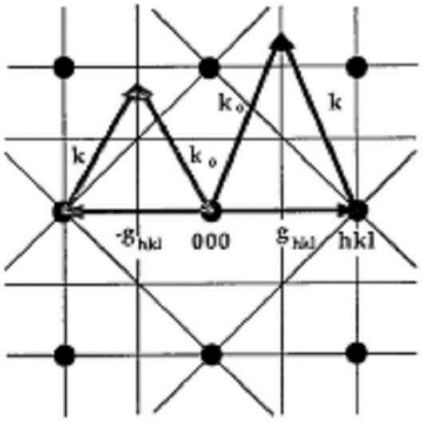

Figure 2.18: Whenever $\vec{k_0}$ ends on a Brillouin zone boundary, elastic scattering is possible [102].

of the Kikuchi lines the reciprocal space has to be considered. Therein the Brillouin zone (BZ) boundaries are given by the planes bisecting the reciprocal lattice vectors perpendicularly. Every wave vector $\vec{k_0}$ of an incident electron, which starts in the origin of the reciprocal lattice and ends on BZ boundary, satisfies the diffraction condition, as it is graphically demonstrated in figure 2.18 [102]. Assuming that $\vec{k_0}$ after one inelastic scattering event has a fixed length but a randomly oriented direction, a sphere can be constructed around the origin of reciprocal space, and every line of intersection with a BZ boundary leads to the appearance of a Kikuchi line on the screen. Every bright line arising by these reasons comes together with a parallel dark line. From one line the electrons are taken out of the background of inelastically scattered electrons as they fulfill the Laue condition and on the other one they appear after elastic scattering. Although this mechanism works in both directions, which means that also electrons from the bright line are scattered onto the dark line, there still exists a difference in brightness, because the background itself is inhomogeneous [103].

For the formation of the Kikuchi lines approximately the topmost ten atomic layers of the sample play a role. Therefore, the lines are only defined, if the surface and the bulk material below possess good crystalline quality. Imperfections of the surface cause a broadening of the lines. Furthermore the Kikuchi lines can be used to orient the sample, as even a small rotation of the surface leads to a movement of the lines. If the line pattern is found to be symmetric, the sample is oriented along one of its main crystal directions.

2.6.3 The Coherence Length

In order to interpret a RHEED pattern correctly it is also important to know the size of the surface area, which contributes to the observed pattern. This

area is the region, which is hit by coherent electrons and can be estimated by help of the coherence length and the coherence width of the electron beam. The coherence length l is defined by [104]

$$l = \frac{\lambda^2}{\Delta\lambda} = \frac{h^2/p^2}{(h/p^2)\Delta p} = \frac{h}{\Delta p} = \frac{h}{\sqrt{3k_B T m_0}}. \tag{2.33}$$

Here λ is the wave length and p is the momentum of the electrons. T denotes the temperature of the cathode, from which the electrons are emitted, and can be estimated to be 1500 K. For an electron energy of 20 keV the coherence length can be calculated to be 28.8 Å. The length of the coherently irradiated surface area, however, depends on the angle of the incoming and reflected beam and for $\theta = 1°$ it amounts a few microns, where the values are larger, when the electron hits the screen closer the shadow edge.

The coherence width b of the beam, however, further restricts the area of coherent electrons. It is given by [104]

$$b = \frac{\lambda}{\delta}, \tag{2.34}$$

where δ is the divergence of the beam, which is specified to amount 10^{-4} rad for the electron gun used during this work. Using equation 2.26 to calculate $\lambda = \frac{2\pi}{k_0}$ the width of the coherently irradiated area for 20 keV electrons can be calculated to be 860 Å. The length of the area is somewhat longer as the beam hits the surface under a small angle. As a result only those features of the surface, which are smaller than about 100 nm, can be resolved. For example, in the case of islands with a diameter of 200 nm and with a flat surface on top, the RHEED pattern will be that of a flat sample.

2.7 Surface Reconstruction

For the growth of thin films surfaces and their properties play an important role. Especially the good quality of the substrate's surface, on which a layer is deposited, is crucial for a successful film growth, since defects on the surface will propagate through the film.

Considering the surface of a solid sample it is obvious that atoms in this region of the crystal are arranged under different conditions than those inside the bulk. Due to the missing neighbors their potential energy is considerably enhanced. In order to lower their energy the atoms tend to change their positions, which leads to a mutation of the lattice structure near the surface. This can be a simple variation of the distances between atoms as for example an enlargement of the bonding length perpendicular to the surface. But also more complex surface structures may occur, when atoms move across the surface in order to saturate dangling bonds, for these are in general energetically disadvantageous. In this case atoms form a new superstructure on the surface, which is called a reconstruction. Often the surface mesh possesses a unit cell, which is several times larger than the lattice constant of the bulk material below.

The reconstruction can be described by the Wood's notation [47], which specifies the size of the unit mesh as well as its orientation. When c_1 and c_2 are the lattice constants of the surface mesh and a_1 and a_2 are those of the bulk material, the reconstruction can be written as

$$\left(\frac{c_1}{a_1} \times \frac{c_2}{a_2}\right) R\alpha, \tag{2.35}$$

where α is the rotation angle between bulk and reconstructed mesh. Additionally p or c may be noted in front of the expression. Here the p means primitive and the c stands for centered, which indicates that an adatom is positioned in the center of the unit mesh. In this case the indicated unit mesh is not the primitive one.

An ordered surface reconstruction with a periodicity reaching over many unit meshes can only occur, if the surface is clean and flat, as any defects will prevent its formation. Therefore the observation of a reconstruction gives evidence for excellent surface quality.

In the case of a silicon (111) surface a 7×7 reconstruction occurs, if the surface is clean from impurity atoms and free of an oxide layer. The surface mesh of this reconstruction possesses a lattice constant, which is seven times larger than the projection of the bulk structure onto the surface.

For the description of the 7×7 reconstruction the DAS model was proposed by Takayanagi *et al.* [105] in 1985. The letters D, A and S stand for dimer, adatom and stacking fault, which are the building blocks of the reconstruction. There are 98 atoms in the topmost two atomic layers of a reconstructed unit mesh, which are arranged as it is shown in figure 2.19.

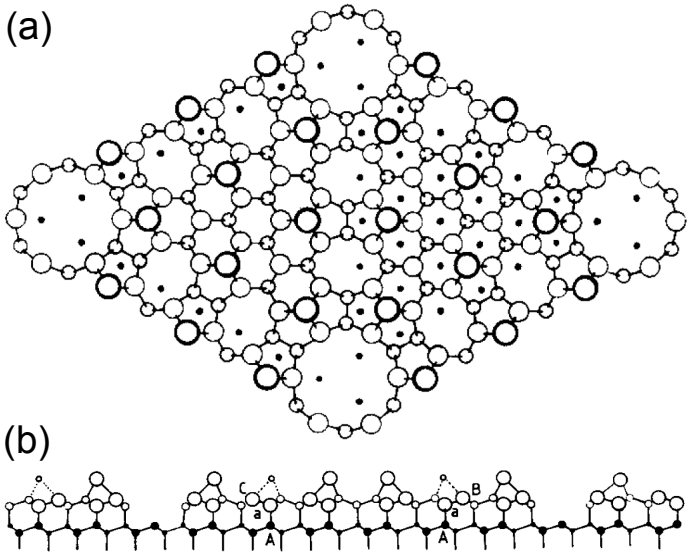

Figure 2.19: Arrangement of atoms in a unit cell of a 7×7 reconstructed Si surface. (a) top view, (b) side view, taken from [105]

The diamond shaped unit mesh can be divided into two triangular subunits. Along the edges of these triangles nine dimers are formed, each consisting of two atoms at a distance which is only $\frac{2}{3}$ of their distance in the unreconstructed case. A stacking fault occurs in the left triangular subunit, but does not exist in the right one. Twelve adatoms are arranged on top of the 7×7 unit mesh, whereas in each corner a vacancy occurs.

A number of different surface reconstructions exists such as 5×5 and 9×9, which have also been observed on Si(111) surfaces [106]. However, calculations based on the DAS model arrived at the conclusion that their surface energy is higher than in the case of the 7×7 reconstruction and therefore 7×7 is the stable configuration [107]. Qian *et al.* [108] showed by energy minimization calculations, that the surface energy per 1×1 unit cell is reduced by 0.40 eV for the 7×7 reconstruction compared to the unreconstructed surface. Nevertheless other surface reconstructions can be generated by the help of adatoms. For example, a $\sqrt{3} \times \sqrt{3}R30°$ surface can be induced by carbon [109] or bismuth [110] adatoms.

In case of an excellent Si(111) surface, which has been in contact with air, the 7×7 reconstruction can be achieved by heating the sample to 1200 °C under UHV conditions and thereby dissolving the oxide layer from the surface. An appropriate method to proof the existence of the reconstruction is RHEED, as it is a very surface sensitive technique that gives information about the surface structure. When the 7×7 reconstruction is present, a large number of additional reflections can be observed in the RHEED pattern. On

each Laue ring there are six weaker spots between the main reflections of the 1×1 surface, and between two neighbored Laue rings six additional rings appear. The expected RHEED pattern along $[\bar{1}\bar{1}2]$ calculated by Wu and Schowalter [111] for an electron energy of 20 keV is shown in figure 2.20.

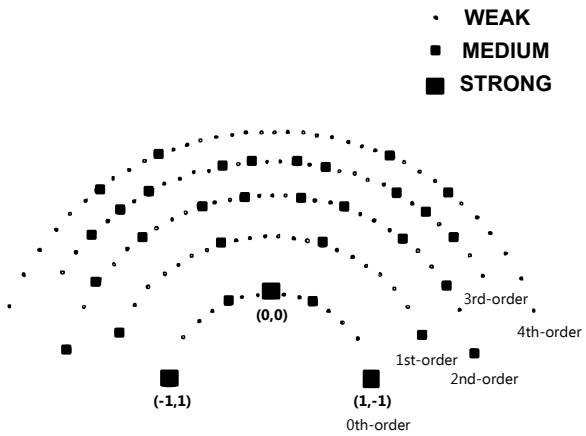

Figure 2.20: Calculated RHEED pattern of a 7x7 reconstructed Si surface with the electron beam directed along $[\bar{1}\bar{1}2]$ [111].

Chapter 3

MnSi Thin Films

The prediction of an enlarged skyrmion phase in the presence of uniaxial anisotropy and its experimental confirmation in the case of a thin layer has encouraged a lot of work on MnSi thin films grown on Si substrates [112–114] and also this work will first concentrate on this system. However, it has become clear during the course of this work that the situation in a thin film grown on a Si(111) surface is different from the case of a free standing layer. In the epitaxially grown film the lattice mismatch between Si and MnSi causes in-plane tensile strain in the film, which gives an additional contribution to the uniaxial distortion.

3.1 Properties of Bulk MnSi

The monosilicide MnSi has attracted considerable attention among researchers over a period beginning in the 1960s and lasting until today. Therefore MnSi is one of the most studied materials in modern physics. This great interest is mostly due to the peculiar magnetic properties of MnSi. Magnetic interactions of different energy scales compete with each other causing the ground state to be a spin helix. By controlling parameters as temperature, magnetic field and pressure the helix can easily be transformed into large variety of different phases, which offer a spacious playground for numerous physicists.

MnSi crystallizes in the cubic B20 structure shown in figure 3.1 with a lattice constant of 4.560 Å [115]. In the B20 crystal structure, which is also inherent to other transition metal compounds such as for example FeSi, CoSi, MnGe, and FeGe, there are eight atoms inside the unit cell. Each Mn atom possesses seven Si neighbors, which are located at distances of 2.30 Å (1 atom), 2.39 Å (3 atoms) and 2.55 Å (3 atoms) [116]. Six more Mn atoms surround the first one each at a distance of 2.79 Å. An important feature of the B20 lattice structure, which belongs to the space group $P2_13$ (T^4), is the lack of inversion symmetry, that causes the existence of two different crystal

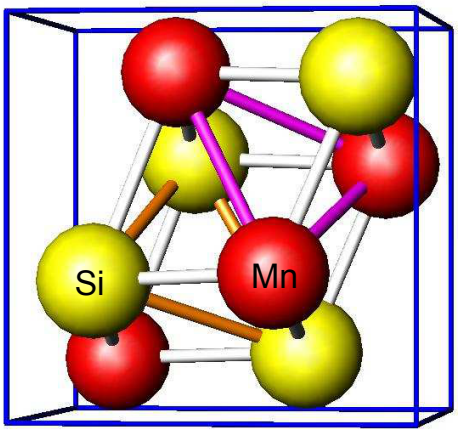

Figure 3.1: B20 crystal structure of MnSi.

types with conversed handednesses.

The investigation of the magnetic properties of MnSi started nearly half a century ago. In 1966 Williams *et al.* [117] discovered a magnetically ordered state below the ordering temperature $T_{c,bulk} = 29\,\mathrm{K}$. A few years later it was shown by neutron diffraction experiments that the ground state of the system is a helical spin structure [118] with a long period of 18 nm. The rotation sense of the helix is connected with the handedness of the crystal structure. Ishida *et al.* [119] proved that crystals with a left-handed lattice structure also form spin helices which are left-handed i. e. the spins of the helix are arranged in an anticlockwise way.

The formation of the helical ground state in zero magnetic field is caused by the competition of three different magnetic interactions of different strength, which is generally described by the magnetic free energy w introduced in section 2.1 [21, 34, 35]:

$$w = A\left(\mathrm{grad}\vec{M}\right)^2 - D\vec{M}\cdot\mathrm{rot}\vec{M} + \sum_i \left[B_{ea}\left(\frac{\partial M_i}{\partial r_i}\right)^2 + K_c M_i^4\right] \qquad (3.1)$$

In MnSi the ferromagnetic exchange specified by the first term is the strongest and favors a parallel alignment of the magnetic moments. The second term describes the weaker Dzyaloshinskii-Moriya (DM) interaction, which effects a canting of the spins. An even smaller contribution to the magnetic free energy is given by exchange anisotropy and cubic anisotropy. These interactions align the wave vector of the helix along the $< 111 >$ crystallographic directions.

The helical magnetic structure can be transformed into different spin configurations by applying an external magnetic field (compare figure 3.2). Since the pinning of the helix propagation vector to the $< 111 >$ crystal

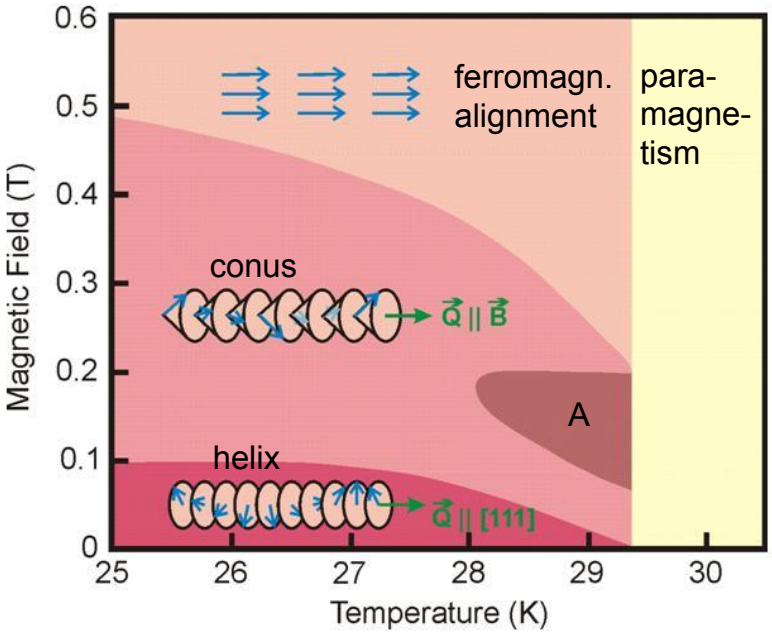

Figure 3.2: Magnetic phase diagram of bulk MnSi.

directions is only weak, a small applied magnetic field of $B_{c1} = 0.1\,\mathrm{T}$ [118] is sufficient to enforce a rotation of the helix axis into the field direction. Magnetic fields larger than 0.1 T generate a conical spin state, where the angle of the cone decreases, when the field increases. When the angle of the cone reaches zero and all spins are aligned with the field, the second critical field $B_{c2} = 0.6\,\mathrm{T}$ [117] marks the onset of induced ferromagnetic spin alignment.

The most curios part of the magnetic phase diagram, however, is a small phase pocket, which is called the A-phase. It is located just below the ordering temperature and is observed in applied magnetic fields between approximately 0.1 and 0.3 T. It was in the 1980th when this phase was already observed in a number of experiments [120–122], but only very recently its nature could be enlightened. In 2009 Mühlbauer *et al.* [12] performed small angle neutron scattering experiments on MnSi and discovered magnetic Bragg peaks arranged in a hexagonal shape. They interpreted their results as being caused by a spin structure composed of three helices at angles of 120°, all of them lying in the plane perpendicular to the direction of the magnetic field. Theoretical studies suggest that this magnetic structure is a lattice of skyrmions (compare section 2.1).

Further evidence for the existence of skyrmions in the A-phase of MnSi was given by Hall effect measurements [62]. In MnSi there are three dif-

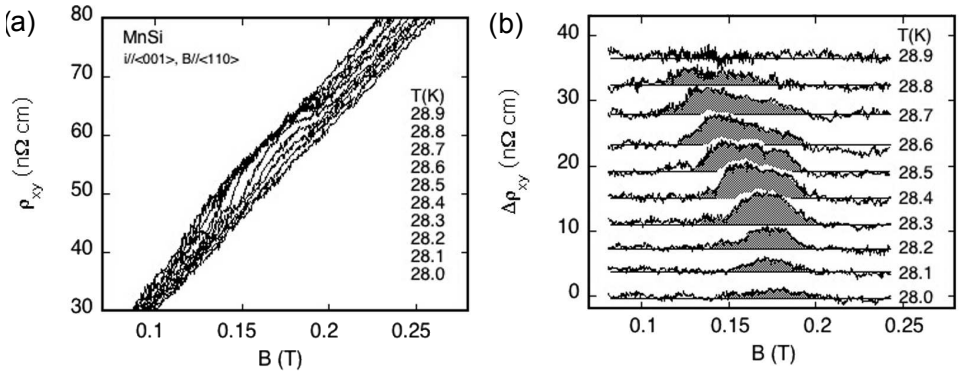

Figure 3.3: Taken from [62]: (a) Hall effect in MnSi for temperatures close to $T_{c,bulk}$, (b) topological contribution to the Hall effect

ferent contributions to the total Hall resistivity ρ_{xy}, which are an ordinary, an anomalous and a topological Hall effect. The normal Hall effect is positive with an almost temperature independent value of $R_0 \approx 10^{-10}\,\Omega\mathrm{m/T}$ [123, 124], which means that the current is predominantly conducted by positively charged holes. The AHE can be described as being proportional to the magnetization and to the square of the longitudinal resistivity [123, 124]. Finally, the THE is an additional small contribution, which adds to the normal and the anomalous Hall resistivity in certain temperature and magnetic field regions (compare figure 3.3). For MnSi ρ_{xy}^{top} appears only in the A-phase and its size is $5 \cdot 10^{-11}\,\Omega m$ [62]. The origin of this contribution is a real space Berry phase, which is picked up by an electron, when it moves through a skyrmion and its spin follows the non-trivial magnetization profile (compare section 2.1).

Another external parameter, which has influence on the magnetic state is hydrostatic pressure. When pressure is applied on MnSi the ordering temperature decreases continuously and magnetic order is suppressed completely at the critical pressure $p_c = 1.46\,\mathrm{GPa}$ [27, 28, 125, 126]. While the resistivity at low temperatures is proportional to T^2 as long as $p < p_c$, it follows a $T^{3/2}$ law at low temperatures above the critical pressure [27, 32, 127].

At a pressure of $p^\star = 1.2\,\mathrm{GPa}$ and the corresponding transition temperature of $T^\star = 12\,\mathrm{K}$ there are signs of a pressure induced crossover. The pressure dependence of T_c changes from a $(p-p_c)^{3/4}$ behavior at low pressure to a $(p-p_c)^{1/2}$ law, when $p > 1.2\,\mathrm{GPa}$ [75, 127]. Furthermore non-Fermi liquid behavior, where the resistivity falls as $T^{3/2}$, can be observed in a temperature range from $T^\star$ to T_c, when p exceeds $p^\star$ [29, 32].

As shown in the phase diagram in figure 3.4 an extended regime of NFL behavior identified by a $T^{3/2}$ resistivity can be found in MnSi at high pressure. In the same regime partial magnetic order was evidenced by neutron

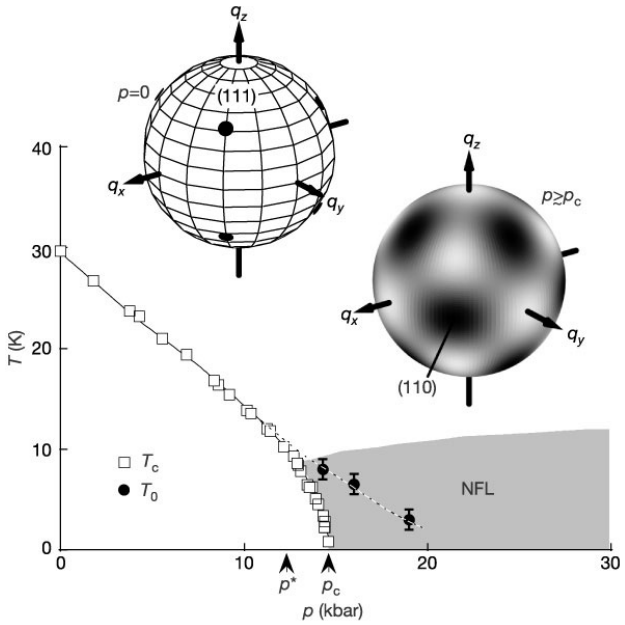

Figure 3.4: Temperature-pressure phase diagram of MnSi taken from [128]. In the NFL regime above $p^\star$ partial order was identified by neutron scattering experiments. In the insets the directions of elastically scattered intensity in reciprocal space are indicated for the ambient and the high pressure case.

scattering experiments [128]. As indicated in the insets of figure 3.4 the scattering intensity in reciprocal space is shifted from the [111] direction, which corresponds to the helix propagation direction in the ordered phase, to an area around [110]. Obviously spin spirals do still exist beyond p_c, but they are unlocked from their propagation direction. This scenario has been described theoretically within the quantum order-by-disorder approach [84] (compare section 2.3), which can nicely account for the measured intensity patterns, but does not explain the $T^{3/2}$ resistivity.

However, recent Hall effect measurements under high pressure have confirmed a topological Hall effect in the NFL regime [32]. This suggests that fluctuating skyrmions form the partially ordered state. The corresponding theory of fluctuating columnar spin textures that cause NFL behavior predicts a $T^{3/2}$ resistivity [85] (compare section 2.3), which is in agreement with the experimental results.

Considering the evolution of the A-phase under pressure also Hall effect measurement have provided new information [129]. A topological Hall signal confirms that the skyrmion phase is clearly enlarged under pressure and also the size of the signal increases. Furthermore skyrmions can be observed even at lowest temperatures, when the pressurized sample is cooled in a magnetic field so that it passes through the A-phase. In this case skyrmions survive as a metastable state, when the sample leaves the A-phase towards lower temperatures.

In conclusion, MnSi is a compound with multifaceted properties. In the past the material has challenged experimentalists as well as theoreticians, but the plenty of work that has been spent on MnSi made it a pioneering example for new physics such as skyrmions. Still ongoing discussions on the critical behavior close to the phase transitions make sure that MnSi is still an up-to-date topic today. For the future especially the growth of thin films offers new perspectives, since the magnetic properties of MnSi can be modified by strain and finite size effects.

3.2 Preparation of MnSi Thin Films

3.2.1 Characteristics and Treatment of the Si Substrate

As substrate material for the growth of MnSi thin films silicon was chosen, because of several reasons. On the one hand its lattice parameter is suitable for epitaxial growth and on the other hand Si is a common material in semiconductor technologies and available with excellent crystalline quality. Furthermore Si is contained in MnSi and this offers the possibility to prepare samples by annealing a Mn layer into the substrate.

Phosphorous-doped Si(111) wafers with a thickness of 280 μm and a nominal resistivity at room temperature between 1 and 10 Ωcm have been used. Their dimensions were $1 \times 1\,\mathrm{cm}^2$ or $1.5 \times 1.5\,\mathrm{cm}^2$ for some larger samples. The substrates were supplied epi-ready with one polished surface.

The evenness of the Si surface was proved by AFM investigations. In figure 3.5a an AFM image showing $4\,\mu\mathrm{m}^2$ of an untreated substrate is depicted. The height profile along the marked scan line illustrates that along a line of 2 μm length differences in height of only 1.5 nm occur (compare figure 3.5b), which corresponds to three times the height of a Si unit cell.

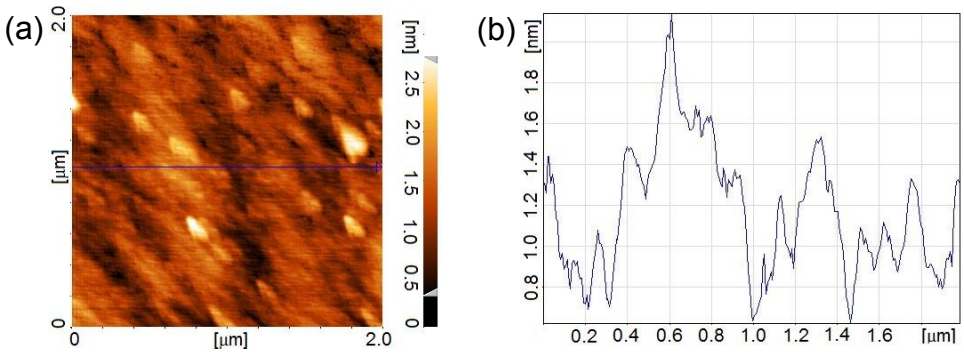

Figure 3.5: (a) AFM image of the untreated Si substrate, (b) line scan across the image along the marked line.

Before a thin film can be grown on the Si surface, the substrates need to be cleaned in order to remove the oxide layer from the surface. Several techniques have been proposed for this purpose. A cleaning procedure described by Karhu *et al.* [112], which consists of etching with a solution of ammonium hydroxide (NH_4OH) and hydrogen peroxide (H_2O_2) and subsequent heating under UHV conditions, was tested first. Furthermore it was tried to clean the surface by sputtering with argon gas. These techniques did not lead to satisfying results, since the Si surface was rather three-dimensional than flat as could be proved by RHEED investigations [130].

A much better outcome was achieved by simply heating the substrate under UHV conditions to 1100 °C. Holding this temperature for five min-

utes and subsequently cooling the sample down to room temperature with a cooling rate of approximately 1 °C/s produces a two-dimensional surface verified by the RHEED pattern (compare figure 3.6). The surface exhibits a 7×7 reconstruction, which gives evidence for its evenness and cleanliness. The appearance of Kikuchi lines confirms the excellent crystalline quality of the Si substrate.

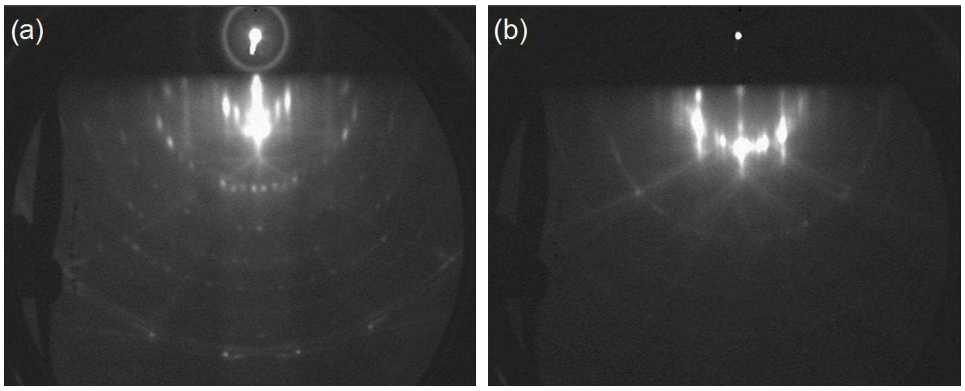

Figure 3.6: RHEED patterns of the Si substrate with 7×7 reconstruction along (a) $[10\bar{1}]$ and (b) $[11\bar{2}]$ directions of the Si crystal.

3.2.2 The Growth of MnSi Thin Films on Si(111)

In order to achieve epitaxial growth of a material on a selected substrate, it is necessary that the lattice parameters of the two crystal structures match each other. In the case of MnSi on Si substrates the lattice spacings in the (111) planes are of interest, as MnSi grows in [111] direction on Si(111). The room temperature lattice parameter of MnSi is 4.560 Å [115], which implies a periodicity within the (111) plane of 6.450 Å. Since this is only 3% smaller than the lattice constant of the $\sqrt{3} \times \sqrt{3}R30°$ reconstructed Si surface, MnSi can be grown epitaxially with tensile strain on Si [26]. The arrangement of the MnSi lattice on the Si crystal is depicted in figure 3.7.

In general, there are two different methods applicable to grow thin films of MnSi inside a MBE set-up. During this work both of them have been utilized and tested extensively. The first technique involves the deposition of a single Mn layer onto a clean Si surface at a properly defined substrate temperature. After deposition the Mn film is heated until a RHEED pattern characteristic for the presence of MnSi can be observed. The second type of films is grown by codeposition of Mn and Si, which means that the two elements are evaporated simultaneously. Using this technique MnSi forms directly without any further annealing procedure. This approach is more challenging than the annealing technique, since its outcome is very sensitive to temperature and deposition rates, but there are indications that the films

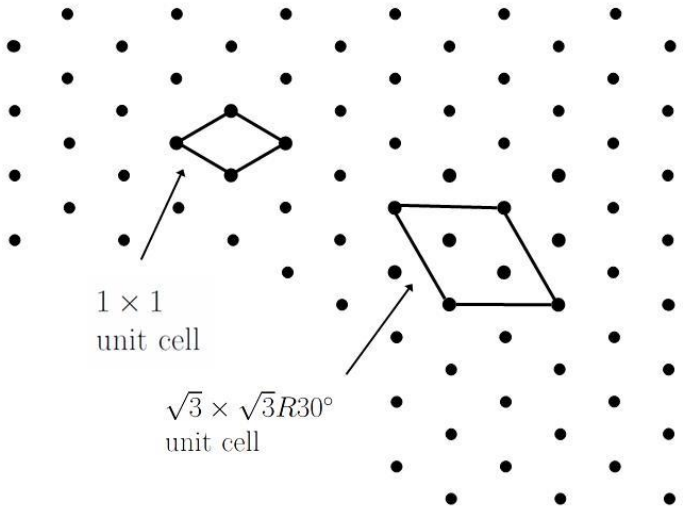

Figure 3.7: View of the alignment of MnSi on the Si surface. The MnSi unit mesh in (111) direction matches the $\sqrt{3} \times \sqrt{3}R30°$ reconstructed unit cell with a misfit of $-3\,\%$.

grown by codeposition possess better quality [131]. In the following the characteristics and differences of both techniques to grow MnSi thin films on Si(111) will be described in detail.

The annealing method

The annealing of a Mn layer into a Si substrate, which is a method of solid phase epitaxy, is a widely used technique to prepare thin films of MnSi [26, 112, 113, 132–143]. However, among all papers, which deal with this method, there exists a variety of different descriptions of the annealing process. Especially regarding the most important parameters of the procedure, namely the annealing temperature and time, large disagreement can be found. For example, Magnano *et al.* [113] indicate that heating a Mn layer of 10 nm thickness to 620 °C is adequate to obtain the desired MnSi thin film. Karhu *et al.* [112], in contrast, anneal their films at 400 °C for one hour, while Higashi *et al.* [142] consider temperatures around 250 °C as sufficient. This manifold of apparently contradictory information encouraged the investigation of the annealing method in order to find the optimum conditions.

First, the suitable temperature for the annealing process needs to be ascertained. Therefore, a 5 Å Mn layer was deposited from an effusion cell onto the clean Si substrate exhibiting a 7×7 reconstruction. During the evaporation of Mn with a rate of 0.1 Å/s the substrate was held at a temperature of

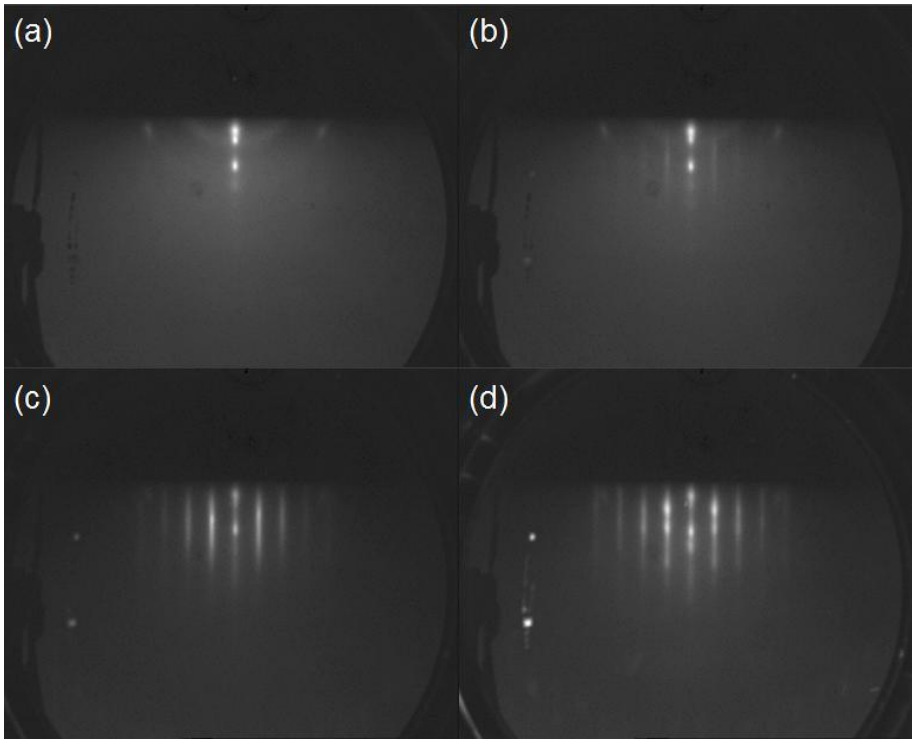

Figure 3.8: Evolution of the RHEED pattern of a 5 Å Mn layer with temperature: (a) directly after deposition at 180 °C, (b) at 300 °C faint streaks appear, (c) at 350 °C MnSi has formed and (d) at 550 °C spots due to three-dimensional islands become increasingly strong.

180 °C. Afterwards it was heated up slowly to 630°C under RHEED observation. During this experiment the evolution of the crystalline configuration and the morphology of the film could be monitored.

In this experiment it could be observed that directly after deposition of the Mn layer the RHEED pattern is very diffuse. As shown in figure 3.8a only some faint leftovers of the Si main reflections and vague indications of polycrystalline reflection rings are observable. Thus, the temperature of 180 °C is not sufficient to effect a reaction of the Mn atoms with the Si of the substrate. Instead, an amorphous Mn layer with some polycrystalline percentage has formed on the substrate.

When the temperature reaches 300°C, streaks which are characteristic for MnSi start to appear (compare figure 3.8b) and become brighter with increasing temperature. As can be seen in figure 3.8c, they are fully developed at 350 °C and remain mainly unchanged until the temperature reaches 450 °C. Above this temperature the RHEED streaks become superimposed by a diffraction pattern known from three-dimensional structures, which originates from electrons that penetrate small islands on the film surface. Around 500°C this 3D pattern becomes more pronounced indicating an increase of the surface roughness (compare figure 3.8d). Thus, the substrate temperature must not be too high in order to prevent the film from forming islands.

From this experiment it can be concluded that the morphologically best MnSi films which maintain mainly two-dimensional character are prepared at an annealing temperature between 350°C and 450°C.

In addition to the suitable annealing temperature, it is important to know the time needed until Mn has completely reacted to form MnSi. This time is strongly dependent on the thickness of the Mn layer that has been deposited on the substrate. When there is only a thin ($\approx 5 - 15$ Å) Mn film on the Si surface, MnSi forms almost immediately in the moment the required temperature is reached.

For Mn layers with a thickness of 20 Å and more, the reaction takes more time and an intermediate Mn rich phase can be observed before MnSi is generated. In order to investigate this process the changes of the crystal structure and morphology of a 25 Å Mn layer during annealing have been monitored by RHEED. Therefore the sample was heated to 360 °C, which has been determined to be an appropriate temperature for good MnSi film quality. Every minute a RHEED image was taken to visualize the changes. Directly after deposition a diffuse background is visible which implies a polycrystalline or even amorphous Mn film (compare figure 3.9a). After 6 minutes of heating some streaks start to occur in the diffraction pattern, which are fully developed after 8 minutes as it is shown in figure 3.9b. The evaluation of the streak distances, however, reveals that the reciprocal lattice vector of the film is $(4 \pm 1)\%$ smaller than the corresponding vector for the

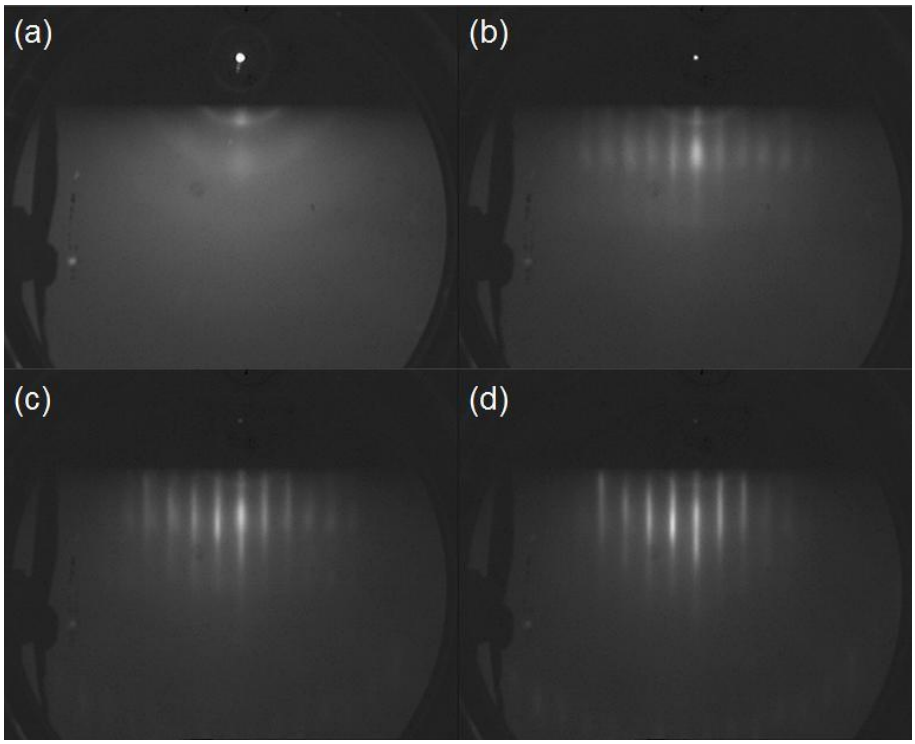

Figure 3.9: RHEED patterns of a 25 Å layer Mn during annealing at 360 °C: (a) at the starting point, (b) after 8 minutes, (c) after 14 minutes and (d) after 20 minutes.

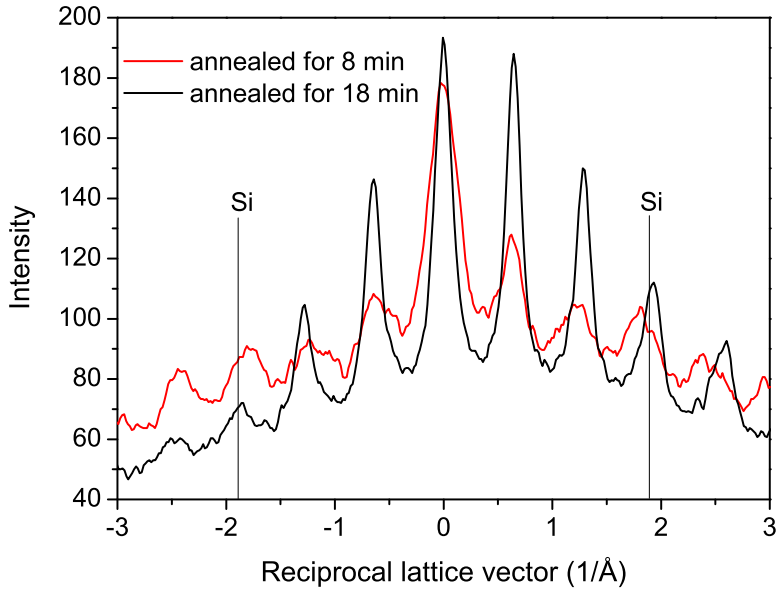

Figure 3.10: Comparison of line scans perpendicular to the streaks of RHEED patterns taken after 8 and 18 minutes of annealing time. Vertical lines mark the positions, where the Si streaks are expected.

Si substrate (compare figure 3.10). This implies a lattice constant of the grown compound of 7.0 Å± 0.1 Å. Thereby the phase present after 8 minutes of annealing can be identified to be Mn_5Si_3. This compound possesses a hexagonal lattice cell with $a_{hex} = 6.917$ Å [144], which is in good agreement with the observed RHEED pattern. The same intermediate phase has also been observed by Ctistis *et al.* [138] during the growth of Mn on Si(111)-$\sqrt{3} \times \sqrt{3}$:Bi.

After additional 5 minutes of annealing the temporary Mn-rich phase starts to transform into MnSi. Now, the RHEED pattern consists of a superposition of two different sets of streaks belonging to crystal structures with slightly different lattice parameters (compare figure 3.9c). After an overall annealing time of 20 minutes the film has completely been transformed into MnSi, which is evidenced by the RHEED pattern in figure 3.9d. When this stage has been reached further annealing does not lead to any changes of the RHEED pattern.

Comparing the RHEED streaks of MnSi to the Si streak positions as shown in figure 3.10 it can be seen that the lattice constant of the film is 1 % smaller than the corresponding surface mesh of Si, but the uncertainty of this value is of the same size. Therefore it can be concluded that the MnSi thin film is strained, since the deviation of the relaxed crystal structure is 3%. However, due to the uncertainty in the evaluation of the RHEED streaks it cannot be ensured, whether the film has grown pseudomorphically or whether it has partly relaxed.

From the described experiments it is concluded that a 20 Å layer Mn must be annealed for 20 minutes at 360 °C until MnSi has formed. For Mn layers with greater thickness, however, the annealing time will be longer. A 60 Å layer, for example, needs to be heated for one hour at 360 °C to obtain pure MnSi. Higher annealing temperatures can reduce the time but only at the expense of the film quality, since higher temperatures lead to the formation of islands. Also in cases where the Si surface is not atomically flat, the reaction proceeds faster because of a larger surface area that provides Si for the forming of MnSi. Nevertheless, it is not advisable to use a substrate with such a suboptimal surface, as the RHEED patterns evidence partly three-dimensional growth in some of these cases.

Codeposition of Mn and Si

The second technique to prepare MnSi thin films on Si(111) is codeposition of Mn and Si. In this process the constituents are evaporated simultaneously and can react directly to MnSi without incorporation of Si atoms from the substrate into the film. For the procedure a clean Si surface is prepared in the same way as for the annealed films. Mn is evaporated from an effusion cell, whereas Si is provided by an electron beam evaporator. In order to maintain stoichiometric MnSi it is of special importance to offer the same

amount of atoms from both elements. The correct ratio of deposition rates can be calculated using the equation

$$\frac{N_{Si}}{N_{Mn}} = \frac{r_{Si}\hat{N}_{Si}\hat{V}_{Mn}}{r_{Mn}\hat{N}_{Mn}\hat{V}_{Si}} \stackrel{!}{=} 1. \tag{3.2}$$

Here, N_{Si} and N_{Mn} denote the total numbers of Si and Mn atoms, respectively, which are supposed to be equal. r_{Si} and r_{Mn} are the deposition rates, $\hat{V}_{Si} = a_{Si}^3 = 9.482 \cdot 10^{-29}\,\mathrm{m}^3$ and $\hat{V}_{Mn} = a_{Mn}^3 = 7.078 \cdot 10^{-28}\,\mathrm{m}^3$ describe the volumes of the unit cells, and $\hat{N}_{Si} = 8$ and $\hat{N}_{Mn} = 58$ are the numbers of atoms present in a unit cell. As a result, the ratio of the deposition rates has to amount

$$\frac{r_{Si}}{r_{Mn}} = 1.64. \tag{3.3}$$

According to this outcome the Mn rate was adjusted to 0.1 Å/s and the Si rate to 0.17 Å/s. Unfortunately, due to fluctuations of the deposition rate of the electron beam evaporator the Si rate cannot be adjusted more precisely to the desired value. However, from the excellent quality of the films prepared with these parameters it can be concluded that small deviations from the 1:1 ratio do not disturb the forming of MnSi. Excess Mn or Si atoms obviously re-evaporate from the substrate as long as the imbalance of the rates is small enough.

During the simultaneous evaporation of Mn and Si the substrate temperature plays a fundamental role, since it affects the surface mobility of the deposited atoms, which need to react to MnSi directly within the deposition process. The flattest films grown by codeposition are obtained at a substrate temperature of 250°C. This is evidenced by well defined streaks in the RHEED pattern indicating two dimensional growth.

Higher substrate temperatures lead to a variety of diffraction spots (compare figure 3.11a) showing that in addition to MnSi also other compounds of Mn and Si are formed. Their lattice parameters are considerably larger than those of MnSi as can be deduced from the small distances between the RHEED reflections. This is a strong indication for the presence of compounds with rather complex crystal structure. For instance, a number of compounds close to the composition $MnSi_{1.7}$ are known to exhibit large unit cells [145].

At substrate temperatures slightly below 250°C island growth is favored. This is evidenced by a 3D RHEED pattern with diffraction spots aligned parallel to the shadow edge as shown in figure 3.11b. At room temperature Mn and Si atoms do not react to form crystalline MnSi. Consequently, no spots or streaks are observed in the RHEED pattern and do not even appear after post-growth annealing.

In figures 3.11c and 3.11d RHEED patterns along the $[11\bar{2}]$ and the $[10\bar{1}]$ directions of the substrate are depicted, respectively, which differ by 30°

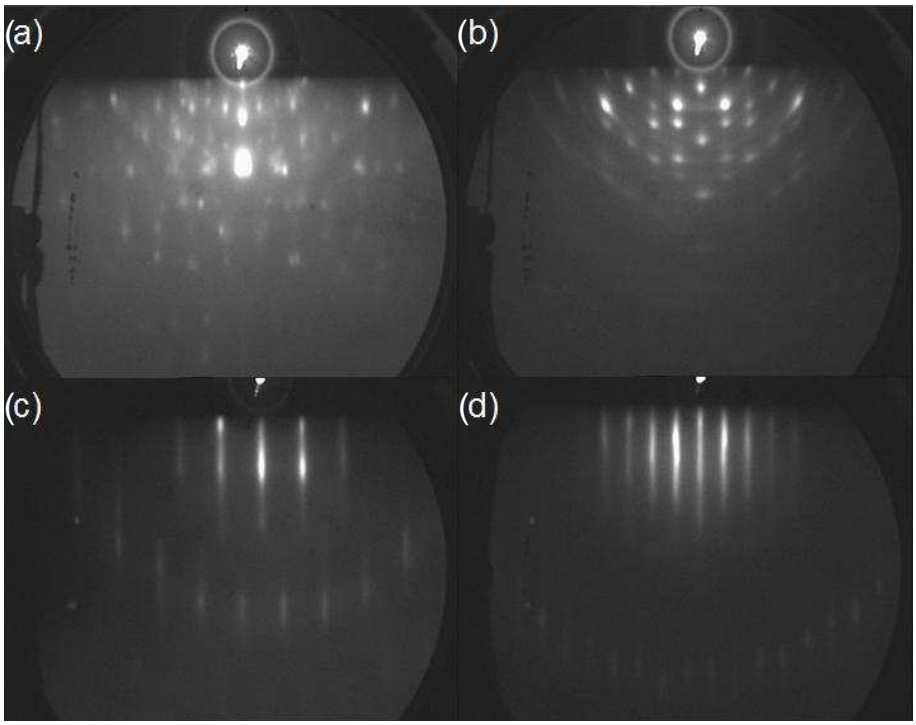

Figure 3.11: RHEED patterns of a 70 Å MnSi film codeposited at a substrate temperature of (a) 400°C and (b) 175°C. RHEED patterns of a 190 Å codeposited MnSi film along the (c) $[11\bar{2}]$ and (d) $[10\bar{1}]$ direction.

in incidence angle. After codeposition growth as well as after annealing diffraction patterns characteristic for MnSi are observed, which recur, when the sample is rotated by 60° with respect to the azimuthal angle. This is most probably an indication of the three-fold symmetry of the MnSi(111) surface. However, the films may also possess an effective six-fold symmetry, which may be induced by different orientations of crystallites on the substrate. [1]

The streakiness of the patterns achieved by codeposition growth is evidence for a predominantly two-dimensional monocrystalline surface with steps that have the dimension of single atomic layers. This is a strong indication that the films prepared by codeposition have an excellent morphological quality, at least on surface areas that have the size of the correlation length of the RHEED electrons.

Recently, it has been proposed that very flat films can be achieved, when a thin seedlayer is prepared by the annealing method before starting the codeposition [146]. To test this suggestion MnSi films were prepared, where first a 5 Å Mn layer was alloyed into the Si substrate before MnSi was codeposited.

[1] For the case of island growth as depicted in figure 3.11b it has been shown that the orientation of the MnSi crystal is rotated by 60° in different islands [130].

As a matter of fact, this procedure produces mostly flat homogeneous MnSi films. Regarding the results of the RHEED investigation, however, their morphological quality could not be evidenced to be better than the codeposited films grown without a seedlayer. On the contrary, in some cases it was observed that the preparation of a seedlayer can promote island growth of the codeposited films. Obviously imperfections existing in annealed layers propagate through the film and disturb the growth of a closed layer.

3.3 Morphological and Structural Characterization

In the previous section two different techniques to prepare thin films of MnSi on Si(111) substrates have been described, namely the annealing method and the codeposition. Using RHEED a first estimation concerning the morphology of the different films was obtained. Under suboptimal conditions island growth evidenced by a three-dimensional pattern or even polycrystalline or amorphous growth were observed, where no well-defined spots or streaks appeared on the RHEED screen. By improving the growth conditions of both preparation methods it was possible to prepare films with good surface quality according to the RHEED investigations. However, the smooth streaks do not guarantee excellent surface quality extending over large areas of the film. Since the correlation length of the electrons is limited, only a surface area of approximately 100 nm in diameter can contribute to the pattern (compare section 2.6.3). As a consequence surface structures that exceed this size cannot be resolved. Therefore AFM and TEM have been used to get images of larger films areas.

3.3.1 Atomic Force Microscopy

AFM images of a large number of MnSi thin films were taken in order to learn how their morphology can be manipulated by the growth conditions and to prove the flatness of good samples. Especially the differences between films grown by the annealing method and by codeposition are of interest, since the method leading to better results should be used to grow a series of films with different thicknesses for measurements of their physical properties.

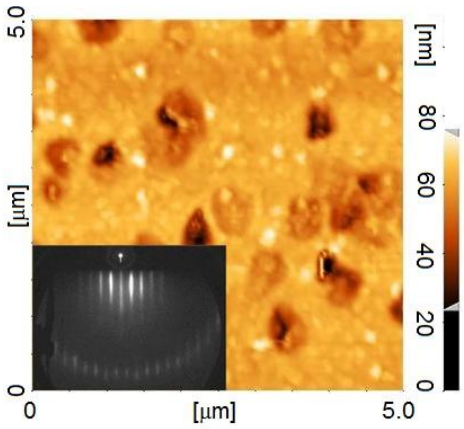

Figure 3.12: AFM image of a 13 nm film prepared by annealing. The inset shows the corresponding RHEED pattern.

In figure 3.12 an AFM image showing a 25 μm^2 surface area of a thin film prepared by the annealing method is depicted. The film has a thickness of 13 nm and its RHEED pattern consists of very smooth streaks (compare inset of figure 3.12) promising a two-dimensional surface. However, the flatness of the surface is not as good as expected. Although there are flat areas with a root mean square (rms) roughness of only 2 nm, the surface is speckled with holes that have a depth of up to 30 nm. This depth is distinctly larger than the thickness of the film, which can be explained by the growth mechanism. Since only Mn is deposited onto the substrate, Si for the MnSi film has to be provided by the substrate. Higashi *et al.* [142] have given evidence that the Si atoms are supplied from craters in the substrate. Therefore it seems to be impossible to grow closed films by the annealing method, at least when their thickness exceeds a few monolayers. Nevertheless, apart from the holes, the film quality is good, as the surface is very flat and homogeneous.

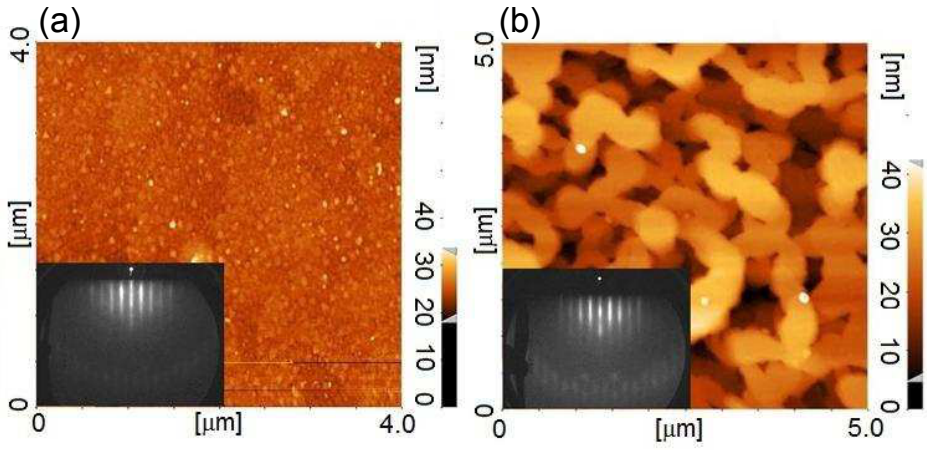

Figure 3.13: AFM images of codeposited films with 19 nm thickness. (a) An example of a flat film, (b) an example of island growth. In the insets the corresponding RHEED patterns are depicted.

For comparison, an AFM picture of a 19 nm codeposited films of excellent flatness is shown in figure 3.13a. In this case the rms roughness of the investigated surface area amounts only 1 nm, since the simultaneous supply of Mn and Si atoms makes layer-by-layer growth of Frank - van-der-Merwe type possible. However, optimal conditions are needed to achieve such a result. In figure 3.13b an example of a different film grown under nearly the same conditions is shown. Although the RHEED patterns of both codeposited films are virtually identical, the AFM image proves island growth in the second case that cannot be resolved by RHEED. The comparison of a number of different films led to the conclusion that island growth is favored in those

cases, where the substrate's surface is not perfect. This can be evidenced by a not fully developed 7×7 reconstruction in the RHEED pattern due to defects or impurities on the surface. Obviously the epitaxial layer-by-layer growth is prevented by the unevenness of the surface.

3.3.2 Transmission Electron Microscopy

For further investigation of the morphology of MnSi thin films two samples have been chosen for transmission electron microscopy. In order to get a view of the film's cross-section the samples have to be prepared by a complex procedure. First two pieces of the same sample are glued together, where the film surfaces are facing each other and the substrate is at the outside. Then the sample has to be thinned in a plane perpendicular to the film, so that the electrons of the microscope can penetrate it. Therefore a Precision Ion Polishing System (PIPS) was used to realize a sample thickness in the order of 100 nm.

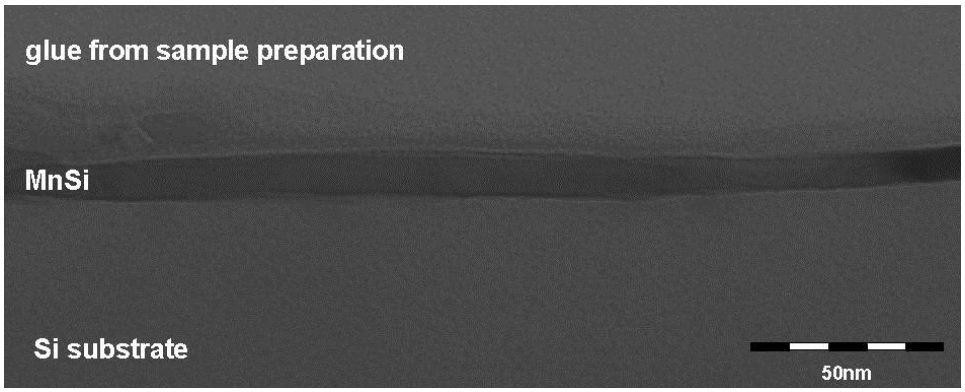

Figure 3.14: Cross-sectional TEM image of a 12 nm thin film MnSi prepared by annealing a Mn layer.

In figure 3.14 the TEM image of a 12 nm MnSi thin film prepared by annealing is shown. Although some imperfections like holes and wavy structures in the film as well as in the substrate were found, there are large areas exhibiting smooth film morphology. The same is true for a 23 nm film grown by codeposition, which is depicted in figure 3.15. Comparing the codeposited film with the one prepared by annealing, it can be concluded that the codeposition process clearly leads to flatter films. Especially the interface between substrate and film is considerably smoother for the codeposited film. This seems reasonable, since atoms of the substrate are incorporated into the film during annealing.

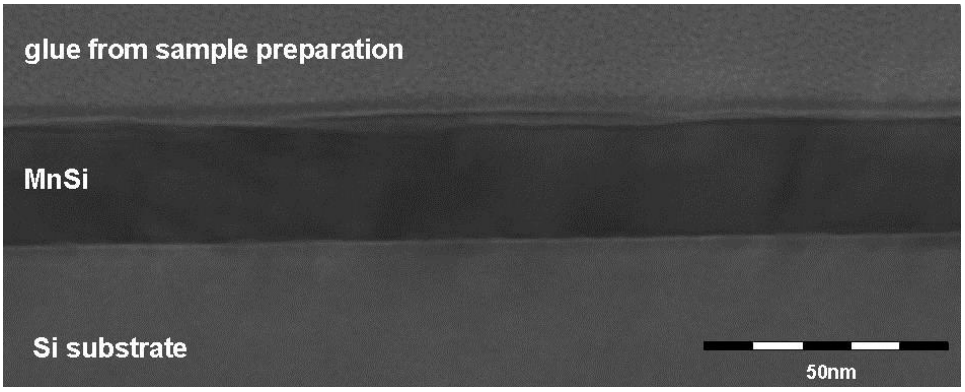

Figure 3.15: Cross-sectional TEM image of a 23 nm film prepared by codeposition.

3.3.3 RHEED

In AFM and TEM images it could be seen that the codeposition method, although much more complex in realization, is better suited for the growth of MnSi thin films. Therefore this technique was chosen for the preparation of a series of thin films with thicknesses between 2 and 30 nm. As already discussed in section 3.2 MnSi with B20 structure grows epitaxially on the $\sqrt{3} \times \sqrt{3}R30°$ reconstructed Si(111) surface. Taking the RHEED pattern of the Si substrate as a reference it is possible to calculate the lattice constant of the MnSi film from the distances between the RHEED streaks. The deviation of the lattice parameter from the MnSi bulk value gives the in-plane strain ϵ of the films as shown in figure 3.16. The error bars were calculated by error propagation from the uncertainty in determination of the streak positions.

Due to the limited resolution of the RHEED system the small deviations of the films' lattice constants from the bulk value possess large error bars, but nevertheless it is obvious that the films are strained. For most of the films ϵ ranges between zero and 2 %. As all values are smaller than the misfit of 3 %, it can be concluded that the films have partly relaxed, i. e. dislocations must have formed during film growth to release part of the strain. Therefore the film growth can be characterized as semi-coherent.

It should be noted that no dependence of the strain on film thickness can be detected by the RHEED evaluation. The thinnest film under investigation (1 nm) has relaxed to the same extent as the thickest (19 nm).

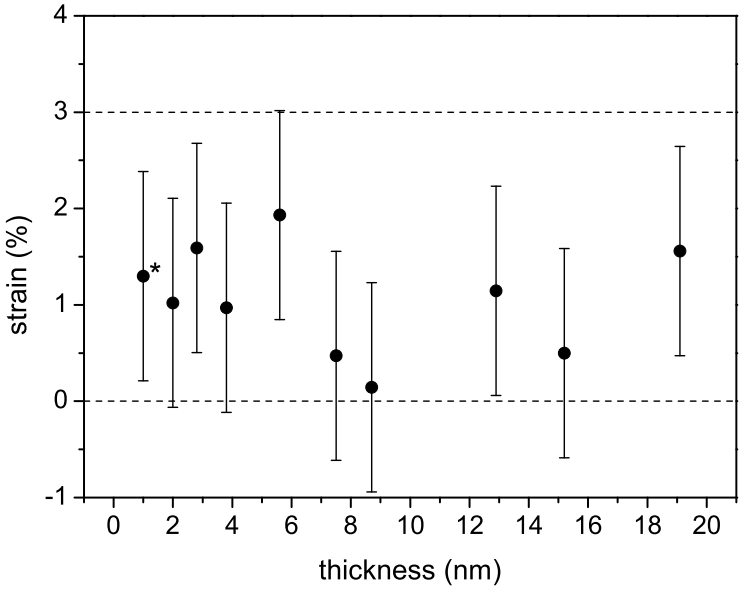

Figure 3.16: In-plane strain derived from RHEED streaks for films of different thickness prepared by codeposition. Dashed lines give the value for complete relaxation (0 %) and the maximal value that can be expected due to the misfit (3 %). ⋆ The 1 nm film has been prepared by annealing.

3.4 Magnetic Characterization

As described in the previous chapters, MnSi thin films have been grown by MBE and investigated by RHEED in-situ, which permitted a first estimation of the sample quality regarding the crystal structure and the morphology of the films. After removing the samples from the UHV chamber AFM and TEM images were taken to get further insight into the geometric properties of the films.

The next step to be performed on a successfully grown film is a magnetic characterization using a SQUID magnetometer, which is an excellent tool to reveal the most important physical properties of the grown material. These include especially the magnetic ordering temperature T_{ord} and the magnetic moment per Mn atom in the ordered state. Furthermore any features in the magnetization curves may hint to magnetic phase transitions as for example the critical field B_{c2}. In the following paragraphs the results of dc-susceptibility and magnetization measurements will be described in detail.

3.4.1 Dimensionality of MnSi Thin Films

Before starting the evaluation of magnetic measurements on MnSi thin films it has to be considered, which kind of behavior can be expected. This is important, since suitable theoretical models need to be chosen in order to fit the data reasonably. Here the question concerning the dimensionality of the thin films arises. Films consisting of only a few monolayers of atoms are known to act like a quasi-two-dimensional system, when spin wave excitations in the direction perpendicular to the film plane are suppressed. For the spin wave component normal to the film plane holds the relation [147]

$$k_{\perp} = \frac{m\pi}{na_0} \tag{3.4}$$

with m being a positive integer, n counting the number of monolayers in the film and a_0 denoting the lattice constant. Thus, the normal components of the spin wave vectors are quantized, and with decreasing film thickness the energy separation between permitted values increases. At a critical thickness N_c only the lowest branch is thermally populated and below this thickness spin waves traveling normal to the film plane can no longer be excited. In this case the system behaves like a two-dimensional system.

For quasi-three-dimensional behavior of a film with given thickness it is required that the thermal energy k_BT is larger than the separation between the excitation energies for spin waves perpendicular to the film plane. Thus, the value for N_c, which must be clearly exceeded, can be calculated to be [148]

$$N_c = \pi\sqrt{\frac{A}{2A_0k_BT}}, \tag{3.5}$$

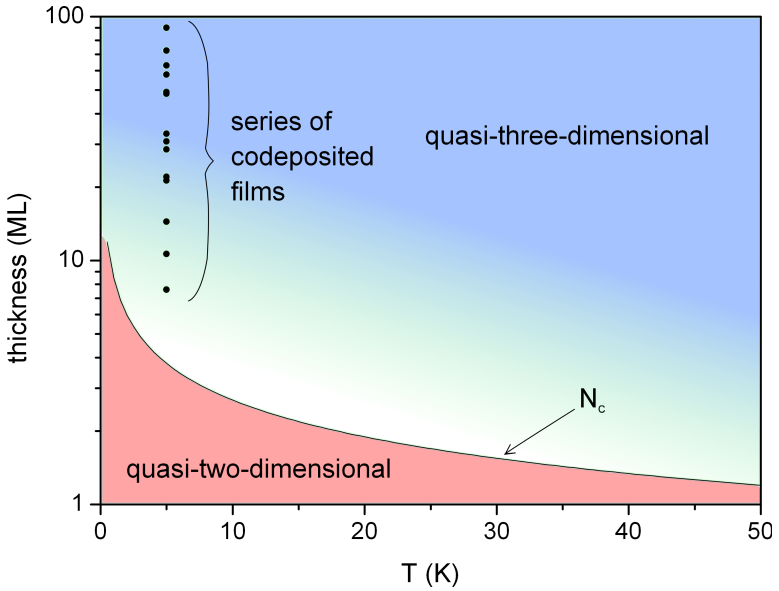

Figure 3.17: Temperature dependence of the critical thickness N_c, below which a thin film MnSi behaves like a two-dimensional system. The thicknesses of the codeposited films are marked as black dots at a temperature of 5 K, which is the lowest temperature reached in magnetization measurements.

where A is the spin wave stiffness and A_0 denotes the area of a unit cell in the film plane.

For MnSi thin films A was determined to amount 0.45 meV nm^2 [44], which leads to a temperature dependence of N_c as shown in figure 3.17. In the diagram the thicknesses of all codeposited films are plotted as black symbols at a temperature of 5 K, since this is the lowest temperature, where magnetization measurements were performed. Above this temperature most of the films are located clearly above the critical thickness (note the logarithmic scale of the ordinate), so that quasi-three-dimensional behavior is to be expected. Only the three thinnest films are quite close to the transition to the quasi-two-dimensional regime. It will be discussed in the following section, whether different critical behavior is observed or whether the same three-dimensional theory as for the thicker films can be applied.

3.4.2 Susceptibility Measurements

The magnetic susceptibility of the MnSi thin films was measured using a SQUID magnetometer of the type *Quantum Design* MPMS-5S SQUID, which offers the possibility to reach temperatures between 1.7 K and 400 K and magnetic fields up to 5 T.

The magnetic moments of a series of codeposited samples were measured

as a function of temperature in a magnetic field of 10 mT applied parallel to the film plane. These measurements provide a well suited method to determine T_{ord} of MnSi thin films, which was shown by Karhu *et al.* [112]. They demonstrated that from measurements in a very small field the same transition temperatures can be derived as from measurements of the remanent magnetization in zero field, but the presence of a magnetic field leads to larger magnetic moment of the sample, which is easier to detect. The measured curves exhibit a Curie-Weiss behavior in the paramagnetic regime and an increase of the magnetic moment at T_{ord}, which is dependent on the film thickness. T_{ord} was determined for every sample by fitting the susceptibility curve with the following expression [149]:

$$M(T) = M_0 \left[\left(1 - \left(\frac{T}{T_{ord}} \right)^p \right) \left(1 - b \left(\frac{T}{T_{ord}} \right)^{3/2} \right) + \left(\frac{T}{T_{ord}} \right)^p \left(1 - \frac{T}{T_{ord}} \right)^{1/2} \right]. \tag{3.6}$$

This formula combines two contributions. On the one hand spin waves cause a deviation from the saturation magnetization at temperatures above 0 K,

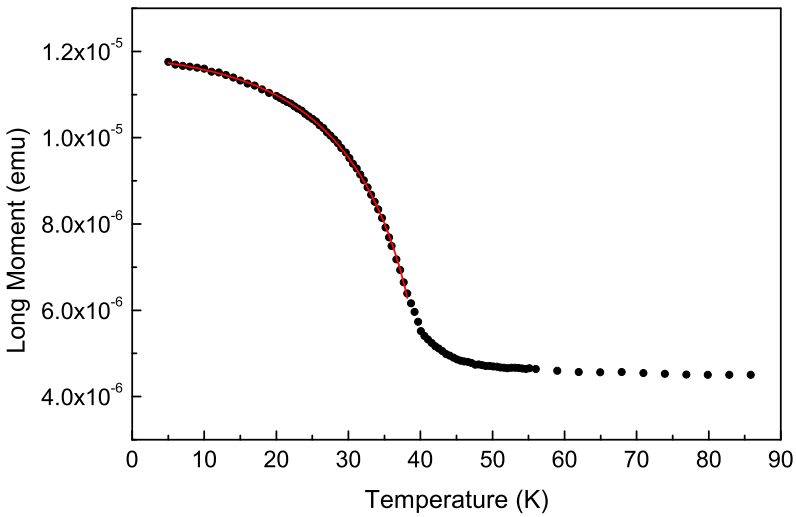

Figure 3.18: Magnetic moment versus temperature for a 9 nm sample measured in an applied field of 10 mT. The red line is a fit following equation 3.6 with the parameters $M_0 = 7.31 \cdot 10^{-6}$ emu, $T_{ord} = 39.5$ K, $b = 0.24$ and $p = 3.0$. Additionally there is a constant background amounting $4.5 \cdot 10^{-6}$ emu.

which can be described by Bloch's $T^{3/2}$ law [150]. On the other hand critical point behavior is dominant near T_{ord} with a critical exponent of 1/2 in good agreement with the value for bulk MnSi [151]. The proportion of the two parts is determined by the parameter p. The equation fits the measured data very convincingly as can be seen in Figure 3.18, where the curve for a 9 nm thin film is shown exemplarily.

As discussed in the previous section the fit using equation 3.6 must be put into question for the thinnest films of the series, since these films are close to the transition to quasi-two-dimensional behavior, whereas the theoretical model assumes a three-dimensional system. Therefore equation 3.6 was tentatively modified for films with two-dimensional character. The $T^{3/2}$ spin wave behavior did not need to be changed in the fitting law, since it can be found in many systems of ultrathin films (compare [152] and references therein) and is thus expected to be present also in films with quasi-two-dimensional behavior. The exponent of the critical point behavior, however, should adopt a value around 0.2 [147, 153, 154], when the films cross over into the two-dimensional regime.

To test whether the three thinnest films with thicknesses below 6 nm must be treated as two-dimensional systems, the corresponding susceptibility curves were tentatively fitted with critical exponents around 0.2. For the 2 nm film no reasonable results could be obtained, since the measurement is very noisy due to the smallness of the magnetic moment. For films with 3 nm and 6 nm thickness a comparison of the best fits with the critical exponent set to 0.2 and 0.5, respectively, is shown in figures 3.19 and 3.20. The comparison reveals that the 3D model fits the data much better than the 2D model, but the deviation between the data and the 2D fit is much smaller for the 3 nm film. Obviously for thicknesses below 3 nm the behavior of MnSi thin films will become quasi-two-dimensional, which is in agreement with the calculated transition shown in figure 3.17.

The ordering temperatures determined by the described method are plotted in figure 3.21 as a function of film thickness. It can be seen that T_{ord} for the codeposited films is strongly dependent on the thickness d of the MnSi thin films. For the thinnest films T_{ord} is smaller than the bulk value of 29 K, but a strong increase with growing film thickness is observed. For a film thickness around 10 nm T_{ord} reaches a saturation value of ≈ 43 K. The error bars in figure 3.21 indicate the uncertainty arising from the determination of T_{ord} from the magnetization measurements. It should be noted that inaccuracies concerning the thickness of the films can also occur, but are not presented in figure 3.21 in order to maintain a clear arrangement of the data. These inaccuracies are estimated to amount up to 10 %. Furthermore morphological differences between different samples can lead to changes of the magnetic properties, which are difficult to quantify and, therefore, also not included in the diagram.

In order to explain the reduction of T_{ord} for films thinner than 10 nm a

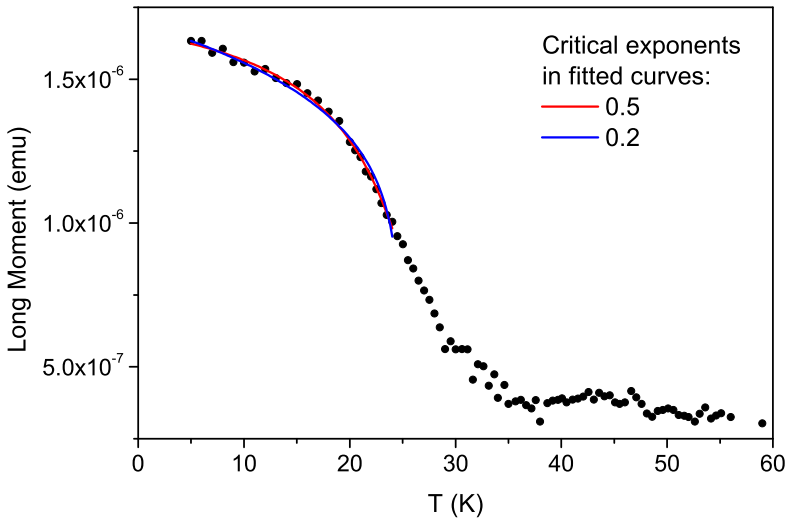

Figure 3.19: Susceptibility curve of a 3 nm thin film MnSi fitted with equation 3.6 with different values for the critical exponent. Fitting parameters for the red curve: $T_{ord} = 27.2\,\mathrm{K}$, $b = 0.27$ and $p = 3.8$. Fitting parameters for the blue curve: $T_{ord} = 24.6\,\mathrm{K}$, $b = 0.27$ and $p = 0.05$.

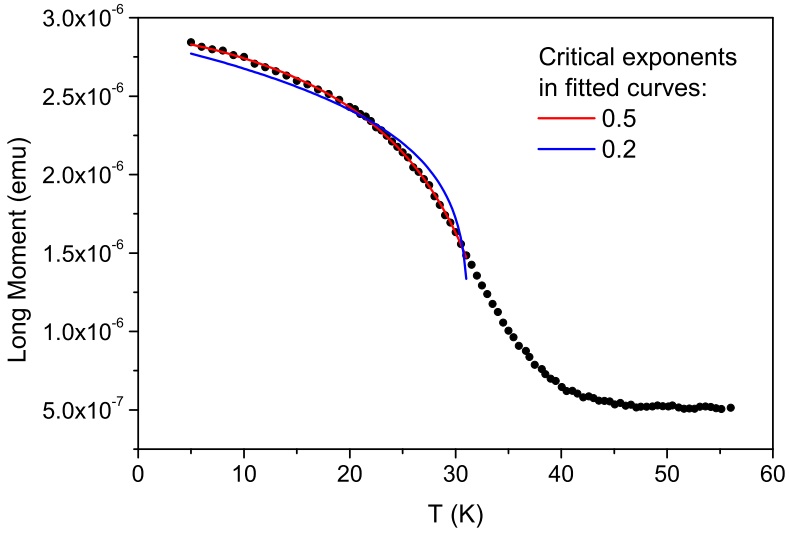

Figure 3.20: Susceptibility curve of a 6 nm film MnSi fitted with equation 3.6 with different values for the critical exponent. Fitting parameters for the red curve: $T_{ord} = 34.0\,\mathrm{K}$, $b = 0.35$ and $p = 3.48$. Fitting parameters for the blue curve: $T_{ord} = 31.2\,\mathrm{K}$, $b = 0.34$ and $p = 0.15$.

model was used, which was proposed by Zhang and Willis [155]. This model ascribes the decrease of T_{ord} in the thin film limit to the reduction of spin-spin interactions at the interfaces. A spin on the surface or interface of the film interacts with fewer neighbors than a spin that is located in the interior of the film material. Therefore the magnetic order will be less stable in the case of very thin films, where the surfaces and interfaces gain more weight compared to the interior of the film. This decreased stability of magnetic order can be observed as a lowered ordering temperature.

According to the model the evolution of T_{ord} with film thickness is quantified in terms of the spin-spin coupling range of the MnSi thin films. Thus it is possible to get an estimation of the spin-spin correlation length N_0 by the evaluation of the data. For this, the reduced ordering temperature $t(n) = 1 - T_{ord}(n)/T_{ord}(\infty)$ as a function of the number of monolayers n in the film is plotted in figure 3.22. Note that 1 ML equals 2.63 Å in the case of MnSi (111) planes [112]. $T_{ord}(\infty)$ is the ordering temperature in the thick film limit, which is 43.5 K as obtained from the susceptibility measurements on the thickest films. [2]

The following equations describe the behavior of $t(n)$ in different ranges

[2] Note that the thick film limit is not identical with the bulk value of $T_{c,bulk} = 29$ K. As discussed in section 3.8 the enhancement of T_{ord} can be ascribed to tensile strain in the films.

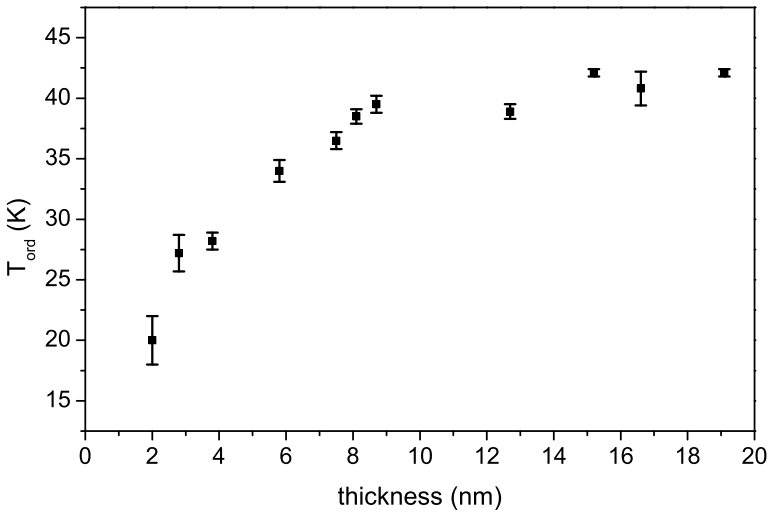

Figure 3.21: Thickness dependence of T_{ord} of codeposited MnSi films. The data were determined from susceptibility measurements in an applied magnetic field of 10 mT.

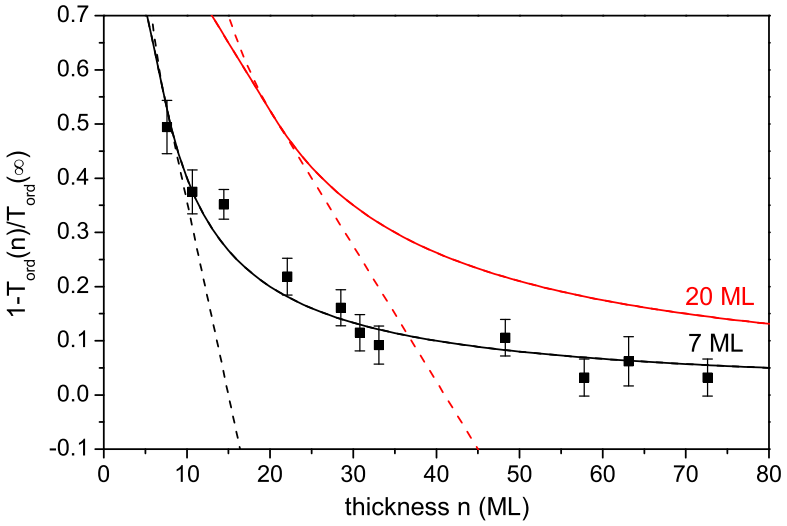

Figure 3.22: Variation of T_{ord} with film thickness according to the model proposed by Zhang and Willis [155] to derive the spin-spin correlation length. The black (red) solid line is a fit assuming a spin-spin coupling range $N_0 =$ 7 ML (20 ML). Dashed lines show the trend of the linear and power law behavior in those regions, where the particular curve is not valid.

of film thickness [155]. It is decisive, whether the thickness exceeds the spin-spin correlation length or not. For $n > N_0$, $t(n)$ follows a power law:

$$t(n) = 1 - T_{ord}(n)/T_{ord}(\infty) = (N_0 + 1)/2n, \tag{3.7}$$

whereas $t(n)$ is linear in n for $n < N_0$:

$$t(n) = 1 - T_{ord}(n)/T_{ord}(\infty) = 1 - (n-1)/2N_0. \tag{3.8}$$

Fitting the data in figure 3.22 by a combination of these two equations gives the range of the spin-spin coupling N_0. Such a fit yields a value $N_0 = 7$ ML (see black line in figure 3.22). This correlation length is a reasonable value, since it is of the same order as that of other metals like Ni (4.7 ML) or Gd (8.6 ML) [155]. Therefore, the decline of T_{ord} with decreasing thickness is fully accounted for by the reduction of spin-spin interactions at the interfaces of the MnSi film. Nevertheless it cannot be excluded that thickness dependent strain in the thinnest films could also effect a change in T_{ord}. However, this topic was not investigated in this work, since exact values for the strain were not available.

Qualitatively the observed thickness dependence of T_{ord} is comparable with data published by Karhu *et al.* [112] in a recent paper. They demonstrated that films grown by annealing a Mn layer into the Si substrate show

a similar behavior, although their samples exhibit a weaker dependence of T_{ord} on the film thickness, with the ordering temperature saturating at $\approx$ 40 K. However, the evaluation presented here is in contradiction to the results published by Karhu *et al.* [112]. These authors conclude that N_0 for their annealed films is of the order of 20 ML. Because of this unconventionally high value they exclude the possibility that the decrease in T_{ord} could be due to the reduction of spin-spin interactions, but should be rather a consequence of strain. However, a closer look at their data reveals a mistake in their evaluation.[3] A curve following equations 3.7 and 3.8 with $N_0 = 20$ ML results in the red line in figure 3.22. This curve clearly does not represent the experimental data of this work.

3.4.3 Field Dependence of the Magnetization

After the magnetic transition temperatures have been determined for all MnSi thin films, it is essential to investigate the dependence of magnetism on the applied magnetic field at temperatures, where the samples are in an ordered state. With the help of such measurements the critical field values can be detected, where the magnetic structure changes from one into another configuration. Therefore, hysteresis curves were measured at 5 K in external magnetic fields between -5 and 5 T. Measurements were performed on all films with the *Quantum Design* MPMS-5S SQUID magnetometer in order to estimate the saturation magnetization. But since the resolution of this conventional SQUID was insufficient to obtain a smooth curve, two selected films were measured using a vibrating sample SQUID magnetometer (*Quantum Design* MPMS SQUID VSM) owned by the IFW in Dresden. These high-resolution measurements are representative for two different thickness ranges.

The measurements were performed on codeposited films in two different geometries, where the magnetic field was applied parallel (in-plane) and perpendicular (out-of-plane) with respect to the film surface.

Since the MnSi thin films are grown on Si substrates, an additional diamagnetic background signal is measured in the magnetization. This linear term can easily be eliminated by fitting and subtracting the slope of the magnetization curve at high fields, where the magnetic signal of the MnSi film is saturated. [4]

Regarding the out-of-plane measurements, the effect of demagnetizing fields has to be considered. While the demagnetization factor D is zero for

[3] A comparison of the data points for the 9 nm (34 ML) and the 11 nm (42 ML) films in the figures 6(b) and 7(b) of reference [112] reveals an inconsistency. While these two films possess the same ordering temperature in figure 6(b), the values for the reduced T_{ord} in figure 7(b) disagree considerably.

[4] In fact, the magnetization of MnSi does not saturate up to fields of approximately 14 T [156], but the small high field susceptibility can be neglected in this context.

any in-plane field direction, it will be $D = 1$ for fields applied perpendicular to the film plane. Therefore the magnetic field H_{sample} experienced by the sample must be calculated by

$$H_{sample} = H_{ex} - DM, \tag{3.9}$$

where H_{ex} is the external field and M the magnetization of the film. The data obtained after taking the demagnetization effects into account and after subtracting the diamagnetic background are presented in the following for two films belonging to different thickness ranges. The quantity, which defines the properties of the film, is the proportion between film thickness and helix length λ. It was shown by Karhu *et al.* [146] that $\lambda = 14$ nm is the correct value for MnSi thin films. Therefore, in the following paragraphs magnetization measurements on two films will be discussed exemplarily: the first is a film with 9 nm thickness, which is less than the helix length, and the second is a 19 nm film exceeding the helix length.

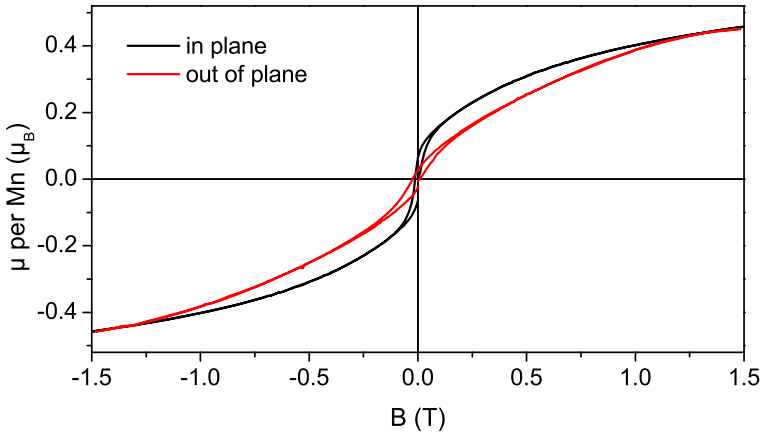

Figure 3.23: Hysteresis loops for a 9 nm thin film MnSi measured in in-plane and in out-of-plane direction. The diamagnetic background has been subtracted and demagnetizing fields were accounted for.

First the measurements on the thinner film will be discussed, which are depicted in figure 3.23. The in-plane curve for the 9 nm film shows a steep increase of the magnetization below 0.1 T and continues to rise with a smaller slope at higher fields. The out-of-plane magnetization, however, exhibits a nearly linear behavior. Both curves do not show any kink-like features that can give information about the critical fields, but it is striking that in- and out-of-plane measurements coincide at fields above 1.3 T, corresponding to B_{c2} as determined from magnetoresistance measurements performed on the

same film (compare section 3.5.4). Above B_{c2} the spins are aligned parallel, but the magnetization still increases with a small high-field susceptibility, in agreement with the behavior of bulk material [156]. The ordered magnetic moment can be derived from the magnetization curve above the critical field B_{c2} and is in accordance with the bulk value of $0.4\,\mu_B$ per Mn atom [156]. Small deviations from this value can most probably be ascribed to the uncertainty of the film thickness, which leads to an over- or underestimation of the number of Mn atoms in the film.

A comparison of the in-plane and out-of-plane magnetization curves reveals that the magnetic anisotropy is of easy plane type. From the area between the virgin magnetization curves with different field orientation the phenomenological effective magnetic anisotropy energy K_{eff} can be derived. Therefore both curves were integrated with respect to the field up to the point, where they coincide. The difference between these integrated values represents the area between the two curves and is a measure for the anisotropy. The anisotropy calculated by this method contains contributions of both, the volume and the interfaces [157]. K_{eff} amounts to $24\,\frac{\text{kJ}}{\text{m}^3}$ for the 9 nm film.

For both sample orientations a small magnetic hysteresis is found. The remanent magnetization and the coercive field are $M_R = (0.06 \pm 0.01)\,\mu_B$ and $H_C = (13 \pm 2)\,\text{mT}$ in the in-plane and $M_R = (0.025 \pm 0.005)\,\mu_B$ and $H_C = (24 \pm 2)\,\text{mT}$ in the out-of-plane direction, respectively.

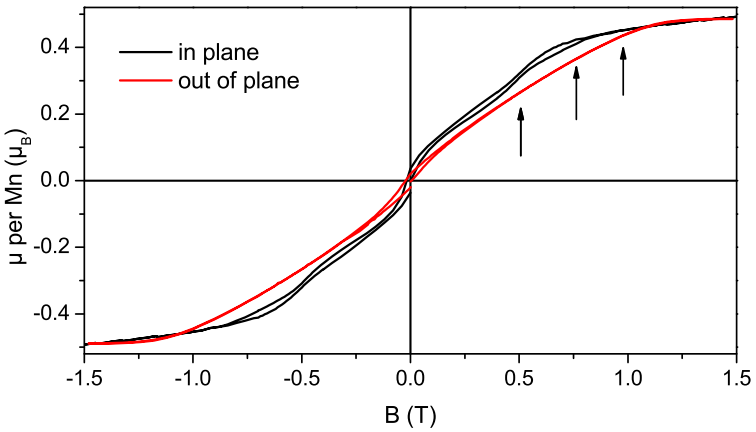

Figure 3.24: In-plane and out-of-plane hysteresis loops for a 19 nm sample after subtracting the diamagnetic background and demagnetizing fields. Steps in the in-plane magnetization curve are marked by arrows.

The hysteresis curves for the film with 19 nm thickness are presented in figure 3.24. In this case the magnetization exhibits some characteristics, which are not observed for the 9 nm sample. In the out-of-plane magnetization a linear increase is observed up to a kink occurring at 1.1 T. This kink marks the position of the critical field B_{c2}, where the spins align ferromagnetically. The curve is very similar to magnetization measurements on bulk MnSi [158]. However, B_{c2} is shifted to higher fields than in bulk ($B_{c2,bulk} = 0.6\,\mathrm{T}$). B_{c1} cannot be observed in the out-of-plane magnetization curve.

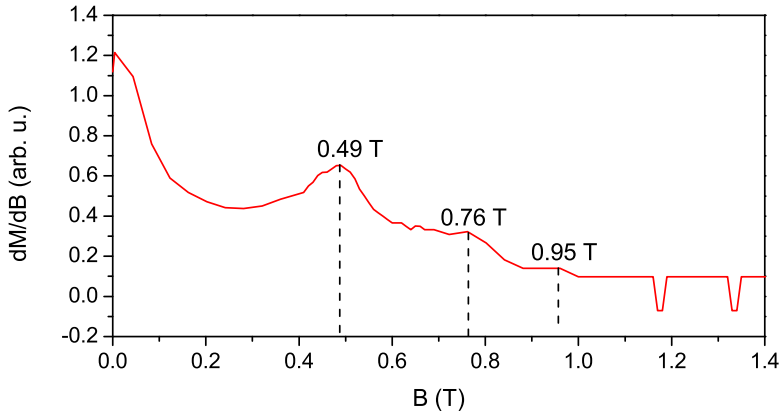

Figure 3.25: Derivative dM/dB of the magnetization of the 19 nm thin film. The indicated maxima yield the positions of steps in the magnetization curve, which are connected with critical field values.

Regarding the in-plane measurement on the 19 nm film some features can be observed, which are not known from bulk MnSi. Three magnetic transitions can be identified by steps in the magnetization curves. Their positions are determined from the maxima occurring in the first derivative of the virgin curve $M(B)$ with respect to B, which is shown in figure 3.25. The first step is observed at 0.49 T and two further shoulders occur at 0.76 T and at 0.95 T. It will be discussed in section 3.7, which magnetic transitions may be responsible for the observed features of the magnetization curve.

Compared to the measurement in an out-of-plane field the in-plane magnetization exhibits a more pronounced hysteretic behavior up to $B = 0.8\,\mathrm{T}$. The remanent magnetization M_R is $(0.036\pm0.005)\,\mu_B$ and $(0.020\pm0.005)\,\mu_B$ per Mn atom for the in- and out-of-plane direction, respectively, which is slightly smaller than for the 9 nm film. The fact that the coercive fields of the 19 nm sample for the in-plane and out-of-plane direction (17 mT and 22 mT, respectively) are close to each other indicates that the effective magnetic anisotropy is considerably smaller than for the thinner film. The evaluation

of the area between the virgin curves yields a value of 13 $\frac{\mathrm{kJ}}{\mathrm{m}^3}$.

3.5 Resistivity and Magnetoresistance Measurements

3.5.1 The van-der-Pauw Method

Resistivity measurements were performed using the van-der-Pauw method, which was introduced by L. J. van der Pauw in 1958 [159, 160]. As it is an established technique for measuring resistivity and Hall effect on flat samples, it is well suited for measurements on thin films. The method was chosen, because it is applicable to samples of arbitrary shape and thus the thin films did not need to be cut or etched.

For the use of the van-der-Pauw method some conditions need to be fulfilled in order to ensure the correctness of the results. For the sample and the attached electrical contacts the following has to be true [159]:

- The thickness must be constant over the whole the sample.
- The area of the sample must be simply connected, i. e. there are no holes.
- The contacts must be positioned at the edges of the sample.
- The area of the contacts must be sufficiently small with regard to the sample area.

If a sample satisfies all these issues the measurements can be performed using a four terminal sensing configuration as shown in figure 3.26. A current is induced trough the contacts A and B, while the voltage is measured between C and D. The resistance $R_{AB,CD}$ is then defined by Ohm's law as the applied voltage divided by the measured current. For a van-der-Pauw measurement the contacts are then rotated and thereby also $R_{BC,DA}$ is determined.

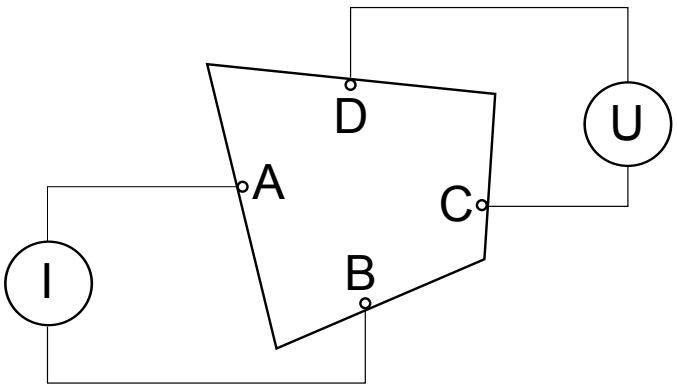

Figure 3.26: Configuration for resistivity measurements using the van-der-Pauw method.

It was proven by van der Pauw [159] that the following relation is true.

$$\exp\left(-\pi R_{AB,CD}\frac{d}{\rho}\right)+\exp\left(-\pi R_{BC,DA}\frac{d}{\rho}\right)=1 \tag{3.10}$$

Here d denotes the thickness of the sample and ρ is its resistivity. This means that the resistivity is fully determined by the two values $R_{AB,CD}$ and $R_{BC,DA}$ and the thickness of the sample. In order to calculate ρ equation 3.10 can be rewritten as

$$\rho=\frac{\pi d}{\ln 2}\frac{R_{AB,CD}+R_{BC,DA}}{2}f\left(\frac{R_{AB,CD}}{R_{BC,DA}}\right). \tag{3.11}$$

The implicit function f is given by the relation

$$\frac{R_{AB,CD}-R_{BC,DA}}{R_{AB,CD}+R_{BC,DA}}=f\operatorname{arccosh}\left(\frac{\exp\left(\ln 2/f\right)}{2}\right) \tag{3.12}$$

and can be approximated by

$$\begin{aligned} f\approx 1-&\left(\frac{R_{AB,CD}-R_{BC,DA}}{R_{AB,CD}+R_{BC,DA}}\right)^2\frac{\ln 2}{2}\\ -&\left(\frac{R_{AB,CD}-R_{BC,DA}}{R_{AB,CD}+R_{BC,DA}}\right)^4\left[\frac{(\ln 2)^2}{4}-\frac{(\ln 2)^3}{12}\right]. \end{aligned} \tag{3.13}$$

Using this equation the resistivity can be calculated, when $R_{AB,CD}$ and $R_{BC,DA}$ have been measured and the thickness of the sample is known. Since $R_{AB,CD}=R_{CD,AB}$ and $R_{BC,DA}=R_{DA,BC}$ applies for symmetry reasons, the measurement in all four possible configurations allows to find more accurate values by averaging.

3.5.2 The Measurement Setup

For the van-der-Pauw resistivity measurements on MnSi thin films the samples were cut to a size of around $0.5\times 0.5\,\mathrm{cm}^2$. The substrate with the film on top was adhered to the sample holder with GE varnish and electrical contacts were attached with the help of conductive silver varnish. The measurements took place in a bath cryostat, where temperatures reaching from helium to room temperature could be adjusted. Superconducting coils inside the cryostat could provide magnetic fields up to 8 T for magnetoresistance measurements. The measurements were performed using an AC resistance bridge, where additionally a switch was interconnected to rotate the configuration of current and voltage contacts as it is necessary for the van-der-Pauw method.

3.5.3 Resistivity Measurements

First the temperature dependence of the resistivity of a Si substrate was measured. This is necessary in order to estimate of the influence of the substrate on resistivity measurements, which are carried out on the thin films. The measurement on the Si substrate was performed in a conventional four-point geometry instead of using the van-der-Pauw method. In order to achieve ohmic contacts on the surface of the semiconductor small pads of yttrium and aluminum were deposited on the ends of a 10 mm × 2 mm bar cut from the Si substrate. The pads were annealed, before the wires for the four-probe measurement were attached.

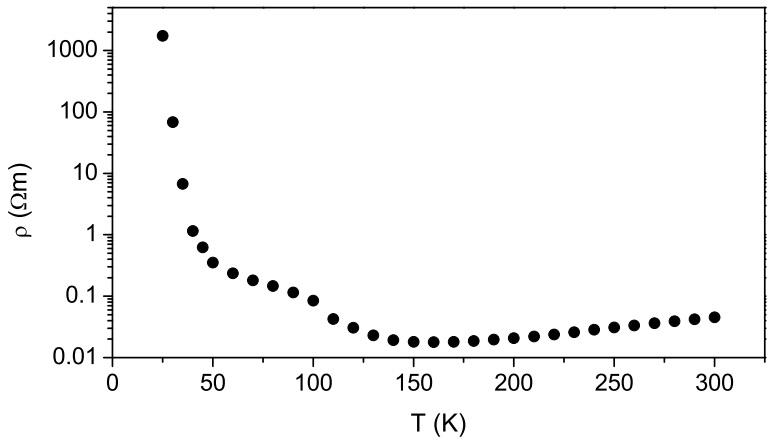

Figure 3.27: Resistivity measurement performed on a 10 mm × 2 mm piece of a Si substrate.

The resistivity was measured in a temperature range from 25 K to 300 K as shown in figure 3.27. Between 300 K and approximately 150 K the resistivity of the Si substrate decreases, when the temperature is lowered, which is caused by the increasing electron mobility [161]. Towards low temperatures the carriers freeze out and an exponential increase of the resistivity is observed as expected for a semiconductor.

Subsequently van-der-Pauw resistivity measurements have been performed on MnSi thin films of different thicknesses in a temperature range from 5 K to 300 K and in magnetic fields up to 5 T. Except from one film, which was prepared by the annealing method, all samples were codeposited films. Since many properties, as for instance the ordering temperature, the critical fields and the entire appearance of the magnetic phase diagram, are sensitively dependent on film thickness, clear differences between the differ-

ent samples are observed in the measurements.

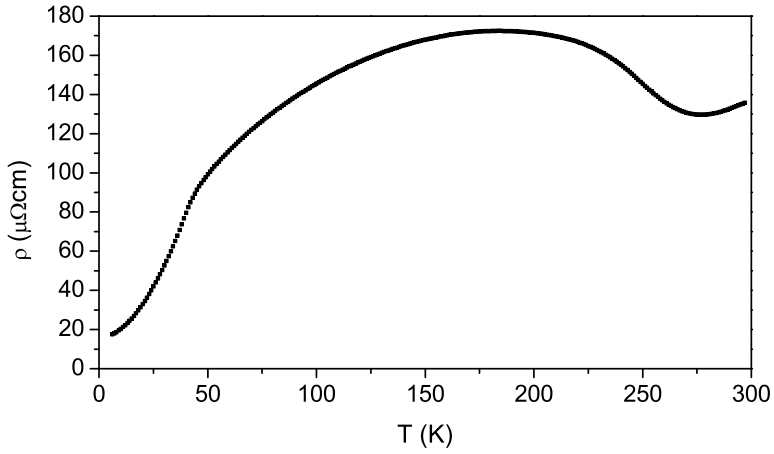

Figure 3.28: Resistivity versus temperature measured on a 29 nm film prepared by the annealing method.

A typical example of the temperature dependent resistivity of a MnSi thin film on a Si substrate is shown in figure 3.28, where a measurement covering a temperature range from 5 K to 300 K is depicted, which has been performed on an annealed sample of 29 nm thickness. The film exhibits metallic behavior, as the resistivity increases with increasing temperature. After reaching a maximum at around 180 K the resistivity of the sample decreases again towards higher temperatures. This is in contrast to the behavior of bulk MnSi, where the resistivity in this temperature range is basically linear.[5]

To explain the deviance between the thin film measurement and the bulk behavior, the influence of the Si substrate has to be taken into account. The resistivity of the phosphor-doped Si is considerably high at low temperatures, but above approximately 100 K its value is in a moderate range (compare figure 3.27), so that the substrate possesses a resistance in a similar order of magnitude as the film. Therefore the substrate may conduct parts of the current and influence the measurement. However, the most interesting part of the resistivity measurements on MnSi thin films is the temperature region up to approximately 60 K. In this range the measurement is essentially unaffected by the influence of the substrate. The signal is mainly governed by the properties of the film and the substrate contributes a deviance, which can be estimated to amount up to 15 %. The shape of the curve, however,

[5]Strictly speaking the resistivity of MnSi can be described by a parallel circuit consisting of two resistors, one of which has constant resistance and the other increases linearly with temperature [162].

is not changed, which is important for the following analysis.

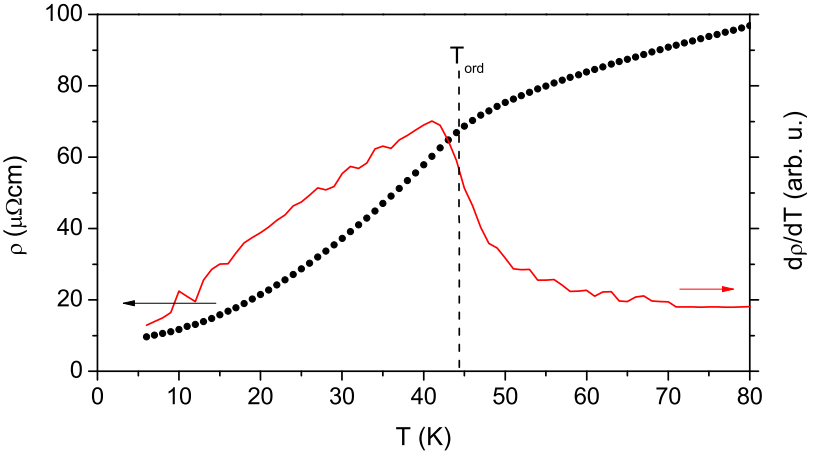

Figure 3.29: Resistivity measurement and $d\rho/dT$ curve for a 19 nm thin film MnSi. The kink at 44 K hints at T_{ord}.

In figure 3.29 the resistivity of a codeposited thin film MnSi with a thickness of 19 nm is depicted for a temperature range reaching from 6 K to 80 K. As already mentioned, the curve is characteristic of a metallic sample. The most outstanding feature of this measurement is a pronounced kink occurring at around 40 K. This kink is a hint to the magnetic phase transition from paramagnetism to helimagnetic order, which takes place at the corresponding temperature. Qualitatively, the measured resistivity is in good agreement with data of bulk MnSi [163], only the position of the kink at T_{ord} is shifted to higher temperatures.

To find the actual ordering temperature from the resistivity measurements the position of the kink must be determined. Therefore the resistivity curves were differentiated with respect to T, as it is shown by the red curve in figure 3.29. At the position of the kink the steepest decrease is observed in the first derivative, which corresponds to a minimum in the second derivative. From the data for the 19 nm film it can be concluded that T_{ord} amounts (44 ± 2) K for this sample.

Further resistivity measurements were performed on samples with different thicknesses, where a very similar behavior was observed. The data are shown in the appendix A.3, and the magnetic ordering temperatures are summarized in the following table.

film thickness	T_{ord} determined from resistivity	T_{ord} determined from susceptibility
3.5 nm	37 K	26.7 K
6 nm	41 K	34.0 K
9 nm	43 K	39.5 K
13 nm	45 K	46.1 K
19 nm	44 K	42.1 K
29 nm, annealed	42 K	-

Since the kinks observed in the resistivity are broadened to some extent, the inaccuracy of these values is larger than for the ordering temperatures determined from susceptibility and can be estimated to amount ±2 K. Within the boundaries of the error bars the values for T_{ord} determined from resistivity and from susceptibility are in good agreement, except from the two thinnest film. Here $T_{ord} = 26.7$ K and $T_{ord} = 34.0$ K for the 3.5 and the 6 nm film, respectively, was found in susceptibility, which is considerably smaller than the value seen in resistivity. Obviously the definition of T_{ord} as the minimum in the second derivative of the resistivity generally differs from its definition in the susceptibility fit.

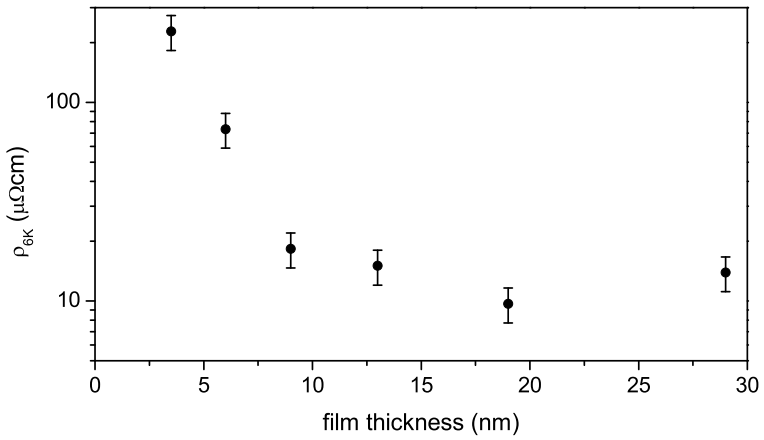

Figure 3.30: Residual resistivity measured at 6 K as a function of film thickness.

The residual resistivity at 6 K is in the range from 10 $\mu\Omega$cm to 20 $\mu\Omega$cm for the different films with thicknesses between 9 and 29 nm (compare figure 3.30). This is around a factor of 10 larger than the residual resistivity expected for a MnSi single crystal [163]. The deviation is unsurprising, since the MnSi thin films exhibit a certain roughness contributing to additional scattering. Differences in film morphology will further affect the transport

properties. As it could be seen in AFM and TEM investigations (compare section 3.3) annealed samples possess larger surface and interface roughness, so that additional scattering from those inhomogeneities will occur.

Considering the series of codeposited films it can be noted that the residual resistivity is larger for the thinner films. Especially for the 3.5 nm film a considerably enhanced residual resistivity of 230 $\mu\Omega$cm is observed, which is more than ten times larger than the value for the 9 nm film. The increase in resistivity for very thin films can easily be explained by the larger surface-to-volume ratio, since a high amount of surface scattering will occur in this case.

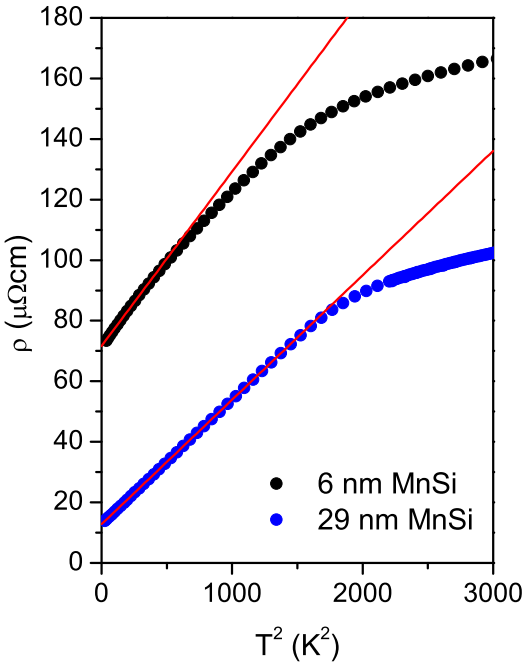

Figure 3.31: Resistivity data of a 6 and a 29 nm thin film plotted versus T^2. The linear fits yield the A-coefficients of the T^2 behavior at low temperatures.

It should be noted that the low temperature regime of the resistivity can be described by $\rho = \rho_0 + AT^2$. To visualize the T^2 behavior the resistivity data were plotted versus T^2, which is shown in figure 3.31 for a 6 nm and a 29 nm film MnSi. The red lines in the diagram represent linear fits in a temperature range from 5 K to 20 K. It can be observed that for the thinner film the deviation from the T^2 behavior is stronger. Regarding the 29 nm film a good agreement between measured data points and fitted curve can be observed up to T_{ord}, whereas for the thinner film there is already a

considerable deviation at temperatures above 20 K. The corresponding fits for samples of 3.5 nm, 9 nm, 13 nm and 19 nm thickness are shown in the appendix A.3. The values for the A-coefficient are presented in the following table.

film thickness	A ($\mu\Omega$cm/K^2)
3.5 nm	0.087
6 nm	0.058
9 nm	0.036
13 nm	0.034
19 nm	0.032
29 nm, annealed	0.041

For the MnSi thin films with thicknesses between 9 nm and 29 nm A agrees with the bulk value, which was reported to be in the range of 0.03 $\mu\Omega$cm/K^2 [127, 162]. However, the thinner films show a considerable enhancement of A. $A = 0.087\,\mu\Omega$cm/K^2 as determined for the 3.5 nm film is around three times larger than the bulk value. It is especially striking that the enhancement occurs in the same thickness range as the decrease of T_{ord}, which has been ascribed to reduced spin-spin interactions (compare section 3.4.2).

The T^2 behavior in weak ferromagnets such as MnSi can be attributed to the scattering of conduction electrons on spin fluctuations [71]. In a self-consistent renormalization theory it was calculated that the coefficient A depends on the reduced interaction parameter $\overline{I}$, which is the product of the Coulomb interaction between electrons and the density of states at the Fermi level [71, 164].

$$A \propto \frac{1}{\sqrt{|\overline{I} - 1|}} \tag{3.14}$$

Obviously in samples with decreased ordering temperature $\overline{I}$ is also decreased, which results in a larger value of A. Thus it can be assumed that the decrease of the interaction parameter $\overline{I}$ is a consequence of the reduced thickness. However, the scaling behavior observed for the decrease of T_{ord} (compare figure 3.22) does not apply to the decrease of $\overline{I}$.

A similar increase of A can be observed in bulk samples, when $T_{c,bulk}$ is decreased by pressure [127].

3.5.4 Magnetoresistivity

The magnetoresistance (MR) effect measures the change of the resistivity in an external magnetic field B and is defined by

$$MR\,(\%) = 100 \cdot \frac{\rho(B) - \rho(0)}{\rho(0)}. \tag{3.15}$$

The effect occurs, when conduction electrons are deflected by the Lorentz force in a magnetic field, which normally leads to an increase of the resistivity, i. e. a positive MR effect. If the sample, which is exposed to an external magnetic field, contains magnetic moments, the field may also change their orientation. Therefore the scattering of conduction electrons on the ordered magnetic structure is influenced, which leads to further contributions to the MR effect, that are normally negative. In this case MR measurements provide an excellent tool to get information about changes in the magnetic state of a material. For example, by anomalies in the magnetoresistivity it is possible to determine field and temperature values, where magnetic transitions take place.

MR measurements were carried out on MnSi thin films at different temperatures and in magnetic fields up to 5 T. The field was applied perpendicular as well as parallel to the film plane. Regarding the film thickness it is again necessary to distinguish between films that are thinner and films that are thicker than the helix length. In the following the same two films will be discussed, which were also used for the magnetization measurements in the previous section.

In figures 3.32 and 3.33 the MR data of the two codeposited films with 19 nm and 9 nm, respectively, are depicted. These measurements were per-

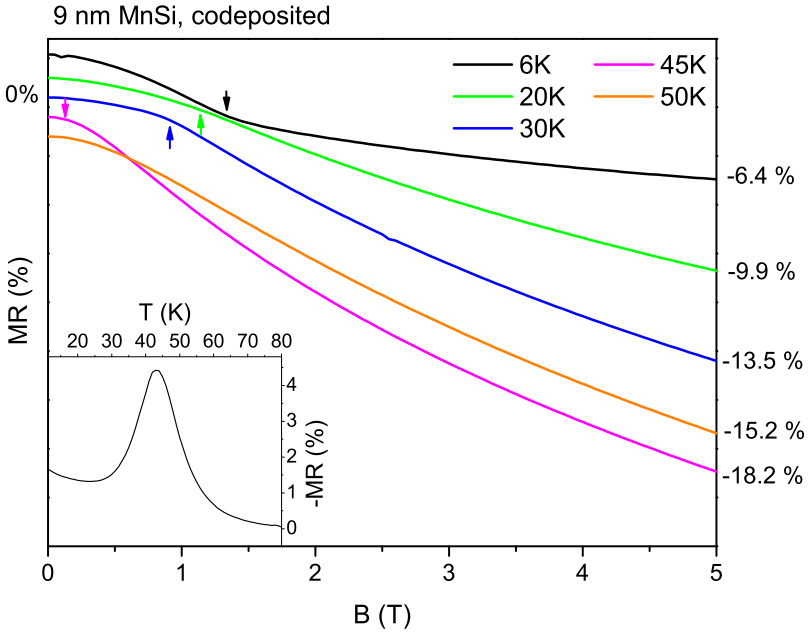

Figure 3.32: MR effect in a magnetic field applied perpendicular to the film plane for a codeposited 9 nm film. Inset: Temperature dependence of the MR effect measured at $B = 1\,\mathrm{T}$.

formed in the out-of-plane configuration, where the field is applied perpendicular to the film plane. In this case the results for both films are very similar. MR is negative for all fields and temperatures and is largest in the vicinity of T_{ord} as shown in the insets of figures 3.32 and 3.33, where the temperature dependency of -MR for $B = 1\,\mathrm{T}$ is shown. MR(1 T) reaches -4.5 % for the 9 nm film and -5.5 % for the 19 nm film, which is considerably less than in bulk MnSi, where the MR effect was determined as -20 % in the same field [163]. However, considering the increased residual resistivity of the thin films this is not unexpected, since the scattering on impurities is not affected by the field.

The shape of the MR curves is the same for the thin films as for bulk MnSi. It was shown by Demishev *et al.* that the negative sign of MR can be attributed to scattering on localized magnetic moments, since the Yosida model [165], which is based on scattering of band electrons on magnetic ions, is well suited for the description of the MR effect in MnSi over large field and temperature ranges [166].

MR data for bulk MnSi exhibit a sharp kink at the upper critical field B_{c2} [163], where the magnetic state changes from a conical structure to ferromagnetic alignment. In the vicinity of this point the curvature of the

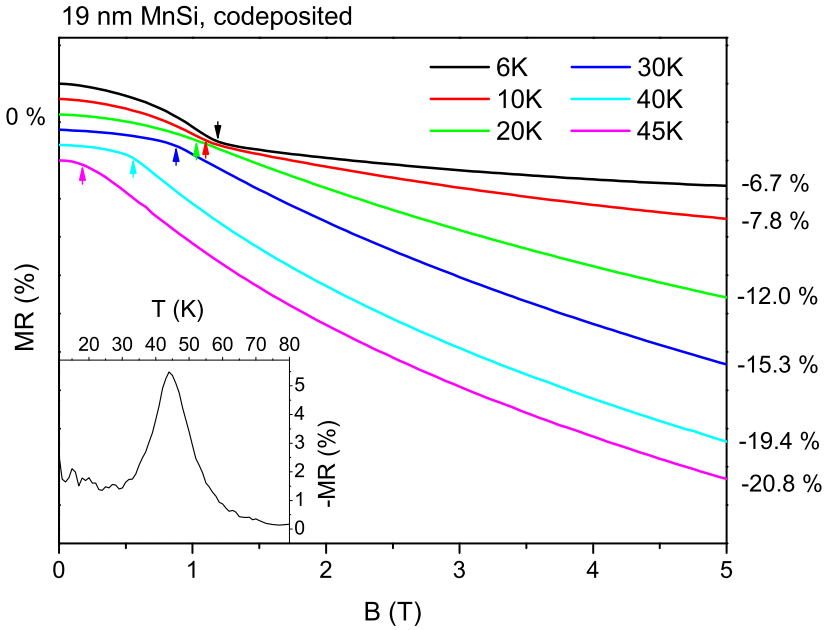

Figure 3.33: MR effect in a magnetic field applied perpendicular to the film plane for a codeposited 19 nm film. The arrows denote the upper critical field B_{c2}. Inset: Temperature dependence of the MR effect measured at $B = 1\,\mathrm{T}$.

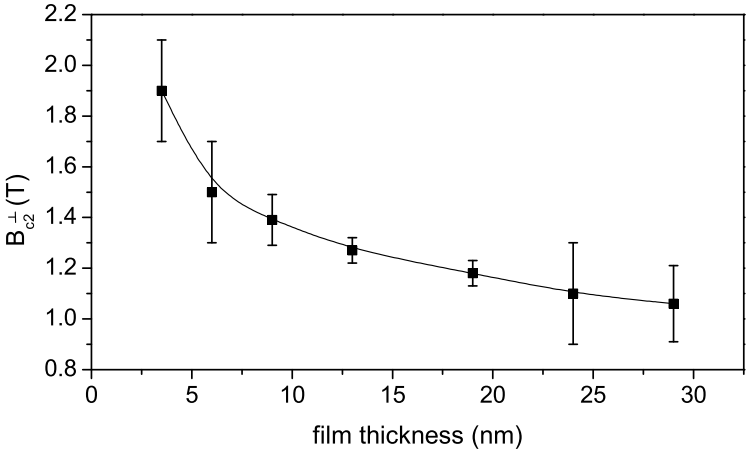

Figure 3.34: Thickness dependence of the critical field $B_{c2}^{\perp}$ determined from MR measurements at 6 K with an out-of-plane magnetic field. The line is guide for the eye.

measured graph changes from negative to positive. Also for the thin films these features can clearly be observed (figures 3.32 and 3.33, marked by the arrows), although the kinks are smeared due to the lower crystal quality of the thin films compared to single crystals. The critical fields for the different temperatures were determined from the position of the kinks by analyzing the second derivative of the MR data. $d^2(MR)/dB^2$ exhibits a maximum at $B_{c2}^{\perp}$ for temperatures lower than 20 K, which develops into a minimum for higher temperatures, since the kink changes its curvature, which is in accordance with the bulk data. The temperature dependence of $B_{c2}^{\perp}$ defines the magnetic phase diagram for the thin films in the case of out-of-plane magnetic fields, which will be shown and discussed in section 3.7. Apart from the critical field $B_{c2}^{\perp}$ no further transitions can be found in the out-of-plane MR measurements.

In figure 3.34 the values of $B_{c2}^{\perp}$ as determined from MR measurements are shown for films of different thickness. The error bars shown in the diagram were estimated from the width of the extremum observed in the second derivative. In comparison with bulk MnSi, where $B_{c2}^{\perp}$ amounts 0.6 T [167], the critical fields of the films are considerably enhanced. Furthermore $B_{c2}^{\perp}$ increases systematically from thick to thin films. Amounting 1.9 T $B_{c2}^{\perp}$ is largest for the thinnest film (3.5 nm), whereas the 29 nm film possesses a $B_{c2}^{\perp}$ of 1.06 T. The enhanced $B_{c2}^{\perp}$ can easily be explained by shape anisotropy, which favors the magnetic moments to lie in the film plane and thereby counteracts the out-of-plane magnetic field. This effect is stronger for the thinner films as reflected by the thickness dependence of $B_{c2}^{\perp}$.

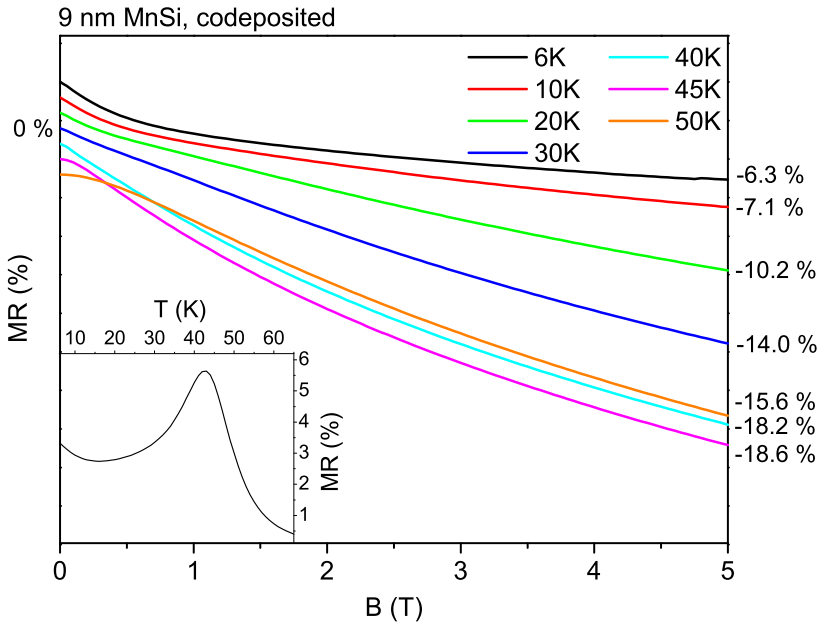

Figure 3.35: MR effect in a magnetic field applied parallel to the film plane for a codeposited 9 nm film. Inset: Temperature dependence of the MR effect measured at $B = 1\,\mathrm{T}$.

In contrast to the out-of-plane measurements, which show in principle the same behavior as bulk MnSi, measurements in the in-plane configuration exhibit some new features. Here the magnetic field was applied parallel to the film plane and resistivity versus field curves were measured for films of different thickness. In this case the behavior of the MR effect depends strongly on the thickness of the film under investigation.

The in-plane MR effect for the 9 nm film is depicted in figure 3.35 for selected temperatures between 6 K and 50 K. In this configuration the magnetoresistance exhibits a behavior that is different from what is known from bulk MnSi. For all temperatures below T_{ord} the curvature of the graphs is positive in the complete field range under investigation. Furthermore no kink as a sign of the critical field occurs. This is an indication for the instability of the helical structure in films, which are thinner than the helix length, as it will be discussed in more detail in section 3.7. For magnetic fields exceeding 1.5 T the in-plane measurements are very similar to the out-of-plane case, both regarding the curvature and the absolute values of the MR effect.

Measuring the in-plane MR effect on a film thicker than the helix length reveals some interesting features, which do not occur in the case of the thinner film. The curves for the 19 nm film are shown in figure 3.36 for temperatures up to 50 K. Here, again, $B_{c2}^{||}$ is enhanced compared to bulk MnSi,

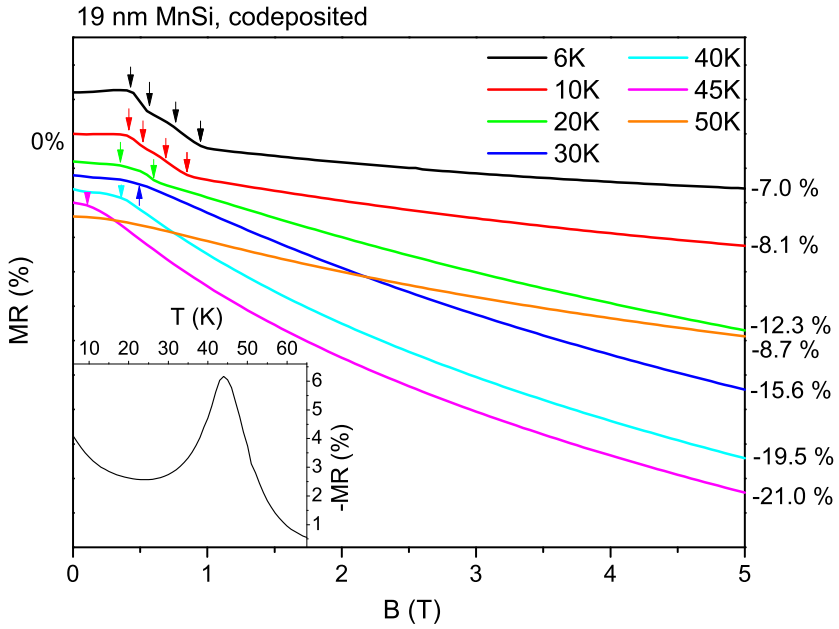

Figure 3.36: MR effect in a magnetic field applied parallel to the film plane for a codeposited 19 nm film. The arrows mark the positions, where kinks occur. Inset: Temperature dependence of the MR effect measured at $B = 1\,\mathrm{T}$.

but amounting $(1.0 \pm 0.1)\,\mathrm{T}$ it is lower than for the thinner film. A number of kink-like features can be observed especially for temperatures below 20 K and magnetic fields below the saturation field $B_{c2}^{||}$. These kinks obviously hint to magnetic phase transitions. From the low temperature measurements four critical field values can be determined as marked by arrows in figure 3.36. However, above 20 K these transitions are no longer resolved. Although a magnetic phase diagram can be built, which contains the lines of phase transitions, it is impossible to predict the magnetic structure of the different magnetic phases solely from the MR measurements. In section 3.7 the magnetic phase diagram as obtained from kinks in the MR effect will be drawn and discussed.

3.6 Hall Effect Measurements

In the previous chapters magnetization and magnetoresistivity measurements on MnSi thin films have given good insight into the magnetic properties the samples. It was discovered that especially those measurements that were performed in an in-plane geometry exhibit some kinks or shoulders, which are not known from bulk MnSi. These features obviously hint to transitions between different magnetic phases and serve as important indications in the search for a possibly enlarged skyrmion phase in MnSi thin films. Measurements in a magnetic field applied in an out-of-plane direction, however, did not exhibit any remarkable features except from the critical field $B_{c2}^{\perp}$, where all spins align ferromagnetically.

A well suited method to identify a skyrmion phase is given by Hall effect measurements on thin films. As discussed theoretically in section 2.2 the non-trivial topology of a skyrmion is the cause for an additional Hall contribution, the so-called topological Hall effect (THE). In MnSi a THE amounting $\rho_{xy}^{top} = 5 \cdot 10^{-11}\,\Omega\text{m}$ can be observed in the A-phase and by its sudden onset at the phase transition, the borders of the A-phase can be mapped [62]. This can also be achieved for MnSi thin films by measuring the Hall effect.

Although Hall effect measurements provide a good tool to find possible skyrmion phases by the THE, there are some constraints, which should be discussed in the beginning. First, in the case of thin films the shape of the samples puts restrictions on the measuring geometries. Because of the Si substrate beneath the MnSi no electrical contacts can be attached to the backside of the thin film and, hence, the only possible geometry is the one shown in figure 3.37, where the magnetic field is applied in the out-of-plane direction. Therefore it will not be possible to verify, whether the kinks observed in the in-plane magnetization and magnetoresistivity are connected to a skyrmion phase.

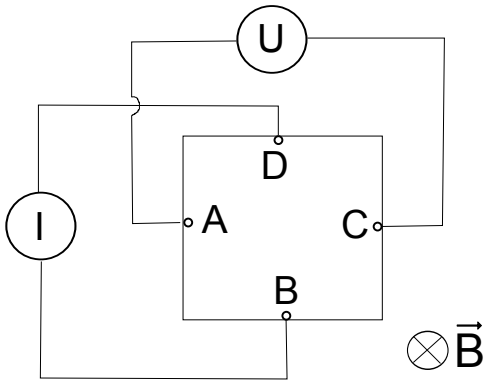

Figure 3.37: Geometry for the Hall effect measurements.

Furthermore the observation of a Hall contribution that appears addi-

tional to the normal and the anomalous Hall effect is no proof for skyrmions, since a THE could also be caused by other non-trivial spin structures. As long as the skyrmion lattice cannot be identified by a direct method such as Lorentz TEM or by neutron scattering, the THE is only an indication.

The Hall effect measurements on MnSi thin films were carried out using the van-der-Pauw method [159, 160].[6] The principles and requirements are the same as introduced in section 3.5.1 for the resistivity measurements, but in the case of Hall investigations the two current and the two voltage contacts, respectively, must be positioned at opposite sites of the sample (compare figure 3.37). In order to get the Hall resistivity the resistance $R_{AC,BD}$ was measured in a positive as well as in a negative field denoted by $R^{+}_{AC,BD}$ and $R^{-}_{AC,BD}$. Half the difference between those two values is the Hall contribution to the resistance. To calculate the Hall resistivity ρ_{xy} averaged over all current directions the following formula is applicable:

$$\begin{aligned}\rho_{xy} = \frac{d}{8}\Big(&R^{+}_{AC,BD} + R^{+}_{BD,CA} - R^{+}_{CA,DB} - R^{+}_{DB,AC} \\ &- R^{-}_{AC,BD} - R^{-}_{BD,CA} + R^{-}_{CA,DB} + R^{-}_{DB,AC}\Big),\end{aligned} \tag{3.16}$$

where d denotes the thickness of the film.

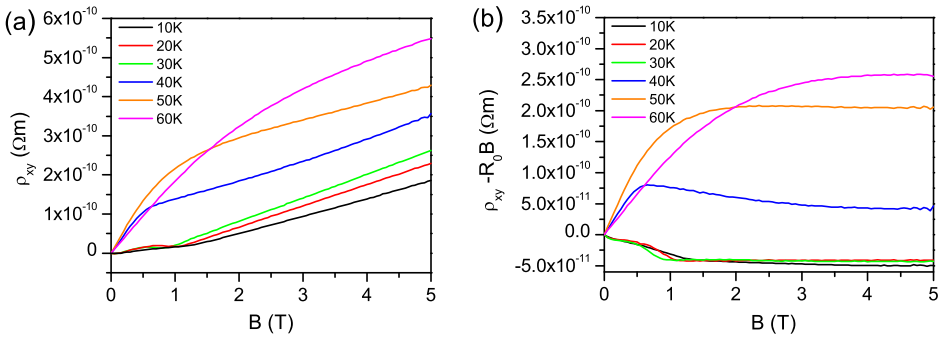

Figure 3.38: Hall effect of a 19 nm thin film MnSi in magnetic fields up to 5 T for different temperatures, (a) as measured and (b) after subtraction of the normal Hall contribution.

In the following the Hall effect data for a 19 nm thin film MnSi are discussed, which were measured in a temperature range from 5 K to 65 K and in magnetic fields up to 5 T. The field dependent measurements depicted in figure 3.38a are characterized by a linear increase, which is observed in fields above approximately 1.5 T. The slope of this increase was fitted and gives

[6] In order to exclude failures that arise from the measuring technique, it was proven that the van-der-Pauw method yields the same results as measurements in a Hall bar geometry [168].

the normal Hall constant R_0 as shown in figure 3.39a. R_0 is almost temperature independent with a value of around $6 \cdot 10^{-11}\,\Omega\mathrm{m/T}$. The fact that R_0 is positive indicates that the current is predominantly conducted by positively charged holes. These results are in reasonable agreement with bulk data for MnSi, where $R_0 \approx 1 \cdot 10^{-10}\,\Omega\mathrm{m/T}$ was found [123, 124].

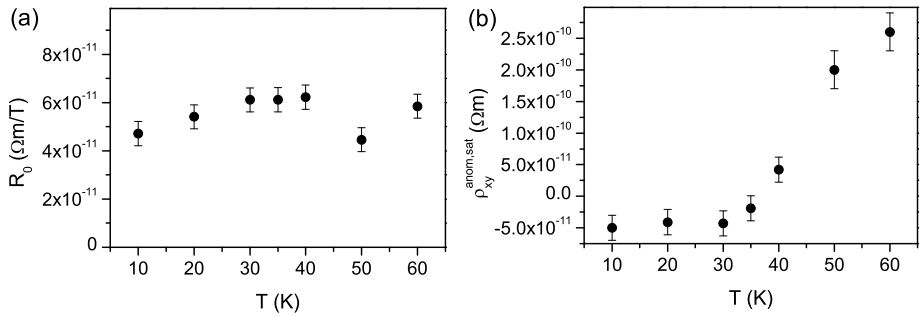

Figure 3.39: (a) Normal Hall constant R_0 and (b) saturated anomalous part of the Hall effect for a 19 nm film. The values were extracted from the curves shown in figure 3.38.

After the normal Hall contribution has been determined, it can be subtracted from the measured curves, which results in the graphic shown in figure 3.38b. Now only the anomalous part of the Hall effect ρ_{xy}^{anom} and an eventually occurring topological contribution ρ_{xy}^{top} remain. Above the saturation field ($B_{c2}^{\perp} = 1.2\,\mathrm{T}$ for the 19 nm film) the AHE reaches a constant value denoted by $\rho_{xy}^{anom,sat}$, which is depicted in figure 3.39b. Regarding the temperature dependence of $\rho_{xy}^{anom,sat}$ a very interesting behavior is observed, since the values are negative for low temperatures and turn positive for higher temperatures. This change of sign around 35 K may occur, when different mechanisms that contribute to the AHE (i. e. skew scattering, side-jump and intrinsic AHE) have different sign and their weight changes with temperature [54]. Indeed, it will be shown in the following paragraphs that the skew scattering, which scales with the residual resistivity, has negative sign, whereas the intrinsic AHE scaling like ρ_{xx}^2 is positive. This means that skew scattering dominates the AHE at low temperatures, whereas at higher temperatures the intrinsic effect is larger, since it scales with the square of the resistivity, which is also increasing.

Searching for a THE a closer look at the Hall effect measurements reveals some features in the region of low magnetic fields. In order to investigate these features further measurements in fields up to 1.5 T were performed (compare figure 3.40). A positive hump-like contribution can be identified for all temperatures in a field range from approximately 0.1 T to $B_{c2}^{\perp}$. The signal is largest around 25 K, where it amounts up to $2 \cdot 10^{-11}\,\Omega\mathrm{m}$. This features

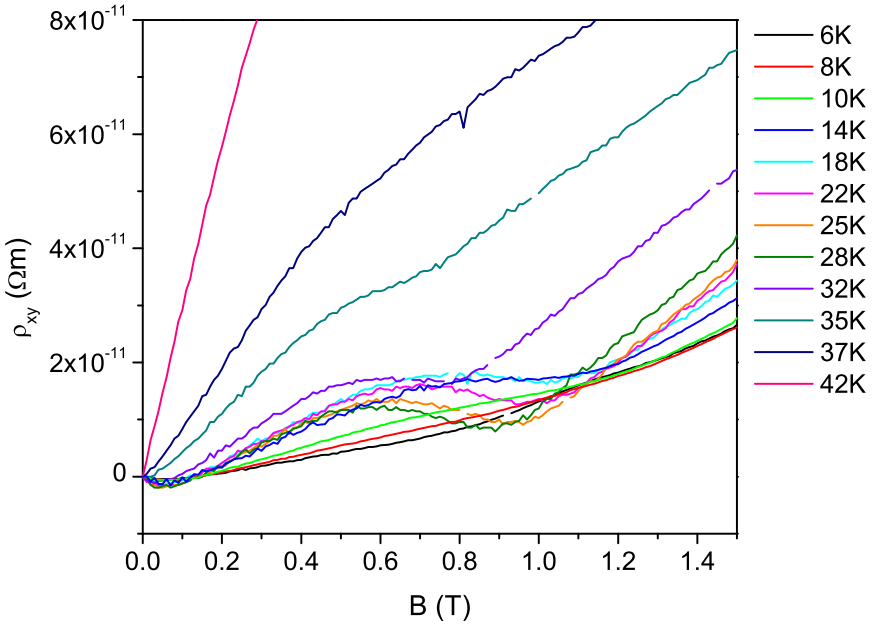

Figure 3.40: Hall effect in small magnetic fields, where the topological contribution is observed.

seems to be a contribution from the THE, although it is somewhat different from ρ_{xy}^{top} known from bulk MnSi. Especially the field and temperature ranges of its occurrence are considerably larger than in bulk MnSi, as they cover almost the complete ordered phase below the saturation field.

To quantify the THE it must be separated from the normal and the anomalous Hall effect (AHE). Therefore these two contributions can be fitted by the theoretical model introduced in section 2.2. Since the AHE scales with the magnetization and with the longitudinal resistivity, data for these two quantities have to be available. In the following the Hall measurements at 6 K will be analyzed using a procedure, which is analogous to the approach in references [54] and [114].

Considering all contributions introduced in section 2.2 the Hall effect can be described by the following equation:

$$\rho_{xy} = R_0 B + (\alpha \rho_{xx0} + \beta \rho_{xx0}^2 + b \rho_{xx}^2) M + \rho_{xy}^{top}, \tag{3.17}$$

where α, β and b are the coefficients of the skew scattering, the side-jump and the intrinsic AHE. As pointed out by Li *et al.* [114] the side-jump effect is negligible, so that only α and b need to be determined. α measures the dependence of the AHE on the residual resistivity ρ_{xx0} and therefore the Hall signal of samples with different ρ_{xx0} values must be regarded. In the

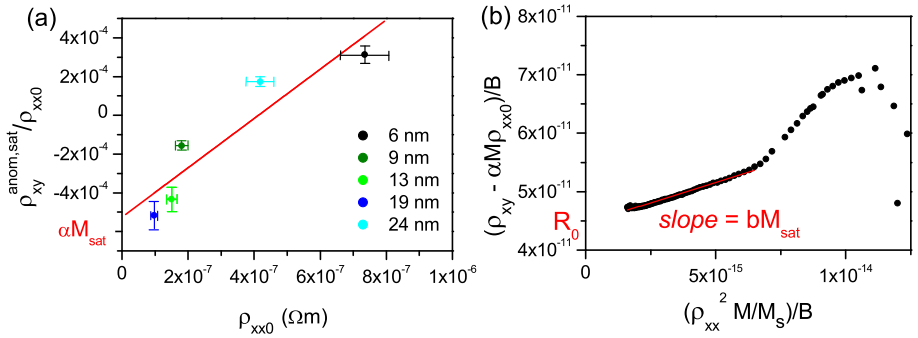

Figure 3.41: (a) Determination of αM_{sat} from a plot of the residual values of the longitudinal resistivity and the AHE for films of 6, 9, 13, 19 and 24 nm thickness. (b) Determination of bM_{sat} and R_0 for a 19 nm film from a plot of $(\rho_{xy} - \alpha\rho_{xx0}M)/B$ versus $\rho_{xx}^2 M/(M_{sat}B)$.

case of high magnetic fields and zero temperature the equation

$$\frac{\rho_{xy}^{anom,sat}}{\rho_{xx0}} = \alpha M_{sat} + bM_{sat}\rho_{xx0} \tag{3.18}$$

describes the relation between the saturated AHE and the residual resistivity. A plot of $\rho_{xy}^{anom,sat}/\rho_{xx0}$ versus ρ_{xx0} for films of different thickness yields the value of αM_{sat} as the intercept of a linear fitting as shown in figure 3.41a. The fit reveals that $\alpha M_{sat} = (-5 \pm 1) \cdot 10^{-4}$ is a reasonable value for all samples, although the error bars in figure 3.41a are too small to account for the deviation of the data points from the fit. Here it must be kept in mind that the specified uncertainties only indicate the error range of ρ_{xx0} and $\rho_{xy}^{anom,sat}$ for a certain film, but they cannot account for morphological differences in different samples, which are the main reason for deviations in the regarded values.

For the determination of b equation 3.17 can be rewritten as

$$(\rho_{xy} - \alpha\rho_{xx0}M)/B = R_0 + \frac{\rho_{xx}^2 M}{M_{sat}B} \cdot bM_{sat}, \tag{3.19}$$

where β was set to zero and the topological contribution was omitted. This relation reveals that a plot of $(\rho_{xy} - \alpha\rho_{xx0}M)/B$ versus $\rho_{xx}^2 M/(M_{sat}B)$ will give bM_{sat} as the slope of the straight line for sufficiently high fields. The corresponding fit shown in figure 3.41b yields a value of $bM_{sat} = (1.4 \pm 1.0) \cdot 10^3\, m/\Omega$. Here the large uncertainty stems from the inaccuracy in αM_{sat}. Furthermore the intercept of the fitted line confirms the normal Hall constant $R_0 = (4.5 \pm 0.1) \cdot 10^{-11}\Omega m/T$.

Now all contributions to the total Hall signal have been determined except from the THE. In figure 3.42 the resulting curve is shown in comparison

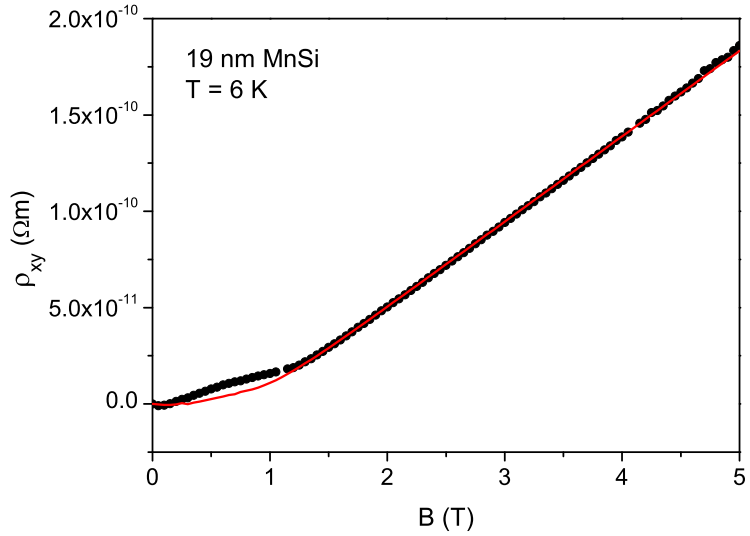

Figure 3.42: Comparison between measured Hall signal and theoretical curve with values α, b and R_0 as determined by the described fitting procedure. A THE can be observed in small magnetic fields.

with the measured Hall resistivity, which reveals a considerable deviation in the region of small magnetic field. This can be interpreted as a positive topological Hall contribution that adds to the normal and the anomalous Hall signal.

In fact, Li *et al.* [114] recently gave evidence that the measured Hall contribution is a topological effect, when they published Hall effect and Lorentz TEM measurements performed on MnSi thin films. They obtained Hall curves very similar to those shown here and they observed a skyrmion pattern in the Lorentz TEM image in exactly those field and temperature ranges, where the THE occurred. However, these Lorentz TEM investigations have recently been put into question [169], as will be discussed in section 3.7.

The results of further investigations of the Hall effect for films of 6 nm to 24 nm thickness are shown in the appendix A.4. Unfortunately it is not possible to draw a consistent picture, where all these measurements fit in. R_0 varies from $5{\cdot}10^{-11}\,\Omega\mathrm{m/T}$ to $1.2{\cdot}10^{-10}\,\Omega\mathrm{m/T}$, but no systematic dependence on the film thickness can be observed. The temperature dependence of the AHE shows a growing from negative to positive for most samples, but there is also an example of $\rho_{xy}^{anom,sat}$ being positive for all temperatures and also for two sign changes from positive to negative and to positive again. Some contributions that can be ascribed to a THE occur for all samples, but the field and temperature regions, where they occur, are different. In conclusion

the Hall effect seems to be very sensitive to the quality of the specific sample. Obviously morphological differences have large influence on the behavior of all three contributions of the Hall effect, which makes it very difficult to compare the results of different samples and to find a comprehensive description for all of them.

3.7 The Magnetic Phase Diagram of MnSi Thin Films

In the previous sections various measurements performed on MnSi thin films have been presented and discussed, which gave hints to several magnetic phase transitions. To find the transition lines the relevant techniques are magnetization, susceptibility, resistivity, magnetoresistance and Hall effect measurements. Although these methods cannot give information about the particular magnetic phases but only about the temperatures and magnetic field values, where phase transitions occur, it seems reasonable to summarize the results in terms of magnetic phase diagrams.

It has become clear that in general four cases of different films and field directions must be distinguished. On the one hand the behavior of the thin films in magnetic fields applied parallel or perpendicular to the film plane is different and, on the other hand, films with thicknesses smaller than the helix length show different transitions than those films, which are thicker than the helix length. In the following the different scenarios will be discussed beginning with the out-of-plane field configurations, which seem to be easier to understand, since less transitions can be observed. However, in this case Hall effect measurements are available and have to be regarded.

Considering the out-of-plane magnetization measurement on a 9 nm thin film MnSi (compare figure 3.23) no signs of a magnetic phase transition can be found. Nevertheless the transition from conical to ferromagnetic alignment exists and the values for $B_{c2}^{\perp}$ can be determined from magnetoresistance data, where a pronounced kink occurs (compare figure 3.32). The magnetization curve of a thicker film (19 nm) exhibits a kink at $B_{c2}^{\perp}$ (compare figure 3.24). However, since the magnetization was measured only at 5 K, again the MR data are stressed to determine critical field values. The temperature dependence of $B_{c2}^{\perp}$ as obtained from MR measurements is shown in figure 3.43 for several films with different thicknesses. As discussed before, shape anisotropy considerably enhances the critical fields compared to bulk MnSi, but since the shape of the MR curves is essentially identical to the bulk data [163], there it can be assumed that the helical magnetic structure is preserved in the thin films.

Regardless of the film thickness the first critical field B_{c1} is not expected to be observed in the case of thin films with a magnetic field applied perpendicular to the film plane. In bulk MnSi the orientation of the helix axis jumps from the $< 111 >$ directions to the field direction at $B_{c1} = 0.1\,\mathrm{T}$. However, for the thin films it is known that without a field the helix always aligns in an out-of-plane direction, as it is shown graphically in figures 3.44a and 3.45a [112]. Thus, an applied field in the same direction will not cause a reorientation, which explains the absence of B_{c1}.

From the similarity between the MR curves for bulk and thin films MnSi

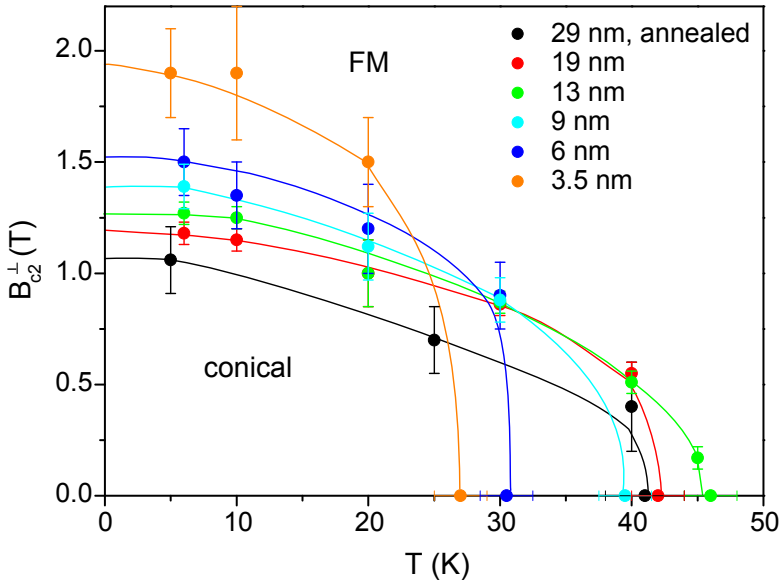

Figure 3.43: Magnetic phase diagram for films of different thickness. $B_{c2}^{\perp}$ marks the transition from the conical phase to ferromagnetic spin alignment.

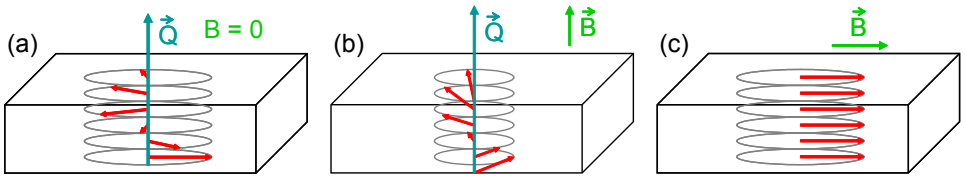

Figure 3.44: Possible spin configurations in the case of films, which are thinner than the helix length. (a) Without a magnetic field a helix is the ground state. (b) With a magnetic field applied perpendicular to the film plane a cone state is formed. (c) When $\vec{B}$ is applied in the film plane, the helix is unstable and the spins rotate continuously into field direction.

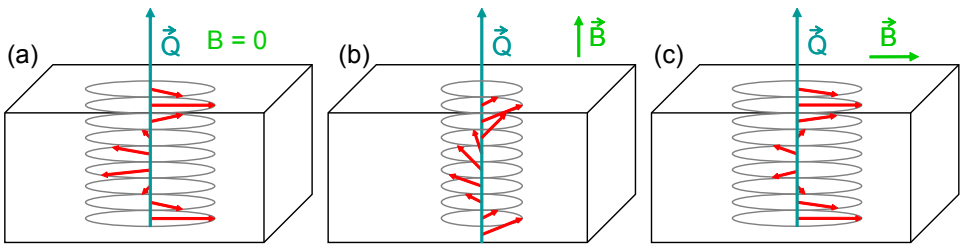

Figure 3.45: Possible spin configurations for films, which are thicker than the helix length. (a) In the ground state the spins form a helix. (b) When a magnetic field is applied out-of-plane a cone state is favored. (c) For small $\vec{B}$ applied parallel to the film plane the helix becomes distorted into a helicoid.

it can be concluded that the conical phase is also inherent in the films. With increasing magnetic field the angle of the cone decreases as depicted in figures 3.44b and 3.45b. At $B_{c2}^{\perp}$ the angle reaches zero and the sample is in an induced ferromagnetic state.

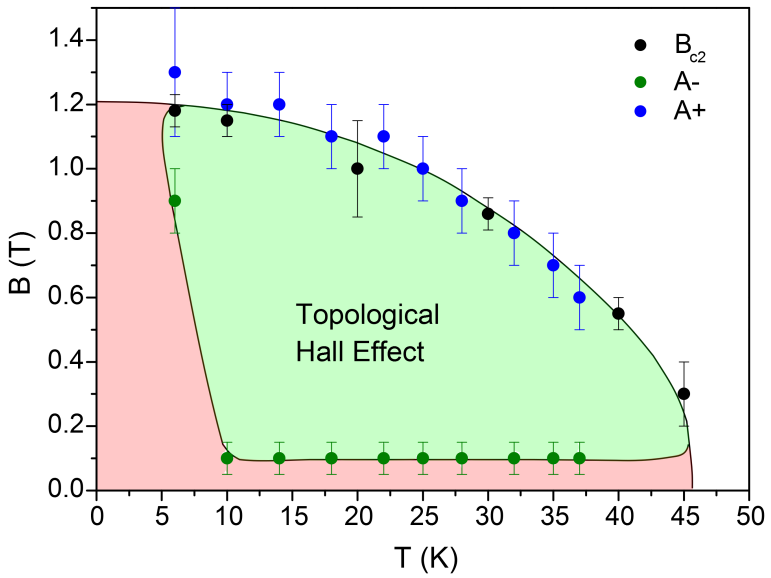

Figure 3.46: Magnetic phase diagram for a MnSi thin film of 19 nm thickness, where a magnetic field is applied out-of-plane. In the major part of the ordered phase a topological Hall signal can be detected.

So far the magnetic phase diagram for MnSi thin films with an out-of-plane magnetic field looks very straightforward and the measurements seem to be easy to understand. The situation changes, when the Hall effect measurements are taken into account. As shown in section 3.6 and in the appendix A.4 a topological Hall signal can be observed for all films, which occurs in most cases in nearly the complete magnetically ordered phase below $B_{c2}^{\perp}$ as it is shown exemplarily for a 19 nm film in figure 3.46.

By its definition the THE occurs due to topologically non-trivial spin configurations, which force a conduction electron to pick up a Berry phase, when its spin aligns with the local magnetization adiabatically. These spin structures may be (anti-)skyrmions, since they possess a non-zero winding number of (-)1. Actually, the Lorentz TEM measurements by Li *et al.* [114] show a pattern of bright and dark dots occurring exactly in the field and temperature ranges, where a THE was observed. These images were interpreted as being caused by skyrmions, which arise in thin films MnSi with a magnetic field applied in an out-of-plane direction.

However, as mentioned before the paper by Li *et al.* has been put into question by Monchesky *et al.* [169], who support a different theory. In a comment on the considered paper it was claimed that the observed Lorentz TEM images, which have been interpreted as skyrmions, can also be realized at room temperature. The authors of the comment explain the contrast to be caused by moiré fringes due to the lattice misfit. According to their interpretation the absence of any features in the magnetization curves of MnSi thin films with out-of-plane magnetic field is a proof that no skyrmion phase exists in this case [43]. To confirm their assumption they stress the theoretical model described in section 2.1, where the magnetic free energy is calculated including uniaxial anisotropy. For the calculations they use a negative constant of uniaxial anisotropy ($K < 0$) corresponding to a hard axis of magnetization. Their results suggest that the conical helix is indeed the only stable spin configuration in MnSi thin films with out-of-plane field direction. Furthermore the same group showed that not only skyrmions can generate a THE, but a conical spin structure with a propagation vector normal to the film plane and an additional modulation in the in-plane direction could also cause a topological Hall contribution [170].

Put together, there are two contradictory interpretations of the magnetic phase diagram of MnSi thin films with out-of-plane magnetic field. On the one hand the THE and the Lorentz TEM images promote a skyrmion phase, but it is not clear, whether the images can be trusted. On the other hand the group of Monchesky does not have a positive proof for their hypothesis of a cone phase covering the whole ordered phase, either. The theoretical calculations are very sensitive to anisotropy terms, which are included in the free energy functional. For example it has been proven that in free layers of MnSi without any strain skyrmions exist in an extended region [25] and this is supported by theory [21]. Possibly the strain in the MnSi/Si(111) system suppresses skyrmions aligned perpendicular to the film surface, but it cannot be excluded that further anisotropy terms in the free energy might support the stability of skyrmions. Furthermore the absence of clear features in the magnetization curves cannot be taken as a proof that a transition does not exist. The ideal magnetization curve for a thin layer of a cubic helimagnet with a skyrmion phase exhibits only faint kinks at the transition between the helical and the skyrmionic phase and a more pronounced kink at the saturation field [36] (compare figure 3.47). Since phase transitions in thin films are usually considerably broadened due to morphological inhomogeneities, it is possible that they cannot be observed, although they might occur.

In conclusion, with the existing experimental data it is not possible to confirm or to rule out the existence of out-of-plane skyrmions in MnSi thin films. Therefore further measurements which doubtlessly picture the actual magnetic structure are needed. These could be reliable Lorentz TEM images, magnetic x-ray or neutron scattering experiments, which will probably clarify the situation soon.

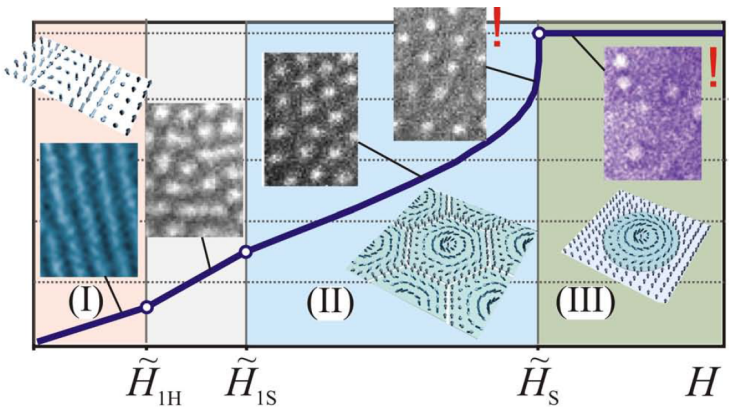

Figure 3.47: Calculated magnetization curve for a thin layer of a cubic helimagnet, where the cone phase is suppressed, taken from [36].

Next, the measurements performed with a magnetic field applied in an in-plane direction must be regarded, where distinctly different behavior for films with different thicknesses is observed.

The magnetization (figure 3.23) and magnetoresistivity (figure 3.35) results for the 9 nm film were completely free of any kink-like features, which would point to phase transitions. This suggests that for films thinner than the helix length the magnetic structure is no longer helical, when a magnetic field is applied parallel to the film plane. The scenario might be the following: In zero field a helix is formed, which is suggested by the out-of-plane measurements. But the helix does not complete a full period because of the restricted film thickness. Therefore, the non-collinear spin configuration is not stable in a magnetic field perpendicular to its propagation direction. Instead of tilting the helix axis, the individual spins will continuously rotate into field direction, until an induced ferromagnetic state is reached (compare figure 3.44). At 5 K this aligned state occurs at (1.3 ± 0.1) T, where the in-plane and the out-of-plane magnetization curves coincide.

In the case of the 19 nm film, which exceeds the helix length, the observed behavior in an in-plane field deviates distinctly from the configurations discussed before. As shown in figures 3.24 and 3.36 the magnetization as well as the MR curves exhibit several kinks. The kink occurring at the largest field value marks $B_{c2}^{||}$. Three further shoulders are named B_x, B_y and B_z, where the sequence is from lower to higher fields. All features readable from the magnetization, susceptibility and MR data are summarized in the phase diagram depicted in figure 3.48. Unfortunately the transitions, which are very pronounced at low temperatures, can not be traced between 20 K and T_{ord}. Most probably the transitions are broadened due to inhomogeneities in the film, so that they partly overlay with each other and cannot be distinguished.

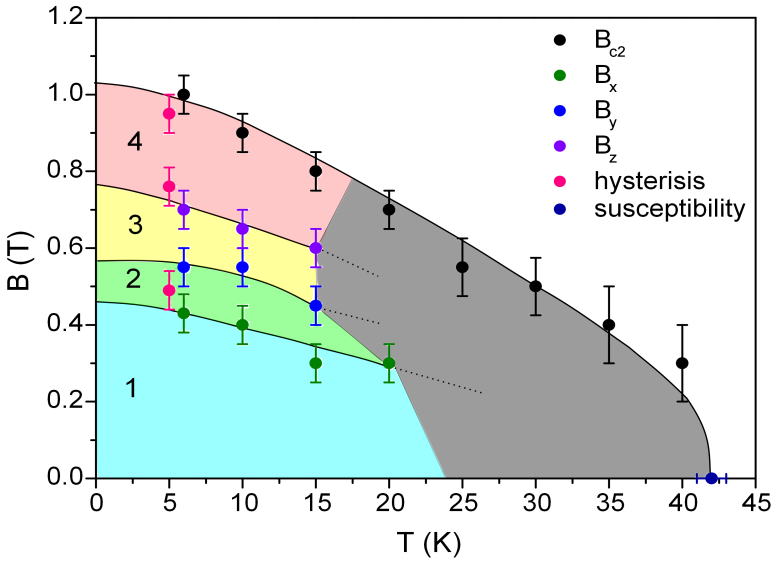

Figure 3.48: Magnetic phase diagram for a 19 nm thin film MnSi with a magnetic field applied in an in-plane direction. Phase transition lines are derived from kinks in the magnetoresistivity data. Data points from the hysteresis measurement at 5 K and T_{ord} as determined from susceptibility are also included. At temperatures between 20 K and 40 K it was not possible to trace the transitions.

In the phase diagram four different phases occur below the critical field $B_{c2}^{||}$, which are labeled 1, 2, 3 and 4 as indicated in figure 3.48. Since it is known that the ground state is a helical spin configuration, phase 1 should be a state consisting of spin spirals. However, the first transition occurs around 0.4 T, which is too high to leave the helix unaffected up this field value. Instead the helix will become distorted, when the spins are slightly pulled into field direction (compare figure 3.45c). Such a distorted helix is often called a helicoid in literature [36].

Concerning the other three phases it is not possible to determine the actual spin structure from our measurements, since only the transitions can be seen but not the properties of the particular phases. However, the group of T. Monchesky has performed polarized neutron reflectometry (PNR) [44, 170, 171] on MnSi thin films, which exhibit the same features in magnetization measurements as the films prepared during this work. Their results will shortly be summarized in the following.

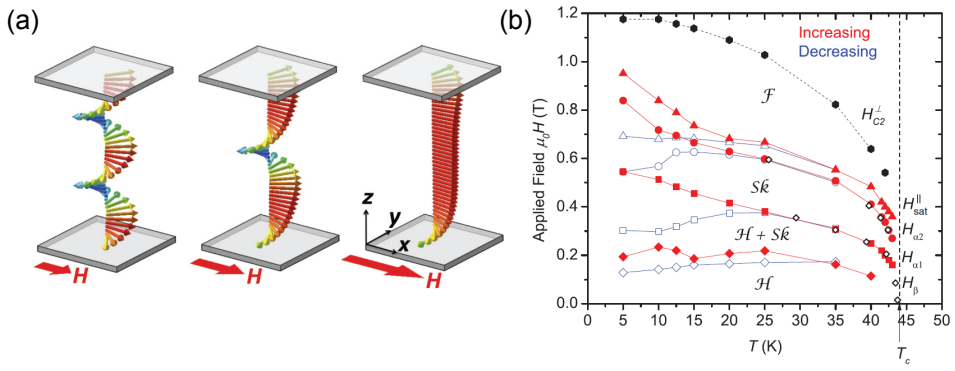

Figure 3.49: (a) Images of the calculated helicoidal states in applied magnetic fields for a thin film MnSi at low temperature, taken from [171], (b) magnetic phase diagram of a thin film MnSi with 27 nm thickness with magnetic fiels applied in-plane, taken from [45].

According to their interpretation of PNR and magnetometry data two temperature regimes have to be distinguished. At low temperatures ($T = 5$ K) the magnetic phase diagram is supposed to consist of discrete helicoidal states as shown in figure 3.49a [171]. The idea is that a helix with a length of several periods propagating perpendicular to the film plane is unwinded stepwise. At each kink occurring in the magnetization curve a winding of the helix is pushed out of the film until at high fields a nearly collinear spin structure is left.

At higher temperatures ($T = 25$ K), however, distinctly different phases occur. While at low magnetic fields the PNR data can be fitted with the magnetization profile of helicoids, at higher fields also skyrmions running in the plane of the film occur [45, 170]. Monchesky and his coworkers obtain

a phase diagram as shown in figure 3.49b, which consists of four distinct phases in agreement with the results of this work. The phase at lowest fields is indeed a helicoidal one. The phases 2, 3 and 4 are a mixed phase containing helicoids and skyrmions, a pure skyrmion phase and a twisted ferromagnetic phase, respectively.

Although this interpretation of the magnetic phases in MnSi thin films seems quite reasonable and in agreement with the experimental situation, a few questions remain. First of all it is still unknown, at which temperature the proposed transition between the discrete helicoidal states at low temperatures and the skyrmions at higher temperatures occurs and how this transition depends on film thickness. Furthermore a theory is needed in order to find the mechanism, which drives the system from the low into the high temperature regime.

3.8 Resistance Measurements under Hydrostatic Pressure

In section 3.4.2 it was shown that the ordering temperature of MnSi thin films is strongly temperature dependent for the thinnest films and for the thicker films it is enhanced compared to bulk MnSi. T_{ord} amounts 43 K for films thicker than approximately 10 nm, while for the bulk $T_{c,bulk}$ is only 29 K [118]. The thickness dependence for films thinner than 10 nm could convincingly be explained by the reduction of spin interactions, when the thickness of the film approaches the spin-spin correlation length. The enhancement of T_{ord} to 43 K, however, is caused by a different mechanism. It is nearby to consider strain as responsible for the enhancement, since the lattice misfit of $-3\,\%$ between the MnSi film and the Si substrate leads to a tensile strain in the film. Although RHEED investigations evidenced that part of it has relaxed, there will most probably be remaining strain in the order of $\epsilon \approx -1\,\%$ (compare section 3.3.3).

The tensile strain in the film can be regarded as a negative pressure acting on MnSi in the film plane. For bulk MnSi it is known that hydrostatic pressure decreases $T_{c,bulk}$ [27, 28]. Magnetic order is completely suppressed at the critical pressure $p_{c,bulk} = 1.46$ GPa. It can be guessed that negative pressure in the form of in-plane strain might evoke the reverse effect and enhance T_{ord} in the case of thin films, although the pressure acting on the films is not hydrostatic. While the lattice spacings in the film plane are elongated, the lattice is compressed in out-of-plane direction according to the Poisson's ratio.

Encouraged by these considerations the behavior of thin films MnSi under applied hydrostatic pressure was investigated. It was expected that the applied pressure would counteract the misfit related negative pressure and thereby decrease T_{ord} to the bulk value again. For even higher pressure T_{ord} should tend to zero in the same way as in bulk MnSi. The observation of this scenario would confirm the assumption that the negative pressure imposed by the substrate is responsible for the enhanced T_{ord} in the thin films.

The first idea for the determination of T_{ord} of a thin film MnSi under pressure was to perform magnetization measurements on a sample placed in a piston cylinder pressure cell. Since the sample space inside the pressure cell is restricted to a size of $\approx 1.5 \times 1.5$ mm^2, the available SQUID magnetometer was not able to resolve the very small magnetic moment of the film masked by the large contribution of the pressure cell itself. Therefore, instead of magnetization measurements, the resistance of the thin film was measured under pressure, since T_{ord} can also be determined from these curves (compare section 3.5.3).

The resistance measurements were carried out at the Hokkaido University in Sapporo (Japan). The collaboration with the work group of Prof.

Amitsuka was supported by the Japan Society for the Promotion of Science.

3.8.1 Experimental Setup for High Pressure Experiments

For the investigation of the high pressure behavior of MnSi thin films a 9 nm sample with $T_{ord} = 44\,\mathrm{K}$ at ambient pressure was chosen. In order to fit into the pressure cell the sample was cut to a size of 1 mm × 0.5 mm × 0.3 mm, where the height includes the substrate and the film.

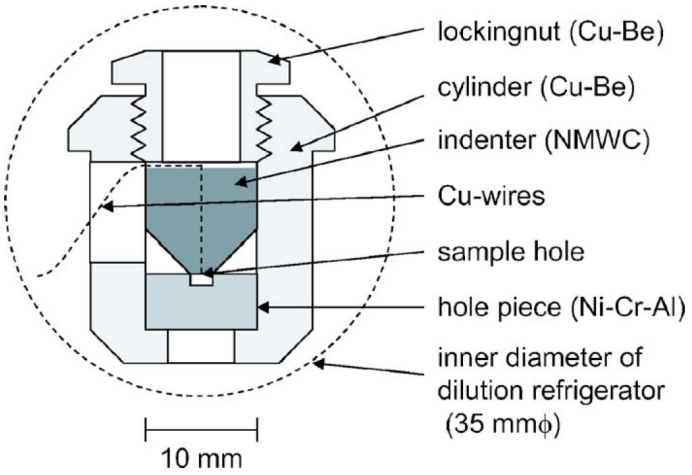

Figure 3.50: Setup of the indenter cell used for resistance measurements under pressure, taken from [172].

For the resistance measurements under pressure an indenter cell as it is shown in figure 3.50 has been used. The cell consists of an outer Cu-Be cylinder, in which a hole piece made of Ni-Cr-Al alloy is positioned. The hole measures 1.6 mm in diameter and approximately 0.7 mm in height. It defines the sample space and is filled with a pressure transmitting medium. The sample is attached to a small plateau on the indenter, which is made of non magnetic tungsten carbide (NMWC). The top of the indenter is pressed into the hole and fixed by a locking nut. When pressure is applied by a hydraulic press, the edges of the hole are deformed by the force transferred by the indenter. With this type of pressure cell is possible to reach hydrostatic pressure up to 4.5 GPa [172].

For the experiments on MnSi thin films Daphne 7474 oil was used as the pressure medium, which does not solidify until a pressure of 3.7 GPa at room temperature is reached [173]. Next to the sample a Pb specimen was placed inside the pressure cell, which was needed for measuring the pressure value at low temperatures by the determination of its superconducting transition temperature T_{SC}. Up to 15 GPa T_{SC} of Pb decreases linearly with increasing

pressure [174], which can be calculated by

$$p = \frac{T_{SC}(0\,\mathrm{GPa}) - T_{SC}(p)}{0.363\,\mathrm{K/GPa}}, \tag{3.20}$$

where $T_{SC}(0\,\mathrm{GPa}) = 7.2\,\mathrm{K}$ is the transition temperature at ambient pressure.

The electrical resistance of the 9 nm film was measured by a four probe method. The Cu wires were introduced into the pressure cell through a small hole in the indenter that was sealed by epoxy. The contacts were attached on the film surface using silver paint. To ensure good conduction between film and wires a thin layer of gold was deposited on those areas of the film surface, where the contacts were positioned. The contacts of the Pb sample were made by spot welding. A photograph of the thin film sample and the Pb specimen attached to the indenter plateau is shown in figure 3.51.

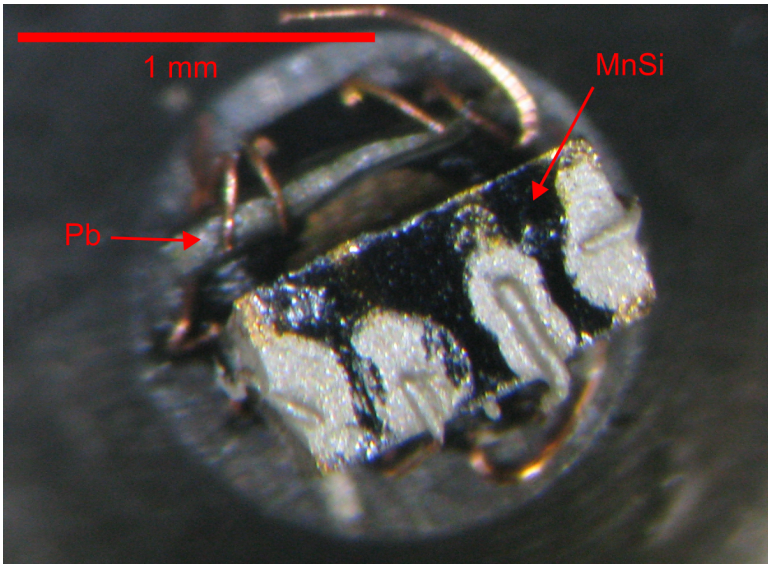

Figure 3.51: Photograph of the contacted thin film and Pb sample attached to the indenter. The picture was taken through a microscope.

For the resistance measurements the indenter cell was inserted into a glass cryostat filled with liquid helium. The temperature could be controlled by varying the height of the sample above the liquid helium level and by a resistive heating installed at the specimen holder. By evacuating the cryostat temperatures down to 1.7 K could be realized. To apply higher pressure it was necessary to take the indenter cell out of the cryostat.

3.8.2 Resistance Measurements

The temperature dependence of the resistance $R(T)$ of the 9 nm MnSi film was measured for various pressure values. The data recorded in a tempera-

ture range from 1.7 K to 60 K are depicted in figure 3.52. In agreement with earlier resistivity measurements at ambient pressure (compare section 3.5.3) the curves in the low-pressure regime show a pronounced kink, which marks the onset of magnetic order. T_{ord} can be derived from the kink position and decreases with increasing pressure. The values of T_{ord} as function of pressure are plotted as black symbols in figure 3.54. The uncertainty in T_{ord}, which is displayed by the error bars, increases at high pressure, because the kink in the $R(T)$ curves broadens progressively. The uncertainty for p results from pressure inhomogeneities, which have been estimated from the width of the superconducting transition of the Pb specimen.

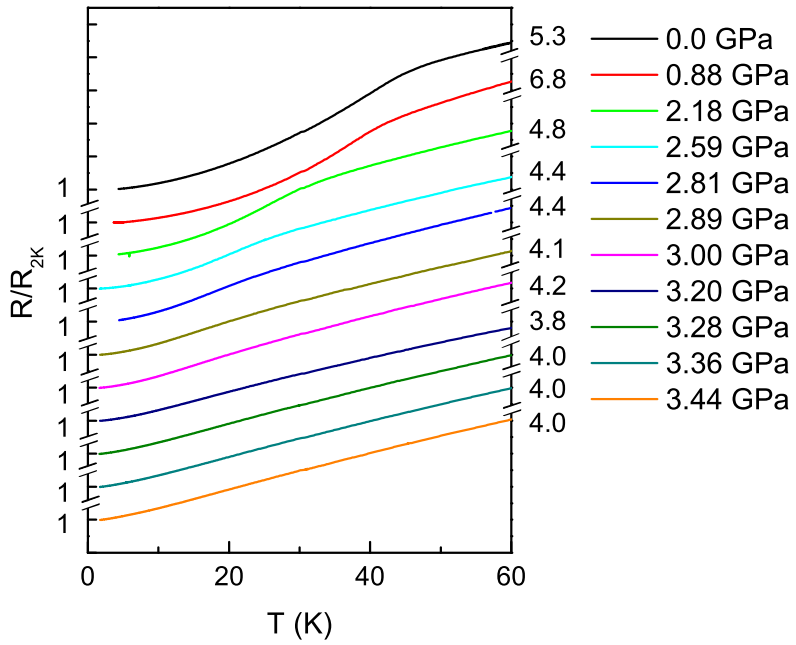

Figure 3.52: Electrical resistance of a 9 nm film MnSi under applied pressure. All data are normalized to the the resistance values R_{2K} measured at 2 K.

For pressures higher than 3 GPa it is not possible to determine T_{ord} any longer. In figure 3.53 the disappearance of the kink in $R(T)$ is illustrated by comparing the first temperature derivatives of the resistance. T_{ord} is defined as the minimum in the second temperature derivative of $R(T)$ corresponding to the point of maximal decrease in the first derivative. This point can precisely be identified in the derivative curves for $p < 3.1$ GPa, where it is marked by arrows in figure 3.53. When the pressure exceeds 3.1 GPa, a solely linear decrease exhibiting no special features is observed in the derivative.

These findings indicate that magnetic order disappears above the critical pressure $p_c = (3.1 \pm 0.1)\,\mathrm{GPa}$.

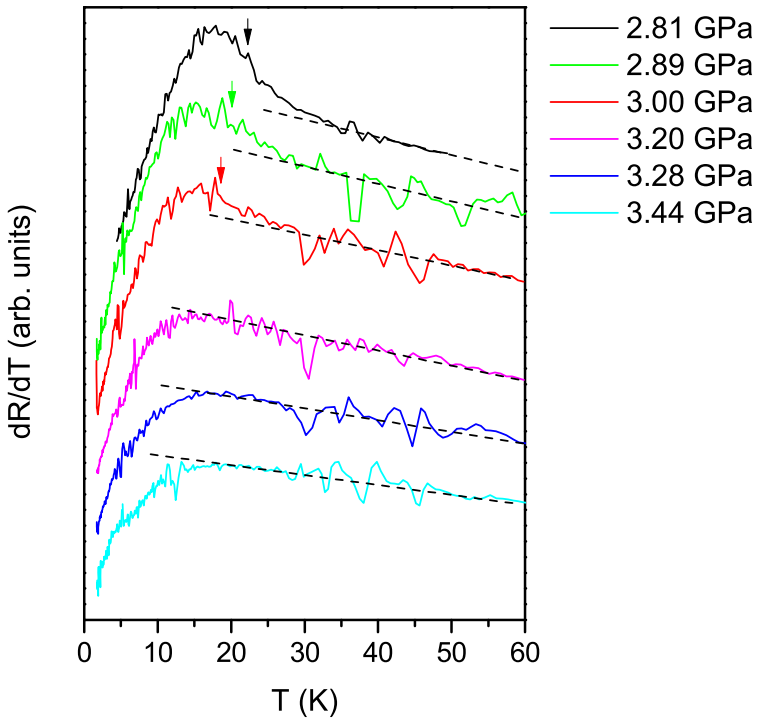

Figure 3.53: Temperature derivatives of the resistance curves for pressure values around 3.1 GPa. For $p < 3.1\,\mathrm{GPa}$ a steep decrease marked by arrows defines T_{ord}. Above 3.1 GPa this feature vanishes.

Thus, the resistance measurements have shown that the enhanced T_{ord} in the MnSi thin film decreases with increasing pressure. This is in agreement with the expectations and supports the assumption that the hydrostatic pressure counteracts the tensile strain induced by the Si substrate. Applied and strain-induced pressure are at equilibrium, when T_{ord} is reduced to the bulk value of 29 K again. The application of even higher pressure forces T_{ord} to zero. In the following it will be analyzed, whether this proceeds in the same way as in bulk MnSi.

Therefore the pressure dependent T_{ord} of the thin film is compared with corresponding data for bulk MnSi taken from references [27] and [28]. In figure 3.54 an overlay of the thin film and bulk data is shown. The graphic was created by positioning the zero-point of the bulk-data pressure scale at 2.3 GPa in the thin film data, where T_{ord} of the film is decreased to

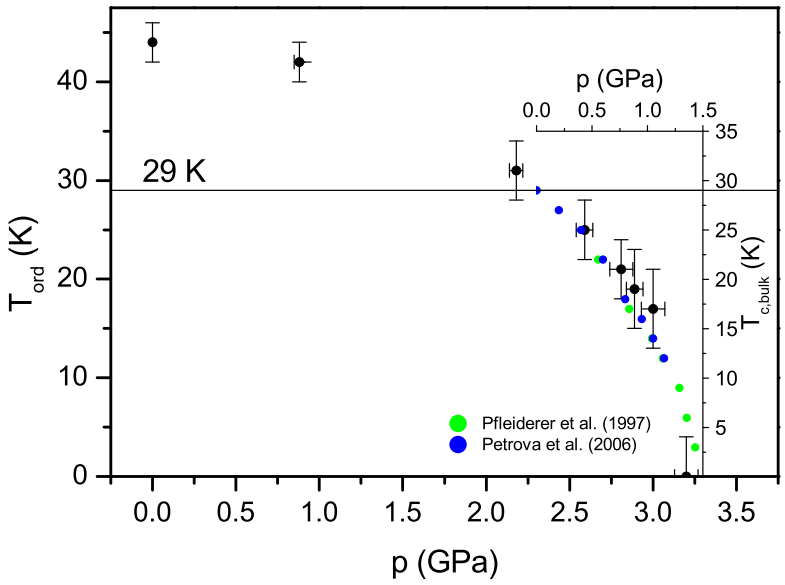

Figure 3.54: Comparison of the pressure dependence of T_{ord} in the thin film and bulk MnSi. Bulk values were taken from references [27] and [28].

29 K. Furthermore the pressure axis of the bulk data is rescaled so that the positions of p_c in both diagrams are the same. The temperature axes of both data sets, however, are identical. These modifications are necessary to account for the interaction between the substrate and the film. The fact that the 9 nm MnSi film is not free-standing but bound to the 280 μm Si substrate results in the adaptation of the film to the lattice of the substrate, which is compressed by the applied pressure.

A pressure of 2.3 GPa has to be applied on the thin film sample in order to decrease T_{ord} to the bulk value of 29 K. Using the bulk modulus of Si ($K_{Si} = 97.6$ GPa) it can be calculated that this pressure imposes a compressive strain of -0.8 % on the Si substrate. A value of similar size (0.95 %) has been published by Karhu *et al.* [44] for the in-plane tensile strain in a 9 nm film MnSi grown on Si(111) and, although burdened by a large uncertainty, the value from the RHEED investigations described in section 3.3.3 is also consistent with this value. Thus, it may be assumed that at 2.3 GPa the strained MnSi unit cell of the thin film is compressed its bulk size. Nevertheless, it must not be neglected that the unit cell is certainly no longer cubic, since it has been deformed by the in-plane strain due to the substrate. The good agreement between bulk and thin film data, however, suggests that this deformation has minor impact on the magnetic and transport properties of MnSi.

The rescaling of the bulk-data pressure scale in figure 3.54 is necessary, because only 1 GPa is needed for the suppression of T_{ord} from 29 K to zero in the thin film instead of 1.5 GPa as in bulk MnSi. Assuming that the MnSi thin film is compressed to the same extend as the Si substrate and taking into account that the bulk modulus of Si is smaller than that of MnSi, it is reasonable that less pressure is needed to compress the film bound to the substrate than to compress bulk MnSi. The ratio of 1.5 GPa to 1 GPa agrees well with the ratio of the bulk moduli $K_{MnSi} : K_{Si} = 137\,\text{GPa} : 97.6\,\text{GPa}$.

A difference between the resistivity measurements under pressure for thin films and bulk MnSi is the sharpness of the kink at T_{ord}. While for the bulk material the kink becomes sharper with increasing pressure [27], it broadens in the case of the thin film. This is most likely caused by morphological inhomogeneities as detected during the structural characterization of the films in section 3.3. Since the film surface is not perfectly flat, there are areas with slightly different thickness and probably also with deviating strain. This leads to an averaged T_{ord}, which will fan out under pressure.

In conclusion it was confirmed that the behavior under applied pressure is qualitatively the same for bulk and thin film MnSi. Since the quantitative differences can be explained by the adherence of the film to the Si substrate, the assumption that the enhanced T_{ord} in thin films is caused by strain could be approved.

3.8.3 NFL Behavior in MnSi Thin Films

As pointed out in section 3.5.3 the resistivity measurements on thin films MnSi at ambient pressure have confirmed a T^2 law of the resistivity at low temperatures. Under applied pressure this behavior changes, especially when the critical pressure is reached or exceeded. In order to determine the exponent n in the resistance law $R = R_0 + AT^n$ for the thin film under pressure, the logarithmic derivative of $(R - R_0)$ was calculated, where R_0 is the resistance at $T = 0\,\text{K}$. This is an approved way to investigate the temperature dependence of n [175].

In figure 3.55 the dependence of $n = d\ln(R-R_0)/d\ln T$ on temperature is depicted for all different pressure values. At ambient pressure $n \approx 2$ is found below $T_{ord} = 44\,\text{K}$. Above T_{ord} n decreases steeply to $n \approx 1$ in the paramagnetic regime. At pressures higher than 2.5 GPa this decrease becomes less steep, so that a temperature regime lying between the magnetically ordered phase and the normal paramagnetic phase can be distinguished by its deviating n value. Above the critical pressure ($p > 3.1\,\text{GPa}$) $n = 1.5$ can be found at lowest temperatures, and above approximately 30 K the temperature dependence of the resistance is nearly linear ($n \approx 1$).

The low temperature values of n for all pressure values are plotted in figure 3.56. Although some data exhibit considerable error bars due to noise in the complex measurement, it is obvious that the T^2 behavior of the resis-

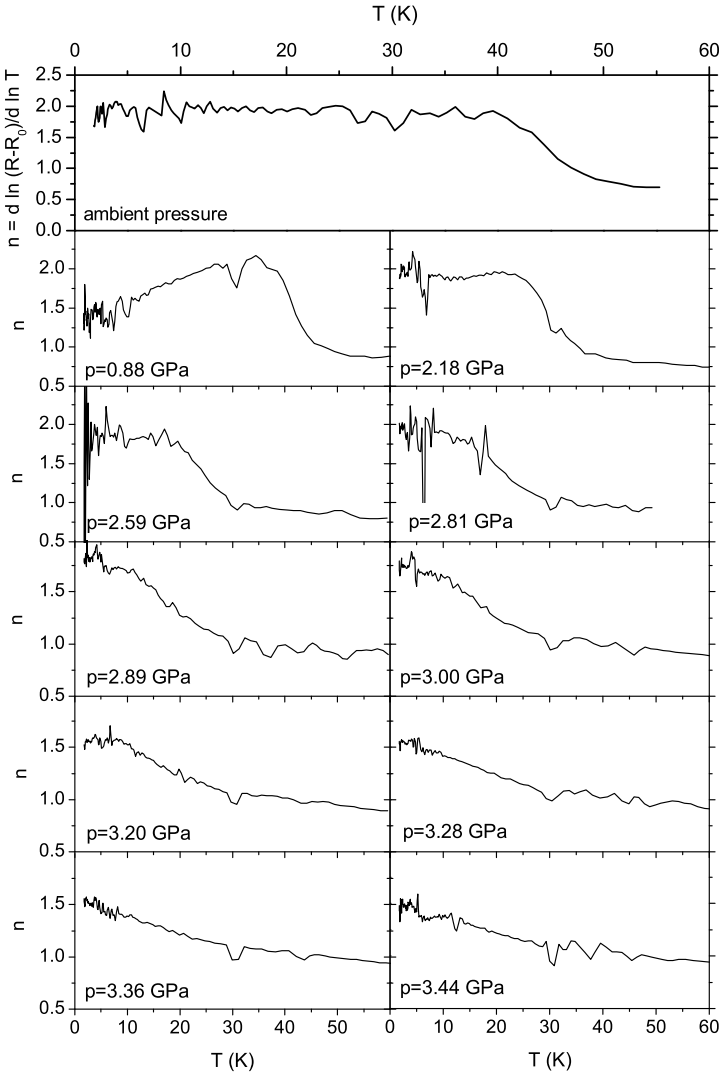

Figure 3.55: Temperature dependence of the critical exponent n defined by $d\ln(R-R_0)/d\ln T$ for different pressure values.

tance changes into a $T^{3/2}$ behavior at high pressure. Also in bulk MnSi it was observed that n jumps from 2 to 1.5, when the pressure exceeds p_c [32]. Due to sample inhomogeneities it is not surprising that for the thin film this crossover is not as sharp as in bulk MnSi. Nevertheless the clear $T^{3/2}$ law above 3.1 GPa gives evidence that a NFL regime exists beyond the critical pressure.

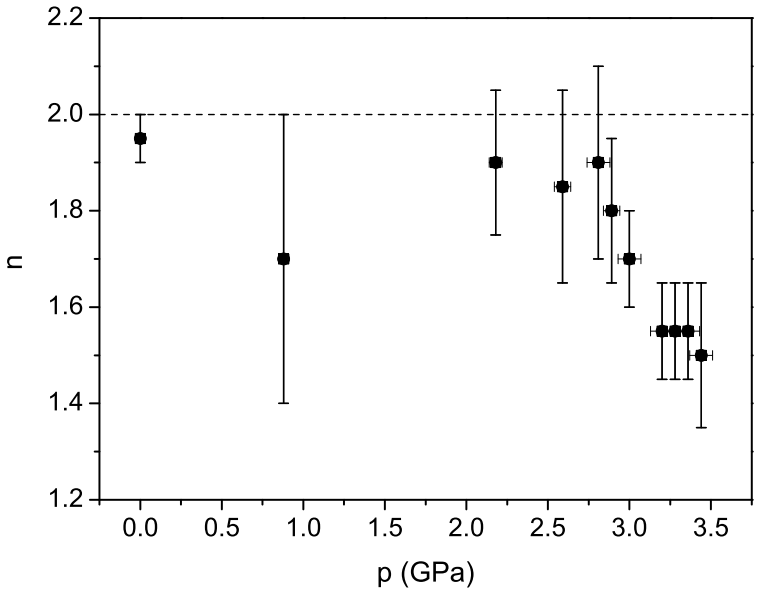

Figure 3.56: Pressure dependence of the exponent n in $R = R_0 + AT^n$ defined by the logarithmic derivative of $(R - R_0)$ at low temperatures.

In some of the diagrams in figure 3.55 certain temperature regimes can be identified, where no constant value of n can be specified. On the one hand this concerns the curves for pressures between 2.5 GPa and p_c, which show a continuous decrease from $n \approx 2$ to $n \approx 1$ in the temperature range between T_{ord} and about 30 K. On the other hand for $p > p_c$ n decreases with temperature from the low temperature value ($n = 1.5$) to $n \approx 1$ at 30 K. In all $d\ln(R - R_0)/d\ln T$ curves for $p > 2.5$ GPa there is a kink around 30 K followed by an approximately linear temperature dependence of the resistance ($n \approx 1$). Therefore T_{lin} is defined as the temperature of the kink, above which the resistance is linear.

In the temperature–pressure phase diagram shown in figure 3.57 the values of T_{ord} and T_{lin} have been included. By these two crossover temperatures the phase diagram is divided into three regions. In the magnetically ordered phase the resistance exhibits a T^2 behavior corresponding to a Fermi-liquid.

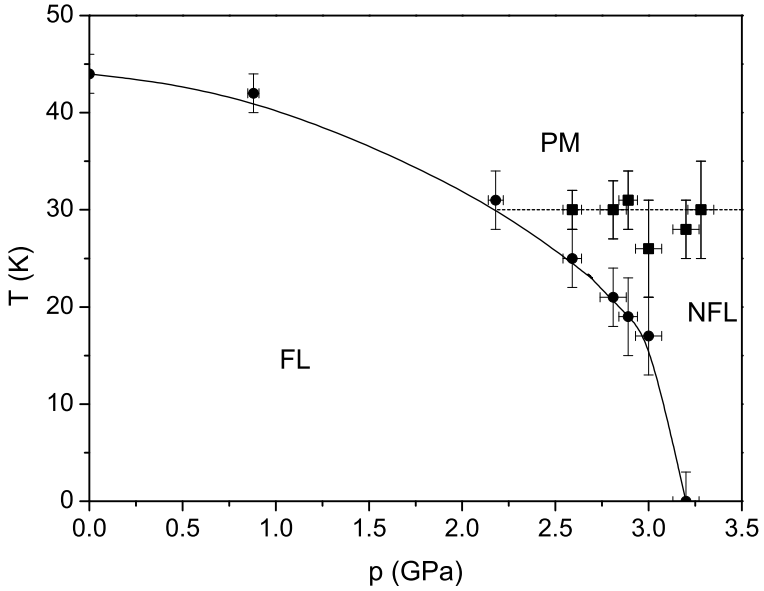

Figure 3.57: Temperature–pressure phase diagram for the MnSi thin film. Round and square symbols mark the values of T_{ord} and T_{lin} (see text), respectively. The lines are guides for the eye.

Above T_{ord} and above $T_{lin} \approx 30\,\mathrm{K}$ the resistance is approximately linear in T, which is expected for a normal paramagnetic metallic state due to phonon scattering[7]. The third region of the phase diagram, which is found beyond p_c and below T_{lin} in the paramagnetic phase, is a NFL regime with $R \propto T^n$, where n deviates from 1. In this regime n adopts a value of 3/2 at lowest temperatures. Also in bulk MnSi NFL behavior occurs at high pressures below a temperature of $T^\star = 12\,\mathrm{K}$, which is much lower than the corresponding temperature $T_{lin} \approx 30\,\mathrm{K}$ for thin films [32, 176]. It is discussed that topologically stable spin structures such as skyrmions are characteristic for the NFL regime [32]. Since the skyrmionic phase is stabilized due to uniaxial anisotropy [21, 45] it appears reasonable in this context that the NFL phase for MnSi thin films is extended towards higher temperatures.

[7]More precisely, in bulk MnSi the resistivity above $T_{c,bulk}$ can be described by two parallel resistors, where one is linear in T and the other is constant [162]. In the case of thin films the Si substrate contributes to in the conduction at high T.

Chapter 4

MnGe Thin Films

In the first part of this work epitaxial thin films of MnSi have been grown successfully on Si(111). Their structural and physical properties were measured and explained, especially with regard to the magnetic behavior. Because of the enlarged skyrmion phase these films are very interesting in the search for materials, which can possibly be used in future spintronic devices. However, the drawback of MnSi is the low magnetic ordering temperature. Although T_{ord} is enhanced in MnSi thin films compared to bulk, it is still considerably below liquid nitrogen temperature. To bring the thin films closer to application, it is desirable to find compounds with similar magnetic properties but higher transition temperatures.

A suitable candidate is MnGe. MnGe crystallizes in the B20 structure as MnSi and its magnetism is governed by the same interactions, primarily the ferromagnetic exchange and the Dzyaloshinskii-Moriya interaction. Therefore also the occurring magnetic states of MnGe are basically the same as for MnSi, but advantageously the magnetic transition temperature $T_N = 170\,\mathrm{K}$ of MnGe is much higher than for its isostructural relative [177].

Unfortunately, the synthesis of bulk MnGe is rather difficult, since it forms only under high pressure and high temperatures [177]. Molecular beam epitaxy offers the advantage that thin films are prepared under strong non-equilibrium conditions, which could make the growth of MnGe possible. Nevertheless, no successful attempt to grow MnGe thin films has been reported in literature. Several experiments, where Mn and Ge were deposited on Ge(111) substrates, evidenced that Mn and Ge tend to form Mn_5Ge_3 [178, 179].

During this work another attempt was made to grow MnGe on Ge(111) surfaces by codeposition of Mn and Ge. However, after this was not successful, Si(111) substrates were used instead of Ge substrates. The lattice constant of bulk MnGe within the (111) plane is 6.781 Å, which matches that of the $\sqrt{3}\times\sqrt{3}R30^\circ$ reconstructed Si surface with a misfit of only 2 %. Thus, compressively strained MnGe films may be grown on Si(111) substrates. Fur-

thermore, Si substrates offer the possibility to prepare a seedlayer of MnSi, which provides the B20 crystal structure for the growth of MnGe.

4.1 Properties of Bulk MnGe

Until now MnGe is one of the least studied compounds among the metal germanides. The problem is that the reaction to form MnGe can only be enforced under high pressure conditions of $4 - 5.5$ GPa and at temperatures between 600 and 1000 °C [177].

Prepared under these conditions MnGe crystallizes in the B20 structure with a lattice constant of 4.795 Å. The compound is metallic and exhibits magnetic order showing characteristics of antiferromagnetism. The Néel temperature amounts $T_N \approx 170\,K$ as determined from the maximum in the magnetic susceptibility [14] (compare figure 4.1b). In the paramagnetic region Curie-Weiss behavior was observed with a positive Curie temperature of 187 K, which gave evidence for ferromagnetic exchange between neighbored Mn atoms [177].

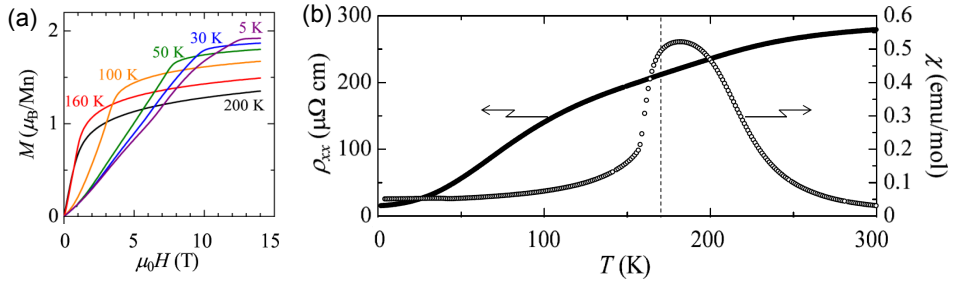

Figure 4.1: (a) Magnetization measurements on bulk MnGe, (b) magnetic susceptibility and resistivity curves, taken from [14].

The magnetic ground state of MnGe is a helical spin structure as Kanazawa *et al.* [14] proved by neutron diffraction experiments. The helix length was calculated to vary between 3 nm at lowest temperatures and 6 nm, when T approaches T_N. Magnetic anisotropy pins the helix axis to the <111> or <100> direction, but an applied magnetic field forces it to align with the field direction. The magnetization saturates at 12 T, where the spins are aligned parallel (compare figure 4.1a).

Furthermore a topological contribution to the Hall effect was measured in MnGe that is about 40 times larger than in MnSi and that is found in a very large field and temperature region [14]. Analogous to the case of MnSi this contribution was associated with the existence of a skyrmion lattice in MnGe.

Very recently small angle neutron scattering experiments gave further evidence for skyrmions in MnGe [180]. For a polycrystalline sample scattered

intensity was observed perpendicular to the applied magnetic field, which must be caused by helices oriented perpendicular to the field direction. The observed pattern is most likely a sign of skyrmions, which can be regarded to consist of helices with propagation directions perpendicular to the field. Due to the SANS measurements the skyrmions occur in magnetic fields around 2 T and stay in a metastable state even after the field has been removed [180].

4.2 Preparation of MnGe Thin Films

For the growth of MnGe thin films many experiences made during the preparation of the isostructural MnSi films could be adopted. The same P-doped Si(111) substrates with a resistivity between 1 and 10 Ωcm at room temperature were used. Prior to film deposition the substrates were heated to 1100 °C under UHV conditions in order to remove the oxide layer and to achieve a clean and flat surface with 7×7-reconstruction, which was verified by in-situ RHEED investigations. The diffraction pattern is the same as shown in figure 3.6.

In a first attempt to grow MnGe on the Si(111) substrate Mn and Ge were deposited directly on the 7×7-surface. In this case the RHEED pattern evidences that no B20 MnGe film is formed (compare figure 4.2a). In order to achieve a better result the growth conditions were varied. The growth rates of Mn and Ge and their ratio were changed and also different substrate temperatures between 175 °C and 275 °C were used, but the RHEED pattern stayed essentially the same as shown in figure 4.2a. The comparison of the distances between the RHEED streaks with the streak positions of Si(111) (compare figure 4.2b) reveals a value of 7.12 Å for the lattice constant of the film material, which deviates less than 1% from the hexagonal lattice spacing in Mn_5Ge_3 ($a_{Mn_5Ge_3} = 7.184$ Å [181]). Furthermore Mn and Ge tend to form Mn_5Ge_3, when deposited on a Ge(111) substrate [178, 182], which possesses the same crystal structure as Si with an only 4% larger lattice constant. Therefore it can be assumed that the formation of Mn_5Ge_3 is favored over that of MnGe.

In order to force Mn and Ge to form the desired B20 compound a special technique was developed. Before growing MnGe, a 5 Å layer of Mn was deposited onto the Si surface and subsequently heated to 300 °C. By this procedure a 10 Å layer MnSi is formed (compare section 3.2.2). This layer possesses the B20 structure and, thus, can be used as a seedlayer for the growth of MnGe. In the next step, MnGe was codeposited by simultaneous evaporation of Mn and Ge from an effusion cell and an electron beam evaporator, respectively. The total deposition rate was 0.15 Å/s, where equal amounts of Mn and Ge atoms were provided. During film growth the substrate was held at a temperature of 250 °C. With the described technique

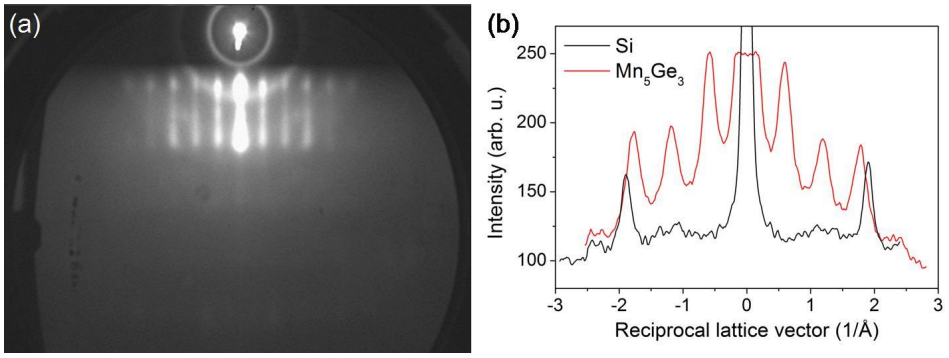

Figure 4.2: (a) RHEED pattern of layer Mn_5Ge_3 along the $[10\bar{1}]$ crystal direction of Si, (b) line scans across the RHEED streaks for the film in comparison with the Si substrate. The scans were taken parallel to the shadow edge.

epitaxial MnGe with B20 structure can be grown on Si(111) as it will be shown in the following paragraphs.

4.3 Characterization of MnGe Films by RHEED

The MnGe films have been investigated by in-situ RHEED in order to determine their structure and morphology. The RHEED patterns of a 14 nm [1] MnGe film observed along the $[10\bar{1}]$ and $[11\bar{2}]$ directions of the Si substrate are shown in figures 4.3a and 4.3b. The streaks indicate two-dimensional epitaxial growth and their arrangement is very similar to the pattern of MnSi thin films. This suggests that MnGe sustains the B20 crystal structure provided by the seedlayer. The uniform intensity of the detected streaks implies a very flat surface, at least for surface areas of around 100 nm in diameter, since this is the length scale, on which the electron beam of the RHEED system is coherently scattered and the electrons contribute to the pattern.

A line scan across the MnGe diffraction pattern observed along $[10\bar{1}]$ is depicted in figure 4.4 in comparison with the Si substrate. A deviance of 3% $\pm$ 1% of the MnGe streaks from the corresponding Si reflections indicates that the MnGe lattice has relaxed to a large extent from the compressive strain imposed by the substrate. This evidences a semi-coherent growth of the MnGe layer.

[1] The film thickness was calculated from the Mn deposition rate and the time of evaporation. Later XRD measurements showed that it is underestimated.

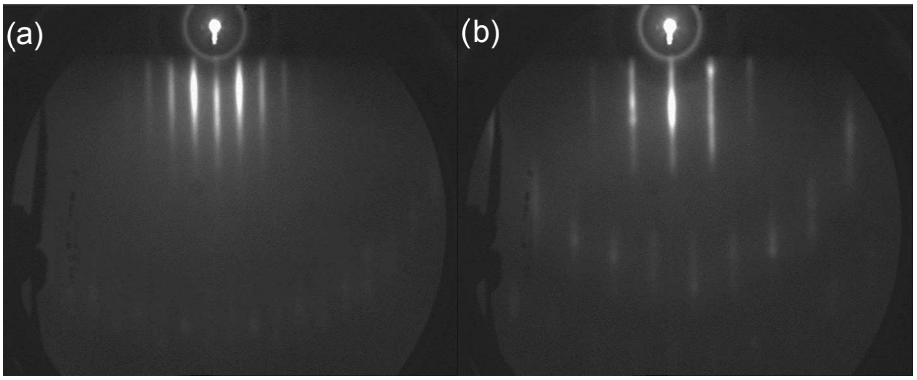

Figure 4.3: RHEED patterns of a 14 nm film (a) along [10$\bar{1}$] and (b) along [11$\bar{2}$].

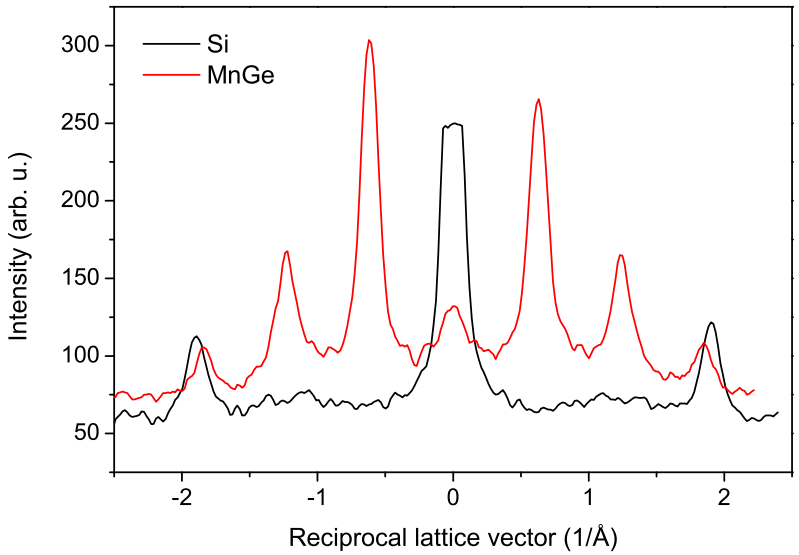

Figure 4.4: Line scans across the RHEED pattern of MnGe along [10$\bar{1}$] in comparison with the Si substrate. The scans were taken parallel to the shadow edge.

4.4 AFM Investigations

MnGe thin films of different thickness were investigated by atomic force microscopy. Images of a surface area measuring $5 \times 2.5\,\mu m^2$ for films with thicknesses of 5, 9 and 14 nm are shown in figure 4.5. For all three films the pictures give evidence that island growth of Volmer-Weber type is the predominant growth mode. The thinnest film of 5 nm thickness (figure 4.5a) consists of small irregular shaped islands with a typical diameter of 100 nm separated by valleys of similar size. With increasing film thickness the islands are enlarged. They merge and gradually fill the space between them. For the 14 nm film only very thin valleys of a few nm can be observed (figure 4.5c), and the morphology has transformed into elongated islands with a length of up to 2 μm and a width of around 200 nm. As it has already been evidenced by RHEED, the surfaces of the islands are very flat and smooth. Only the 14 nm film possesses some small areas, where the morphology is different. It is possible that here a phase with deviating stoichiometry has formed.

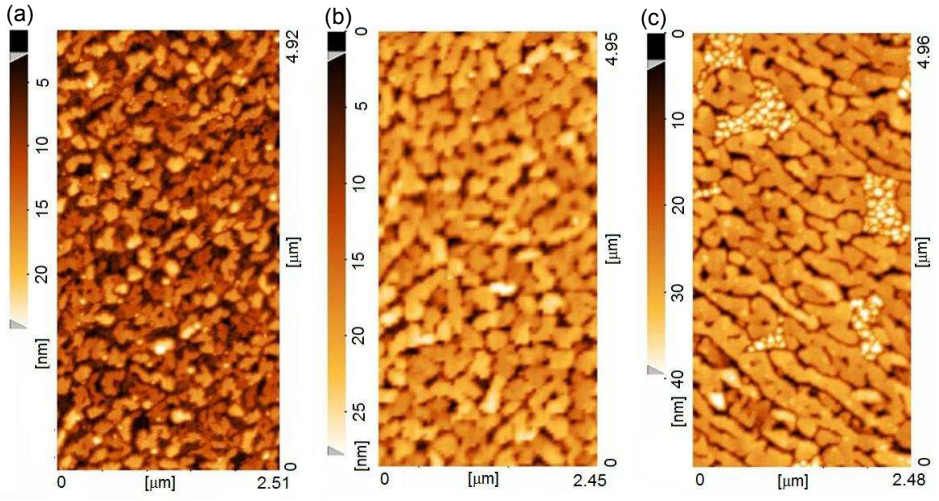

Figure 4.5: AFM images of MnGe films grown on Si(111) with a thickness of (a) 5 nm , (b) 9 nm, and (c) 14 nm .

4.5 XRD Measurements

X-ray diffraction measurements on a MnGe thin film were performed by Vadim A. Dyadkin at the Swiss-Norwegian Beamline BM1A of the ESRF in Grenoble. The PILATUS@SNBL diffractometer with synchrotron radiation with $\lambda = 0.6824\,\text{Å}$ was used to investigate the 135 nm film and reveal its crystal structure. The measurement shown in figure 4.6 confirms the B20

structure of the MnGe. In the diffraction pattern the (111) and (333) peaks of the Si substrate and the MnGe thin film are clearly resolved as single crystal peaks. In the inset of figure 4.6 an integrated intensity profile along the [111] direction is presented. From the position of the MnGe(111) peak the lattice parameter of the MnGe film can be calculated as (4.750 ± 0.004) Å. This value is 1% smaller than the lattice constant of bulk MnGe ($a_{MnGe} = 4.795$ Å [177]), which can be explained by the compressive strain imposed by the Si substrate.

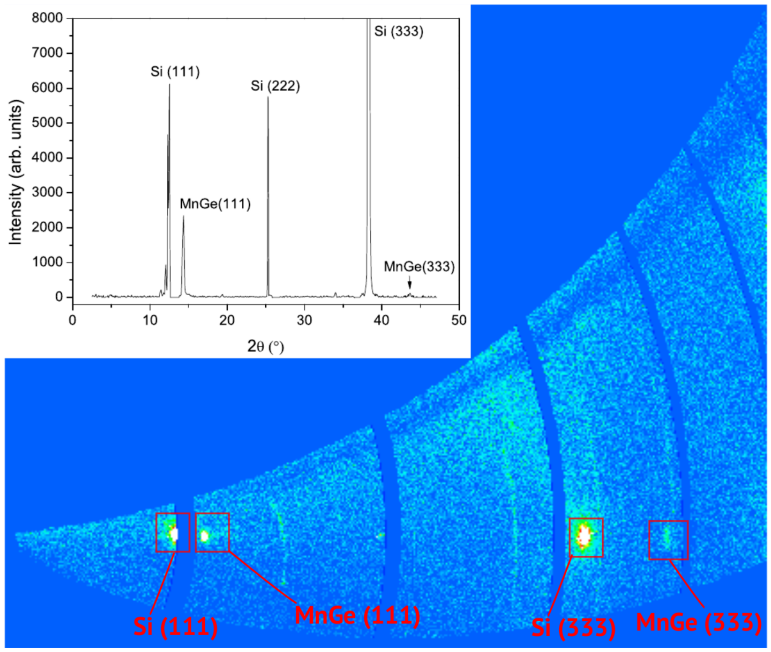

Figure 4.6: XRD measurement on a 14 nm sample MnGe. The plane of the picture is spanned by the [111] and [0$\bar{1}$1] crystal directions. Inset: Intensity plot along the [111] direction.

Taking together the results from XRD and RHEED investigations evidence has been given that the grown films consist of MnGe with B20 crystal structure, which is slightly compressed compared to bulk MnGe.

4.6 Magnetic Measurements

The next step in the analysis of MnGe thin films will involve measurements, which reveal their magnetic properties. It can be expected that they are modified with regard to the bulk compound. However, the high critical field value (12 T for bulk MnGe [14]) will cause difficulties, since magnetic fields of such strength cannot be reached with the available equipment.

The magnetic characterization of the MnGe films was carried out using

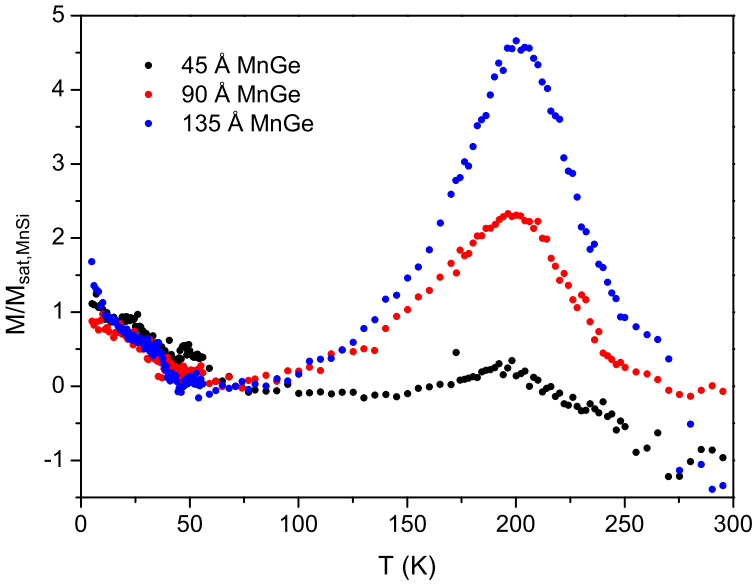

Figure 4.7: Temperature dependent magnetization of different MnGe films measured in a magnetic field of 10 mT. The data are normalized with respect to the saturation magnetization of the MnSi seedlayer.

a Quantum Design MPMS-5S SQUID magnetometer. For films of different thickness the temperature dependence of the magnetic susceptibility has been measured in applied magnetic fields of 10 mT. The data for the temperature range from 5 K to 300 K are depicted in figure 4.7. To explain the observed behavior it has to be considered that a thin layer of MnSi was used as a seedlayer for the growth of MnGe. Therefore the measured susceptibility is a combination of the properties of MnGe and MnSi.

Below approximately 40 K the susceptibility of all samples slightly increases due to the MnSi seedlayer, that orders magnetically in this temperature range. Since this layer has the same thickness for all three films, the measurements were normalized with respect to the saturation magnetization of the MnSi seedlayer. The susceptibility of MnGe films exhibits a broad peak at (200 ± 5) K, which occurs for all three samples. This points to an ordering temperature of $T_{ord} = (200 \pm 5)$ K. Regarding MnGe bulk material, the susceptibility shows a qualitatively similar behavior with $T_N \approx 170$ K [14], i. e. for thin films MnGe the ordering temperature is enhanced by (18 ± 3) % compared to bulk MnGe.

Also for MnSi thin films an enhancement of the ordering temperature is observed (compare section 3.4.2). However, amounting almost 50 % the enhancement was much larger for MnSi and it could be ascribed to the tensile strain imposed by the substrate (compare section 3.8.2). In contrast, in the case of MnGe a small compressive strain exists in the films. Nevertheless a similar mechanism may be responsible for the enhancement. As described by the Poisson's ratio a compression of the crystal structure in the film plane is accompanied by an enlargement of the lattice constant in out-of-plane direction. Probably this decompression effects the enhancement of T_{ord}.

In contrast to MnSi thin films, no thickness dependence of T_{ord} can be detected for MnGe films between 5 and 14 nm. Possibly, the spin-spin correlation length is shorter than the value for MnSi films (7 monolayers as determined in section 3.4.2). The thickness dependence may occur for MnGe, when the films are thinner than investigated in this work.

Field dependent magnetization measurements at $T = 200$ K were carried out on the same three MnGe films that were used for the susceptibility measurements. As shown in figure 4.8 the magnetization increases in fields up to 1 T for all samples. The inset of this figure shows a magnetization measurement on the 135 nm film in fields up to 5 T, which reveals that saturation is reached around 1 T. This is in agreement with measurements performed on bulk MnGe at temperatures close to T_{ord} [14]. Since the helix length is considerably shorter than the size of the MnGe islands, the magnetic behavior is not expected to be very different from bulk MnGe. In order to determine the critical field value, where ferromagnetic alignment of the spins is induced, a

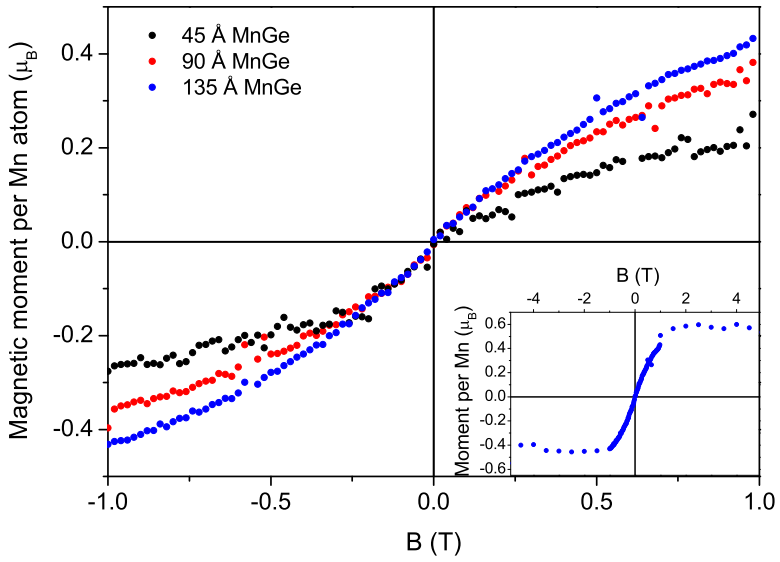

Figure 4.8: Magnetization curves measured at 200 K on thin MnGe films of different thickness. Inset: Magnetization at 200 K up to 5 T for the 14 nm film.

magnetization measurement at lowest temperatures and in magnetic fields up to around 15 T would be necessary. Unfortunately this was not possible with the available magnetometer.

The magnetic moment per Mn atom was calculated assuming that the complete amount of Mn deposited during growth has reacted to MnGe. This results in a saturated moment for the 14 nm film at 200 K and 5 T of only $0.5\,\mu_B$ per Mn atom. Compared to the bulk value measured under the same conditions (approximately $1.3\,\mu_B$ [14]) the magnetic moment of the thin film amounts less than half of this value. Obviously some part of the deposited Mn did not react to MnGe.

Furthermore, an apparently smaller magnetic moment can be observed for the thinner films. This can be explained by the assumption that especially in the beginning of MnGe growth not every Mn atom is incorporated into the MnGe crystal. Evidence for this is also given by magnetization measurements at 5 K, where mainly the ordering of the MnSi seedlayer is observed, since in the considered field range MnGe is far below its saturation field and, thus, only gives a small linear contribution, which can be subtracted. These measurements reveal a magnetic moment of the MnSi layer that is about twice as large as expected for 1 nm MnSi. From this it can be concluded that some part of the deposited Mn has reacted with Si from the substrate to form MnSi.

4.7 Resistivity and Magnetoresistivity

Resistivity and MR effect measurements were performed on a MnGe thin film in order to obtain information about the ordering temperature and about critical field values. These transitions should leave their marks in the measured curves, when the sample changes into a different magnetic state. Unfortunately, the influence of the Si substrate causes some difficulties in the temperature range above 100 K as discussed in the following.

Resistivity and magnetoresistance were measured on the 14 nm film using the van-der-Pauw method. As depicted in figure 4.9 the sample was found to be metallic, since the resistivity decreases at low temperatures. The residual resistivity at 0 K was determined as $\rho_0 = 83.5\ \mu\Omega$cm. At temperatures below 50 K the MnGe film exhibits Fermi liquid behavior characterized by a resistivity which follow the relation $\rho(T) = \rho_0 + AT^2$ with $A = 0.022\,\mu\Omega\text{cm/K}^2$. The A value is in the same order of magnitude as for the MnSi thin films (compare section 3.5.3).

Above approximately 100 K the measured resistivity curve deviates from the behavior that can be expected for MnGe. A maximum occurs around 200 K, which can only be explained by the influence of the Si substrate. Since the thin film is in direct contact with the substrate, the measured resistance is a parallel connection of the metallic MnGe and the semiconducting Si.

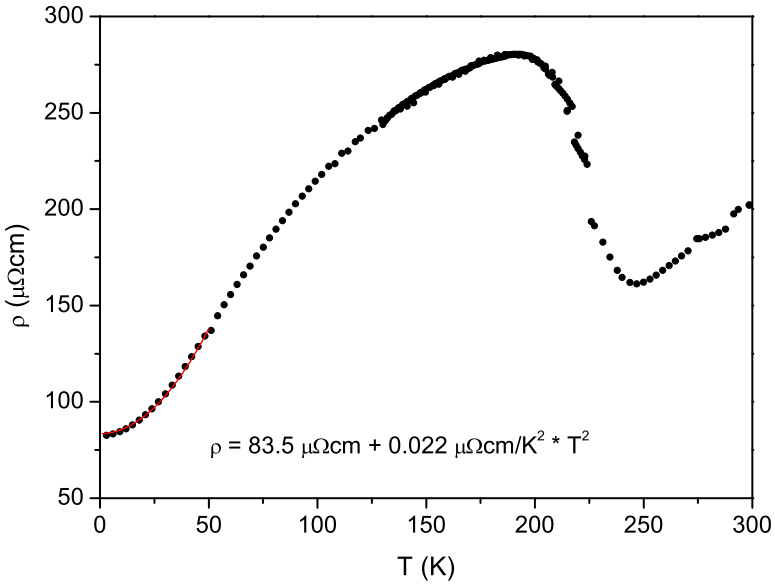

Figure 4.9: Temperature dependence of the resistivity of a 14 nm film MnGe grown on a Si substrate measured using the van-der-Pauw method.

With increasing temperature the resistance of the film increases, while that of the substrate decreases. Therefore it is possible to measure the resistivity of the film at temperatures below 100 K, but at higher temperatures the substrate conducts large parts of the current and masks the properties of the film. For this reason the ordering temperature of the film cannot be determined from resistivity measurements as it should occur around 200 K.

The field dependence of the resistivity was measured in magnetic fields up to 5 T for several temperatures. In figure 4.10 three curves are depicted, which represent the magnetoresistivity defined by $\mathrm{MR} = 100 \cdot [\rho(B) - \rho(0)]/\rho(0)$. The data were obtained at temperatures between 60 K and 100 K, where the thin film is in a magnetically ordered state. The MR effect is negative for all temperatures and fields and exhibits no remarkable features in the investigated field range. The largest effect is observed at 100 K, where MR amounts 3.5 % in a field of 5 T.

For comparison, the equivalent data for a 19 nm film MnSi are shown in the inset of figure 4.10. In the case of MnSi the critical magnetic field B_{c2} occurs around 1 T. At this field value a clear kink accompanied by a change in curvature is observed in the MR effect. Furthermore the size of the magnetoresistivity is considerably larger for MnSi films. Regarding MnGe thin films it can be concluded from the absence of magnetic phase transitions in moderate magnetic fields and from the smallness of the magnetoresistivity

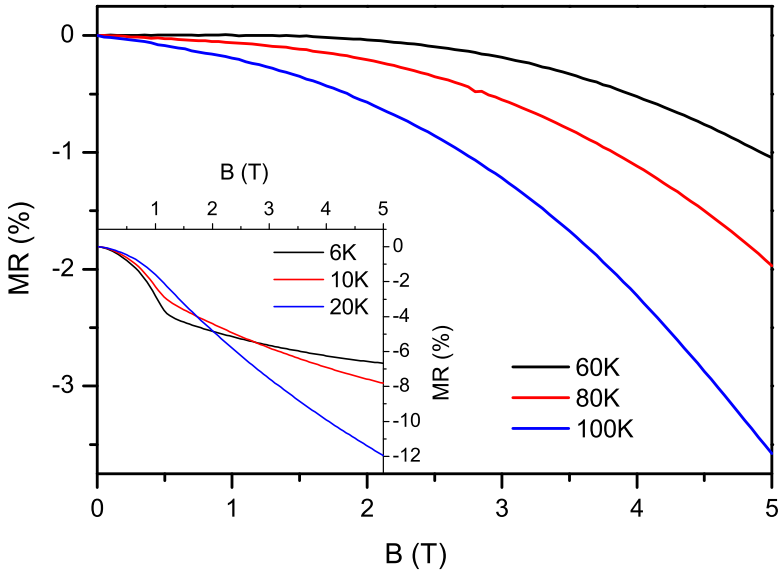

Figure 4.10: Magnetoresistivity of a 14 nm MnGe film measured at different temperatures. Inset: Comparison with equivalent measurements on a 19 nm MnSi film.

that the helical structure is more rigid than in MnSi. As discussed in the following paragraph this can be ascribed to a stronger Dzyaloshinskii-Moriya interaction.

4.8 Discussion

In order to explain the differences in the magnetic behavior of MnGe and MnSi the main magnetic interactions must be regarded, which define the properties of the helical structure. Most important are the ferromagnetic exchange represented by the exchange stiffness A and the Dzyaloshinskii-Moriya interaction expressed by the constant D. These two parameters determine the length of the helix as well as the critical field B_{c2}.

The exchange stiffness can be calculated from the value of B_{c2} using the equation [183]

$$g\mu_B B_{c2} \approx Ak^2, \tag{4.1}$$

where g is the Landé factor and k is the helix wave vector. With $B_{c2} = 0.6\,\mathrm{T}$ and a helix length of 18 nm A_{MnSi} can be estimated to amount approximately $0.50\,\mathrm{meV\,nm^2}$ for bulk MnSi [183]. The relation $k = D/A$ further reveals the Dzyaloshinskii constant $D_{MnSi} \approx 0.18\,\mathrm{meV\,nm}$. For MnSi thin films the constants $A_{MnSi,film} = 0.45\,\mathrm{meV\,nm^2}$ and $D_{MnSi,film} = 0.203\,\mathrm{meV\,nm}$ have been published by Karhu *et al.* [44], which deviate only slightly from the bulk values.

For the MnGe thin films it was not possible to determine B_{c2} and k, but regarding the case of MnSi it can be assumed that the size of the magnetic interactions in MnGe thin films will be similar to the bulk values. In bulk MnGe the critical field B_{c2} occurs at 12 T and the length of the helix is 3 nm [14], which leads to $A_{MnGe} \approx 0.3\,\mathrm{meV\,nm^2}$ and $D_{MnGe} \approx 0.7\,\mathrm{meV\,nm}$.

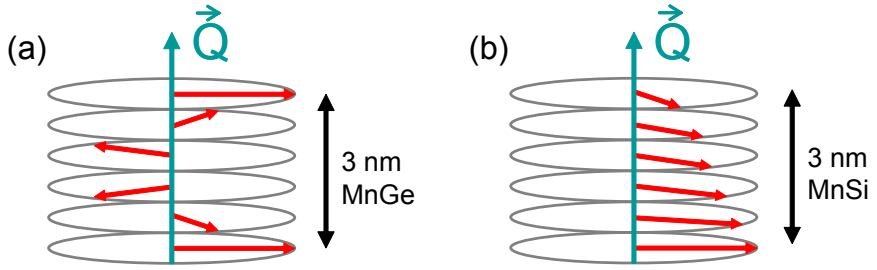

Figure 4.11: Comparison of the helical modulations in MnGe and MnSi. (a) Considering a piece of MnGe with a length of 3 nm the helix completes a full period. (b) In MnSi only a small fraction of the helix fits into the same length.

The different properties of the helical structure of MnGe and MnSi can be explained by the relative strength of the Dzyaloshinskii-Moriya interaction

with respect to the ferromagnetic exchange. The ratio A/D constitutes the helix length, which is very short in MnGe, because D is large compared to MnSi. Thus, along the helix propagation direction neighbored spins are strongly tilted with respect to each other (compare figure 4.11a) and the local magnetic structure is more related to antiferromagnetism, which is observed by the peak in the susceptibility. Furthermore the short helix length implicates a high value of B_{c2} (equation 4.1 reveals $B_{c2} \propto k^2 \propto 1/\lambda^2$), which means that the helix cannot easily be deformed by a magnetic field, i. e. the helix is very rigid.

In contrast, the modulation length of the helix in MnSi is very long and the critical field, where ferromagnetic alignment occurs, is small. It can be seen in the susceptibility measurements that a small magnetic field easily deforms the soft helix and induces a net magnetization. The magnetic behavior is reminiscent of a ferromagnet, since neighbored spins are canted only by a small angle (compare figure 4.11b).

Chapter 5

$Mn_{1-x}Fe_xSi$ Thin Films

In section 3.8 the suppression of magnetic order by applied hydrostatic pressure was investigated for MnSi thin film. In this chapter, MnSi films will be doped with a few percent of Fe in order to induce a similar effect.

In a recent paper it was shown that $Mn_{1-x}Fe_xSi$ films prepared by an annealing method possess an enlarged skyrmion phase, which was identified by a topological Hall contribution [184]. A decrease of T_{ord} was also observed, but the critical concentration was not yet reached. This work aims to suppress magnetic order completely by preparing $Mn_{1-x}Fe_xSi$ thin films by codeposition of the three constituents.

5.1 Properties of Bulk $Mn_{1-x}Fe_xSi$

The magnetic properties of the iron doped system $Mn_{1-x}Fe_xSi$ were first investigated in the 1980s by means of magnetization measurements and Mössbauer spectroscopy [30]. The data for bulk samples with Fe content between $x = 0.005$ and $x = 0.4$ revealed that magnetic order is suppressed by doping and disappears for $x > 0.15$. A comparison with the relative compound $Mn_{1-x}Co_xSi$ indicates that the driving force for the suppression of magnetism is the increased number of d electrons, which affects the density of states at the Fermi level [30, 31].

Although the ordering temperature decreases with increasing Fe percentage, the overall appearance of the magnetic phase diagram is unchanged (compare figures 5.1a and 5.1b). The magnetic ground state is a spin helix with a length that is reduced with increasing x. While the helix wavelength λ amounts 18 nm for pure MnSi, the compound, where 10 % of the Mn atoms are substituted by Fe, is characterized by $\lambda \approx 10\,\mathrm{nm}$ [19]. The critical field $B_{c1} = 0.1\,\mathrm{T}$, where the helix is reoriented into field direction, and the field of ferromagnetic alignment $B_{c2} = 0.6\,\mathrm{T}$ are essentially unaffected in the doped compounds. Also the A-phase occurring close to T_{ord} can be found for all Fe-doped samples which show magnetic order [19, 31].

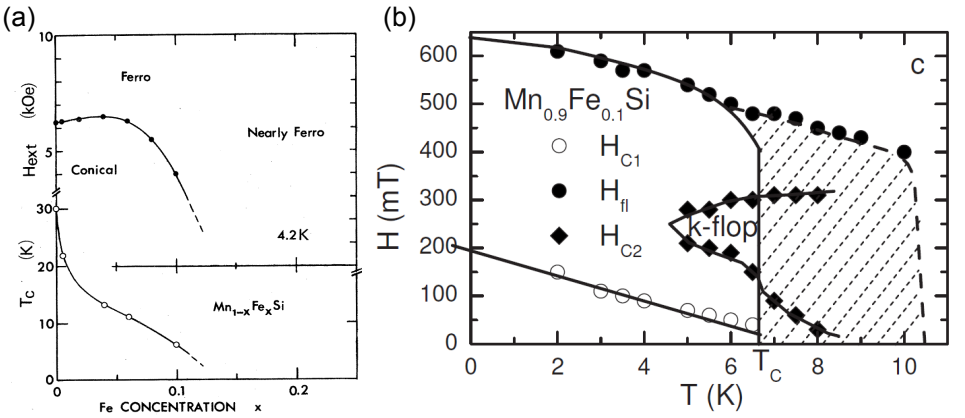

Figure 5.1: (a) Dependence of the ordering temperature and the critical field B_{c2} on Fe doping, taken from [30], (b) magnetic phase diagram for a $Mn_{0.9}Fe_{0.1}Si$ sample, taken from [19].

Magnetization measurements on $Mn_{1-x}Fe_xSi$ reveal that the saturated magnetic moment per Mn site is reduced from the MnSi value of $0.4\,\mu_B$ to $0.2\,\mu_B$ for $x = 0.19$ [31] (compare figure 5.2a). As shown in figure 5.2b the resistivity of $Mn_{1-x}Fe_xSi$ exhibits a kink at T_{ord}, which is shifted towards lower temperatures with increasing x and disappears for $x = 0.15$ [185]. Furthermore the residual resistivity is strongly enhanced for samples with Fe doping.

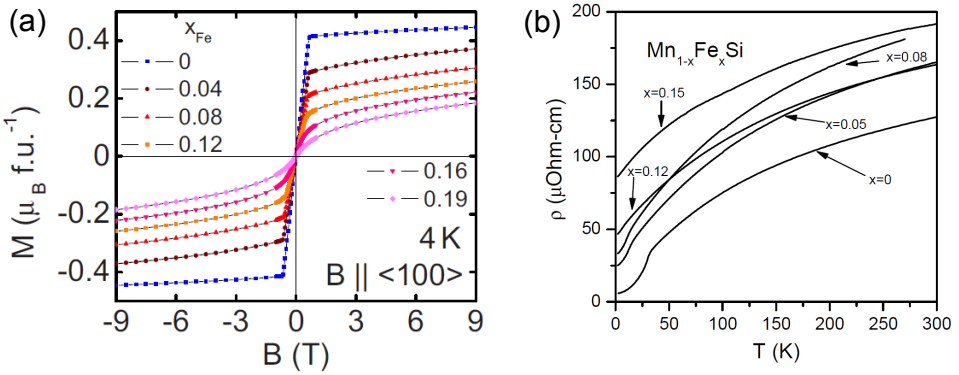

Figure 5.2: (a) Magnetization measurements on $Mn_{1-x}Fe_xSi$ with x between zero and 0.19, taken from [31], (b) resistivity measurement on various $Mn_{1-x}Fe_xSi$ samples, taken from [185]

As an example the phase diagram of $Mn_{0.9}Fe_{0.1}Si$ is shown in figure 5.1b. The compound exhibits a relatively large phase occurring above T_{ord}, where the magnetic structure is fluctuating. Polarized small angle neutron scattering images show a half-moon picture closely above T_{ord}, that can be

interpreted as caused by fluctuating helices with random orientations [19]. This phase is also observed in pure MnSi [186], but upon Fe doping it is much more extended compared to the size of the ordered phase.

Apart from the A-phase the most interesting feature of $Mn_{1-x}Fe_xSi$ is the quantum critical behavior close to the point, where T_{ord} is forced to zero. Recent studies [31, 187] revealed that more than one critical concentration exist. Three transition temperatures $T_1 < T_c < T_2$ can be distinguished, which tend to zero at the corresponding critical concentrations $x_1 = 0.15$, $x_c = 0.19$ and $x_2 \approx 0.23$. At x_1 a quantum phase transition characterized by the suppression of helimagnetic order occurs, which is observed for example in susceptibility measurements. Above x_1 the $Mn_{1-x}Fe_xSi$ compounds pass through a short-range ordered regime, which is suppressed at x_2. The saturated moment in the ferromagnetic regime is forced to zero at the critical concentration x_c, which is located between x_1 and x_2. There are strong indications that a quantum critical point exists at x_c, since the corresponding phase transition at T_c stays second order for all samples.

5.2 Preparation of $Mn_{1-x}Fe_xSi$ Thin Films

After some practical experience had been made with the preparation of MnSi thin films the growth of $Mn_{1-x}Fe_xSi$ on silicon could quite easily be performed under very similar conditions. Si(111) substrates were used as before and were prepared for deposition by heating them to 1100°C. When a 7×7-reconstruction was observed, manganese, iron and silicon were evaporated simultaneously. Thereby Mn was provided with a rate of 0.075 Å/s from an effusion cell and Si was evaporated by an electron beam evaporator with a rate of approximately 0.15 Å/s. For the Fe supply the mini electron beam evaporator described in section 2.5.3 was used, which provided very low rates in the order of 0.01 Å/s. During growth the Si substrate was held at a temperature of 280°C. Samples with different Fe content were obtained by the variation of the Fe flux only. With this procedure a series of $Mn_{1-x}Fe_xSi$ films with x between zero and 0.17 ± 0.04 was prepared. The thickness of all films was 9 nm. A second series of films was annealed for 30 minutes at 330°C after deposition. During the preparation of some of these samples the Si supply was insufficient due to a non-constant Si rate and partly Fe-doped Mn_5Si_3 had formed, which could be transformed into the desired $Mn_{1-x}Fe_xSi$ by heating. In the following analysis and discussion the two types of films will be considered separately and their properties will be compared.

The iron concentration x was calculated from the Fe rate, which had been provided by the mini e-beam evaporator during growth. From the Mn rate and the Fe rate the total number of Mn and Fe atoms deposited on the substrate per second could be inferred. Due to the estimated uncertainties of 0.0005 Å/s for the Fe rate and 0.003 Å/s for the Mn-rate the uncertainty

in the Fe content x is around 0.05. Furthermore, possibly some Fe atoms have not been incorporated into the film, and Fe might be inhomogeneously distributed over the film. It should also be mentioned that after preparation of the first series of films, the Fe rod in the mini electron beam evaporator was changed. For the first series Fe was evaporated from a rod with a diameter of 2 mm, and for the second series a 6 mm rod was used.

5.3 Structure and Morphology

For all $Mn_{1-x}Fe_xSi$ films the crystal structure and the orientation on the Si(111) surface is identical to pure MnSi, which is verified by the occurrence of the same RHEED patterns as shown in chapter 3. In figure 5.3 a comparison between the RHEED patterns of a codeposited and an additionally annealed $Mn_{1-x}Fe_xSi$ thin film is shown, which reveals no remarkable differences between the two preparation techniques. Smooth streaks with low background noise give evidence for a flat two-dimensional surface on length scales in the order of 100 nm corresponding to the RHEED correlation length.

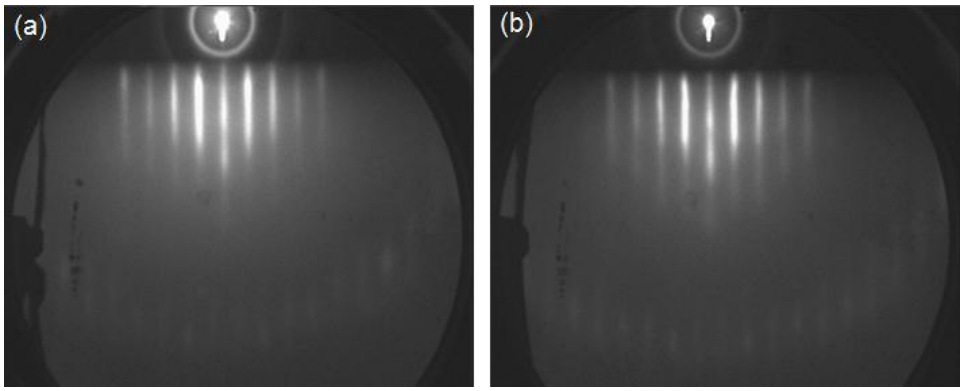

Figure 5.3: Comparison of RHEED patterns of two 9 nm $Mn_{1-x}Fe_xSi$ films with $x = 0.15 \pm 0.05$, (a) a codeposited film and (b) a codeposited film, which has been annealed afterwards.

An AFM investigation of the two types of films, however, detects considerable differences of the film morphology. The codeposited films exhibit a very flat surface with an average rms roughness of 1.5 nm. The surfaces of most of the codeposited films were speckled with ring-shaped structures (compare figure 5.4a). The diameter of the ring varies between 700 nm and 3 μm, while the center spot has approximately the same size for all films ($\approx$ 500 nm). An energy-dispersive x-ray (EDX) investigation gave evidence that the observed structures contain a high concentration of carbon, as it can be seen in the spectra shown in figure 5.5. Most probably this contamination is introduced by the Fe source, since it was not observed in the case of pure

MnSi thin films.

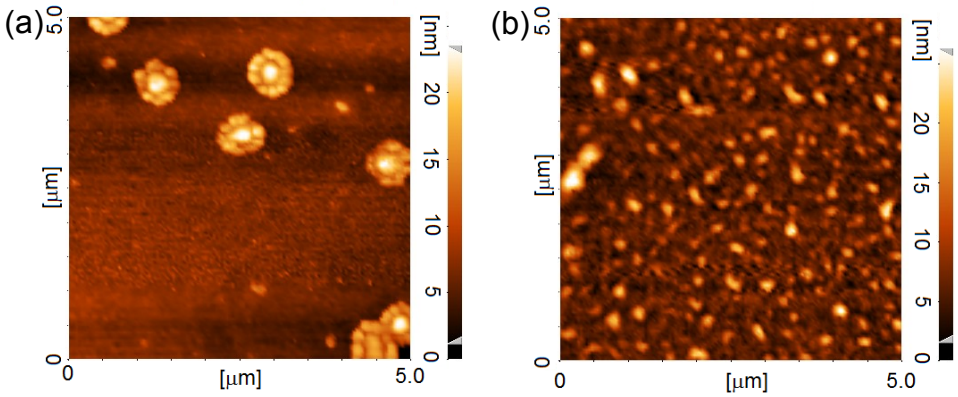

Figure 5.4: AFM images of a codeposited $Mn_{1-x}Fe_xSi$ films with (a) $x = 0.01 \pm 0.06$ and (b) $x < 0.01 \pm 0.06$

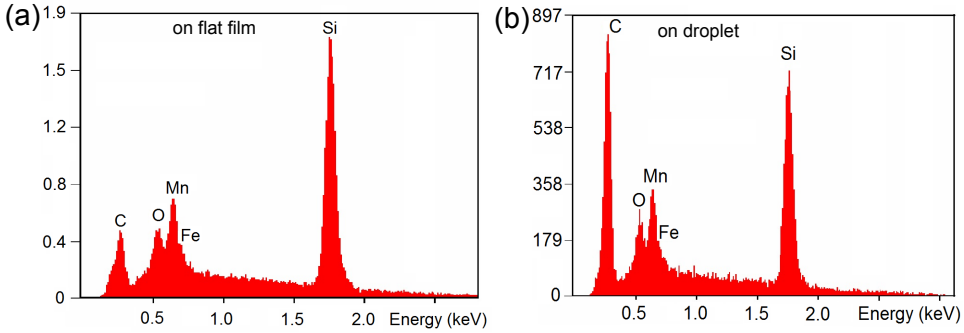

Figure 5.5: EDX spectra of a codeposited $Mn_{1-x}Fe_xSi$ film with $x = 0.04 \pm 0.05$ taken (a) on the flat film surface and (b) on a droplet.

Only for the codeposited film with the smallest Fe doping of $x = 0.00 \pm 0.06$ no droplets have been observed. Instead, islands have formed and accordingly the surface roughness is considerably higher compared to the other films (rms roughness $\approx 3.5\,\text{nm}$, compare figure 5.4b). Samples with such low Fe content must be grown with substrate temperatures lower than 280°C. As discussed in section 3.2.2 also pure MnSi thin films favor island growth, when they are deposited at temperatures higher than 250°C.

The films, which were annealed after codeposition, do not possess droplets on the film surface, either. However, it must be expected, that the morphology had been similar to the first series of films, before the samples were annealed. Thus, there are two possibilities: either the droplets were incorporated into the film or they were vaporized during annealing, so contamination with carbon cannot be excluded.

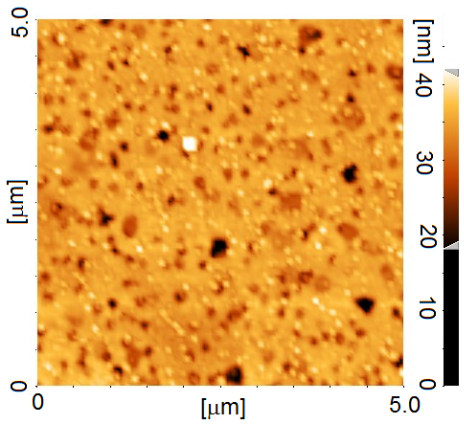

Figure 5.6: AFM image of an annealed film with $x = 0.06 \pm 0.05$.

The surface of the annealed film is not as flat as for the first series of codeposited films. The rms roughness amounts 2.5 nm, which is owing to holes in the film (compare figure 5.4b). From these holes Si is provided by the substrate to react with some excess amount of Mn. The morphology is therefore the same as known from the MnSi thin films prepared by annealing.

5.4 Magnetic Characterization

5.4.1 Susceptibility

The temperature dependence of the susceptibility of $Mn_{1-x}Fe_xSi$ thin films was measured in a SQUID magnetometer with an applied magnetic field of 10 mT. As shown in figures 5.7 and 5.9 for the codeposited and the annealed films, respectively, a distinct influence of the Fe-doping can be observed for both series of films. With increasing iron concentration T_{ord} and the size of the magnetic moment at low temperatures decrease, which is very similar to the behavior of bulk $Mn_{1-x}Fe_xSi$ [31]. However, taking a closer look at the measurements on the two different series of films some pronounced differences can be detected.

Among the codeposited films the sample with the smallest amount of Fe doping exhibits a considerably larger magnetic moment than the other films. Its value is approximately of the same size as for MnSi films without Fe doping, while the samples with larger x show a magnetic moment, which is more than ten times smaller. Therefore, the question arises whether any Fe atoms have been incorporated in this sample with $x < 0.01 \pm 0.06$ at all. Comparing the temperature dependence of the magnetic moment with the equivalent measurement performed on a pure MnSi thin film reveals that the shapes of these two curves are different. To illustrate this the square of the magnetic moment was plotted as a function of the square of the

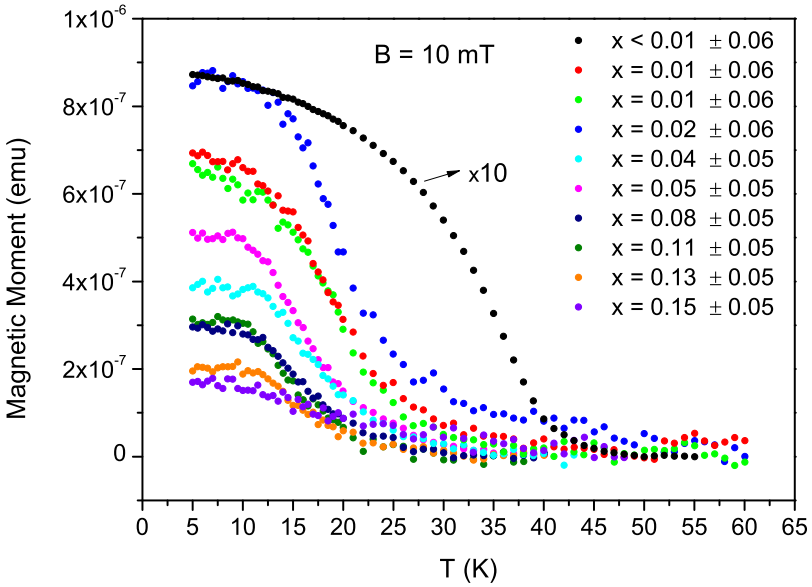

Figure 5.7: Susceptibility measurements on codeposited $Mn_{1-x}Fe_xSi$ thin films. The curve for the sample with $x < 0.01 \pm 0.06$ has been divided by 10 to fit into the diagram.

temperature for the two films (compare figure 5.8). Evidently $m^2 = m_0^2(1 - T^2/T_{ord}^2)$ as characteristic of itinerant ferromagnets holds for $Mn_{1-x}Fe_xSi$, where m is the field induced magnetic moment and m_0 is its value at 0 K, respectively. However, considerable deviations from this behavior can be observed for MnSi. The same situation has been reported for the saturation magnetization of bulk samples of the two compounds [31]. Therefore it can be concluded that the thin film with $x < 0.01 \pm 0.06$ contains a small amount of Fe.

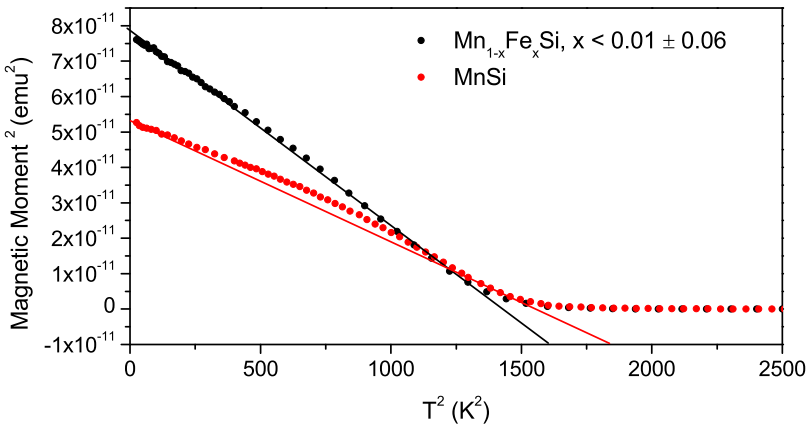

Figure 5.8: The square of the magnetic moment plotted versus the square of the temperature for a Fe-doped sample and a pure MnSi film.

All further codeposited films seem to contain a much larger Fe percentage, as their transition temperatures are considerably reduced and the observed magnetic moments are very small. It is remarkable that despite of the varying nominal Fe content all films have a similar T_{ord} in the range from 15 K to 22 K, which can be made out by a steep increase of the magnetization. The values of T_{ord} have been determined by a fit using equation 3.6. Although it has been shown in figure 5.8 that the shape of the susceptibility curve is well described by $m^2 = m_0^2(1 - T^2/T_{ord}^2)$ for the film with $x < 0.01 \pm 0.06$, the same model as used for MnSi thin film has been applied for the fit. A fit according to this model reproduces the susceptibility curves of $Mn_{1-x}Fe_xSi$ thin films quite well and, thus, assures the comparability with MnSi. The ordering temperatures are presented in figure 5.16 and will be further discussed in section 5.6. Only for the sample with $x = 0.15 \pm 0.05$ no transition to magnetic order can be observed, since it has been completely suppressed.

The $Mn_{1-x}Fe_xSi$ thin films, which have been annealed after deposition, cover a wider range of transition temperatures. As depicted in figure 5.9

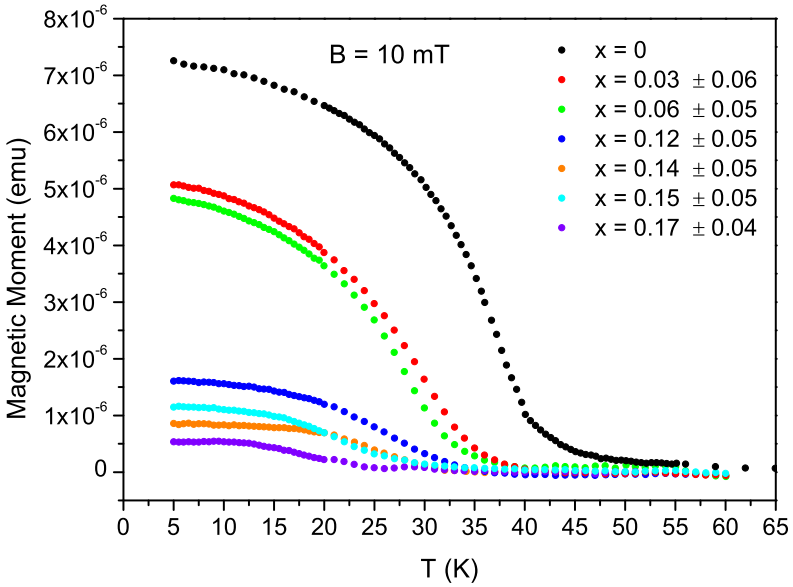

Figure 5.9: Susceptibility of a series of $Mn_{1-x}Fe_xSi$ films that were subsequently annealed. A measurement on a 9 nm film of pure MnSi is shown for comparison.

a continuous suppression of T_{ord} from approximately 40 K to 20 K and a smooth decrease of the magnetic moment can be observed. However, although the nominal Fe concentration in the most heavily doped film is larger than the concentration range covered by the first series of films, no complete suppression of magnetic order occurs.

5.4.2 Field Dependence of the Magnetization

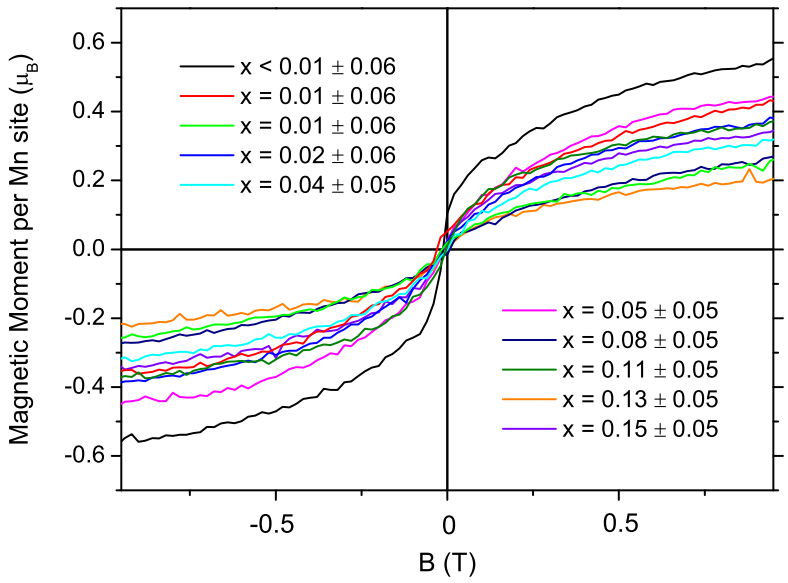

Figure 5.10: Magnetic field dependence of the magnetization measured on codeposited $Mn_{1-x}Fe_xSi$ thin films at a temperature of 5 K.

In figure 5.10 the field dependence of the magnetic moment per Mn site for the codeposited $Mn_{1-x}Fe_xSi$ films as measured at 5 K in a SQUID magnetometer is shown. The measurements reveal that the saturation magnetization covers a wide range of values between $0.2\,\mu_B$ and $0.55\,\mu_B$ per Mn site for films with x between zero and 0.15 ± 0.05. The occurrence of magnetic moments larger than the bulk value of $0.4\,\mu_B$ is unexpected and can most probably be explained by uncertainties of the film thickness, which lead to an underestimation of the number of Mn sites contained in the film. The saturation magnetic moments for the films with different Fe concentration are summarized as black symbols in figure 5.12. A trend towards smaller magnetic moments for films with a higher Fe doping can be observed, which is indicated by the dashed line. However, considering the uncertainties in both directions only seven of the ten samples agree with this trend, while the

others deviate clearly. These deviations are remarkable, since the susceptibility curves do not show such in a wide variance in the magnetic properties of the codeposited films. Obviously the films are characterized by large inhomogeneities, as will be discussed in section 5.6.

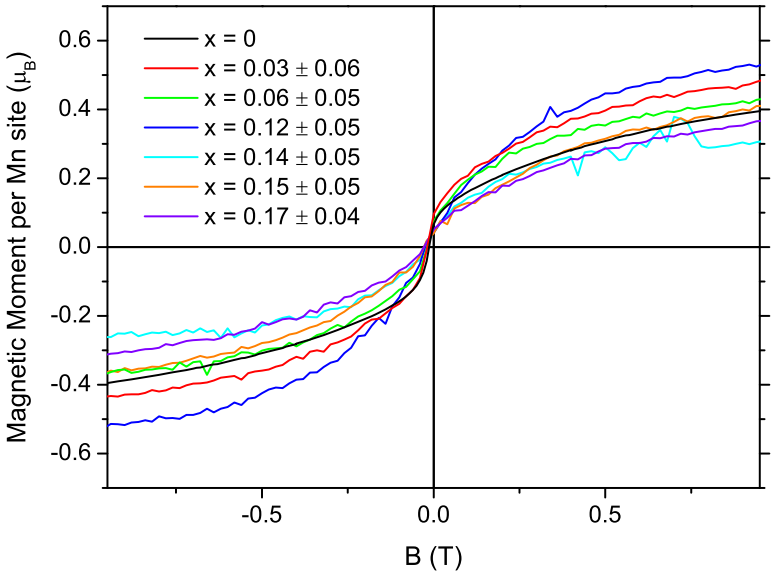

Figure 5.11: Magnetic field dependence of the magnetic moment measured on codeposited and annealed $Mn_{1-x}Fe_xSi$ thin films at a temperature of 5 K. For comparison the curve of a pure MnSi thin film has been added.

For the annealed $Mn_{1-x}Fe_xSi$ thin films the magnetization curves measured in fields of up to 1 T are shown in figure 5.11. Despite of the large range of Fe doping the saturated magnetic moments cover a smaller range of values than for the codeposited films. The magnetic moments per Mn site are included as red symbols in figure 5.12 for all annealed films. In this case no dependence of the saturation moments on the Fe doping is evident, which is in contrast to the behavior of bulk $Mn_{1-x}Fe_xSi$ [31]. Probably the actual range of x is smaller than assumed, which can be attributed to the large uncertainties occurring in the calculation of the Fe concentrations.

5.5 Resistivity Measurements

The temperature dependence of the resistivity has been measured for a number of $Mn_{1-x}Fe_xSi$ thin films using the van-der-Pauw method. For the codeposited films the measurements on five different samples are shown in figure

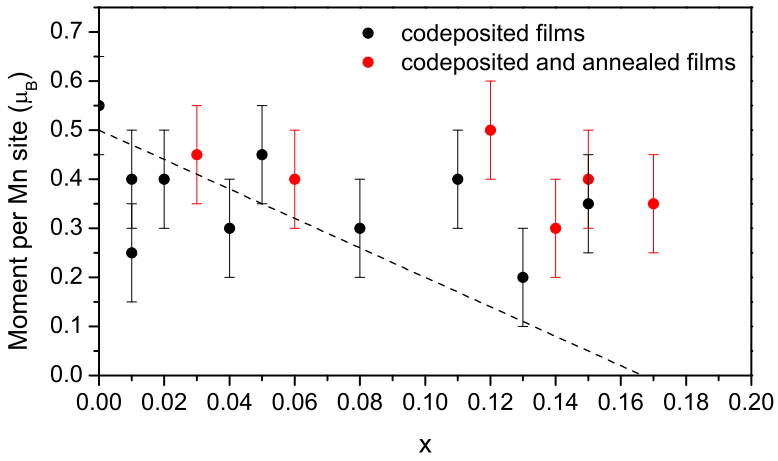

Figure 5.12: Saturation magnetic moment per Mn site plotted versus Fe concentration. Black and red symbols represent the codeposited films and the annealed films, respectively. Error bars in x-direction have been omitted to maintain a clear arrangement of the data. The dashed line indicates a trend of decreasing moments observed for the codeposited films.

5.13. One peculiarity of these curves is the large range of values covered by the residual resistivity. While the film with the lowest Fe content possesses a residual resistivity, which is similar to the MnSi thin films, the resistivity increases with Fe doping and reaches a value, which for the sample with $x = 0.15 \pm 0.05$ is around 10 times larger than for MnSi.[1] The strong increase of the residual resistivity with increasing x is an intrinsic property of $Mn_{1-x}Fe_xSi$, which has also been observed in measurements on single crystals [185].

All $Mn_{1-x}Fe_xSi$ films exhibit a metallic behavior, as the resistivity increases with increasing temperature. The codeposited samples with low Fe doping possess a pronounced kink signalizing the transition to magnetic order. With increasing x the kink is shifted from 46 K to lower temperatures and becomes broader. Finally it disappears for $x = 0.15 \pm 0.05$. Analogous to the resistivity measurements on MnSi thin films, T_{ord} was determined from the minimum in the second temperature derivative of ρ. The values are included in figure 5.16.

For the $Mn_{1-x}Fe_xSi$ film with $x = 0.15 \pm 0.05$ magnetic order is suppressed. Taking a closer look at the corresponding resistivity measurement it reveals a minimum, which is shown in detail in figure 5.14.

A minimum of this kind is described by the Kondo theory introduced by

[1] The film with $x = 0.13 \pm 0.05$ possesses a considerably higher resistivity, which is obviously due to large inhomogeneities, as will be discussed later in this section

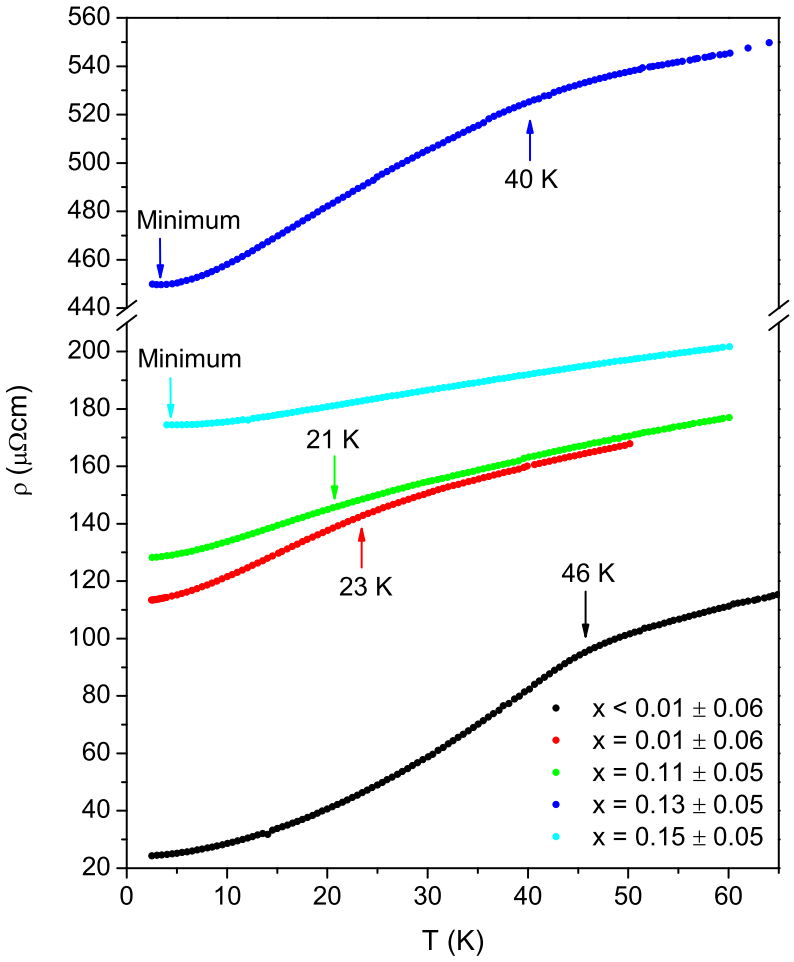

Figure 5.13: Resistivity measurements on codeposited $Mn_{1-x}Fe_xSi$ films.

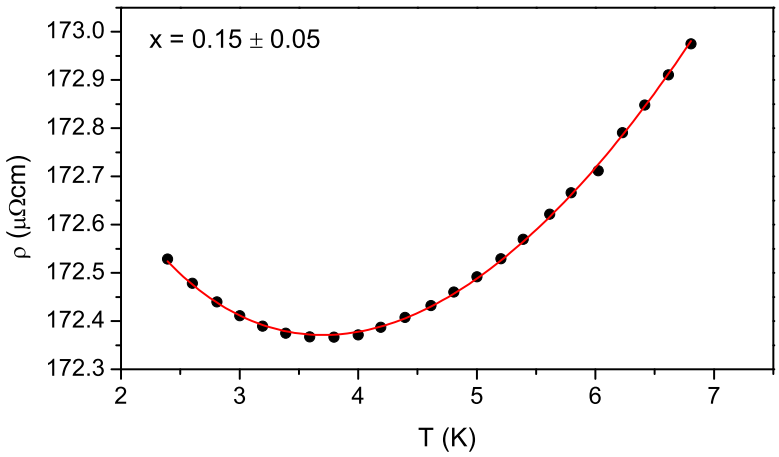

Figure 5.14: Fit of the resistance Minimum applying the Kondo formula with the following parameters: $\rho_0 = 172\,\mu\Omega\text{cm}$, $a = 0.038\,\mu\Omega\text{cm/K}^2$, $\rho_K = 1.05\,\mu\Omega\text{cm}$, $T_0 = 3.20\,\text{K}$.

Jun Kondo in 1964 [188]. The minimum occurs in non-magnetic alloys with impurities, which possess local magnetic moments. While theses impurities are not correlated with each other, the conduction electrons interact with their magnetic moments by s-d interaction and form a cloud of electrons around the impurity, where the spins of these electrons are antiparallel to the local moment. Since the cloud of conduction electrons screening the impurity spin grows larger with decreasing temperature, the scattering cross section of the impurity is strongly enhanced, which causes an increase of the resistivity proportional to $\ln T$.

The phenomenological expression for the temperature dependence of the resistivity is

$$\rho(T) = \rho_0 + aT^2 + \rho_K \ln\left(\frac{T}{T_0}\right), \tag{5.1}$$

where ρ_0 is the residual resistivity due to non-magnetic impurities, the second term describes the electron-electron scattering and the last term is the Kondo contribution. As shown in figure 5.14 the resistivity minimum observed for the $Mn_{1-x}Fe_xSi$ film with $x = 0.15 \pm 0.05$ can be fitted convincingly with equation 5.1.

The presence of a Kondo effect suggests that Fe atoms occupy different sites in the $Mn_{1-x}Fe_xSi$ thin film. Most of the Fe atoms are located on the Mn sites, where they affect the suppression of the magnetic order. However, for $x = 0.15 \pm 0.05$ there are too many Fe atoms to consider them as uncorrelated, which is a requirement for the Kondo mechanism. Thus, there

must be some Fe atoms occupying Si sites or interstitial sites, which must be regarded irrespective of the Fe atoms on Mn sites. These atoms might act as magnetic impurities evoking the Kondo effect.

A Kondo minimum signalizing the absence of magnetic order also occurs in the resistivity measurement on the sample with $x = 0.13 \pm 0.05$. In this case, however, an additional kink can be observed at around 40 K, while the transition temperature derived from the susceptibility curve is $T_{ord} = (17 \pm 2)$ K. This contradictory information about the magnetism in this sample suggests that the film is very inhomogeneous. Obviously there are regions with strongly varying Fe content, so that magnetic order with different transition temperatures is present in some areas, while others are non-magnetic.

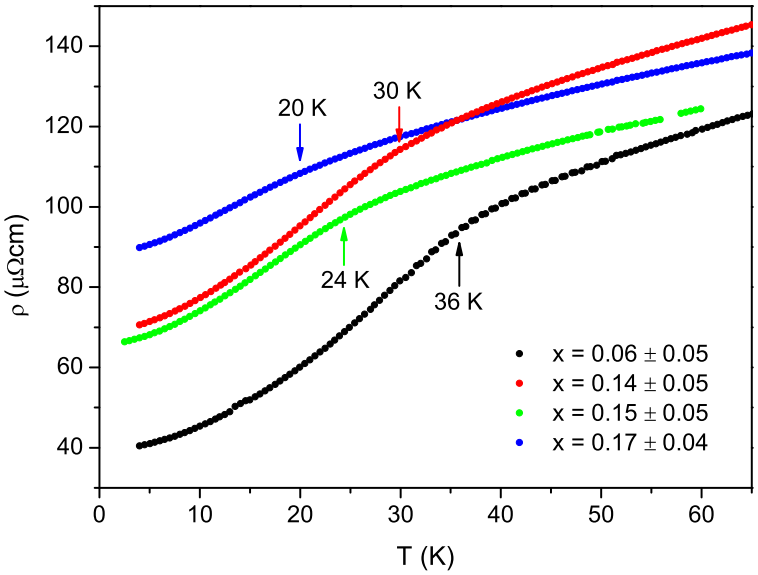

Figure 5.15: Resistivity measurements on annealed $Mn_{1-x}Fe_xSi$ films.

Regarding the annealed $Mn_{1-x}Fe_xSi$ thin films a transition to magnetic order can be observed for all samples investigated by resistivity measurements (compare figure 5.15). The values for T_{ord} are included in figure 5.16 and will be discussed in the following section.

5.6 Discussion

The most important property characterizing a $Mn_{1-x}Fe_xSi$ thin film is its magnetic ordering temperature, as it reveals to what extent the magnetism is

suppressed by the Fe doping. The values of T_{ord} obtained from susceptibility and resistivity measurements are summarized in figure 5.16a and 5.16b for the codeposited and the annealed films, respectively.

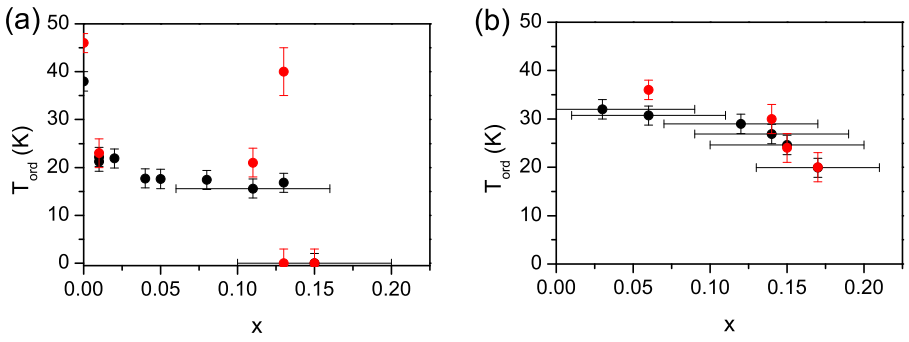

Figure 5.16: Dependence of T_{ord} on the Fe concentration for (a) codeposited films and (b) subsequently annealed films. Black symbols represent T_{ord} as determined from susceptibility and red symbols reflect the resistivity measurements. The error bars in x-direction have partly been omitted in order to maintain a clear arrangement of the data.

It has already been mentioned that most of the codeposited films exhibit very similar ordering temperatures in a range between 15 K and 22 K. This is remarkable, since nominally the films cover the complete range between the two films with $x < 0.01 \pm 0.06$ and $x = 0.15 \pm 0.05$, where $T_{ord} \approx 40$ K and complete suppression of magnetic order has been observed, respectively. However, within the error bars in x it is possible, that all these films exhibit the same Fe content $x \approx 0.08$, which would explain the nearly identical magnetic ordering temperatures. In this scenario it seems unlikely to assume that the Fe and Mn rates during deposition have accidentally adopted the same ratio for every film, although they were set to different values. It is more probable that, indeed, varying Fe rates have been provided, but for some reason the growth of $Mn_{1-x}Fe_xSi$ films with $x \approx 0.08$ is preferred. Possibly a fraction of the deposited Fe atoms re-evaporates, when the Fe rate is higher than required for the growth of $Mn_{1-x}Fe_xSi$ with $x \approx 0.08$. Another possibility is that the excess Fe atoms form a $Mn_{1-x}Fe_xSi$ compound, in which magnetism is suppressed completely, so that it cannot be identified in the susceptibility curve. This assumption is supported by the small magnetic moments observed in the susceptibility. Obviously only a fraction of the film orders magnetically.

However, despite of the large uncertainties of the Fe percentage in the codeposited films one main result is indisputable: A Fe concentration of $x_c = 0.15 \pm 0.05$ is sufficient to suppress magnetic order in $Mn_{1-x}Fe_xSi$ thin films. This value is in the same range as the critical concentration in bulk

$Mn_{1-x}Fe_xSi$ [30, 31]. Obviously the critical behavior of $Mn_{1-x}Fe_xSi$ is not strongly affected by the anisotropies and finite size effects present in thin films.

For the $Mn_{1-x}Fe_xSi$ films, which were annealed after deposition, T_{ord} was varies between 36 K and 20 K for x between 0.03 ± 0.06 and 0.17 ± 0.04. Regarding the susceptibility curves larger magnetic moments have been measured than for the codeposited films with similar Fe doping. Furthermore it can be seen in figure 5.16b that the decrease of T_{ord} proceeds continuously, which is in contrast to the step-like decrease observed for the codeposited films.

Obviously the annealed $Mn_{1-x}Fe_xSi$ films are more homogeneous than the codeposited samples. The annealing seems to generate a uniform distribution of Fe in the film, since there are no signs of a coexistence of magnetic and non-magnetic $Mn_{1-x}Fe_xSi$ compounds. However, the calculated values for x must be put into question. Generally the ordering temperatures of the annealed films are higher than observed for codeposited films with similar nominal doping, which suggests a smaller actual Fe doping. There are two possibilities to explain this: On the one hand the Fe doping may have been changed during annealing by a re-evaporation of Fe atoms. On the other hand, it is possible that, within the error bars, the Fe rate has actually become smaller than during the preparation of the first series of film. As mentioned in section 5.2, the Fe rod in the mini e-beam evaporator had been changed prior to the preparation of the second series of films. Probably the evaporation behavior of the 6 mm rod is different from that of the 2 mm rod used before.

Returning to the original question, whether a quantum critical point exists in $Mn_{1-x}Fe_xSi$ thin films, the behavior of the resistivity close to the suppression of magnetic order must be investigated. Therefore the exponent in the equation $\rho = \rho_0 + AT^n$ can be determined from the logarithmic derivative of $(\rho - \rho_0)$, as described in section 3.8.3.

Unfortunately the exponent n cannot be determined for the codeposited films, since a Kondo minimum masks the critical behavior in the case, where magnetic order is suppressed. Also for the films with a non-zero T_{ord} $d\ln(\rho - \rho_0)/d\ln T$ diverges towards low temperatures, so that n cannot be determined. Possibly all films contain a percentage of non-magnetic $Mn_{1-x}Fe_xSi$, which exhibits a Kondo minimum. When this minimum occurs at temperatures below the lowest temperature, that was reached in the resistivity measurements, it remains concealed, but the critical behavior of the resistivity may be masked by a logarithmic contribution.

For the annealed $Mn_{1-x}Fe_xSi$ films, however, the logarithmic derivative of $(\rho - \rho_0)$ yields reasonable results as shown in figure 5.17. For all films $n = d\ln(\rho - \rho_0)/d\ln T$ increases, when the temperature is decreased below T_{ord}. This increase is steeper for the films with low Fe doping. For the sample with $x = 0.06 \pm 0.05$ the low temperature exponent of the resistivity

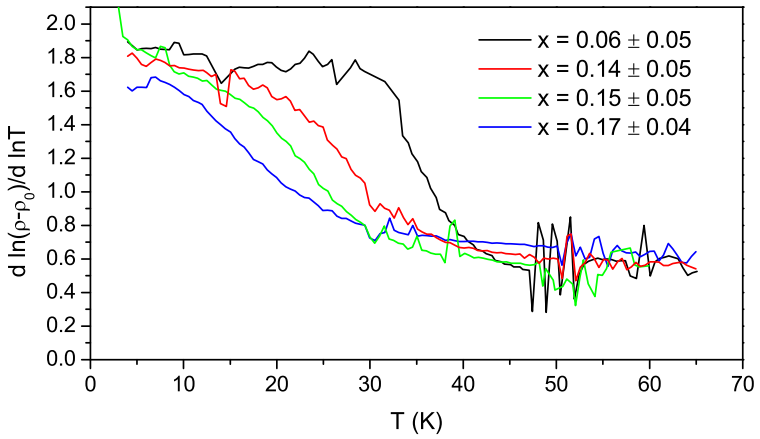

Figure 5.17: The logarithmic derivatives of $(\rho - \rho_0)$ yield the exponents of the temperature dependence of the resistivity for the annealed samples.

is 1.8 ± 0.1, which is close $n = 2$ as expected for a Fermi liquid. For higher Fe concentrations n slightly decreases. However, no conclusions can be drawn for the behavior close to the quantum critical point, since the complete suppression of magnetic order is not approached. For the sample with $x = 0.15 \pm 0.05$ $d \ln(\rho - \rho_0)/d \ln T$ diverges towards low temperatures, which is probably a hint to a small fraction of non-magnetic $Mn_{1-x}Fe_xSi$ exhibiting a Kondo effect.

Chapter 6

Summary

MnSi, MnGe and $Mn_{1-x}Fe_xSi$ thin films were investigated to specify the influence of uniaxial anisotropy as well as finite size effects and strain on the properties of the B20 compound. Different preparation techniques have been established and the structural and morphological properties of the films have been investigated. In comparison to bulk material, thin films of the B20 compound especially show modified magnetic properties, which could be observed by a shift of phase transitions toward higher fields and temperatures. Even evidence for new magnetic phases was found, which are of particular interest in the search for skyrmions.

The work on MnSi thin films concentrated mainly on three different fields of interest, which were the preparation, the determination of the magnetic phase diagram and the behavior of the thin films under high pressure.

Naturally the first step was the growth of MnSi thin films, which was carried out by MBE. To obtain the optimal samples it was necessary to compare different preparation techniques and to optimize their parameters. The first films were grown by an annealing method, where a Mn layer was deposited on a Si substrate and subsequently heated to react with the substrate to form MnSi. Although this method was easy to operate, it could be proven by RHEED, AFM and TEM investigations that the films are characterized by a considerable amount of surface and interface roughness. Furthermore the MnSi layers exhibited holes, which developed during the annealing process, when Si was provided from the substrate [142]. Because of these shortcomings of the annealing method the further work concentrated on improving the codeposition technique, which was suggested to enhance the homogeneity of MnSi thin films [131]. The simultaneous deposition of Si and Mn with a rate of approximately 0.2 Å/s onto a substrate held at 250°C yielded flat and homogeneous films with a good crystalline quality, which were well suited for further investigations to clarify their physical properties.

The next and most important issue was to establish the magnetic phase

diagram of MnSi thin films. In this context the magnetic ordering temperature T_{ord} was determined from susceptibility measurements performed on a series of codeposited films. It could be proven that T_{ord} is dependent on the film thickness for those films, which are thinner than 10 nm. The observed decrease of T_{ord} was convincingly explained by the reduction of spin-spin interactions at the surfaces and interfaces of the films. For thicker films T_{ord} was found to be enhanced compared to bulk MnSi, which is due to strain as verified by high pressure experiments.

After the temperature range of magnetic order had been ascertained, the evolution of the magnetic state under an applied magnetic field was investigated in order to determine further phase transitions. For this purpose magnetization and magnetoresistivity measurements were performed. When these experiments were carried out with an out-of-plane field direction all films showed essentially the same behavior as known from bulk MnSi, except for the absence of the critical field B_{c1} and an enhancement of $B_{c2}^{\perp}$ compared to the bulk value caused by shape anisotropy. Hall effect measurements in the same field configuration contained a topological contribution, which appeared in almost the complete ordered phase below $B_{c2}^{\perp}$. Since the occurrence of a THE is conflicting with the absence of phase transitions in the magnetization and MR measurements, the existence of skyrmions aligned perpendicular to the film plane is still under discussion.

Measurements with a magnetic field applied in the film plane revealed a more complex behavior. From the absence of magnetic phase transitions for films thinner than one helix length, it was argued that the incomplete helix is unstable with respect to external in-plane magnetic fields. Thicker films, however, displayed a variety of transitions, which gave evidence of a multifaceted phase diagram with at least four different phases occurring below $B_{c2}^{||}$. PNR data of another group give evidence for skyrmions aligned in the film plane, which occur in a certain field and temperature range [44, 45].

Apart from the search for skyrmions in MnSi thin films high pressure experiments were performed to enlighten the role of strain. The lattice misfit of -3 % between the film and the substrate causes an enlargement of the in-plane mesh of MnSi, which was shown to provide a plausible explanation for the enhanced T_{ord}. Furthermore the experiments under high pressure revealed a regime of NFL behavior beyond the critical pressure $p_c = 3.1$ GPa, where long range magnetic order is suppressed. At pressures exceeding 2.5 GPa the resistivity crosses over into a $T^{3/2}$ law, when the temperature is getting below 30 K. The enlargement of the NFL regime towards higher temperatures than in bulk MnSi was discussed to be an indication for the increased stability of partial order, which is supposed to be the origin of the NFL behavior. When the partial order is assumed to consist of skyrmionic textures as proposed in recent literature [32], the uniaxial anisotropy provides an explanation for their enhanced stability.

In summary MnSi thin films have been grown successfully and the main consequences of finite size effects and strain have been enlightened. The phase transitions in the presence of magnetic fields and high pressure have been mapped in magnetic phase diagrams, and in particular the thickness dependence of the T_{ord} could be explained. The NFL behavior observed under pressure is of special interest for investigating the impact of uniaxial anisotropy on the stability of skyrmionic textures. Thus, an important contribution has been made to the understanding of the mechanisms that govern the behavior of MnSi thin films, which is valuable in the search for skyrmions in thin film samples.

MnGe thin films have been investigated, because this compound exhibits a considerably higher ordering temperature than MnSi. This is a promising characteristic regarding the practicability of the films for applications in future data storage devices.

Although various attempts to grow MnGe directly on the surface of Si(111) or Ge(111) substrates had failed in the past, a successful method could be established now. Therefore a 1 nm layer of MnSi was prepared on a Si substrate prior to deposition of MnGe. This seedlayer provided the B20 crystal structure for the growth of MnGe by codeposition. It was proven by XRD measurements that MnGe films prepared by this method exhibit the B20 crystal structure. The lattice constant is reduced by 1 % compared to bulk MnGe, which is caused by the compressive strain induced by the misfit between the film and the substrate. Islands can be observed by AFM, since the growth of MnGe on Si(111) with a seedlayer of MnSi is of Volmer-Weber type. Comparing the morphology of MnGe films with different thicknesses reveals that the islands coalesce with increasing film thickness.

The susceptibility of MnGe thin films revealed a slightly enhanced ordering temperature compared to bulk MnGe, which is possibly effected by a distortion of the unit cell due to compressive strain. Furthermore the susceptibility curve is reminiscent of an antiferromagnet, which is reasonable due to the short helix length. Magnetization and magnetoresistivity measurements on MnGe thin films gave evidence for very high saturation fields, probably in the range of the bulk value amounting 12 T. This means that the magnetic structure of MnGe is very rigid. Comparing the properties of MnGe and MnSi thin films leads to the conclusion that the Dzyaloshinskii constant of MnGe is much larger than for MnSi.

In the last part of this work $Mn_{1-x}Fe_xSi$ thin films have been prepared by two different procedures. A first series of samples was codeposited on a Si(111) surface and a second one was codeposited and annealed afterwards. For all films with Fe doping a decreased T_{ord} could be observed.

For the codeposited samples it was concluded from susceptibility and resistivity measurements that these films are not completely homogeneous.

Some films show evidence for fractions with magnetic order coexisting with fractions, where magnetic order is completely suppressed. Domains with $x \approx 0.08$ seem to form preferentially, which can be concluded from the similar transition temperatures found for samples with considerably different nominal Fe concentrations. In films or fractions of a film, where magnetic order is completely suppressed, a Kondo minimum was observed in the temperature dependence of the resistivity. Obviously some Fe atoms occupy Si sites or interstitial sites, where they act as magnetic impurities. The occurrence of a resistivity minimum at low temperatures obstructs the identification of non-Fermi liquid behavior close to the critical concentration $x = 0.15 \pm 0.05$.

In contrast, the $Mn_{1-x}Fe_xSi$ films, that have been annealed after codeposition, are more homogeneous. However, their morphology is similar to MnSi films prepared by annealing, i. e. they exhibit some holes. The magnetic ordering temperature has been decreased to 20 K for a film with $x = 0.17 \pm 0.06$. A comparison between the values of T_{ord} of the codeposited and the annealed films suggests that the Fe concentration in the annealed films is smaller than the nominal value.

Appendix A

Supplemental Data

A.1 Calibration of the Ceramic Heater

During the preparatory work for this project the UHV system was equipped with a ceramic heater, which can achieve temperatures considerably higher than the tantalum heater in the growth chamber. This new heater is positioned between the load lock and the growth chamber and is needed to heat the silicon substrates prior to growth. The heater consists of a boron nitride plate with wires made of pyrolytic graphite running trough it. With an output of 1440 W temperatures of 1800°C can be reached. In order to ensure an optimum heat transfer from the heater to the sample, the sample holder is pressed directly onto the ceramic surface of the heater. Therefore the construction shown in figure A.1 is used, which holds the sample holder and is adjustable in height.

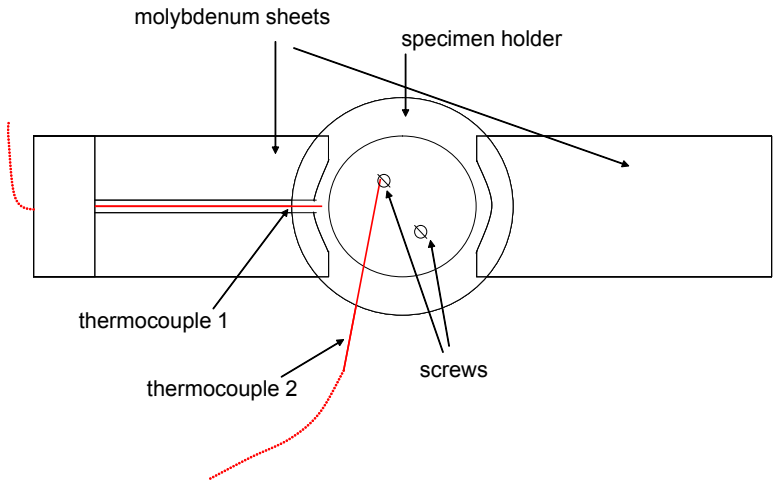

Figure A.1: Sample holder at the ceramic heater equipped with thermocouples, view from below.

During the heating process the temperature of the sample is measured by a type C thermocouple (tungsten - rhenium), which is installed at the sample holder (thermocouple 1 in figure A.1). Since this thermocouple is not exactly at the position of the sample, it was necessary to perform a calibration to get the true temperature at the sample. Therefore a second thermocouple was positioned at the bottom side of the sample holder and fixed with the same screws, which were later used to fix the substrate. While the temperature of the heater was increased slowly, the temperatures displayed by the two thermocouples were monitored. This process was repeated several times in order to obtain the calibration curve shown in figure A.2. It turned out that the temperature at the sample is considerably higher than measured by the permanently installed thermocouple 1. Therefore special attention is required, when a Si substrate is heated, since the melting point of Si can easily be reached. A displayed temperature between 880 °C and 900 °C was found to be suitable to achieve an excellent clean Si surface.

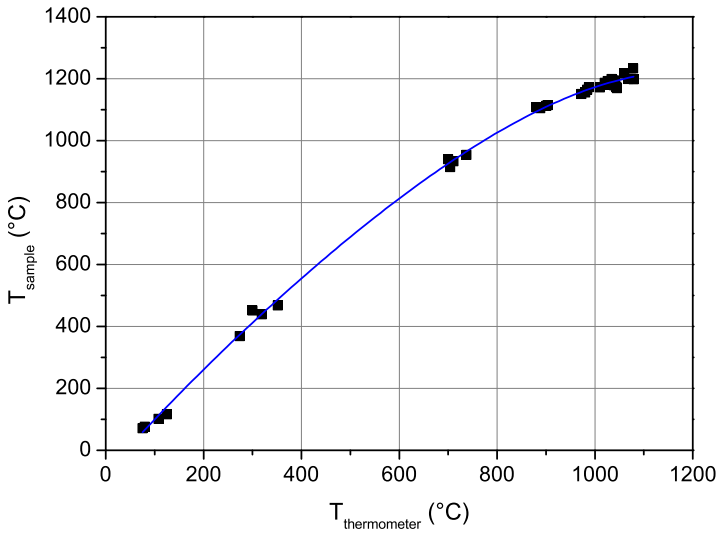

Figure A.2: Calibration of the sample temperature at the ceramic heater

A.2 Calibration of the Tantalum Substrate Heater

In order to control the temperature of the sample during the deposition process a heater is needed inside the growth chamber. Therefore, a sinusoidally winded tantalum wire is installed directly above the sample holder, which can be resistively heated by an applied current. A thermocouple is positioned close to the wire to monitor the temperature.

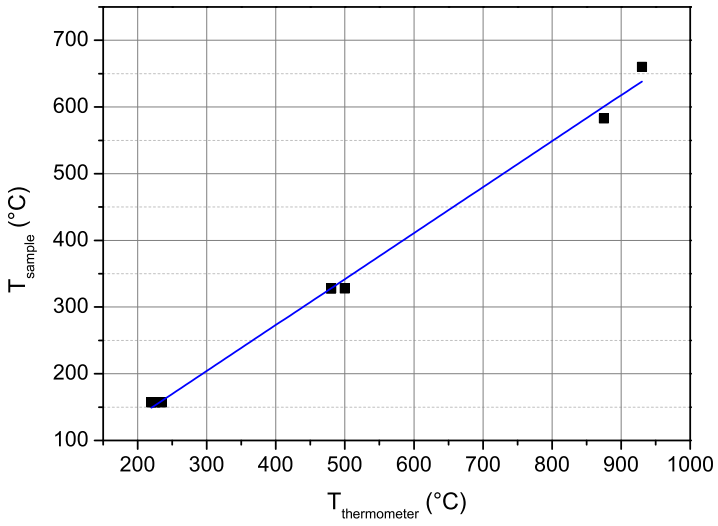

Figure A.3: Temperature calibration for the tantalum heater located in the growth chamber.

For the temperature calibration pieces of different metals were attached to the sample holder and heated until they melted. From the melting points and the displayed temperatures the calibration curve shown in figure A.3 was obtained in accordance with a former calibration [90]. The plotted data points stem from the melting points of lead, indium and aluminum (Pb: 328°C, In: 157°C, Al: 620°C). Additionally the temperature of deoxidation of a GaAs surface (T_{Deox} = 583°C) was determined by RHEED investigations and related to the displayed temperature value.

A.3 Resistivity Data

In the following the resistivity curves for five thin films MnSi of different thickness are shown in combination with their first temperature derivatives. The data were obtained by measurements with the van-der-Pauw method. The positions of T_{ord} are marked in the diagrams and the corresponding values are given in the caption.

In figure A.9 the T^2 behavior of the resistivity at low temperatures is visualized for films with thicknesses between 3.5 nm and 19 nm.

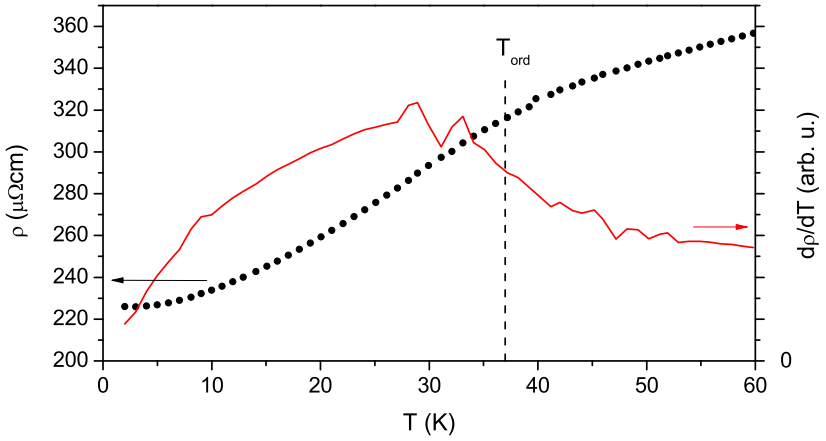

Figure A.4: Resistivity measurement on a 3.5 nm film MnSi and first temperature derivative of the curve. From the data $T_{ord} = 37\,\mathrm{K}$ can be determined.

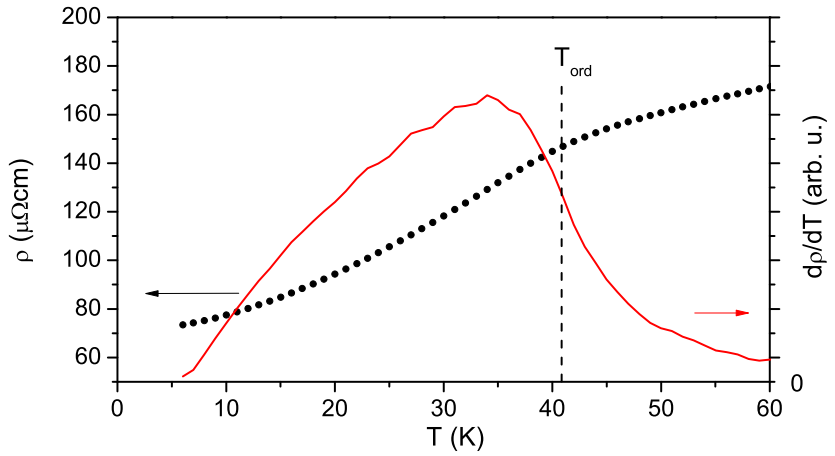

Figure A.5: For the 6 nm film we find $T_{ord} = 41\,\mathrm{K}$ from the resistivity measurement.

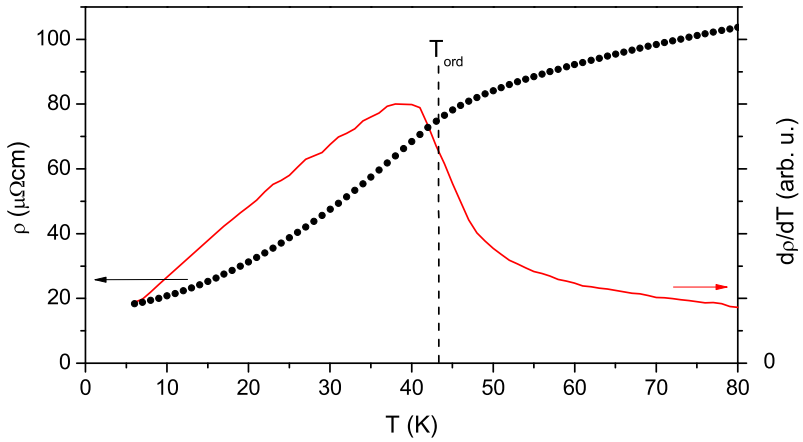

Figure A.6: Resistivity and $d\rho/dT$ curves for a 9 nm thin film MnSi. The magnetic ordering temperature amounts $T_{ord} = 43\,\mathrm{K}$.

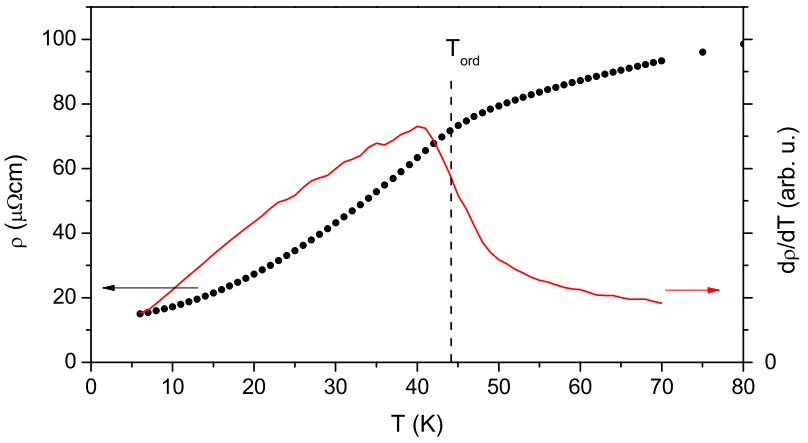

Figure A.7: For the 13 nm film $T_{ord} = 44$ K can be determined from the resistivity measurement.

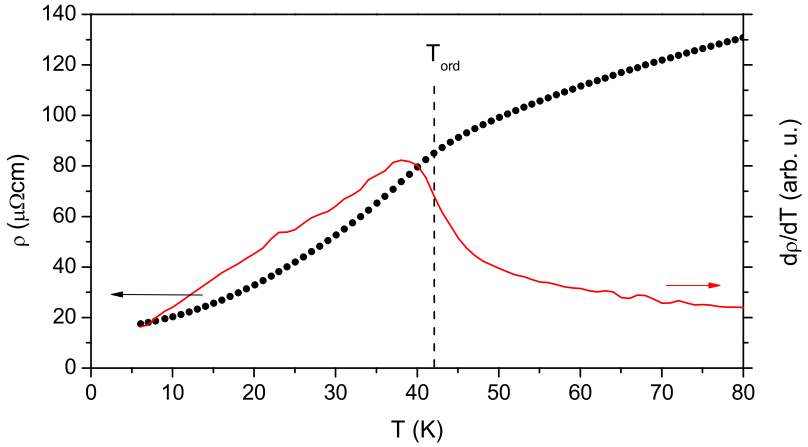

Figure A.8: The 29 nm film exhibits an magnetic ordering temperature of $T_{ord} = 42$ K as determined from the resistivity measurement.

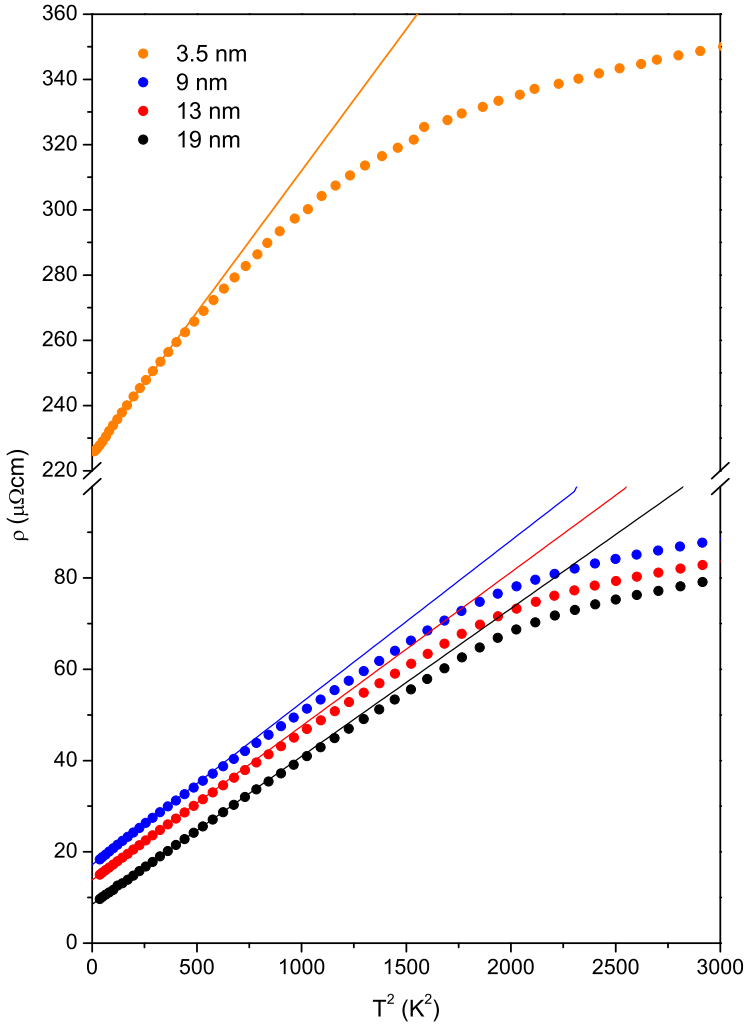

Figure A.9: Resistivity data for films of different thicknesses plotted versus T^2. The solid lines correspond to fits with $\rho(T^2) = \rho_0 + AT^2$. The A-coefficients are given in section 3.5.3.

A.4 Hall Effect Data

In the following Hall data for several MnSi thin films with thicknesses between 6 nm and 24 nm are shown. As discussed in section 3.6 the Hall effect seems to be very sensitive to the film morphology, since all three contributions differ considerably for the different samples and no systematic thickness dependence can be detected. Therefore it is not possible to draw a consistent picture of the Hall effect for all films. In the following a short description of the main features observed in the Hall effect will be given for every sample.

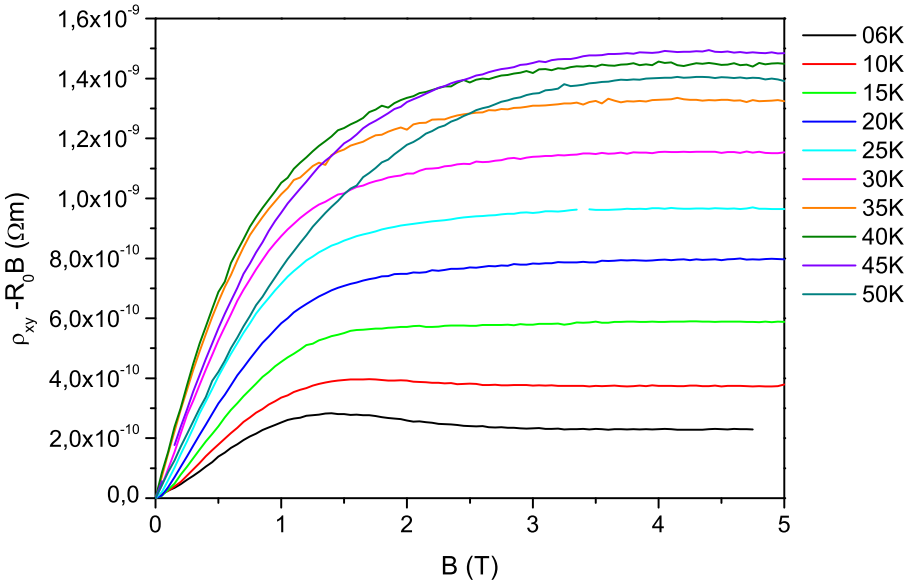

Figure A.10: Hall effect measurement on a 6 nm codeposited film MnSi ($T_{ord} = 34\,\mathrm{K}$) after subtraction of the normal Hall effect.

In figure A.10 the Hall data for a 6 nm film MnSi are shown, where the normal Hall effect $R_0 B$ has already been subtracted. R_0 is almost temperature independent with a value of $1.2 \cdot 10^{-10}\,\Omega\mathrm{m/T}$. The AHE is positive and grows with increasing temperature. The THE is not pronounced for this sample. Only for the lowest temperatures small contributions seem to be present. However, it should be noted that the anomalous Hall effect is considerably larger for this sample than for the thicker films, which makes the identification of a small topological contribution more difficult. In figure A.11 a fitted curve including the normal and the anomalous contributions is shown. The deviation between the calculated curve and the data is due to the THE.

The Hall data for a 9 nm film are depicted in figure A.12. The nor-

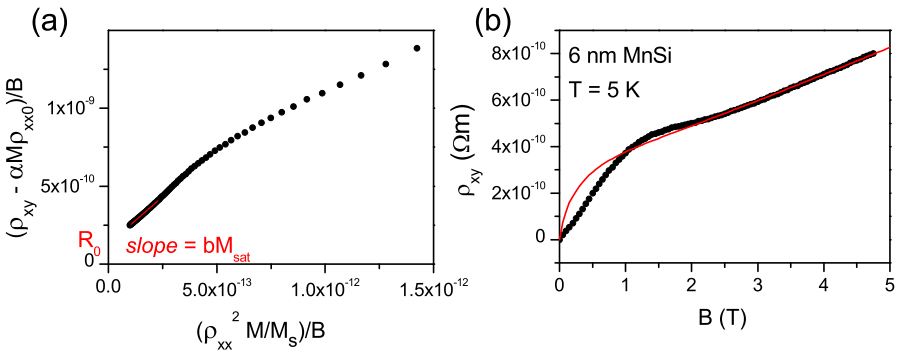

Figure A.11: (a) Plot to determine bM_{sat} and R_0 analogous to the procedure described in section 3.6. (b) Fit of the normal and the anomalous Hall contribution for the 6 nm film MnSi with the following parameters: $\alpha M_{sat} = -5 \cdot 10^{-4}$, $bM_{sat} = 1.2 \cdot 10^3\, m/\Omega$ and $R_0 = 1.3 \cdot 10^{-10}\,\Omega$m/T.

mal Hall effect is almost temperature independent with a value of $R_0 = 6.5 \cdot 10^{-11}\,\Omega$m/T and has been subtracted. The AHE is negative for lowest temperatures, but grows to positive around 15 K. In the case of this sample the THE is a broad negative contribution that can be observed for temperatures below T_{ord} and in magnetic fields below $B_{c2} = 1.5$ T. The fit in figure A.13 underlines that the THE at 5 K is negative for this 9 nm sample.

For a 13 nm film the Hall effect after subtraction of the normal contribution $R_0 B$ with $R_0 \approx 6 \cdot 10^{-11}\,\Omega$m/T is shown in figure A.14. The AHE is negative for temperatures below 20 K and positive above that temperature. The THE can be observed at low temperatures as a small positive contribution (compare figure A.15). A negative bump-like effect observed between 20 K and 30 K in small fields up to 0.5 T may also be of topological origin.

In figure A.16 the Hall data for a 24 nm film MnSi are depicted. Here the normal Hall constant is $R_0 \approx 1 \cdot 10^{-10}\,\Omega$m/T. The Hall effect of this sample is the most curious. The anomalous Hall contribution is positive for lowest temperatures, but turns negative between approximately 10 K and 25 K. For higher temperatures it is positive again. Also the THE is partly positive and partly negative. Since also the ordering temperature is lower than expected for a film of 24 nm thickness, it seems obvious that the quality of the sample is not sufficient to compare it with other samples. In figure A.17 the THE at 5 K is illustrated, which is negative in small magnetic field, but seems to turn slightly positive above 1 T.

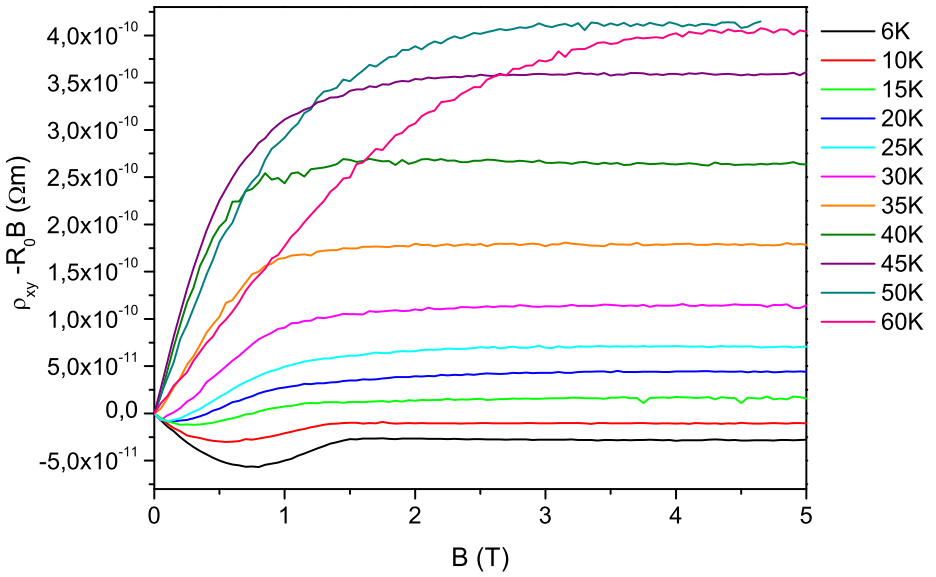

Figure A.12: Hall effect measurement on a 9 nm codeposited film MnSi ($T_{ord} = 40\,\mathrm{K}$) after subtraction of the normal Hall effect $R_0 B$.

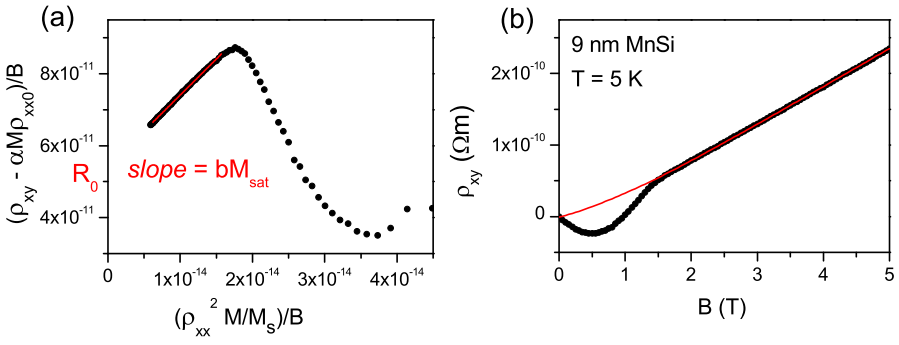

Figure A.13: (a) Plot to determine bM_{sat} and R_0 analogous to the procedure described in section 3.6. (b) Fit of the normal and the anomalous Hall contribution for the 9 nm film MnSi with the following parameters: $\alpha M_{sat} = -5 \cdot 10^{-4}$, $bM_{sat} = 2.0 \cdot 10^3\, m/\Omega$ and $R_0 = 5.4 \cdot 10^{-11}\,\Omega\mathrm{m/T}$.

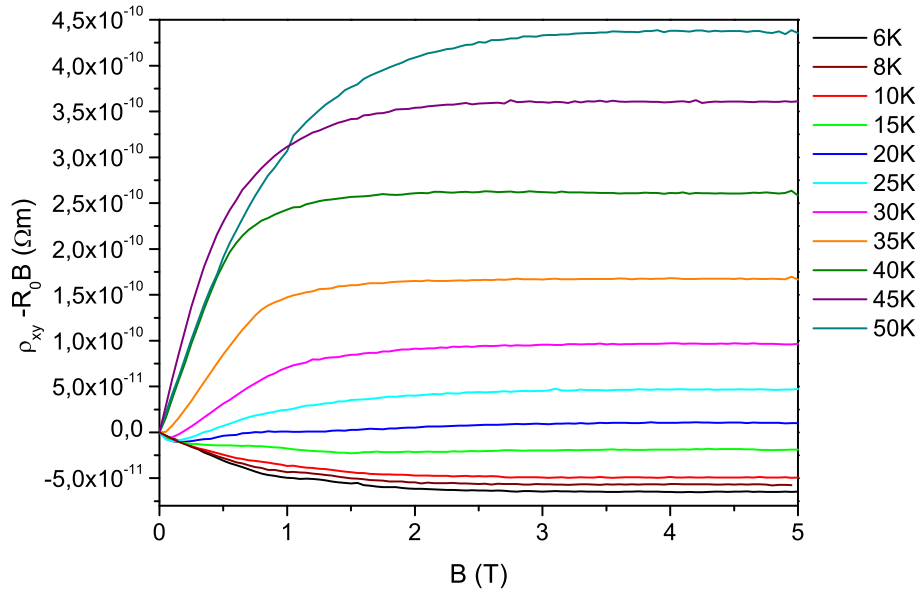

Figure A.14: Hall effect measurement on a 13 nm codeposited film MnSi ($T_{ord} = 46\,\mathrm{K}$) after $R_0 B$ has been subtracted.

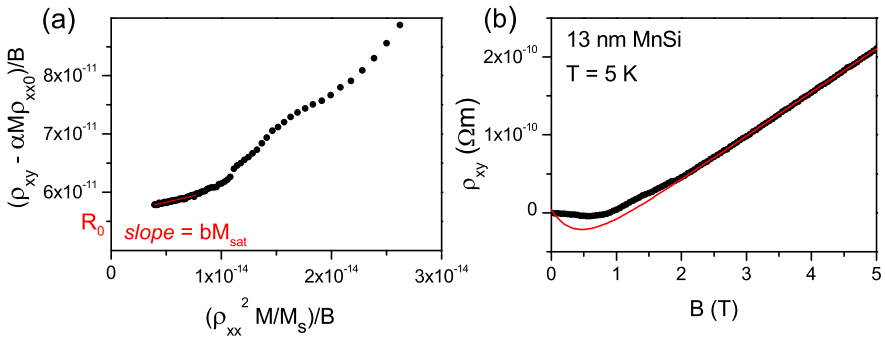

Figure A.15: (a) Plot to determine bM_{sat} and R_0 analogous to the procedure described in section 3.6. (b) Fit of the normal and the anomalous Hall contribution for the 13 nm film MnSi with the following parameters: $\alpha M_{sat} = -5 \cdot 10^{-4}$, $bM_{sat} = 440\,m/\Omega$ and $R_0 = 5.6 \cdot 10^{-11}\,\Omega\mathrm{m/T}$.

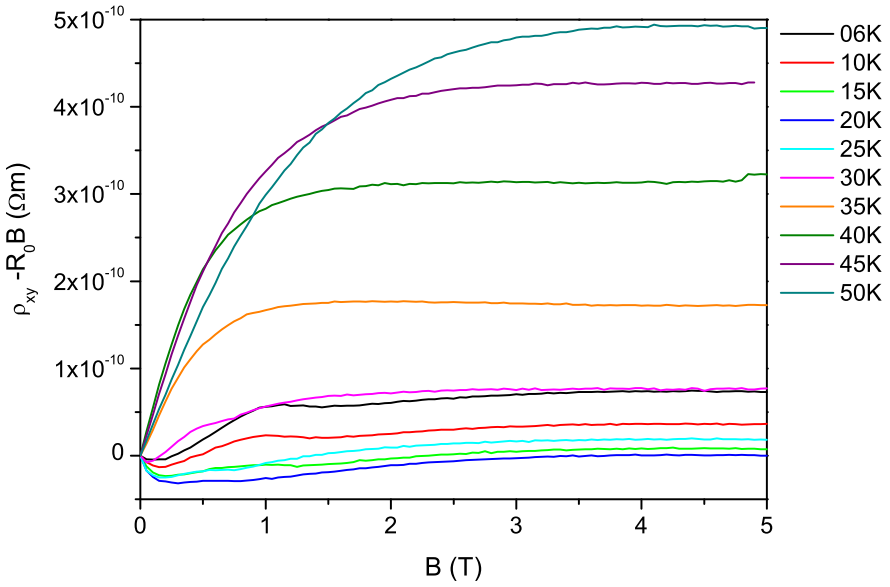

Figure A.16: Hall effect measurement on a 24 nm codeposited film MnSi ($T_{ord} = 37\,\mathrm{K}$) after subtraction of the normal Hall effect $R_0 B$.

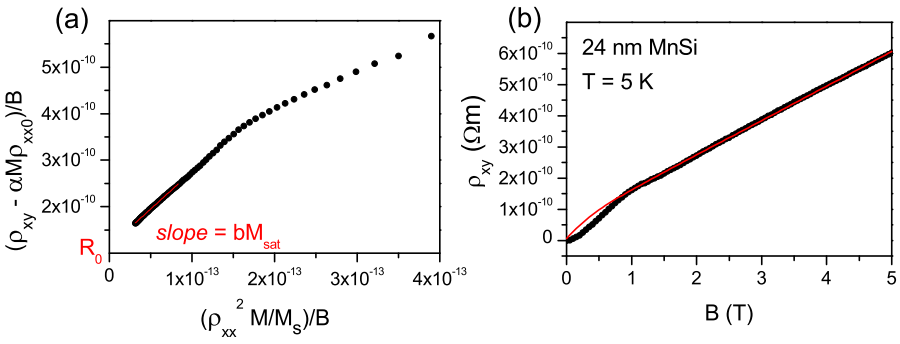

Figure A.17: (a) Plot to determine bM_{sat} and R_0 analogous to the procedure described in section 3.6. (b) Fit of the normal and the anomalous Hall contribution for the 24 nm film MnSi with the following parameters: $\alpha M_{sat} = -5 \cdot 10^{-4}$, $bM_{sat} = 1.6 \cdot 10^3\, m/\Omega$ and $R_0 = 1.15 \cdot 10^{-10}\,\Omega\mathrm{m/T}$.

Acknowledgments

Arriving at the end of this work I would like to say *Thank You* to all people, who supported me during the past years and thereby made this thesis possible.

First of all I would like to thank Priv.-Doz. Dr. Dirk Menzel for giving me the opportunity to work on the interesting and up-to-date topic of thin films of B20 compounds, and for the supervision of this thesis. I appreciate his support and advice at any time during the past years.

Furthermore I thank Prof. Dr. Paul Fumagalli that he agreed to referee this thesis.

I would also like to thank Prof. Dr. Stefan Süllow for helpful discussions and advices, whenever I was fighting with some unexpected new data. Further, I want to thank Prof. Dr. Jochen Litterst, who supported me during my bachelor and master theses, and who gave me the opportunity to visit Rio de Janeiro twice.

Thinking of my work in the clean room, where I spent many hours during the past years, I am glad that Thilo Lampe with his experience in vacuum technology always helped me with any problems concerning the MBE facility. Also Lutz Naggatz, Susi Bittner, Sarah Pommerien and Lisa Hoffman were reliable assistants in all technical challenges.

Further, I would like to thank Gudrun Zeising for the elaborate sample preparation, which was necessary for the TEM investigations, and Lars Hoffmann for his help with these measurements.

During my work I frequently needed access to an AFM and I am thankful that Priv.-Doz. Dr. Andrey Bakin, Alexander Wagner, Harald Scherg, and Manal Ali Deeb let me use the instrument belonging to the Institute of Semiconductor Technology. In the same institute I could perform DekTak measurements and I thank Angelika Schmidt for her assistance.

A number of EDX measurements were performed in the Institute for Physical and Theoretical Chemistry. Here I would like to thank Birgit Gerke, who was very patient with my samples and did not capitulate in view of the small x-ray signal.

An important and also very joyful period during my PhD time was my stay in Japan. I am thankful that I was welcomed so pleasantly at the Hokkaido University by the whole group of the VLT Lab. Especially I would

like to thank Prof. Dr. Hiroshi Amitsuka for making this stay possible by inviting me and being my host researcher. I am glad that the 'Japan Society for the Promotion of Science' supported my research in Sapporo. Furthermore I want to thank Hiroyuki Hidaka and Teisei Seguchi for their dedicated support during the high pressure experiments.

Some master students joined my work at the MBE facility and with the MnSi thin film. I am thankful for the fruitful collaboration and the enjoyable atmosphere in the clean room with Tommy Reimann, Niklas van Elten and David Schröter.

Last but not least, I would like to mention the pleasant and entertaining company in our office and its neighborhood. Thank you for the good times!

References

[1] T. Shinjo (Editor), *Nanomagnetism and Spintronics* (Elsevier, Oxford, 2009).

[2] W. Thomson, Proc. Royal Soc. London **8**, 546 (1857).

[3] P. Grünberg, R. Schreiber, Y. Pang, M. B. Brodsky, and H. Sowers, Phys. Rev. Lett. **57**, 2442 (1986).

[4] M. N. Baibich, J. M. Broto, A. Fert, F. Nguyen Van Dau, F. Petroff, P. Eitenne, G. Creuzet, A. Friederich, and J. Chazelas, Phys. Rev. Lett. **61**, 2472 (1988).

[5] J. Mathon and A. Umerski, Phys. Rev. B **63**, 220403(R) (2000).

[6] S. Yuasa, T. Nagahama, A. Fukushima, Y. Suzuki, and K. Ando, Nature Mat. **3**, 868 (2004).

[7] J. Akerman, Science **308**, 508 (2005).

[8] S. Parkin (2003), Patent: US 6834005 B1, *Shiftable magnetic shift register and method of using the same.*

[9] S. S. P. Parkin, M. Hayashi, and L. Thomas, Science **320**, 190 (2008).

[10] S. S. P. Parkin, Scientific American, June 2009, pp. 76–81 (2009).

[11] S. Fukami, M. Yamanouchi, Y. Nakatani, K.-J. Kim, T. Koyama, D. Chiba, S. Ikeda, N. Kasai, T. Ono, and H. Ohno, J. Appl. Phys. **115**, 17D508 (2014).

[12] S. Mühlbauer, B. Binz, F. Jonietz, C. Pfleiderer, A. Rosch, A. Neubauer, R. Georgii, and P. Böni, Science **323**, 915 (2009).

[13] T. Schulz, R. Ritz, A. Bauer, M. Halder, M. Wagner, C. Franz, and C. Pfleiderer, Nature Phys. **8**, 301 (2012).

[14] N. Kanazawa, Y. Onose, T. Arima, D. Okuyama, K. Ohoyama, S. Wakimoto, K. Kakurai, S. Ishiwata, and Y. Tokura, Phys. Rev. Lett. **106**, 156603 (2011).

[15] X. Z. Yu, N. Kanazawa, Y. Onose, K. Kimoto, W. Z. Zhang, S. Ishiwata, Y. Matsui, and Y. Tokura, Nat. Mater. **10**, 106 (2010).

[16] T. Adams, S. Mühlbauer, A. Neubauer, W. Münzer, F. Jonietz, R. Georgii, B. Pedersen, P. Böni, A. Rosch, and C. Pfleiderer, J. Phys.: Conference Series **200**, 032001 (2010).

[17] W. Münzer, A. Neubauer, T. Adams, S. Mühlbauer, C. Franz, F. Jonietz, R. Georgii, B. Pedersen, M. Schmidt, A. Rosch, et al., Phys. Rev. B **81**, 041203(R) (2010).

[18] X. Z. Yu, Y. Onose, N. Kanazawa, J. H. Park, J. H. Han, Y. Matsui, N. Nagaosa, and Y. Tokura, Nature **465**, 901 (2010).

[19] S. V. Grigoriev, V. A. Dyadkin, E. V. Moskvin, D. Lamago, T. Wolf, H. Eckerlebe, and S. V. Maleyev, Phys. Rev. B **79**, 144417 (2009).

[20] T. Adams, A. Chacon, M. Wagner, A. Bauer, G. Brandl, B. Pedersen, H. Berger, P. Lemmens, and C. Pfleiderer, Phys. Rev. Lett. **108**, 237204 (2012).

[21] A. B. Butenko, A. A. Leonov, U. K. Rößler, and A. N. Bogdanov, Phys. Rev. B **82**, 052403 (2010).

[22] S. Heinze, K. von Bergmann, M. Menzel, J. Brede, A. Kubetzka, R. Wiesendanger, G. Bihlmayer, and S. Blügel, Nat. Phys. **7**, 713 (2011).

[23] K. von Bergmann, S. Heinze, M. Bode, E. Y. Vedmedenko, G. Bihlmayer, S. Blügel, and R. Wiesendanger, Phys. Rev. Lett. **96**, 167203 (2006).

[24] N. Romming, C. Hanneken, M. Menzel, J. E. Bickel, B. Wolter, K. von Bergmann, A. Kubetzka, and R. Wiesendanger, Science **341**, 636 (2013).

[25] A. Tonomura, X. Yu, K. Yanagisawa, T. Matsuda, Y. Onose, N. Kanazawa, H. S. Park, and Y. Tokura, Nano Lett. **12**, 1673 (2012).

[26] K. Schwinge, C. Müller, A. Mogilatenko, J. J. Paggel, and P. Fumagalli, J. Appl. Phys. **97**, 103913 (2005).

[27] C. Pfleiderer, G. J. McMullan, S. R. Julian, and G. G. Lonzarich, Phys. Rev. B **55**, 8330 (1997).

[28] A. E. Petrova, E. D. Bauer, V. N. Krasnorussky, and S. M. Stishov, Phys. Rev. B **74**, 092401 (2006).

[29] C. Pfleiderer, G. J. McMullan, and G. G. Lonzarich, Nature **414**, 427 (2001).

[30] Y. Nishihara, S. Waki, and S. Ogawa, Phys. Rev. B **30**, 32 (1984).

[31] A. Bauer, A. Neubauer, C. Franz, W. Münzer, M. Garst, and C. Pfleiderer, Phys. Rev. B **82**, 064404 (2010).

[32] R. Ritz, M. Halder, M. Wagner, C. Franz, A. Bauer, and C. Pfleiderer, Nature **497**, 231 (2013).

[33] F. Schwabl, *Statistische Mechanik, 3. Auflage* (Springer, Berlin Heidelberg, 2006).

[34] D. Dzyaloshinskii, Sov. Phys. JETP **19**, 960 (1964).

[35] P. Bak and M. H. Jensen, J. Phys. C: Solid St. Phys. **13**, L881 (1980).

[36] U. K. Rößler, A. A. Leonov, and A. N. Bogdanov, J. Phys.: Conference Series **303**, 012105 (2011).

[37] A. Leonov (2011), Dissertation, Technische Universität Dresden, *Twisted, localized, and modulated states described in the phenomenological theory of chiral and nanoscale ferromagnets.*

[38] K. Everschor (2012), Dissertation, Universität zu Köln, *Current-Induced Dynamics of Chiral Magnetic Structures.*

[39] T. H. R. Skyrme, Proc. Roy. Soc. **260**, 127 (1961).

[40] A. N. Bogdanov and D. A. Yablonskiĭ, Sov. Phys. JETP **68**, 101 (1989).

[41] A. Bogdanov and A. Hubert, J. Magn. Magn. Mater. **195**, 182 (1999).

[42] S. Mühlbauer (2009), Dissertation, Technische Universität München, *Vortex Lattices in Superconducting Niobium and Skyrmion Lattices in Chiral MnSi: An Investigation by Neutron Scattering.*

[43] M. N. Wilson, A. B. Butenko, A. N. Bogdanov, and T. L. Monchesky, Phys. Rev. B **89**, 094411 (2014).

[44] E. A. Karhu, U. K. Rößler, A. N. Bogdanov, S. Kahwaji, B. J. Kirby, H. Fritzsche, M. D. Robertson, C. F. Majkrzak, and T. L. Monchesky, Phys. Rev. B **85**, 094429 (2012).

[45] M. N. Wilson, E. A. Karhu, A. S. Quigley, U. K. Rößler, A. B. Butenko, A. N. Bogdanov, M. D. Robertson, and T. L. Monchesky, Phys. Rev. B **86**, 144420 (2012).

[46] E. H. Hall, Amer. J. Math. **2**, 287 (1879).

[47] C. Kittel, *Einführung in die Festkörperphysik, 14. verbesserte Ausgabe* (Oldenbourg Wissenschaftsverlag GmbH, München Wien, 2006).

[48] N. W. Ashcroft and D. N. Mermin, *Festkörperphysik, 3. Auflage* (Oldenbourg Wissenschaftsverlag GmbH, München, 2007).

[49] N. Nagaosa, J. Sinova, S. Onoda, A. H. MacDonald, and N. P. Ong, Rev. Mod. Phys. **82**, 1539 (2010).

[50] R. Karplus and J. M. Luttinger, Phys. Rev. **95**, 1154 (1954).

[51] N. P. Ong and W.-L. Lee, Foundations of quantum mechanics in the light of new technology (ISQM Tokyo 2005) p. 121 (2006).

[52] J. Smit, Physica **21**, 877 (1955).

[53] J. Smit, Physica **24**, 39 (1958).

[54] Y. Tian, L. Ye, and X. Jin, Phys. Rev. Lett. **103**, 087206 (2009).

[55] L. Berger, Phys. Rev. B **2**, 4559 (1970).

[56] C. Pfleiderer and A. Rosch, Nature **465**, 880 (2010).

[57] J. Ye, Y. B. Kim, A. J. Millis, B. I. Shraiman, P. Majumdar, and Z. Tešanović, Phys. Rev. Lett. **83**, 3737 (1999).

[58] M. V. Berry, Proc. R. Soc. Lond. A **392**, 45 (1984).

[59] S. Zhang and S. S.-L. Zhang, Phys. Rev. Lett. **102**, 086601 (2009).

[60] K. Everschor-Sitte and M. Sitte, J. Appl. Phys. **115**, 172602 (2014).

[61] P. Bruno, V. K. Dugaev, and M. Taillefumier, Phys. Rev. Lett. **93**, 096806 (2004).

[62] A. Neubauer, C. Pfleiderer, B. Binz, A. Rosch, R. Ritz, P. Niklowitz, and P. Böni, Phys. Rev. Lett. **102**, 186602 (2009).

[63] B. Binz and A. Vishwanath, Physica B **403**, 1336 (2008).

[64] L. D. Landau, Sov. Phys. JETP **3**, 920 (1957).

[65] A. J. Schofield, Contemp. Phys. **40**, 95 (1999).

[66] G. R. Stewart, Rev. Mod. Phys. **73**, 797 (2001).

[67] D. L. Cox, Phys. Rev. Lett. **59**, 1240 (1987).

[68] O. O. Bernal, D. E. MacLaughlin, H. G. Lukefahr, and B. Andraka, Phys. Rev. Lett. **75**, 2023 (1995).

[69] S. Sachdev, *Quantum Phase Transitions* (University Press, Cambridge, 2011).

[70] A. J. Millis, Phys. Rev. B **48**, 7183 (1993).

[71] T. Moriya, *Spin Fluctuations in Itinerant Electron Magnetism* (Springer, Berlin Heidelberg, 1985).

[72] J. A. Hertz, Phys. Rev. B **14**, 1165 (1976).

[73] T. Moriya and T. Takimoto, J. Phys. Soc. Jpn. **64**, 960 (1995).

[74] A. Ishigaki and T. Moriya, J. Phys. Soc. Jpn. **67**, 3924 (1998).

[75] C. Pfleiderer, G. J. McMullan, and G. G. Lonzarich, Physica B **206&207**, 847 (1995).

[76] C. Thessieu, Y. Kitaoka, and K. Asayama, Physica B **259-261**, 847 (1999).

[77] A. E. Petrova, V. N. Krasnorussky, J. Sarrao, and S. M. Stishov, J. Exp. Theo. Phys. **102**, 636 (2006).

[78] A. E. Petrova, V. N. Krasnorussky, J. Sarrao, and S. M. Stishov, Phys. Rev. B **73**, 052409 (2006).

[79] A. E. Petrova, V. N. Krasnorussky, T. A. Lograsso, and S. M. Stishov, Phys. Rev. B **79**, 100401 (2009).

[80] C. Pappas, E. Lelièvre-Berna, P. Falus, P. Bentley, E. Moskvin, S. Grigoriev, P. Fouquet, and B. Farago, Phys. Rev. Lett. **102**, 197202 (2009).

[81] A. E. Petrova and S. M. Stishov, Phys. Rev. B **86**, 174407 (2012).

[82] M. Janoschek, M. Garst, A. Bauer, P. Krautscheid, R. Georgii, P. Böni, and C. Pfleiderer, Phys. Rev. B **87**, 134407 (2013).

[83] T. Vojta, D. Belitz, T. R. Kirkpatrick, and R. Narayanan, Ann. Phys. (Leipzig) **8**, 593 (1999).

[84] F. Krüger, U. Karahasanovic, and A. G. Green, Phys. Rev. Lett. **108**, 067003 (2012).

[85] T. R. Kirkpatrick and D. Belitz, Phys. Rev. Lett. **104**, 256404 (2010).

[86] M. Ohring, *The Materials Science of Thin Films* (Academic Press, Inc., San Diego, 1992).

[87] H. Lüth, *Surfaces and Interfaces of Solid Materials, Third Edition* (Springer, Berlin Heidelberg, 1998).

[88] W. Kleber, H.-J. Bautsch, J. Bohm, and D. Klimm, *Einführung in die Kristallographie, 19. Auflage* (Oldenbourg Wissenschaftsverlag GmbH, München, 2010).

[89] J. W. Matthews and A. E. Blakeslee, J. Cryst. Growth **27**, 118 (1974).

[90] A. Borgschulte (2002), Dissertation, Technische Universität Braunschweig, *Elektronenbeugungs- und Photo- emissionsstudien an magnetischen und optischen Funktionsschichten.*

[91] P. W. Atkins and J. de Paula, *Physikalische Chemie, Vierte, vollständig überarbeitete Auflage* (Wiley - VCH Verlag GmbH & Co. KGaA, Weinheim, 2006).

[92] *http://www.techniklexikon.net/d/effusionszelle/effusionszelle.htm* (03.06.2014).

[93] *Sycon Instruments STC-200 Deposition Rate Controller, Users Manual* (1994).

[94] B. Müller, *Profilanalyse bei der Reflexionselektronenbeugung (RHEED): elastische und inelastische Streuung* (VDI Verlag, 1994).

[95] W. Braun, *Applied RHEED - Reflection High-Energy Electron Diffraction During Crystal Growth* (Springer, 1999).

[96] M. Henzler and W. Göpel, *Oberflächenphysik des Festkörpers* (Teubner, 1994).

[97] J. E. Mahan, K. M. Geib, G. Y. Robinson, and R. G. Long, J. Vac. Sci. Technol. A **8**, 3692 (1990).

[98] S. Kikuchi, Jap. J. Phys. **5**, 83 (1928).

[99] A. Ichimiya and P. I. Cohen, *Reflection High Energy Electron Diffraction* (Cambridge University Press, 2004).

[100] J. L. Beeby, NATO ASI Series, Series B: Physics **188** (1988).

[101] C. H. Chen, J. Silcox, and R. Vincent, Phys. Rev. B **12**, 64 (1975).

[102] M. Gajdardziska-Josifovska and J. M. Cowley, Acta Cryst. A **47**, 74 (1990).

[103] P. B. Hirsch, A. Howie, R. B. Nicholson, D. W. Pashley, and M. J. Whelan, *Electron Microscopy of Thin Crystals* (Butterworth, 1965).

[104] C. Giftge, *Reflexionselektronenbeugung an II-VI-Halbleitern* (Cuvillier Verlag Göttingen, 1995).

[105] K. Takayanagi, Y. Tanishiro, M. Takahashi, and S. Takahashi, J. Vac. Sci. Technol. A **3**, 1502 (1985).

[106] K. Miyake, M. Ishida, M. Uchikawa, K. Hata, H. Shigekwa, Y. Nannichi, and R. Yoshizaki, Appl. Surf. Sci. **151**, 357 (1996).

[107] K. Takahashi, C. Nara, T. Yamagishi, and T. Onzawa, Appl. Surf. Sci. **151**, 299 (1999).

[108] G.-X. Qian and D. J. Chadi, Phys. Rev. B **35**, 1288 (1987).

[109] X. Peng, L. Ye, and X. Wang, Surf. Sci. **548**, 51 (2004).

[110] C. Park, R. Z. Bakhtizin, T. Hashizume, and T. Sakurai, Jpn. J. Appl. Phys. **32**, L290 (1993).

[111] Z.-C. Wu and L. J. Schowalter, J. Vac. Sci. Technol. B **6**, 1457 (1988).

[112] E. Karhu, S. Kahwaji, and T. L. Monchesky, Phys. Rev. B **82**, 184417 (2010).

[113] E. Magnano, F. Bondino, C. Cepek, F. Parmigiani, and M. C. Mozzati, Appl. Phys. Lett. **96**, 152503 (2010).

[114] Y. Li, N. Kanazawa, X. Z. Yu, A. Tsukazaki, M. Kawasaki, M. Ichikawa, X. F. Jin, F. Kagawa, and Y. Tokura, Phys. Rev. Lett. **110**, 117202 (2013).

[115] J. E. Jørgensen and S. E. Rasmussen, Powder Diffr. **6**, 194 (1991).

[116] L. Pauling and A. M. Soldate, Acta Cryst. **1**, 212 (1948).

[117] H. J. Williams, J. H. Wernick, R. C. Sherwood, and G. K. Wertheim, J. Appl. Phys. **37**, 1256 (1966).

[118] Y. Ishikawa and K. Tajima, Solid State Commun. **19**, 525 (1976).

[119] M. Ishida, Y. Endoh, S. Mitsuda, Y. Ishikawa, and M. Tanaka, J. Phys. Soc. Jpn. **54**, 2975 (1985).

[120] Y. Ishikawa and M. Arai, J. Phys. Soc. Jpn. **53**, 2726 (1984).

[121] S. Kusaka, K. Yamamoto, T. Komatsubara, and Y. Ishikawa, Solid State Commun. **20**, 925 (1976).

[122] M. Date, K. Okuda, and K. Kadowaki, J. Phys. Soc. Jpn. **42**, 1555 (1977).

[123] M. Lee, Y. Onose, Y. Tokura, and N. P. Ong, Phys. Rev. B **75**, 172403 (2007).

[124] A. Neubauer, C. Pfleiderer, R. Ritz, P. G. Niklowitz, and P. Böni, Physica B **404**, 3163 (2009).

[125] J. D. Thompson, Z. Fisk, and G. G. Lonzarich, Physica B **161**, 317 (1989).

[126] A. E. Petrova, E. D. Bauer, V. N. Krasnorussky, and S. M. Stishov, J. Exp. Theo. Phys. **104**, 47 (2007).

[127] C. Thessieu, J. Flouquet, G. Lapertot, A. N. Stepanov, and D. Jaccard, Solid State Commun. **95**, 707 (1995).

[128] C. Pfleiderer, D. Reznik, L. Pintschovius, H. v. Löhneysen, M. Garst, and A. Rosch, Nature **427**, 227 (2004).

[129] R. Ritz, M. Halder, C. Franz, A. Bauer, M. Wagner, R. Bamler, A. Rosch, and C. Pfleiderer, Phys. Rev. B **87**, 134424 (2013).

[130] T. Reimann (2011), Master Thesis, Technische Universität Braunschweig, *Wachstum und Charakterisierung von epitaktischen MnSi-Filmen.*

[131] E. Magnano, E. Carleschi, A. Nicolaou, T. Pardini, M. Zangrando, and F. Parmigiani, Surf. Sci. **600**, 3932 (2006).

[132] M. M. R. Evans, J. C. Glueckstein, and J. Nogami, Phys. Rev. B **53**, 4000 (1996).

[133] S. M. Shivaprasad, C. Anandan, S. G. Azatyan, Y. L. Gavriljuk, and V. G. Lifshits, Surf. Sci. **382**, 258 (1997).

[134] T. Nagao, S. Ohuchi, Y. Matsuoka, and S. Hasegawa, Surf. Sci. **419**, 134 (1999).

[135] Q. Zhang, M. Tanaka, M. Takeguchi, and K. Furuya, Surf. Sci. **507-510**, 453 (2002).

[136] Q. Zhang, M. Takeguchi, M. Tanaka, and K. Furuya, J. Cryst. Growth **237-239**, 1956 (2002).

[137] A. Kumar, M. Tallarida, M. Hansmann, U. Starke, and K. Horn, J. Phys. D: Appl. Phys. **37**, 1083 (2004).

[138] G. Ctistis, U. Deffke, K. Schwinge, J. J. Paggel, and P. Fumagalli, Phys. Rev. B **71**, 035431 (2005).

[139] E. Carleschi, E. Magnano, M. Zangrando, F. Bondino, A. Nicolaou, F. Carbone, D. van der Marel, and F. Parmigiani, Surf. Sci. **601**, 4066 (2007).

[140] J. H. Grytzelius, H. M. Zhang, and L. S. O. Johansson, Phys. Rev. B **78**, 155406 (2008).

[141] S. Higashi, Y. Ikedo, P. Kocán, and H. Tochihara, Appl. Phys. Lett. **93**, 013104 (2008).

[142] S. Higashi, P. Kocán, and H. Tochihara, Phys. Rev. B **79**, 205312 (2009).

[143] H. Suto, K. Imai, S. Fujii, S. Honda, and M. Katayama, Surf. Sci. **603**, 226 (2009).

[144] J. Leciejewicza, B. Pencb, A. Szytula, A. Jezierskic, and A. Zygmuntd, Acta Physica Polonica **113**, 1193 (2008).

[145] H. W. Knott, M. H. Mueller, and L. Heaton, Acta Cryst. **23**, 549 (1967).

[146] E. A. Karhu, S. Kahwaji, M. D. Robertson, H. Fritzsche, B. J. Kirby, C. F. Majkrzak, and T. L. Monchesky, Phys. Rev. B **84**, 060404(R) (2011).

[147] F. Huang, M. T. Kief, G. J. Mankey, and R. F. Willis, Phys. Rev. B **49**, 3962 (1994).

[148] R. P. Erickson and D. L. Mills, Phys. Rev. B **44**, 11825 (1991).

[149] X. Guo, X. Chen, Z. Altounian, and J. O. Ström-Olsen, J. Appl. Phys. **73**, 6275 (1993).

[150] F. Bloch, Z. Physik **61**, 206 (1930).

[151] S. V. Grigoriev, S. V. Maleyev, A. I. Okorokov, Y. O. Chetverikov, R. Georgii, P. Böni, D. Lamago, H. Eckerlebe, and K. Pranzas, Phys. Rev. B **72**, 134420 (2005).

[152] M. Sperl, W. Kipferl, M. Dumm, and G. Bayreuther, J. Appl. Phys. **99**, 08J703 (2006).

[153] W. Dürr, M. Taborelli, O. Paul, R. Germar, W. Gudat, D. Pescia, and M. Landolt, Phys. Rev. Lett. **62**, 206 (1989).

[154] C. A. Ballentine, R. L. Fink, J. Araya-Pochet, and J. L. Erskine, Phys. Rev. B **41**, 2631 (1990).

[155] R. Zhang and R. F. Willis, Phys. Rev. Lett. **86**, 2665 (2001).

[156] D. Bloch, J. Voiron, V. Jaccarino, and J. H. Wernick, Phys. Lett. **51A**, 259 (1975).

[157] M. T. Johnson, P. J. H. Bloemen, F. J. A. den Broeder, and J. J. de Vries, Rep. Prog. Phys. **59**, 1049 (1996).

[158] A. Bauer and C. Pfleiderer, Phys. Rev. B **85**, 214418 (2012).

[159] J. L. van der Pauw, Philips Res. Repts. **13**, 1 (1958).

[160] J. L. van der Pauw, Philips Tech. Rev. **20**, 220 (1958/59).

[161] C. Canali, C. Jacoboni, F. Nava, G. Ottaviani, and A. Alberigi-Quaranta, Phys. Rev. B **12**, 2265 (1975).

[162] F. P. Mena, D. van der Marel, A. Damascelli, M. Fäth, A. A. Menovsky, and J. A. Mydosh, Phys. Rev. B **67**, 241101 (2003).

[163] K. Kadowaki, K. Okuda, and M. Date, J. Phys. Soc. Jpn. **51**, 2433 (1982).

[164] A. I. Schindler and M. J. Rice, Phys. Rev. **164**, 759 (1967).

[165] K. Yosida, Phys. Rev. **107**, 396 (1957).

[166] S. V. Demishev, V. V. Glushkov, I. I. Anisimov, V. Y. Ivanov, T. V. Ishchenko, M. S. Karasev, N. A. Samarin, N. E. Sluchanko, V. M. Zimin, and A. V. Semeno, Phys. Rev. B **85**, 045131 (2012).

[167] C. Thessieu, C. Pfleiderer, A. N. Stepanov, and J. Flouquet, J. Phys.: Condens. Matter **9**, 6677 (1997).

[168] N. van Elten (2012), Master Thesis, Technische Universität Braunschweig, *Magnetotransportmessungen an dünnen epitaktischen Mangansilizium-Filmen.*

[169] T. L. Monchesky, J. C. Loudon, M. D. Robertson, and A. N. Bogdanov, Phys. Rev. Lett. **112**, 059701 (2014).

[170] M. N. Wilson (2013), Master Thesis, Dalhousie University Halifax, *Magnetic skyrmion phase in MnSi thin films.*

[171] M. N. Wilson, E. A. Karhu, D. P. Lake, A. S. Quigley, A. N. Bogdanov, U. K. Rößler, and T. L. Monchesky, Phys. Rev. B **88**, 214420 (2013).

[172] T. C. Kobayashi, H. Hidaka, H. Kotegawa, K. Fujiwara, and M. I. Eremets, Rev. Sci. Inst. **78**, 023909 (2007).

[173] K. Murata, K. Yokogawa, H. Yoshino, S. Klotz, P. Munsch, A. Irizawa, M. Nishiyama, K. Iizuka, T. Nanba, T. Okada, et al., Rev. Sci. Inst **79**, 085101 (2008).

[174] B. Bireckoven and J. Wittig, J. Phys. E: Sci. Instrum. **21**, 841848 (1988).

[175] F. M. Grosche, P. Agarwal, S. R. Julian, N. J. Wilson, R. K. W. Haselwimmer, S. J. S. Lister, N. D. Mathur, F. V. Carter, S. S. Saxena, and G. G. Lonzarich, J. Phys.: Condens. Matter **12**, L533 (2000).

[176] S. Arsenijevic, C. Petrovic, L. Forro, and A. Akrap, EPL **103**, 57015 (2013).

[177] H. Takizawa, T. Sato, T. Endo, and M. Shimada, J. Solid State Chem. **73**, 40 (1988).

[178] S. Olive-Mendez, A. Spiesser, L. A. Michez, V. L. Thanh, A. Glachant, J. Derrien, T. Devillers, A. Barski, and M. Jamet, Thin Solid Films **517**, 191 (2008).

[179] R. Gunnella, L. Morresi, N. Pinto, R. Murri, L. Ottaviano, M. Passacantando, F. D'Orazio, and F. Lucari, Surf. Sci. **577**, 22 (2005).

[180] N. Kanazawa, J.-H. Kim, D. S. White, N. Egetenmeyer, J. L. Gavilano, S. Ishiwata, Y. Onose, T. Arima, B. Keimer, and Y. Tokura, Phys. Rev. B **86**, 134425 (2012).

[181] J. B. Forsyth and P. J. Brown, J. Phys.: Condens. Matter **2**, 2713 (1990).

[182] R. P. Panguluri, C. Zeng, H. H. Weitering, J. M. Sullivan, S. C. Erwin, and B. Nadgorny, phys. stat. sol. (b) **242**, R67 (2005).

[183] S. V. Grigoriev, S. V. Maleyev, A. I. Okorokov, Y. O. Chetverikov, P. Böni, R. Georgii, D. Lamago, H. Eckerlebe, and K. Pranzas, Phys. Rev. B **74**, 214414 (2006).

[184] T. Yokouchi, N. Kanazawa, A. Tsukazaki, Y. Kozuka, M. Kawasaki, M. Ichikawa, F. Kagawa, and Y. Tokura, Phys. Rev. B **89**, 064416 (2014).

[185] C. Meingast, Q. Zhang, T. Wolf, F. Hardy, K. Grube, W. Knafo, P. Adelmann, P. Schweiss, and H. von Löhneysen, Properties and Applications of Thermoelectric Materials, NATO Science for Peace and Security Series B: Physics and Biophysics pp. 261–266 (2009).

[186] B. Roessli, P. Böni, W. E. Fischer, and Y. Endoh, Phys. Rev. Lett. **88**, 237204 (2002).

[187] S. V. Demishev, I. I. Lobanova, V. V. Glushkov, T. V. Ischenko, N. E. Sluchanko, V. A. Dyadkin, N. M. Potapova, and S. V. Grigoriev, JETP Lett. **98**, 829 (2013).

[188] J. Kondo, Prog. Theor. Phys. **32**, 37 (1964).